Εθνικό Μετσόβιο Πολυτεχνείο
Σχολή Πολιτικών Μηχανικών
Εργαστήριο Εδαφομηχανικής

National Technical University of Athens
School of Civil Engineering
Soil Mechanics Laboratory

Μεταπτυχιακή Εργασία

Ευαγγελίας Κορρέ

Επιβλέπων:

Καθηγητής Γ. Γκαζέτας

Λικνιστική Απόκριση Ελαφρώς Εγκιβωτισμένου Θεμελίου: Ανάλυση και Πείραμα Φυσικής Κλίμακας

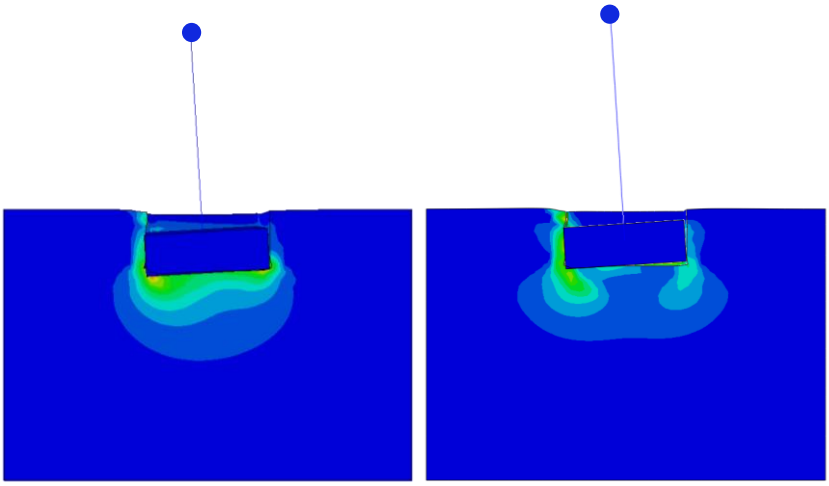

Rocking Response of Slightly Embedded Foundation: Analysis and Large Scale Testing

MSc Thesis by

Evangelia Korre

Supervised by:

Professor G. Gazetas

Αθήνα, Οκτώβριος 2015

Athens, October 2015

Ευχαριστίες

Με την ολοκλήρωση αυτής της εργασίας, θεωρώ υποχρέωσή μου να ευχαριστήσω θερμά όσους συνέβαλαν, ο καθένας με τον τρόπο του, στην επίτευξή της.

Θα ήθελα να απευθύνω ένα μεγάλο ευχαριστώ στον επιβλέποντα καθηγητή της εργασίας, κύριο Γ. Γκαζέτα, για την εμπιστοσύνη που έδειξε με την ανάθεση του θέματος, για την επιστημονική του καθοδήγηση καθώς και τις συμβουλές και αμέριστη υποστήριξη που μου προσέφερε καθ' όλη τη διάρκεια εκπόνησης της εργασίας.

Θερμές ευχαριστίες θα ήθελα να απευθύνω στη διδάκτορα Φανή Γελαγώτη, για τα καίρια σχόλιά της και τις πολύτιμες συμβουλές της καθώς και τη διδάκτορα Μαριάννα Λώλη για την πολύτιμη συμβολή της στην επίτευξη της εργασίας αυτής.

Ευχαριστώ πολύ τον υποψήφιο διδάκτορα Άγγελο Τσάτση για τη βοήθειά του στην εκμάθηση του λογισμικού καθώς και όλα τα παιδιά του εργαστηρίου για τη συνεργασία τους και το ευχάριστο κλίμα συνεργασίας που προσέφεραν.

Τέλος θα ήταν παράλειψή μου αν δεν εξέφραζα ένα μεγάλο ευχαριστώ στους: Μ. Παναγιώτου, Bruce Kutter και Α. Γαβρά για την ευγενική τους γενναιοδωρία να παραχωρήσουν τα αποτελέσματα των πειραμάτων τους, προκειμένου να τα επεξεργαστώ για τις ανάγκες αυτής της ερευνητικής δουλειάς.

Ευαγγελία Κορρέ

Στη μνήμη του αγαπητού μου πατέρα

TABLE OF CONTENTS

Chapter 1

Chapter 1

Literature Review

STUDY INCENTIVE

Over the last decades the design philosophy of the structures has adopted the idea of performance based design. This means that the engineering community has accepted the fact that overdesigning a structure will not necessarily lead to a behavior ensuring increased safety. This happens mainly because when it comes to dynamic loads such as earthquake motions, the structural behavior cannot be determined in absolute terms. On one hand there are factors related to the nature of the ground motions, which may affect different structures in different ways, due to their frequency content, PGA, PGV, duration, pulse sequence, asymmetry of motion etc.). In other words there is uncertainty when it comes to foresee an actual earthquake excitation. On the other hand the soil layering, on which the structure is founded, interacts with the structure (Soil – Foundation – Structure - Interaction, henceforth *SFSI*), thus modifying the seismic response. Consequently, we are led to a design which might be quite expensive, without however ensuring the corresponding level of safety. For these reasons, the philosophy of elastic design is nowadays considered obsolete.

Nowadays, it is widely accepted that extensively inelastic material behavior is inevitable to occur under the maximum considered earthquake (henceforth *MCE*), of the location of interest and for the specific soil where the structure is founded. The current trend is to accept and try to control the damages, which will inevitably occur during an earthquake, by taking advantage of the inelastic response of the system soil-structure. The existing codes specify the so called "ductility design". This design philosophy is based on the idea that the structural components sustain dynamic loads exceeding their capacity, without however collapsing. "Ductility" levels of the order of 3 or more are usually allowed to develop under seismic loading, implying that the strength of a number of critical bearing elements is fully mobilized [Gazetas, 2014]. This idea is materialized by guiding the damages to members of secondary importance for the whole structure. The terminology for this phenomenon is widely known as "plastic hinging" and the materialization of the methodology is based on the exact fact of allowing plastic hinges to develop, without compromising however the overall stability of the structure. It is crucial for the successful application of this methodology that the failure at those members will be flexural, diminishing any possibility of a brittle failing mechanism occurring first.

As far as the design of the foundation is concerned, the phrasing used in EC8 (Part2, Section 5.8) for example states "*foundations shall not be intentionally used as sources of hysteretic energy dissipation and therefore shall, as far as practicable, be designed to remain elastic under the design seismic action*". It is the general consensus of the current practice of foundation design that mobilization of strength should not occur on the foundation system, which practically means that no plastic hinge is allowed to develop at the foundations of the structure. Inevitably, the structure will have to maintain an elastic behavior in its supporting system. Limit states which would, under this philosophy imply failure of the structure include but are not limited to:

- Sliding between soil and footing interface
- Uplifting, especially for a shallow foundation
- Passive or shear failure of the soil along the normal compressing sides of an embedded foundation
- Mobilization of the bearing capacity failure mechanism due to cyclic uplifting of shallow foundations

This conventional philosophy unavoidably leads to factors of "over - strength" and by extension to over-design of the foundation, so that the engineer has the certainty that the performance of the foundation will be satisfactory, sustaining practically no damage. After all, inspection and repair of possible damages due to a seismic shock is practically an unfeasible solution.

However, apart from the practicality of the problem which calls for a more conservative approach, this traditional scope of foundation design arises also to a large extent from a pseudo-static way of thinking. Extensive research work has been performed over the last years to demonstrate that such a philosophy may not only burden the budget of a structure with too expensive foundation but also it may compromise its safety.

More specifically, the kinematic and cyclic nature of a seismic excitation may mobilize foundation "failure" mechanisms, which however do not necessarily lead to a system failure. Such mechanisms exploit the inelastic response of the SFSI system. Sliding, rocking and mobilization of the bearing capacity of the system are the prevailing inelastic response mechanisms which lead to remarkable energy dissipation and affect the dynamic characteristics of the soil-foundation-structure system. Apart from that, all aforementioned mechanisms have as a result the reduction of the inertial forces which are transmitted to the superstructure; hence they constitute a form of seismic isolation, the *rocking isolation*. The concept of "rocking isolation" [Mergos and Kawashima, 2005] has its origins from the very old works Housner [1963] and Meek [1975], where it was first demonstrated that allowing the foundations to uplift and rock may have a favorable effect on the behavior of the structures. By being able to rock, the foundation sets an upper bound to the inertial forces which are transmitted to the superstructure, acting thus as a means of seismic isolation. The possible perks of such a seismic design concept have been verified by several studies [e.g., Beck and Skinner, 1974; Huckelbridge and Ferencz, 1981; Priestley et al., 1996; Chen et al., 2006; Sakellaraki and Kawashima, 2006; Palmeri and Makris, 2008; Algie et al., 2009; Hung et al., 2011], and reservedly employed in practice mostly for the retrofit of existing structures [ATC-40; FEMA, 1997; Dowdell and Harmersley, 2000], but also in a few cases of newly designed large-size ("monumental") bridges [e.g., Yashinsky and Karshenas, 2003; Pecker, 2005].

The influence of the rocking isolation has been proven to be beneficial for the overall behavior by numerous researchers so far [Paolucci, 1997; Pecker, 1998, 2003; FEMA-356, 2000; Martin & Lam, 2000; Makris & Roussos, 2000; Faccioli et al., 2001; Kutter et al., 2003; Gazetas et al., 2003; Gazetas & Apostolou, 2005; Gajan et al., 2005; Harden et al., 2006; Paolucci et al., 2008; Kawashima et al., 2007; Gajan & Kutter, 2008; Chatzigogos et al., 2009; Gerolymos et al., 2009; Anastasopoulos et al. 2010].

A growing body of researchers applauds this new emerging design philosophy, according to which the failure in the form of plastic hinge is led to the soil (plastification of the soil takes place), leaving in this way the superstructure unharmed. Anastasopoulos et al. [2010] have introduced this concept by proposing that instead of using over - strength factors which would involve over designed foundation, in order to ensure that the strength of the footings exceed that of the columns and that the inertial loads be safely transmitted to the ground, act in the opposite way: Under - design the foundation "to act as a safety valve". To illustrate this suggestion, they compare two SDOF piers from a bridge structure supported on footings: one designed conventionally and the other adopting the new philosophy. The main difference in their mechanism is that in the former case plastic hinging occurs on the superstructure whereas in the latter plastification occurs in the soil. **Figure** 1.1 (a) is an illustrative comparison between the conventional and the new concept of design. The contrasting detail is that according to the conventional design, the plastic hinge is developed on the superstructure, whereas in the case of the innovative design the plastification occurs in the soil. A real example of plastic "hinging" in the superstructure is

shown in **Figure 1.1 (b)**, whereas a real example of unintentional plastification in the soil is depicted in **Figure 1.1 (c)**. The former failure occurred in the destructive earthquake in Kobe, 1995 and the latter in Adapazari (Turkey, 1999). As far as the second case in concerned, the slender building depicted founded on very soft, developed an extensive differential settlement. The soil plastification seems to have acted as buffer for the superstructure, which survived practically without damages. Of course the fact that the structure remained structurally intact is accompanied by the obvious drawback of the extensive residual rotation and settlement, which in this specific case, but not necessarily always, cannot be considered acceptable within serviceability limits.

The results of this study verified that this new concept of design provides larger margins in terms of ductility demand, the structure avoids collapse and sustains practically no structural damage for excitations which exceed the design earthquake of the structure. The cost to pay is an increased (but tolerable) foundation settlement and residual rotation.

Apart from SDOF systems, also frame structures supported on rocking foundations have been the subject of extended current research. Gelagoti et al. 2010 have investigated the response of a typical two - storey frame, which is rocking isolated, i. e its foundations have the potential of uplifting with the simultaneous yielding of the soil underneath. The building designed in accordance with the new innovative philosophy was directly compared to an identical building, designed following the conventional capacity regulations. **Figure 1.2** illustrates the two models. The structure was excited with 24 strong ground motions and the outcome was in favor for the rocking isolation. Foundation uplift proved to be advantageous, since the structure not only survived the excitations, but also did not suffer practically any significant damage. On the other hand, the conventionally founded frame collapsed during 3 excitations.

The concept of rocking isolation in the form of foundation yielding and uplifting has been investigated by many a number of researchers ever since [Anastasopoulos 2010, Gajan et al. 2005, Gajan et al. 2008, Gelagoti 2010 et al.,Gazetas et al. 2003, Gelagoti et al. 2012, Harden et al. 2006, Kourkoulis et al. 2012, Mergos et al. 2005, Paolucci 1997, Pecker 2003, Pender 2007, etc.].

A pressuring need has arisen to articulate the favorable effects of nonlinear SFSI in modern seismic design. A plethora of analytical studies has been conducted proving that nonlinear foundation response when allowed during a strong motion, leads to developing displacements and rotations, which do not compromise the stability of the structure. These analytical studies use a variety of methods such as:

(i) finite element (FE) or boundary element approaches, in which both the structure and the soil are modeled together in one single system through an assemblage of elements [Bransby et al. 1998, Butterfield et al. 1994, Gazetas et al. 2004, Gouvernec 2007, Ukritchon et al., 1998,Martin et al. 2001, ,Gouvernec et al. 2003, Taiebat and Carter, 2000; Anastasopoulos et al., 2011; Panagiotidou et al., 2012];

(ii) rigorous plasticity-based macro- element formulations [e.g., Nova et al.,Paolucci 1997, Le Pape et al. 2001, Crémer et al. 2001, Chatzigogos et al. 2009, ,Figini et al. 2012, Grange et al., 2008];

(iii) Winkler-based approaches, where the soil is replaced by a series of distributed nonlinear springs and dashpots [e.g., [Houlsby et al. 2005,Allotey et al. 2007, Raychowdhury et al. 2009, Yim and Chopra, 1985; Houlsby et al., 2005; Allotey and El Naggar, 2008; Raychowdhury and Hutchinson, 2009];

(i) simplified approaches, such as the iterative procedure proposed by Paolucci et al. [Paolucci et al. 2011] to be incorporated to the Direct Displacement-Based Design (DDBD) method [Priestley et al. 2007].

In all aforementioned cases, testing as a means to verify the arithmetic simulation was a crucial element to calibrate and validate the model for each case. Only through experimental simulation is it possible and yet of vital importance to provide evidence on the mechanisms and factors affecting the response. Experimental studies can be broadly categorized in 1 g testing, either under cyclic loading [Negro et al., 2000; Faccioli et al., 2001] or through shaking table tests [Shirato et al., 2008; Paolucci et al., 2008], and centrifuge model testing [Kutter et al., 2003; Gajan et al., 2005; Gajan and Kutter, 2008; 2009].

Although a test is necessary for the validation of the model, there are numerous factors acting during the experiment, which might compromise the experimental procedure and thus its results. Examples of such factors are provided in Chapter 2. For this reason an integral analysis to investigate the behavior of a specific system can be fulfilled only by combining the two methodologies. In other words, the testing is used to determine whether a real structure, with all its uncertainties involved (materials, eccentricities etc.) sustains the imposed loads. On the other hand, the FE model is validated according to the tests, but provides a much more detailed view in terms of stresses and deformations in areas not visible for the human eye and undetectable by any instrumentation. A cross – check between these two methodologies is of vital importance for the engineer to be certain that the test provides realistic results and that the model reflects the reality.

The objective of this study is to serve the purpose of the exact need described above. The object of study are the last large scale shake table tests of two piers supported on rocking foundations, which took place on the Large High Performance Outdoors Shake Table at the University of California in San Diego. The target is to create a validated 3D finite element model simulating the experiments, in order to further investigate their dynamic behavior. A consensus among the arithmetic and the experimental results will ensure the validity of the methods and will take us one step further towards the establishment of this new philosophy as a valid concept of foundation design.

1. THEORETICAL BACKGROUND

1.1. Kinematic and Inertial SFSI

In an effort to obtain a clearer view of the seismic performance of structures, extensive efforts in research have been devoted to the area of Soil–foundation–structure interaction (SFSI). Especially the dynamic response of the structures as well as the dynamic SSI phenomena under strong ground motions have been extensively investigated over the last decades. According to a comprehensive study by Mylonakis et al. 2006 on the problem of dynamic SSI, during a dynamic excitation the soil deforms due to the seismic waves which propagate through its mass. The structure "trying" to follow the response of the soil, develops inertial loads (forces and moments), which are induced to the soil. In this way dynamic loads accumulate on the mass of the underlying soil. This procedure of constant dynamic interaction by transmission and accumulation of loads from the soil to the superstructure and the other way around describes practically two phenomena occurring simultaneously and are known in literature as kinematic and inertial interaction (Kausel et al., 1976; Kramer, 1996; Stewart et al., 1999).

The overall response of the system soil – foundation – structure is determined as superposition of these two types of interaction and is depicted in **Figure 1.3**. The former refers to the modification of the seismic excitation due to the presence of a shallow or an embedded rigid foundation in the soil, whereas the latter refers to the overall response of the system soil – foundation – structure under a seismic excitation at the base, as it resulted from the kinematic interaction. Kinematic interaction stems from the lack of strain compatibility between the response of the soil and the rigid foundation. Hence the seismic excitation at the foundation of the system is different than the free field ground motion. This difference lies on one hand on the motion at the foundation, which has lower amplitude compared to the free field, and on the other hand on the inclusion of a rotational component in the motion at the foundation. Elsabee et al. [1977], Harada et al. [1981], Tassoulas [1984], Mita & Luco [1989], Wolf [1994] have proposed some of the most popular expressions concerning the estimation of both the translational and rotational component of the seismic excitation for both shallow and embedded foundations as well as for different types of incidentseismic waves. The inertial interaction is analyzed in two steps:

Initially is determined the dynamic stiffness (springs and dashpots) for all modes of vibration of the foundation – soil system. After the soil is replaced by the system of springs and dashpots in accordance with the previous step, the seismic response of the structure is calculated under the seismic excitation at its base. The determination of the complex value of dynamic stiffness for a system has been a topic of research in numerous studies: Richard et al. [1970], Gazetas [1983], Wong & Luco [1985], Vrettos [1999], who studied the seismic interaction of structures founded on shallow foundations, for a variety of soil types and shapes of footings. Stokoe & Richart [1974], Bielak [1975], Tassoulas & Kausel [1983], Apsel & Luco [1987], Mita & Luco [1989], Gazetas [1991] studied the dynamic response of

embedded foundations. The complex value of the dynamic stiffness for a foundation – soil system is an imaginary number and is written in the following form:

$K = \overline{K} + i\omega C$, where $\overline{K}$ represents the elastic stiffness of the system and the inertia of the soil elements and C stands for the total damping of the system, which includes also the inelastic hysteretic damping as well as the damping due to radiation. Both $\overline{K}$ and C are functions of the excitation frequency and hence not constant.

1.2. The Effect of Embedment

Both the kinematic and inertial interactions are affected by the embedment of a foundation. As far as the former is concerned, the embedment bounds the translational component of the excitation whereas it implements to it also an additional rotational component of motion (*rocking*). In general, the greater the ratio of embedment, the less significant the translational component and the more significant becomes the rocking.

Thus it comes as a reasonable conclusion that rocking is an integral component in the dynamic response of the foundation. If neglected and in combination with the assumption of a reduced translational component, it is possible that we are led to results not necessarily in favor of safety. For the sake of convenience it is practical to use as excitation of the system the one in free field. Indeed, for shallow foundations under vertically propagating shear waves it has been proven that the motion of the base of the foundation practically coincides with the one in free field. Even in lightly embedded foundations, neglecting the kinematic interaction often leads to pro safety results [Gazetas, 1983; Aviles & Rocha, 1998]. However, when it comes to slender structures, which might be founded in great depth, they are subjected to a significant rotation at the base with direct consequences in the response of the structure. In such cases ignoring the kinematic interaction, might lead to unsafe design.

As far as the inertial interaction in concerned, the embedment of the foundation in general leads to an increased value of dynamic stiffness between the footing and the soil. The peripheral contact areas between the footing walls and the surrounding soil, lead not only to an increased elastic stiffness $\overline{K}$, but also to an increased damping coefficient C of the system. However, the actual surface of “good” contact between the side walls and the soil is many a time significantly smaller than the total nominal surface of the side walls of the footing. Neglecting the aforementioned case may lead to an unrealistic estimation of the overall stiffness. Moreover subjecting embedded foundations to horizontal forces causes apart from horizontal, also rotational oscillations. Thus, apart from the conventional expressions of dynamic stiffness, which refer to a specific direction, there are also coupled complex stiffnesses. In the case of lightly embedded foundations, the coupled stiffnesses play a noticeable role in the response of the system, hence ignoring those leads to incorrect results [Mylonakis et al. 1997].

2. THE CONCEPT OF SAFETY FACTORS WELL BELOW 1.0 FOR ROCKING FOUNDATIONS

In order for the theoretical background of rocking to be introduced, it is important to address the idea of safety factors well below 1.0 for rocking foundations. The idea of F_E <1.0 stems from the fact that a dynamic safety factor below 1.0 does not necessarily imply failure for the following reasons:

a. The cyclic nature of seismic loading entails rapidly alternating cycles. The advantage we exploit in this case is the rather limited duration of the imposed dynamic loading. The subsequent displacements are reversed due to the load reversal before they reach the threshold of failure.

b. Seismic motion is an imposed oscillatory displacement at the base, i.e. it is a kinematic excitation, not an external "pre-determined" load on the superstructure [Gazetas et al. 2013]. The perk of this fact is that the factor which will ultimately bound the extent to which the loads are transmitted from the base, upwards to the superstructure is the capacity of the base or of the interface separating the structure from the base. It is obvious then that only the apparent "engineering" FS drops instantly below 1.0. Other than that, the result of F_E < 1 is a residual, inelastic deformation of the system in the form of rotation, horizontal, vertical displacement of the foundation, etc.

In **Figure 1.4** is depicted a rigid rectangular block (2bx2bx2h) resting on a rigid base with tensionless, frictional contact. Such a block was the specimen of Shake Table Tests, which took place in the Shaking Table of the Laboratory of Soil Mechanics in the National Technical University of Athens. Under quasi static conditions, the overturning acceleration of the block, as it will be discussed also subsequently, is equal to:

$A_C = \left(\frac{b}{h}\right) g$, as explained also in **Figure 1.4.**

When the block is subjected to $A > A_C$ under a constant one-directional base acceleration (i.e. under "pseudo-static" loading) just exceeding the critical acceleration, the block will overturn. Instead it is subject it to the so-called Ricker wavelet, an interesting simple motion containing three main peaks of amplitudes: A = 1.20g (the largest) and 0.72g the other two. Given the aspect ratio of the block b/h = 0.30, the apparent FS = 0.3/1.20 = 0.25.

Three different dominant frequencies are selected parametrically for the wavelet: 0.5Hz, 1Hz, and 4Hz, with the former to be used in order to introduce the effects of near-fault forward-rupture "directivity" and "fling-step" (Gerolymos et al. 2005). The latter are two representative dominant frequencies of a usual seismic ground motion. The results of the tests show that in none of the three cases occurs overturning. Apart from that, no residual rotation is observed, since the system is self-centering. The most dangerous of the three wavelets, the one of the lowest frequency, leads to the development of a maximum rotation angle close to the "overturning" one. On the other hand, higher frequencies lead to

much more limited rotations. Hence, an engineering FE much less than 1 does not lead to failure by over topping of slender rigid structures.

3. ROCKING OF SHALLOW FOUNDATIONS

3.1. Rocking On Rigid Base

The response of rigid body by considering uplift and toppling was first studied by Milne & Perry in 1881. Their studies attracted the interest of numerous other researchers, over the next years. Housner's study in 1963 on the rocking response of a solid standing on a rigid base stands out. The block was subjected to a horizontal excitation with orthogonal and a half cycle of a sinus pulses. By means of an energy approach Housner shed light on how the size of the block affects the possibility of the block's toppling. According to his findings, the larger a block is even when it has the same geometry and slenderness with a smaller one, the more resistant it is against overturning. We owe to him also the introduction of the frequency as a factor whose impact is noticeable in rocking response. This introduction was achieved by proving that the overturning of a rigid block is a function of the product of the amplitude of the acceleration pulse multiplied by its duration.

Ishiyama in 1982 pushed research one step further by investigating the combined sliding and rocking response of a rigid block standing on a rigid base. For this coupled problem he established the prerequisites for toppling. After him Spanos and Koh in 1986 investigated thoroughly the rocking response, when a harmonic excitation is imposed on the rigid block. Their analytical methods for the computation of the natural modes led to the formulation of stability graphs, which correlated the amplitude of the excitation with its frequency content and provided "safety" and "non - safety" regions. Makris et al. [2000, 2001] worked on the temporary rocking response of solid blocks, when subjected to near fault ground motions ideally simulated as trigonometric pulses. They produced analytical equations for the determination of the minimum acceleration leading to toppling and they identified the most influential parameters in the rocking response. Such parameters are: the amplitude of the acceleration pulse, the frequency of the excitation, the sequence of the pulses, the size of the rigid block as well as its slenderness.

3.1.1. Problem Statement and Kinematic Equations

To begin with, a rigid orthogonal block is considered having an aspect ratio of b/h, where b is half the width and h is half its height (**Figure 1.5 a**). It is standing on a rigid base with a friction coefficient μ high enough to prevent any parasitic sliding. The rigid block is subjected to horizontal oscillation. Provided that the overturning developing moment around the edge of the base due to its inertial force ($ma_g h$) is lower than the value mgb, which stands for the restoring moment, the block oscillates horizontally and remains fixed

to the base. By the time the restoring moment is exceeded, the rigid block loses contact with the base, i. e it uplifts and rocking behavior makes commences. Once uplifting occurs and under quasi – static conditions, the rigid block inevitable topples. Thus, in this case, the minimum acceleration needed to cause overturning of the rigid block within the static regime, practically coincides with the minimum acceleration required to cause the rigid block to uplift.

$$\alpha_{over,stat} = \alpha_c = \frac{b}{h} \quad \textbf{(1)}$$

Where $\alpha_{over,stat}$ is in units of g (acceleration of gravity).

However, the response of the rigid block alters when the conditions are dynamic. Under a dynamic excitation, the inertia force changes direction very abruptly, as the acceleration changes sign. In this way overturning is prevented. In fact under dynamic conditions as rocking occurs, whether there will be overturning or not, depends on a number of factors.

Rocking is materialized as an oscillation which takes place between the two corner points of the base being alternately pivot points. Between two consecutive impacts the governing equation of rocking motion can be expressed in the form

$$\ddot{\vartheta}\,(\mathrm{t}) = -\,\mathrm{p}^2\{\sin[\vartheta_\mathrm{c}\mathrm{sgn}\vartheta(\mathrm{t}) - \vartheta(\mathrm{t})] + \mathrm{a_g}(\mathrm{t})\cos[\vartheta_\mathrm{c}\mathrm{sgn}\vartheta(\mathrm{t}) - \vartheta(\mathrm{t})]\} \quad \textbf{(2)}$$

Where:

$\vartheta(t)$ represents the angle of rotation about the pivot points

$\vartheta_c = \arctan\left(\frac{b}{h}\right)$ is the angle depicted in **Figure 1.5**

$p = \sqrt{\frac{mgR}{I_0}}$ is a characteristic frequency parameter and

$R = \sqrt{b^2 + h^2}$ is half the diagonal of the rigid block

As long as the rigid block rocks freely, the frequency of vibration is directly dependent on the amplitude of rotation. For this reason, the factor p is not the eigenfrequency of the system, but merely a measure of the dynamic characteristics of the block. This parameter is quite influential on the rocking response of the rigid block and affects greatly the possibility of overturning (Spanos & Koh, 1986; Makris & Roussos, 2000; Apostolou et al., 2003). It is practically a regressive function of the size of the block, i. e the larger the size of the block, the smaller the value of p. Especially for orthogonal solid blocks, the parameter p equals with:

$$p = \sqrt{\frac{3g}{4R}}$$

And I_0 equals with:

$$I_0 = \frac{4}{3}mR^2$$

The special case of crucial interest for civil engineering applications is the one of a SDOF oscillator (**Figure 1.5 b**) Accepting practically negligible rotational inertia of the mass, the moment of inertia about the rotation point equals with:

$$I_0 = mR^2$$

Consequently, the frequency factor p equals with:

$$p = \sqrt{\frac{g}{R}}$$

Obviously, the system of the SDOF oscillator is a corresponding one with that of the rigid rectangular block, provided that $R_{SDOF} = \frac{4}{3}R_{BLOCK}$ (Apostolou et al. 2006). In the case of the two systems behaving in a similar way, when their base is subjected to a horizontal excitation, both of them can rotate around their centers of rotation O and O' respectively. Depending on the value of the ground acceleration and the friction coefficient, each structure may be transferred along with the base, it may slide, it may rock or it may slide and rock simultaneously. In the problems we investigate, with the rocking response being the prevailing one, we consider practically negligible sliding, by taking into account a sufficiently large value of the friction coefficient μ.

During the rocking motion around the pivot points, occurs impact on the ground and the system loses a part of its kinetic energy, even if this collision has a purely elastic nature. It's angular velocity after the impact is only a percentage of the angular velocity prior to impact. This fraction is known in the literature as the "coefficient of restitution" (often notated with the symbol e^2).

If we apply the principle of momentum preservation and neglect any energy losses due to collision, we obtain for the coefficient of restitution the well-known expression:

$$r = \left(1 - \frac{3}{2}sin^2\vartheta_c\right)^2 = e^2 \qquad \textbf{(3)}$$

The value of the coefficient of restitution calculated by Eq. (3) is the maximum possible for a block with critical angle ϑ_c set on rocking motion, under elastic impact

conditions. In reality, some additional energy is lost, depending on the nature of the materials at the impact surface.

For the sake of presenting an order of magnitude for the coefficient of restitution, an example from Apostolou et al. 2007 is cited: Let's consider a block with dimensions b = 5m and h = 12 m. From what is stated above, this would mean that the angle $\boldsymbol{\vartheta_c}$ = 0.4 rad and the maximum value of r with elastic impact is 0.60. Blocks with a larger slenderness ratio (small aspect ratio) have the tendency to maintain their angular kinetic energy, whereas less slender blocks exhibit geometric nonlinearity to a much greater extent during an impact. At the limit state of the ϑ_c reaching the value of ϑ_c = 0.95 rad (≈54°), the coefficient of restitution becomes practically zero, even if the impact conditions are purely elastic. From this stage on, no rocking can be continued after the first impact.

The governing equation of motion (Eq. (2)) along with the impact condition (Apostolou et el. 2007), can prescribe the rocking motion of a rectangular block (or any rigid structure) on a rigid base.

The correlation of moment – rotation for a rigid block is illustrated in **Figure** 1.6. The moment capacity, which the foundation can withstand, is equal to:

$$M_u = mgb = ma_g h$$

Therefore, the maximum acceleration, which can be developed at the center of mass of the block is:

$$\alpha_c = tan\vartheta_c$$

This maximum value is applied momentarily on the structure and as soon as the block uplifts, a nonlinear behavior stemming from geometric non linearity makes its presence, even in the case of purely elastic collision. After the rocking has initiated, the moment – rotation relationship enters a phase of softening, due to second order phenomena (P-Δ effects). The stiffness of the system decreases until $\boldsymbol{\vartheta = \vartheta_c}$. For this reason, rocking is an oscillating motion with a period of oscillation depending on the angle of rotation, and thus not constant. In fact, as the angle of rotation increases, the period of the system increases as well and becomes infinite at the limit state of toppling.

3.1.2. Parameters of The Problem

In this paragraph it will be described how sensitive the response is to certain crucial factors, which are mentioned below. As discussed above, in the static regime the aspect ratio (b/h) or slenderness ratio (h/b) is practically the only factor controlling the overturning response. According to the aforementioned, under dynamic conditions though, the intensely nonlinear nature of the rocking response of the structure is dependent on a group of parameters, which have to do not only with the geometry of the structure, but also with the characteristics of the excitation. As stated in Makris and Roussos [2000], there are three parameters, which determine under a horizontal excitation whether and when overturning will occur. These parameters are: the slenderness, the acceleration of the pulse normalized

to the slenderness α_p/α_g, the size of the block and the frequency ratio ω_p/p, where ω_p is the frequency of the excitation and p is the already discussed frequency parameter.

❖ **Slenderness Of The Structure**

It has already been mentioned, that the slenderness ratio (h/b) of the structure (the inverted aspect ratio) controls primarily the commencement of the rocking response, since it provides the critical acceleration value of the excitation, for which the block loses contact from its rigid base ($\alpha_c \geq tan\vartheta_c$). Ergo, the less slender is a structure, the more stable it is and the smaller rotation angles it develops. Additionally, as also discussed previously, the restitution coefficient is also dependent on the slenderness of the block; hence it comes as no surprise the assumption that the energy loss during impact is directly and uniquely dependent on the slenderness ratio. In fact, for structures intensely slender, with small ratios b/h, the attenuation of the vibration is much slower compared to less slender structures, since the coefficient $\boldsymbol{r}$ in the former case is much larger than in the latter; i. e. in the first case than fraction of the maintained kinetic energy is much more significant than in the latter.

❖ **Size of the Block and Frequency of the Excitation**

The most significant conclusion extracted from the nonlinear nature of the rocking response, is the fact that the minimum acceleration required to provokeoverturning, is a function of the block size and the excitation frequency. Both parameters affect the results of the function significantly, as reported and confirmed by many researchers over the past 50 years [Milne, 1881, Perry, 1881, Ishiyama, 1980, Housner, 1963, Makris and Roussos, 2000, Zhang and Makris, 2001, Ishiyama, 1982]. Kirkpatrick managed to correlate the two aforementioned parameters with the overturning acceleration under sinusoidal excitation, accepting small rotations and large slenderness ratios, resulting in the following formula:

$$\alpha_{over} = \frac{b}{h}\sqrt{1 + \frac{\omega_E^2}{p^2}}$$

It has been widely accepted, that a larger size of the block or a higher frequency of excitation, act in favor of the system's response [Kirpatrick, 1927; Housner, 1963; Makris and co-workers, 2000, 2001; Apostolou et al., 2003; Gerolymos et al., 2005]. A crucial question, which inevitably arises by the previous conclusion is whether high-rise buildings and tall bridge piers may safely uplift from their foundation under very strong shaking. After all, these are the main applications which capture our interest concerning the adoption of this pioneering design. Apostolou et al. (2007) investigated further the answer to this question by approaching parametrically this problem. As depicted in **Figure 1.7** for a single cycle of sinusoidal pulses with periods of 0.40 s and 0.80 s, the minimum acceleration required for toppling is strongly influenced by the size of the structure; with smaller structures being more vulnerable to toppling than larger ones, considering equal slenderness for either of them. Apart from that, it is evident that, for values of the

frequency parameter p lower than unity, the likelihood of aslender block (h/b = 5) to overturn is negligible, even under extremely strong and long-period motions. By adjusting appropriately both the slenderness ratio and the size of the structure, they investigated the overturning potential by computing the response of a rectangular block with a constant half-width b. As presented in **Figure 1.8** under a long-duration one-cycle sinus pulse of T_E = 0.8 s, a block of b = 0.5 m and h = 1.0 m must be subjected to a peak ground acceleration of 0.7 g to topple. When the half-height h increases by 1m, the overturning acceleration sinks to the value of 0.35 g. This finding is an example of the negative effect of slenderness ratio on the toppling potential;. By further increasing the half height B, the critical acceleration becomes practically constant; a fact that indicates the gradual overshadowing of the importance of slenderness ratio in favor of the size parameter. At the end of the day, the outcome is that for a sufficiently tall structure the slender a block, the more vulnerable to overturning. Thus we can safely assume that a large slender structure survives toppling even under severe seismic shaking. The experimental work performed by Huckelbridge and Clough confirms this finding; since it clarified that transient uplifting response would in no way imply imminent toppling.

Another comments worth mentioning at this point, stemming from **Figure 1.8** is the negative effect, which long period pulses have, as far as the rocking response is concerned, since we notice that for a given slender ratio, the values of the critical acceleration between T_E = 0.4 sec and T_E = 0.8 s differ by an order of magnitude! Recent studies by Makris et al. shed light to the adverse role of long-period pulses inherent in near fault ground motions.

Consequently, smaller structures develop larger rotation angles and topple more easily rather than larger structures with the same aspect ratio. It is worth mentioning that the rocking response remains constant, for a given slenderness ratio, when the fraction of $\frac{\omega_E^2}{p^2}$ (excitation frequency over frequency coefficient p) remain constant.

- **Sequence of Pulses_Overturning Spectra of Rectangular Blocks**

Apart from the frequency content, a dominant effect in the rocking response is attributed to the potential asymmetry and the exact sequence of the pulses in the time history of the excitation. This effect has been examined and acknowledged by Makris and Zhang [2001], after studying the differences in the rocking response under different trigonometric pulses. It has already been mentioned that the amplitude and the frequency content of the excitation are very influential factors modifying the uplifting – overturning behavior of rigid blocks. The presence of pulses with long duration in the excitation, also affect significantly the investigated response. Makris and Roussos [2000] concentrated on the rocking response of rigid blocks sitting on rigid base, when subjected to near-fault ground motions, which where simulated ideally as trigonometric pulses. They resulted in spectrums providing the minimum acceleration and velocity amplitudes required to trigger toppling to a free standing rigid block. The analytical solution for the overturning response was provided a year later by Zhang and Makris, as a result of their study investigating the

transient rocking response of free standing rigid blocks subjected to trigonometric pulses. Two modes are identified in the response: exhibiting one or two impacts or no impact at all. **Figure 1.9** presents the amplification overturning spectra for a rigid block with coefficient of restitution equal to 0.80, when subjected (a) to single single – sinus cycle pulse, (b) to single – cosinus cycle pulse and (c) to a Ricker pulse. Consequently, it is understandable that the acceleration amplitude alone cannot lead univocally to safe assumptions, as of whether the block will overturn or not.

Gerolymos et al. (2005) extended this study by performing a neural network analysis, in order to derive overturning acceleration spectra for rigid blocks of three different sizes. He also presented the effect of the asymmetry in the pulses of the induced motion, by using Ricker and T - Ricker type excitations, one - cycle sinus and one - cycle cosinus pulses, and rectangular pulse. Representative results of this work are illustrated in **Figure 1.10**.

3.2.1 Rocking on Compliant Soil

Having described the rocking response on a rigid base, the investigation of the rocking response is extended considering a compliant soil. This investigation is separated into two parts; the former describes the phenomenon of rocking on an elastic soil and the latter on an inelastic soil.

In general, the main difference between a rigid base and a deformable soil, is that in the latter case, additional degrees of freedom are introduced in the system. Moreover, for a structure founded on a compliant soil, rocking commences at smaller amplitudes of acceleration and rocking oscillation of the structure does not necessarily mean loss of contact with the underlying soil. In the case where soil deformability is present, rocking response is identified mainly by uplifting on one side of the footing and soil yielding on the other. The impacts, which occur during the rocking motion, absorb more energy in comparison to the case of the rigid base. Thus, the oscillation decays faster.

The behavior of the system is characterized by intense nonlinearity, either if the soil is elastic or inelastic. This nonlinearity primarily stems from the fact that the system reaches equilibrium in the deformed condition. The gradual decrease of the effective width of the footing, due to a smaller area being in contact with the soil, along with second order P - Δ effects, due to the large developing rotational angles; account for this geometric nonlinearity. Apparently, the geometric nonlinearity of the system will be bolder, when a structure is more slender and flexible.

Material nonlinearity is introduced in the system accordingly due to the constitutional hysteretic model, i. e. the relation between stresses and strains of the underlying soil.

A plethora of researchers have studied the rocking response of rigid foundations on compliant soil. Psycharis and Jennings [1983] introduced the deformability of the soil via a viscoelastic Winkler model using tensionless springs and they produced analytical

expressions which describe the response of the system during the phase, when the system is in full contact with the soil, as well as during its uplifting. Koh et al. [1986] expanded this work by implementing the flexibility of the superstructure. Later on Psycharis [2007] updated his previous work by studying the dynamic response of a rigid foundation which is attached to the superstructure through a column and rests on an elastic tensionless Winkler model. Since the linear stress distribution of the Winkler model cannot capture concentration of contact stresses in the proximity of the edges, Apostolou et al. [2003, 2007] used FE analyses in order to simulate the soil as an elastic continuum and reflect more realistically the distribution of the stresses underneath the footing.

As far as the published literature concerning the approach of inelastic soil, Allotey and El Naggar [2003; 2008] investigated the rocking response using an elastoplastic Winkler model and resulted in a solution, which took into account the condition of uplift - yield foundation defining in this way the response in terms of moment – rotation, without however allowing P - Δ effects to occur. Experimental proof was provided for the validation of the aforementioned model. The results of this study pointed out the defining impact of the inverse safety factor on both the response of the foundation through uplifting and soil yielding as well as on the maximum moment, which the system can develop. Raychowdhury and Hutchinson [2009] suggested a nonlinear Winkler model, after having calibrated it using centrifuge experimental results. The model concerned square and strip footings with various aspect ratios and numerous cases of safety factors under static and dynamic conditions. The same researchers in 2010 used their framework in order to assess the performance of buildings with shear walls standing on shallow spread footings.

The conventional “Winkler” approach ignoring the second order P - Δ effects, was replaced by Apostolou and Gazetas [2007], when they investigated in detail the rocking response of shallow footings on compliant soil by means of a macroscopic model taking into account the nonlinearities of the system soil – footing. Their model successfully reflected the regime of large displacements, which are a characteristic of the response in such systems. They developed analytical expressions for the calculation of moment, rotation, and settlement of the footing, integrating both geometric and material nonlinearities and considering both elastic and inelastic soil.

Considerable effort was dedicated toward the development of a macro element capable to describe such systems. Initially, Nova and Montrasio [1991] created a nonlinear model with isotropic hardening for the soil – foundation system. Paolucci [1997] modified this model, for applications which included real dynamic loading. Later on, in 2007 he improved his work by implementing in his model the gradual reduction of the contact area between the soil and the footing, due to consecutive cycles of loading by incorporating a a foundation stiffness degradation parameter.. In 2001 and 2002, Cremer et al. presented a sophisticated nonlinear macroelement model, capable to take into account the geometric and material nonlinearities included.

As far as the experimental works on the field of rocking response are concerned, Huckelbridge and Clough [1978] conducted in a scale of 1/3 shake table tests checking the

response of 9-story steel moment frames and concluded that the transitory uplift of the structures is favorable to their response. Additionally, remarkable contribution on findings concerning on shallow rocking foundations has been achieved by the experimental work by Gajan et al. [2005]. They performed centrifuge tests on model foundations which were attached to a rigid shear wall and were subjected to vertical and lateral slow cyclic and dynamic loading at 20g gravitational field.

3.2.2 Elastic and Inelastic Soil

In the case of lightly loaded footings or very stiff soils, the consideration of the soil as an elastic continuum is not only a logical assumption, but also it enables a convenient calculation of the response for the rocking systems (Apostolou and Gazetas, 2007). For ideally elastic behavior of the soil, the geometric nonlinearity in the response emerges with the commencement of the uplift on the foundations and as already stated, this nonlinearity is enhanced by the P - Δ phenomena, especially when it comes to very slender, flexible structures.

Due to the soil deformability, the foundation may rotate by maintaining contact with the underlying soil, as long as the amplitude of this rotation does not supersede the critical value at the initiation of the uplift. As soon as the critical value is superseded, the footing is detached from the soil. Hence, in the rocking response for a shallow footing two separate phases are identified:

- The linear phase of full contact between the soil and the footing
- The nonlinear phase when uplift occurs (**Figure 1.11**).

The influence of the soil compliance on the rocking response for an elastic soil was investigated via 2 - D FE analyses by Apostolou and Gazetas [2003; 2007]. They indicated that given a very stiff soil, the uplifting prevails during the response of the structure, whereas as the deformability of the soil layer increases, the effective width of the footing increases and the contribution of the uplifting in the overall response is limited. When it comes to the evaluation of the effect, which the compliance of the soil has on the response of the structure, the answer is not univocal. In fact, the impact may vary from beneficial to detrimental depending on the relationship connecting the rotational period of the foundation (affected by the soil characteristics), and the fundamental period of the excitation. It comes as no surprise, that at the moment when these two values have similar values, then the system demonstrates the maximum rotation angle.

For a footing resting on an elastic deformable soil, the developing moment triggering uplifting, is a fraction of the corresponding moment for a footing on a rigid base. The latter is calculated by the following formula:

$$M_{ult} = Nb$$

Where N is the total vertical load sustained by the system and b is half the width of the footing (**Figure 1.12**). In the case of a Winkler model, the threshold of moment signifying uplift is:

$$M_{uplift} = Nb/3$$

Apostolou and Gazetas [2007] resulted in a slightly different expression, by using an elastic continuum for the simulation of a homogenous soil and plain stain conditions:

$$M_{uplift} = Nb/2$$

As depicted in **Figure 1.12** as soon as the uplifting initiates due to the decreased effective width of the footing and the development of P - Δ effects, the stiffness of the system enters a softening phase, bounding in this way the maximum moment, which can be developed on the system. This upper limit corresponds to the moment capacity of the foundation.

Assuming an elastic behavior of the soil, however convenient it might be, it is of much higher interest and practical importance to assume an inelastic behavior, since plastifications underneath the edges of the footing develop already during the vertical loading, due to the distribution of the vertical stresses. In correspondence with the elastic soil, there are two distinctive phases which determine the rocking response:

- For low moment values full contact between the footing and the underlying soil is maintained. In contrast to the elastic soil however, the pole of rotation does not remain fixed at the midpoint, but its position changes among the edges of the footing, alternating toward the unloaded edge. Consequently, settlement develops during the motion at the center of the footing during this phase, contrary to the case of the elastic soil, where to pole is not only fixed at midpoint, but also there is no developing settlement at the center of the footing.
- For the same critical angle as for the case of elastic soil [Apostolou and Gazetas, 2007] commences the uplifting of the foundation. For a footing resting on an inelastic soil, the prevailing factor affecting the rocking response, is the ratio of the vertical load over the ultimate vertical load, as described mathematically below:

$$x = N/Nult$$

This factor x is no other than the inverse safety factor for vertical loading, FS_v. For large values of FS_v values of this parameter, i. e for lightly loaded structures or soils of very good quality, the uplifting prevails in the overall response, with very limited plastifications on the soil (**Figure 1.13 a**). On the other hand, increased vertical loading entails limited contribution of uplift and increased impact of the soil yielding (**Figure 1.13 b**). Both, the plastifications of the soil as well as the footing uplift result in residual rotation and settlement after the end of loading. This residual deformation is dependent on the aforementioned parameter $\boldsymbol{x}$, but is also related to characteristics of the dynamic excitation (acceleration amplitude, frequency, sequence and asymmetry of the pulses).

3.3 Flexibility of The SDOF Oscillator In Rocking

In most cases of civil engineering interest, the structures at hand (tall slender structures such as a bridge pier) rarely behave or can be sufficiently simulated as rigid blocks. In other words, no reference has been made yet concerning the flexibility of the oscillator. In general, the response of a flexible SDOF oscillator resting on a rigid base (a structure like a bridge pier) is described by the angle of rotation ϑ and the horizontal relative displacement of the mass center $\boldsymbol{u}$ as illustrated in **Figure 1.14**. An assumption not very far away from the reality is that there are two phases identified in the response of such a system: the phase of full contact between the soil and the footing and the phase when uplifting occurs. During the first phase, the observed response is limited to a flexural deformation of the oscillator, while there is no loss of contact between the two surfaces. On the other hand, during the second phase, the response consists both of flexural deformation and uplifting. In the case that the SDOF oscillator is resting on deformable soil, the first phase is no longer present, since even for very low excitation amplitudes, the deformability of the soil leads to coupled flexural and rocking oscillations (**Figure 1.15**).

On this issue it was decisive the contribution provided by Psycharis [1983; 1991], who investigated the dynamic response of a multi - storey building simulated as a n - degree of freedom oscillator, supported on elastic foundation, allowed to uplift. Moreover, he addressed the issue of the problem at hand being quite sensitive to the frequency content of the excitation. The interaction between structural and soil flexibility was also examined by Apostolou and Gazetas [2005]. According to them, when it comes to slender but quite flexible structures the inertial loading results to flexural vibration of the superstructure with marginal rocking motion.

4. MOBILIZATION OF BEARING CAPACITY MECHANISMS

4.1 Shallow and Embedded Foundations

The calculation of the bearing capacity of the foundations has been a focal point of attention for numerous researchers over the years. Apart from its importance as a topic in geotechnical engineering, it plays a remarkable role in the rocking response of slender structures, since the moment and shear loading induced on the soil – foundation system, may mobilize the bearing capacity of the system. Potential failure mechanisms include creation of shear zone, creation of a general rotational type mechanism or shear failure due to punching, according to which the footing gradually penetrates the underlying soil.

Referring to the published literature it was Prandtl in 1921 who first calculated the bearing capacity in the static regime for a shallow foundation strip, on a homogenous and

cohesive soil subjected to central vertical load. According to his results, the critical failure stress is equal to:

$$p_u = (\pi + 2)S_u$$

To account for factors like the inclination and the eccentricity of the loading and the shape of the foundation (rectangular and strip), Terzaghi [1943], Meyerhof [1953] and Vesic [1975] implemented in their analytical expressions of the bearing capacity appropriate factors.

The most well-known formula which is used in current practice is practically an updated version of the formula derived by Terzaghi:

$$q_u = \frac{Q_u}{BL} = cN_c\zeta_c + \frac{1}{2}B\gamma N_\gamma \zeta_\gamma + qN_q\zeta_q \quad (\mathbf{1.3})$$

Where:

q_u is the critical stress of the soil, Q_u is the corresponding critical loading for the foundation, B is the minimum plan dimension of the foundation, L is the maximum plan dimension of the foundation, c is the soil cohesion and γ is its specific weight. The factors N_c, N_γ, N_q are known as generalized coefficients of bearing capacity and are determined as a function of the friction angle φ of the soil. The geostatic stress at the level of the foundation is given by the factor q and ζ_c, ζ_γ and ζ_q are coefficients which account for parameters such as the shape of the footing, the inclination and eccentricity of the loading, the slope of the topography, the depth of embedment etc.

Especially for embedded foundations, the bearing capacity is calculated by means of an introduced "depth" factor (included in the analytical expression of ζ_c), which accounts for the increase in strength due to embedment referring to a foundation strip embedded to a depth equal to D from the soil surface.

The embedment increases both the strength and the stiffness of the soil regardless of the loading. This is attributed on one hand on the fact that the foundation is placed in a trench (trench effect) and on the other hand on the contribution of the side walls of the footing (sidewall effect).

Let's imagine a horizontal plane which crosses the footing at its base. Then, for the case of a shallow footing, it is free to deform, without the effect of external stresses. In the case of the embedded foundation however, the overlying soil imposes normal and shear stresses at the footing plane that constrain its deformation. This is the contribution of the trench effect and it's an effect which makes its presence even if the embedded footing has no side walls (or its side walls have practically a zero friction coefficient for a vertical loading).

The contribution of the sidewall effect stems from the fact that a part of the imposed loading on the footing is transferred to the soil through normal and shear stresses. Those develop on the interface between the side walls of the footing and the surrounding soil. The contribution of individual factors on the increase of the stiffness and the strength of the foundation depends on the type of loading and the interface characteristics among the footing and the soil. In general, the sidewalls contribute the most to the bearing

capacity of the system in the case of lateral loading, when the forces are transmitted mainly through normal stresses to the surfaces of the sidewalls.

Numerous expressions for the depth factors have been suggested in the literature for the estimation of the bearing capacity of embedded foundations, for a variety of surface conditions. The representative group of those is depicted in **Table 1.1** below.

Depth Coerfficient $\boldsymbol{d_c}$	Researchers
$1 + 0.2D/B$c	Skempton [1951]
$1 + \pi D/B$ $0.2 \leq \pi \leq 0.4$	Meyerhof [1953]; Hansen [1970]
$1 + D/B$	Bransby and Randolph [1999]
$1 + 0.27\sqrt{D/B}$	Salgado et al. [2004]
$1 + 0.86\, D/B\ - 0.16\left(\frac{D}{B}\right)^2$	Gouvernec [2008]

Table 1.1 Depth coefficients for central vertical loading of soils under undrained conditions.

The differences between these expressions are mainly the ourtcome of different assumptions for the interface between the soil and the foundation. Secondarily, the different methodologies adopted for each case, of course account also for the aforementioned dissimilarities in the approximations above. More specifically, the conventional semi-empirical relations provided by Skempton [1951] and Brinch, Hansen [1970], have been used in several applications despite the fact that they refer to a completely frictionless interface. The same applies also for Salgado et al., [2004], who have used limit analyses of upper and lower bound, without however taking into account the contribution of the sidewalls of the footing. On the contrary, Bransby and Randolph [1999] by means of an upper bound solution, assume that the foundation and the surrounding soil are fully attached to each other. This assumption leads to full mobilization of the shear capacity at the interface. The hypothesis is also adopted by Gouvernec [2008], who provides a more realistic expression of the depth coefficient, by performing 2D FE analyses.

Comparing the analytical expressions shows the significant error which will be present when estimating the bearing capacity, unless we know exactly the assumed interface conditions and the methodologies followed, leading to each and every one of them. It is underlined at this point that most of the aforementioned expressions refer only to embedment ratios $D/B \leq 1.0$.

The conventional analytical expression (1.3) for the calculation of the system's bearing capacity implies that the aforementioned depth coefficient and the shape factor are not correlated. The latter is usually considered constant regardless of the embedment ratio. For example, considering a rectangular footing with dimensions B x L (B ≤ L), the most popular shape factor is provided by Meyerhof [1953] and Hansen [1970]:

$$s_c = 1 + 0.2\frac{B}{L}$$

It comes however as no surprise that an embedded foundation has an increased shape factor, since the additional friction surfaces in the transversal direction of the loading, extend beyond the level of the foundation. According to Salgado et al. [2004] the shape factor is given as a function of the embedment ratio of the foundation as follows:

$$s_c = 1 + C_1 \frac{B}{L} + C_2 \sqrt{\frac{D}{B}}$$

Where C_1 and C_2 are coefficients dependent on the shape of the footing. It is noted however that Salgado et al. do not incorporate in their analytical expressions of the shape factor, the contribution of the additional shear stresses developing on the side walls of the footing. Those are awaited to increase even more the value of the shape factor.

4.2 Coupling Of Horizontal Translation and Rotation

When a shallow foundation is subjected to a horizontal displacement at its base, it develops a reaction in the form of the maximum shear force, which equals to: $A\tau_u$, where A is the area of the base of the footing and τ_u is the shear strength of the supporting soil. In the case that the interface between the soil and the footing observes the constitutive Coulomb model, then the shear strength of the system will be equal to $\boldsymbol{\mu N}$, where $\boldsymbol{\mu \approx 0.7}$ is the friction coefficient of the interface and $\boldsymbol{N}$ is the total vertical load stemming mainly from the weight of the superstructure. In the case of an embedded foundation, due to the resistance provided by the passive stresses, the foundation rotates and the maximum developing resisting shear force does not coincide with the capacity of the system. This phenomenon describes the coupling of the translational and the rotational degree of freedom, due to the embedment. In **Figure 1.16** are depicted failure mechanisms of embedded foundations, fully attached to the surrounding soil. Two embedment ratios are considered: $D/B = 0.25$ and $D/B = 1.0$. A lateral displacement is imposed on the footings and two scenarios are taken into account: with restricted rotation (nonzero moment) and unrestricted rotation (zero moment) [Gourvenec, 2008]. The more embedded is a footing, the more the rotational response prevails over the translational, in the case that rotation in unrestricted of course.

In a similar manner, when a rotation is imposed at the base of the footing, due to the coupling of the two degrees of freedom the translational response coexists with the rotational. In the **Figure 1.17** such failure mechanisms are presented for the case of the footing being subjected to rotation and two scenarios are taken into account: with restricted translation (nonzero shear reaction) and unrestricted translation (zero shear reaction).

4.3. Bearing Capacity for Combined Loading & Shallow Foundations

As mentioned above, the formula (1.3) is applied in common practice by many engineers. However we should bear in mind that it is merely a semi empirical expression based on a number of simplifications, which might lead to misguiding results, concerning the soil bearing capacity. It considers for example a simple linear superposition for the combined act of the cohesion, the loading of the overlying soil and the self-weight; although it is known that the soil demonstrates a purely and intensely nonlinear behavior. Apart from that, this analytical expression implies that there is no correlation between the shape and the depth factors and as for other parameters such as the inclination and the eccentricity of loading are introduced in the form of coefficients, ignoring in this way the triaxial nature of the problem. All these uncertainties lead inevitably to the adoption of unnecessarily high safety factors and by extension to an over conservative design.

The need to have a more credible analytical expression to determine the bearing capacity of the soil led to the development of new methodologies in order to approach the problem under the scope of combined loading. The most recent research is based on the derivation of interaction curves to describe the interaction of axial, shear and moment in the loading of the system. This approach has had many supporters from the research community who have examined the issue of the bearing capacity for several cases of foundation geometry, soil and interface conditions [Butterfield & Gottardi, 1994; Martin, 1994; Bransby & Randolph, 1998, 1999; Taiebat & Carter, 2000; Yun & Bransby, 2007; Gourvenec, 2007, 2008]. Most of these works refer to loading of soils under undrained conditions and the general formula for the calculation of the enveloping failure curve has the following form:

$$f\left(\frac{N}{AS_u}, \frac{Q}{AS_u}, \frac{M}{BAS_u}\right) = 0$$

Where: N is the vertical axial force, Q is the lateral shear force, M is the overturning moment, A is the plan area of the footing, B is the width or the diameter of the footing, and S_u is the undrained shear strength of the soil.

Planar FE analyses and upper bound limit state analyses were performed by Bransby and Randolph in 1998 to investigate the bearing capacity of shallow footings under full contact conditions for the interface, hence suggesting the following analytical expression to describe the failure area under combined N, Q, M loading.

$$f = \left(\frac{N}{N_{ult}}\right)^{2.5} - \left(1 - \frac{Q}{Q_{ult}}\right)^{1/3}\left(1 - \frac{M^*}{M_{ult}}\right) + \frac{1}{2}\left(\frac{M^*}{M_{ult}}\right)\left(\frac{Q}{Q_{ult}}\right)^5 = 0 \qquad \textbf{(1.4)}$$

Where $M^* = M - LQ$

L stands for the height above the level of the rotation pole of the footing at failure, when subjected to rotation at its base. N_{ult}, Q_{ult} and M_{ult} are the capacities in axial and shear force as well as in moment respectively.

In 2003 Allotey and El Naggar proposed analytical expressions based on a nonlinear Winkler model, describing the moment – rotation relationship for the two distinguished prevailing mechanisms: uplifting (x = $N/N_{ult} < 0.5$) and soil yielding (x = $N/N_{ult} > 0.5$). **Figure 1.18** depicts the different stages of the M-ϑ curve under monotonic loading.

Based on a Winkler model, Apostolou and Gazetas [2007] derived a formula describing the failure curve under N, M combined loading.

$$M = Nb\left(1-\frac{N}{N_u}\right)$$

Or in nondimensional terms:

$$\tilde{m} = \frac{\tilde{n}}{2}(1-\tilde{n})$$

Where: $\tilde{n} = \frac{N}{N_u} = x$ and $\tilde{m} = \frac{M}{BN_u}$ are the dimensionless vertical load and moment, respectively and B stands for the total foundation width.

The developing interaction curves are presented in **Figure 1.19** in dimensionless terms. Areas of linear and nonlinear response can be identified, taking also into account the soil yielding and uplifting. Areas where each of these mechanisms prevails are also identified. It is worth mentioning that a purely symmetric response is observed about the vertical axis when $x = 0.5$, which is in agreement with Allotey's and El Naggar's remark [2003], that $\boldsymbol{x}$ has a significant effect on the response of the system.

Gouvernec [2007] worked specifically on rectangular footings with various aspect ratios subjected to combined loading resulting in the derivation of enveloping failure curves under Q-N, N-M and N-Q-M loading conditions. She founded her assumptions on both analytical expressions and FE analyses, considering for the interface zero and infinite tension strength. She did not take into consideration second order P – Δ effects. Especially for N – Q – M plane of loading, the analytical expression below, in normalized terms, provides the enveloping curve:

$$\left(\frac{h}{h^*}\right)^2 + \left(\frac{m}{m^*}\right)^2 = 1.0$$

Where: $h^* = \frac{0.25-(\nu-0.5)^2}{0.25}$ and $m^* = 4(\nu-\nu^2)$

ν stands for the normalized vertical load, i. e. $\nu = \frac{V}{V_{ult}}$. In other words $\boldsymbol{\nu}$ is the inverse factor of safety , also referred to as $\boldsymbol{x}$.

$\boldsymbol{m}$ stands for the normalized moment, i. e. $m = \frac{M}{M_{ult}}$, where M_{ult} is the maximum developing moment for a given ν load. **Figure 1.20** depicts the 3D enveloping curve for V – H – M combined loading (equivalent notation for N – Q – M) and for tensionless interface. **Figure 1.21** illustrates a number of enveloping curves, in planes of H – M for $\nu = 0.25$, $\nu = 0.50$ and $\nu = 0.75$ for various aspect ratios of footings unable to sustain tension.

Based on experimental results, Butterfield and Gottardi [1994] suggested an analytical expression describing a 3D surface, which is composed by all possible loading combinations resulting in failure and does not include the inclination or eccentricity factors. The aforementioned 3D surface is presented in **Figure 1.22**.

Last but not least on the shallow foundations, Paolucci and Pecker [1997] examined the bearing capacity under seismic excitations for shallow foundation strips resting on dry soil, following a constitutive Mohr – Coulomb model. By means of incorporating kinematic mechanisms to account for the uplifting under loading of great eccentricity, they investigated the detrimental effect of the bearing capacity mobilization, due to the transmitted inertial loads of the structure and the soil. This kinematic failure mechanism is presented in **Figure 1.23.**

4.2 Embedded Foundations

Moving on the embedded foundations, as it is awaited they have been the subject of research to a much more restricted extent compared to the shallow ones. It was Martin [1994], Bransby and Randolph [1999] who first looked into the problem of combined loading for embedded foundations. They both agreed that the embedment ratio does not affect the shape of the enveloping curve; it only leads to a greater range of values, as it increases. This finding became an assumption for the majority of the modern building codes, by means of incororating the depth coefficients. Thus, a curve (formula 1.4) normalized by the capacities N_{ult}, Q_{ult} and M_{ult} can be used for the determination of the bearing capacity of both shallow and embedded foundations. A different view is presented by Yun and Bransby, [2007] and Gouvernec, [2008], claiming that the shape of the enveloping curve changes significantly as a result of the change in the embedment ratio. Their interpretation of this finding was merely the fact that an increase in the embedment leads to a stronger coupling between the translational and the rotational degree of freedom.

The formers presented a group of results stemming from planar FE analyses aiming to determine the enveloping failure curve under H-M conditions for an embedded foundation strip, fully bonded with the soil. It is noted that the notation of these researchers differs than the one of the previous ones: V stands for the axial force, H for the shear and M for the moment. **Figure 1.24** depicts the derived enveloping curves for a range of embedment ratios, in dimensionless terms and normalized by the respective capacities (H_{ult} or H_0 and M_{ult} or M_0). It is worth commenting on the significant eccentricity characterizing the interaction curves, as the embedment ratio increases. This is attributed, as already explained, to the coupling between the translational and rotational degrees of freedom becomes becoming more and more intense. For design purposes they provide the following analytical expression of the failure envelope satisfactorily provided that as point of load application for the calculation of the developing N-Q-M is the midpoint of the footing at a distance equal to in a D/2 from the level of the foundation.

$$\left(\frac{H}{H_{max}}\right)^2 + \left(\frac{M^*}{M_0}\right)^2 = 1.0$$

Where $M^* = M - LH$ is the developing moment at the midpoint of the footing, and $L = \frac{D}{2}$ is the distance of the benchmark from the level of the foundation. M stands for the moment at the foundation level.

Gouvernec in 2008 derived for the exact interface conditions between the footing and the soil, the enveloping curves under conditions V-H, V-M, M-H and V-H-M of combined loading. In **Figure 1.25** are depicted the results for the case of V-H loading, in dimensionless terms and normalized by the capacities V_{ult} and H_{ult}.

The analytical expression, in which she resulted is:

$$\frac{V}{V_{ult}} = \left(1 - \frac{H}{H_{ult}}\right)^{p}$$

Where the exponent $\boldsymbol{p}$ is associated with the embedment ratio D/B.

Figure 1.26 presents the interaction curves for V-M combined loading conditions and in this case the form of the curve does not seem to be affected by the embedment ratio. The formula describing this curve is:

$$\frac{V}{V_{ult}} = \left(1 - \frac{M}{M_{ult}}\right)^{p0.23}$$

As for the combined loading in terms of M-H, the results of Gouvernec are in accordance with those of Yun and Bransby. The lack of symmetry in the enveloping curve proves the fact that translation and rotation do not act independently of each other. In fact, the shape of the curve varies depending on the embedment ratio. On the other hand, for a specific embedment ratio the shape is not affected by the vertical load. This is illustrated in **Figure 1.27**, where sections of the enveloping curves with the M-H loading plane are presented, for several stages of vertical loading.

FIGURES OF CHAPTER 1

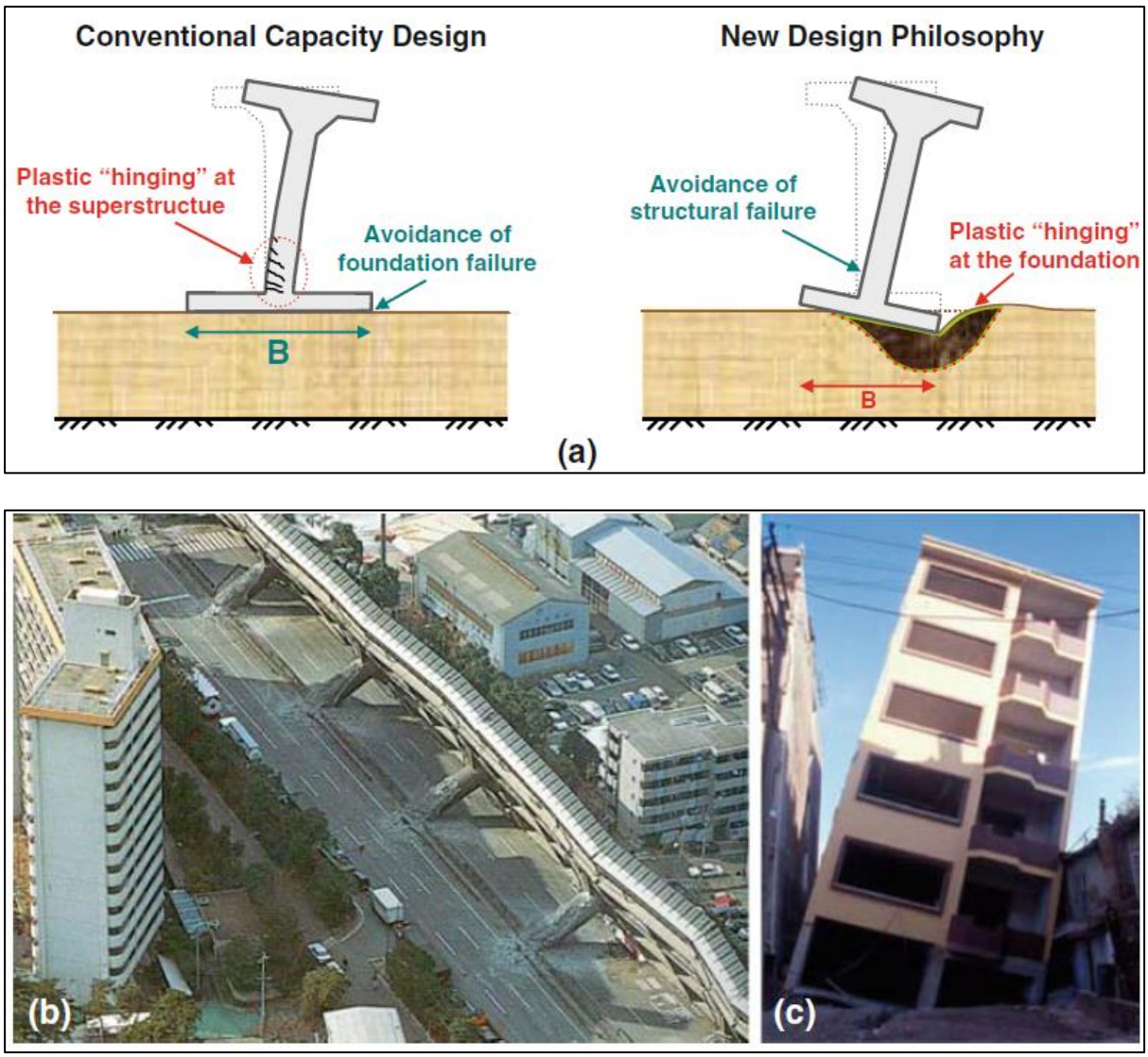

Figure 1.1 (a) Presentation of the conventional design and the design adopting the new philosophy. The main difference is that the conventional design foresees the development of plastic hinge on the superstructure, whereas the pioneering design guides the plastification to occur in the soil.

(b) Real example conventional design: Collapse of the Fukae Bridge during the Kobe, 1995 earthquake.

(c) Real example of unforeseen plastification in the soil. The slender building in Adapazari after the Kocaeli (Turkey) 1999 earthquake, founded on very soft soil, developed an extensive differential settlement. (*Source: I. Anastasopoulos et al. 2009*)

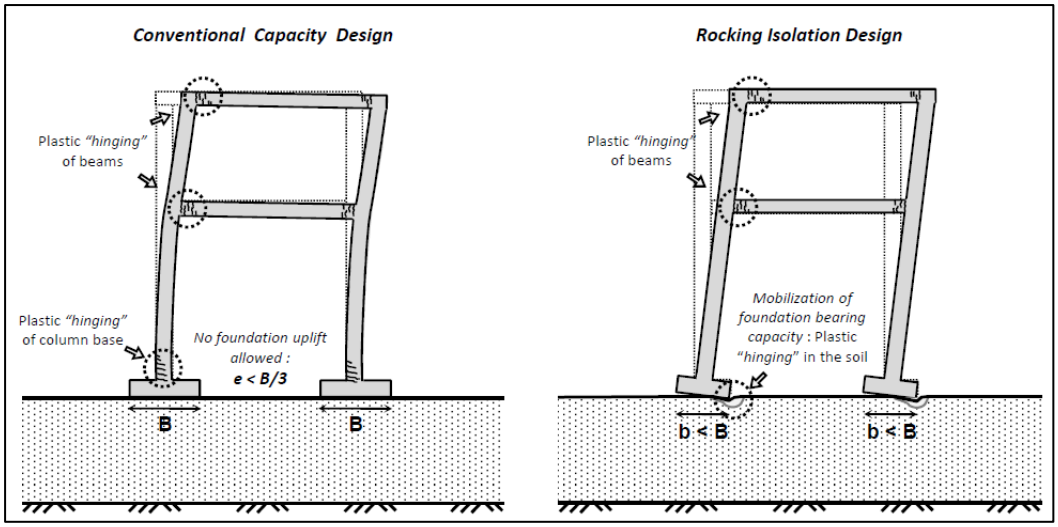

Figure 1.2 Presentation of **(a)** conventional capacity design for a typical two – storey building frame contrasted with **(b)** rocking–isolation design for of a typical two - storey rocking isolated frame *(Source Gelagoti et al. 2010)*

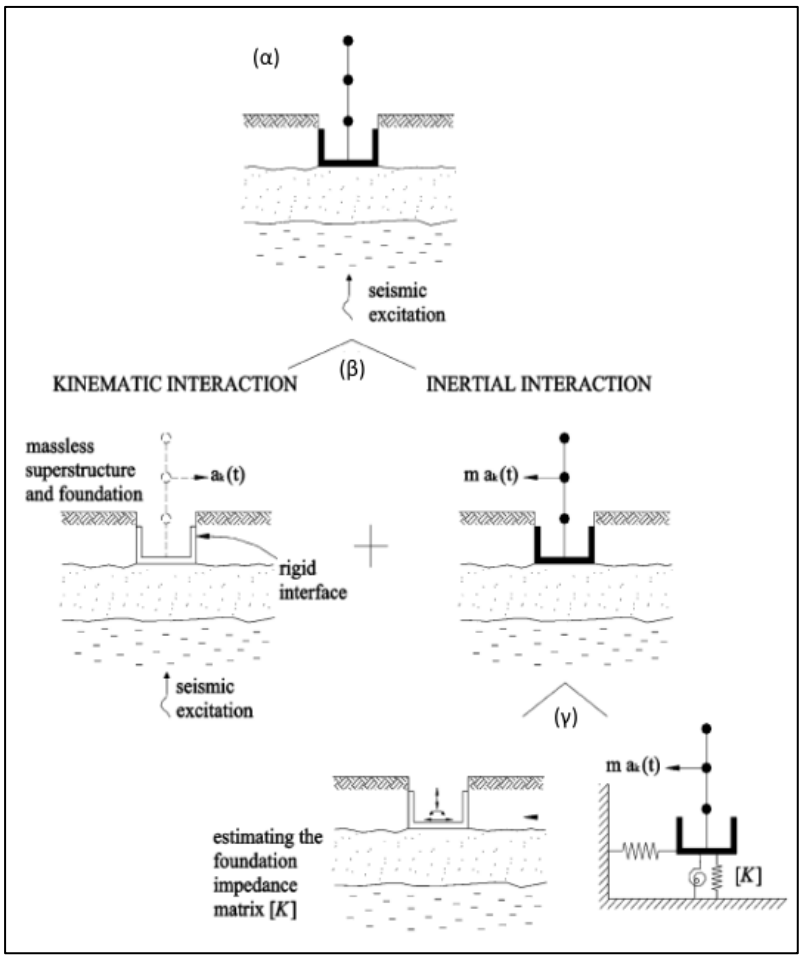

Figure 1.3 (a) Description of the problem: Dynamic Soil – Structure – Interaction (SSI), **(b)** Superposition of the kinematic and inertial interaction, **(c)** analysis of the inertial interaction in two steps *(Source: Mylonakis, 2006)*

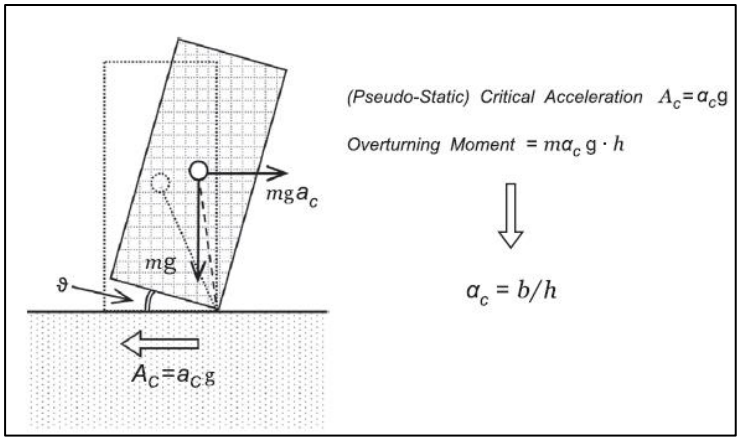

Figure 1.4 Example of slender rigid block (2bx2h): Definition of critical pseudo - static acceleration. *(Source: Gazetas et al. 2013)*

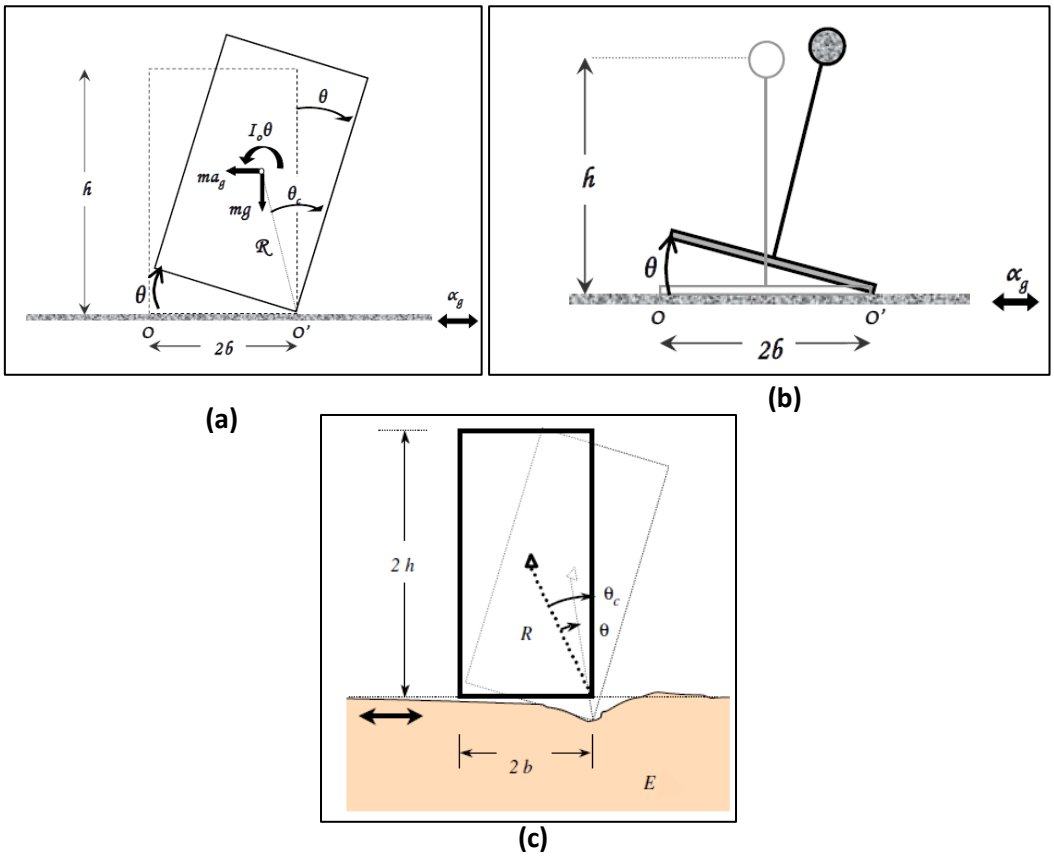

Figure 1.5 (a) Rocking of a rigid block on rigid base, **(b)** Rocking of a SDOF rigid oscillator on rigid base, **(c)** Rocking of a rigid block on compliant, elastic base.

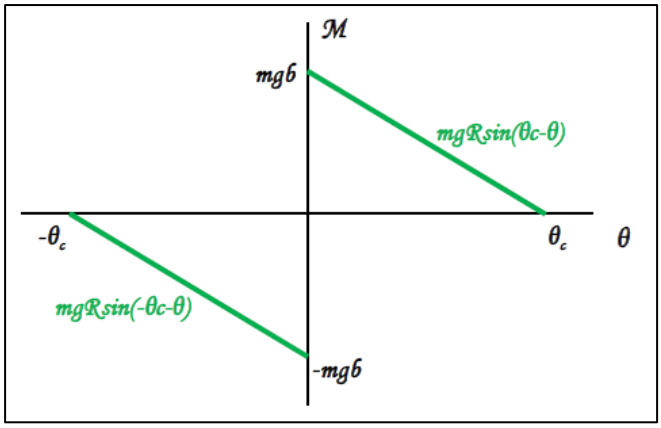

Figure 1.6 Moment – Rotation Correlation for a rigid block rocking on a rigid base

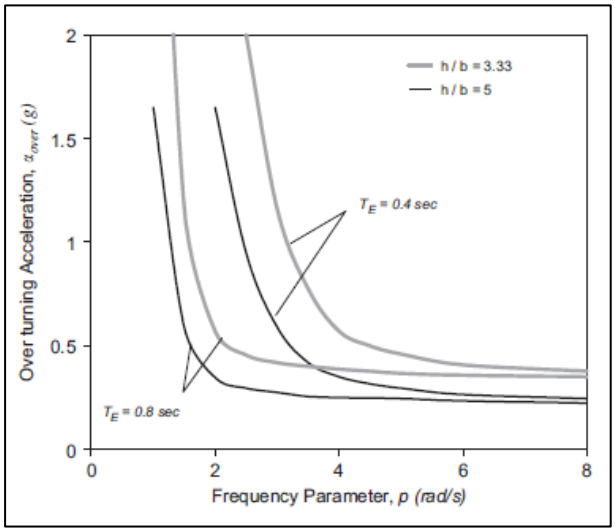

Figure 1.7 Spectra correlating the frequency parameter p with the overturning acceleration (Overturning Spectra). Blocks with aspect ratio b/h = 0.2 and 0.3 are considered and subjected to a single-cycle sinusoidal excitation. *(Source Apostolou et al. 2007)*

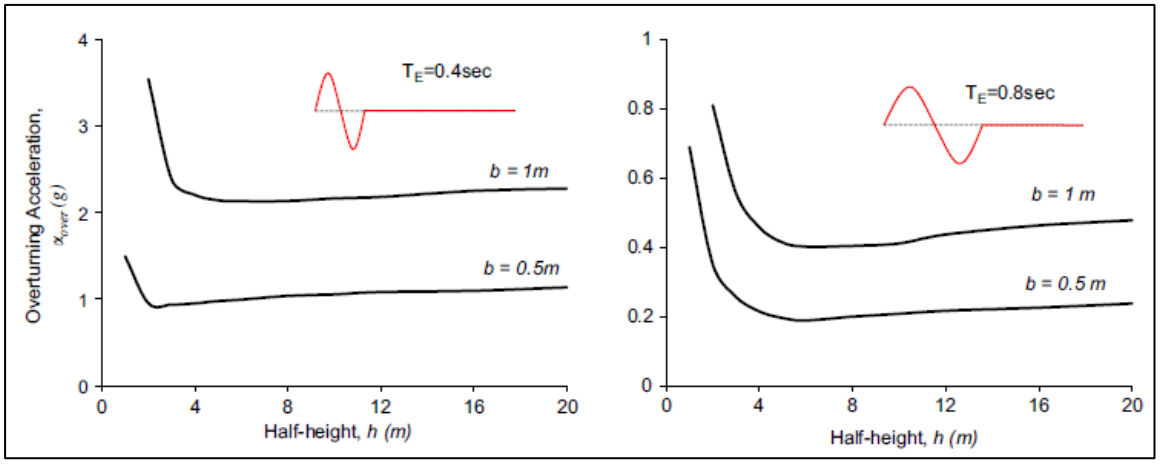

Figure 1.8 Overturning spectra for rigid blocks of various slenderness ratios, subjected to a single - cycle sinus pulse of period 0.4 s (left) and 0.8 s (right) *(Source Apostolou et al. 2007)*

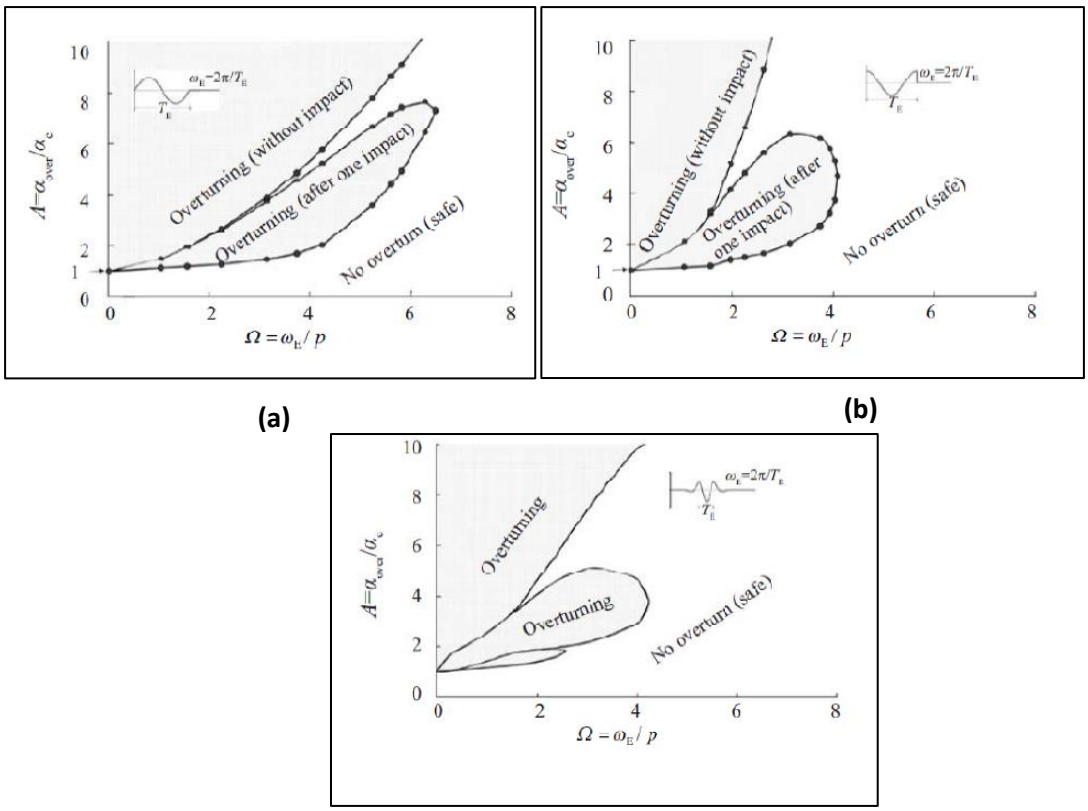

Figure 1.9 Overturning amplification ratio for slender blocks with coefficient of restitution 0.8 under **(a)** single – cycle sinus pulse, **(b)** under single – cycle cosinus pulse and **(c)** under Ricker pulse by numerically integrating the equation of motion (dots) and by analytical formula (solid lines) *(Source Zhang and Makris, 2001)*

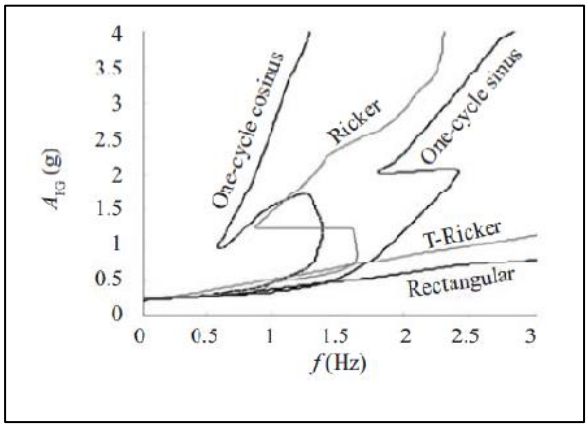

Figure 1.10 Overturning acceleration spectra of a free standing rigid block subjected to five acceleration pulses, computed by an artificial neural network *(Source: Gerolymos et al. 2005)*

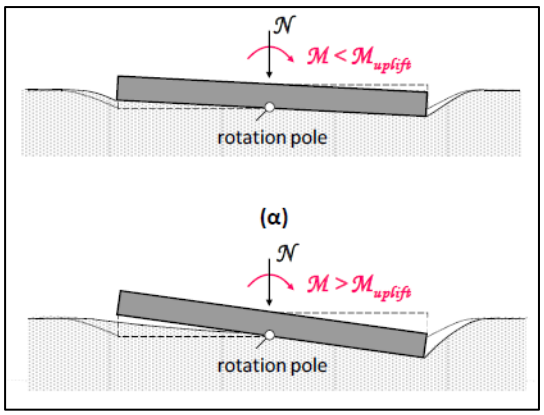

Figure 1.11 Rocking of a rigid footing on elastic soil **(a)** linear full contact phase **(b)** non-linear uplifting phase *(Source: Apostolou & Gazetas, 2007)*

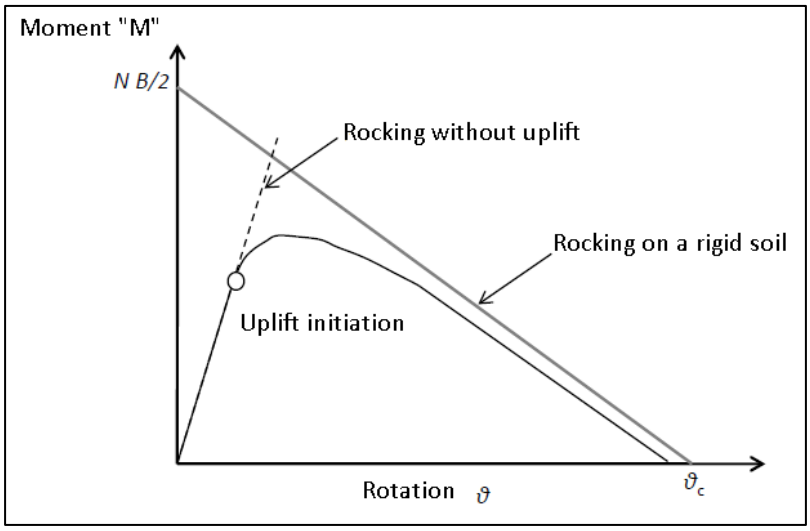

Figure 1.12 Moment – Rotation diagram for a shallow footing, considering P – Δ effects *(Source: Apostolou & Gazetas, 2005)*

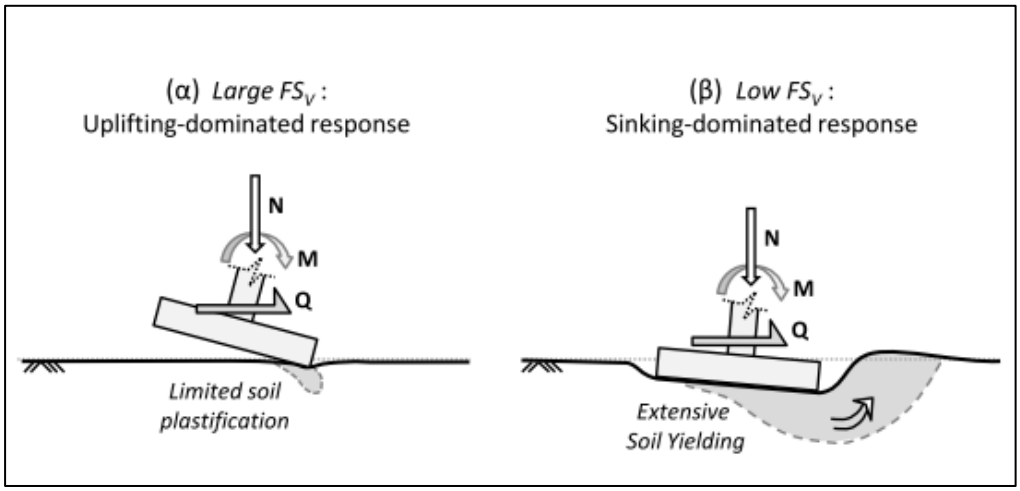

Figure 1.13 Rocking response of a shallow footing subjected to combined loading: **(a)** high values of $\boldsymbol{FS_v}$, **(b)** low value of $\boldsymbol{FS_v}$ *(Source: Anastasopoulos et al., 2011)*

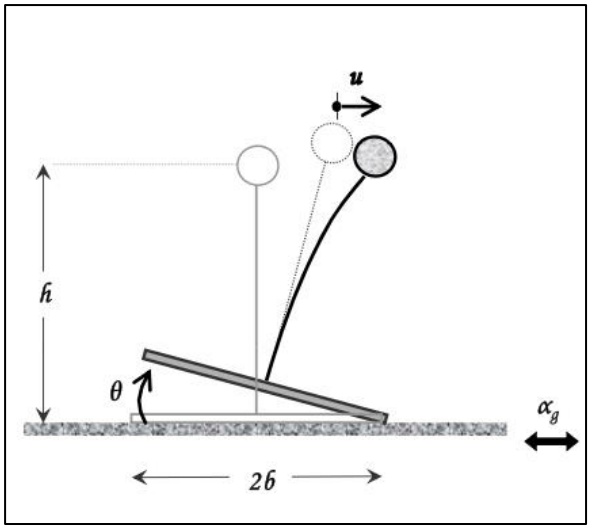

Figure 1.14 A flexible SDOF oscillator rocking on a rigid base. The response is described by the angle of rotation ϑ and the horizontal relative displacement of the mass center.

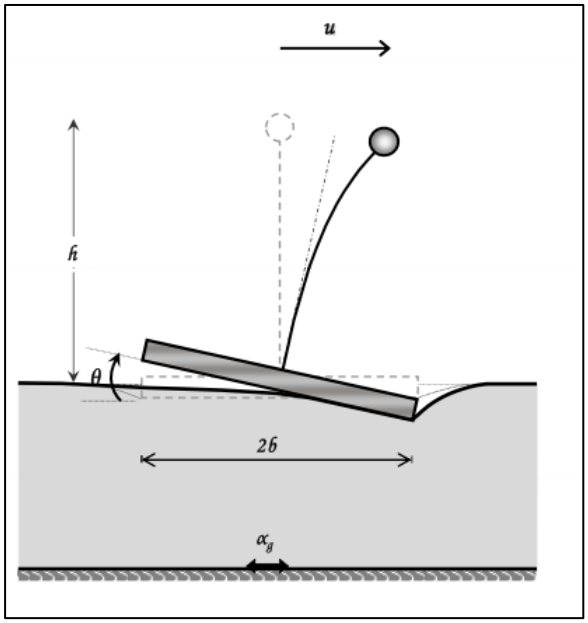

Figure 1.15 A flexible SDOF oscillator rocking on a compliant soil. The response of the system consists of coupled flexural and rocking oscillations

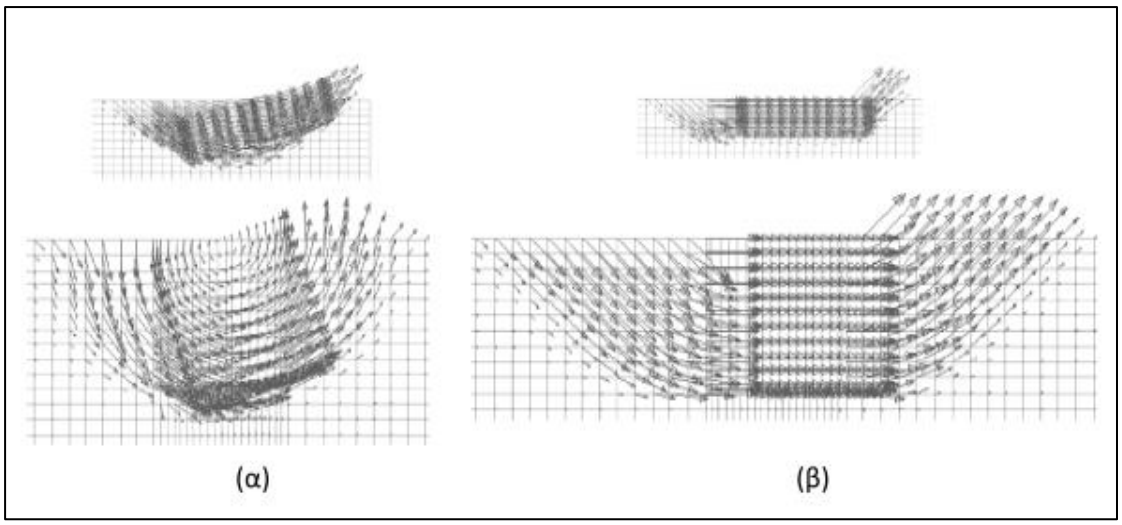

Figure 1.16 Failure mechanisms for embedded foundations subjected to horizontal loading at the base. The embedded ratios considered are: D/B = 0.25 and D/B = 1.0. In case **(a)** the rotational degree of freedom is constricted, whereas in case **(b)** it is free. *(Source: Gouvernec, 2008)*

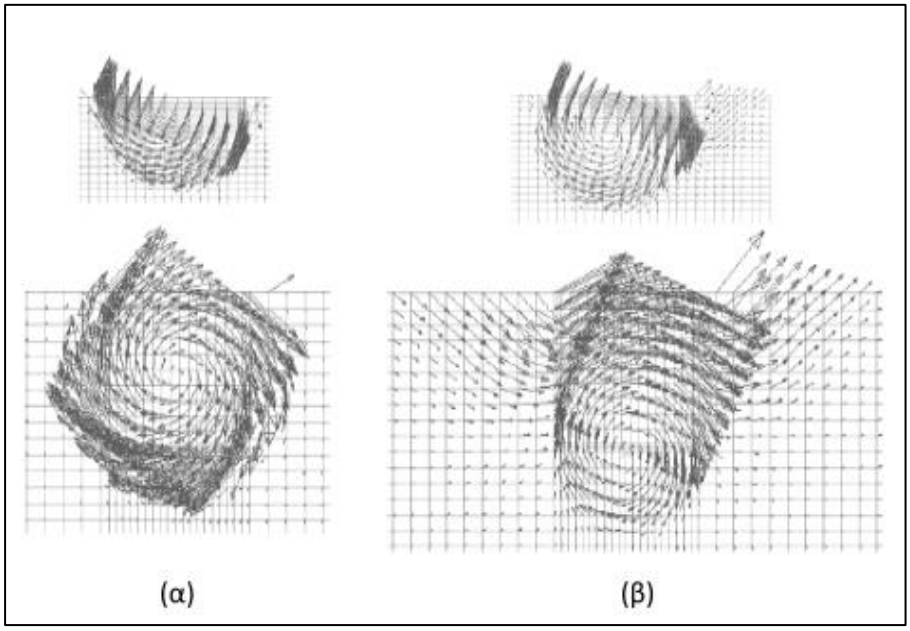

Figure 1.17 Failure mechanisms for embedded foundations subjected to moment at the base. The embedded ratios considered are: D/B = 0.25 and D/B = 1.0. In case **(a)** the translational degree of freedom is constricted, whereas in case **(b)** it is free. *(Source: Gouvernec, 2008)*

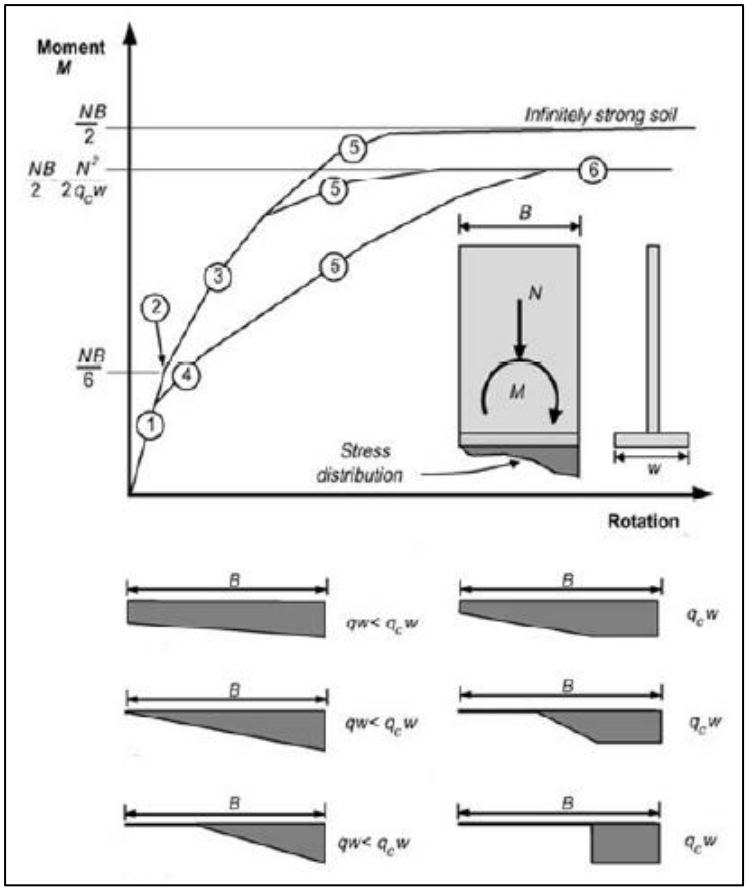

Figure 1.18 Rocking of a shear wall on a strip foundation. On the curve are visible the different stages of the relation moment – rotation under monotonic loading are discernible *(Source: FEMA 274)*

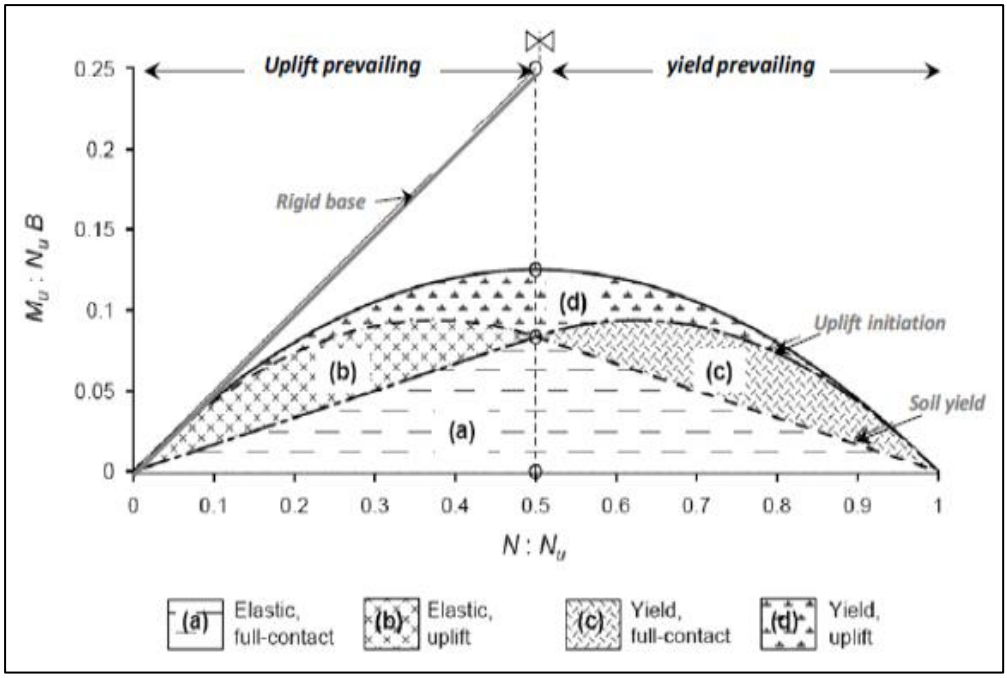

Figure 1.19 Interaction curves for shallow foundations in the M-N plane for rigid and compliant soil. The two prevailing response mechanisms, uplifting and soil yielding are decoupled *(Source: Apostolou and Gazetas, 2007)*

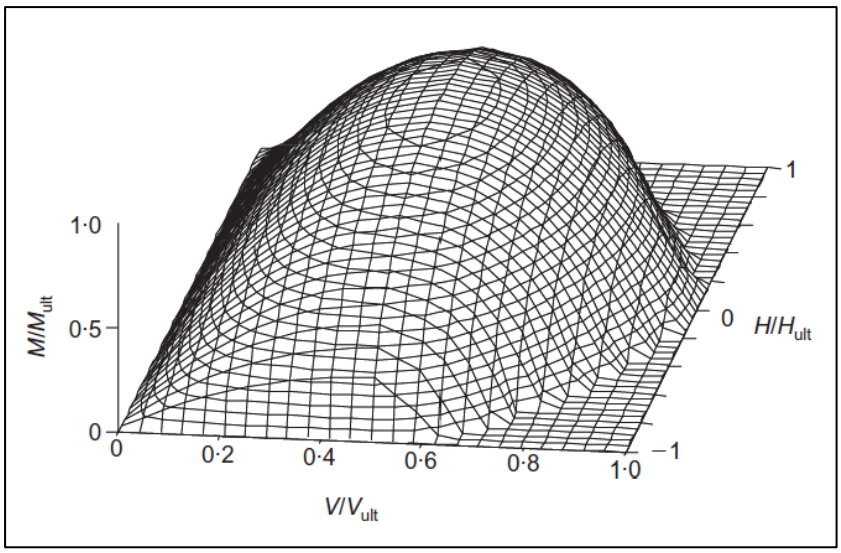

Figure 1.20 3D failure envelopes for V – H – M loading and tensionless interface [Gouvernec, 2007].

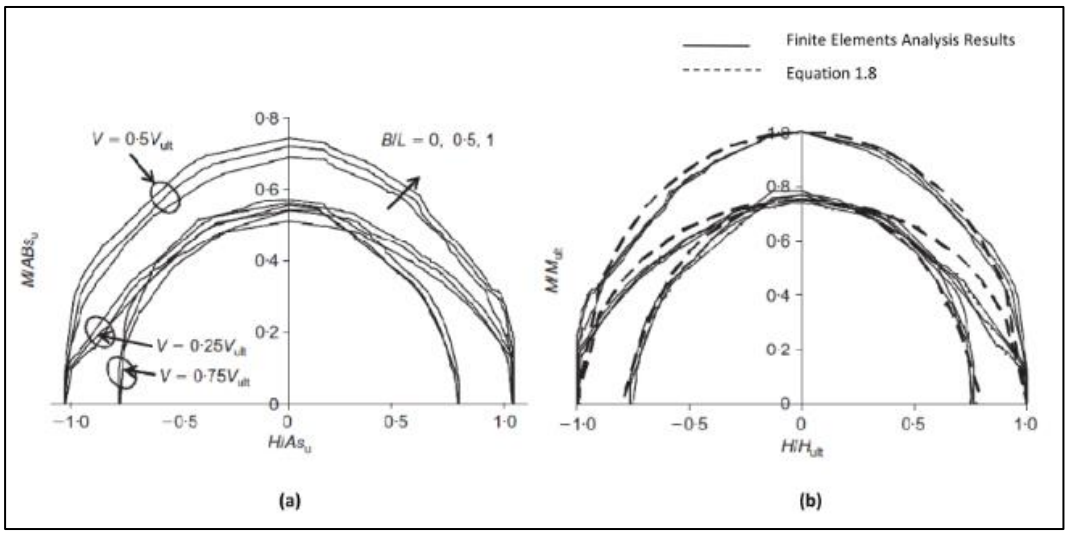

Figure 1.21 Failure envelopes for V – H – M loading and tensionless interface (a) dimensionless load space, (b) normalized load space

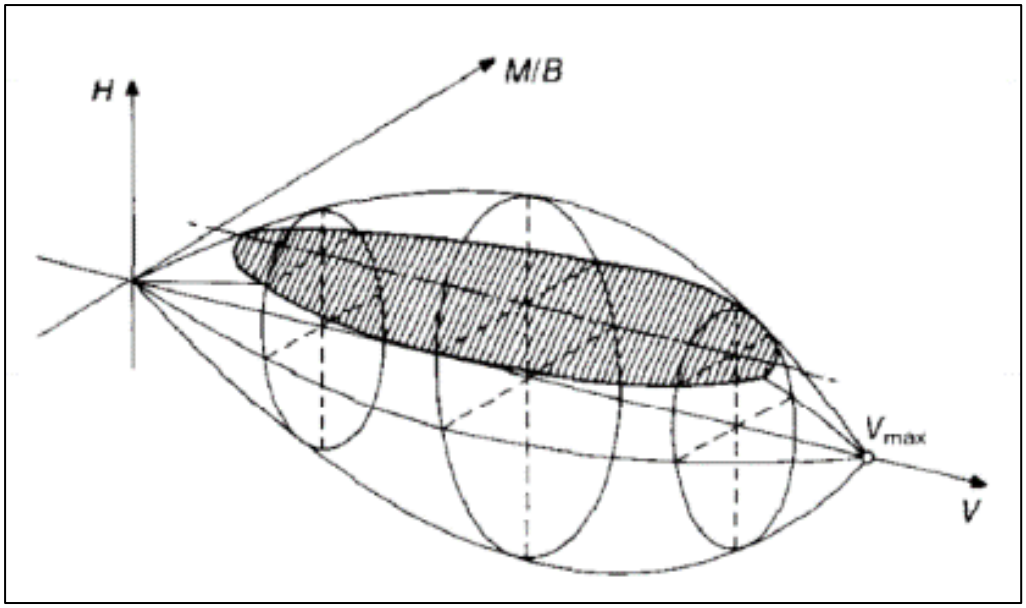

Figure 1.22 3D bearing capacity failure envelope of shallow foundation on sand (Butterfield & Gottardi [1994])

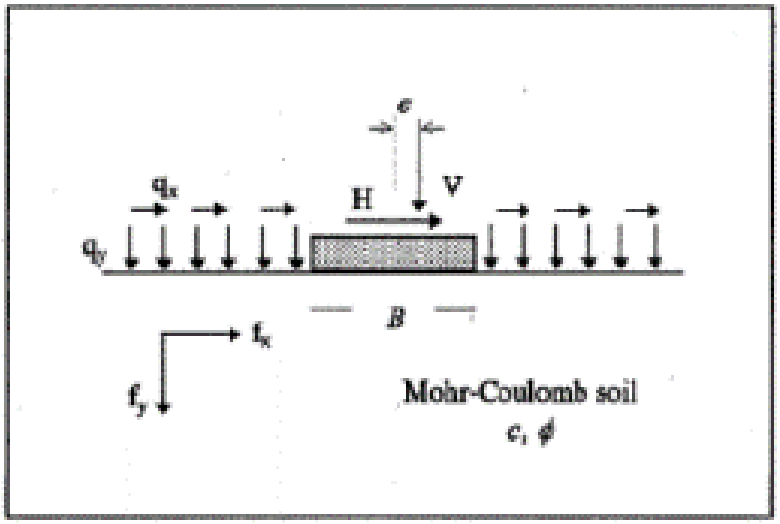

(a)

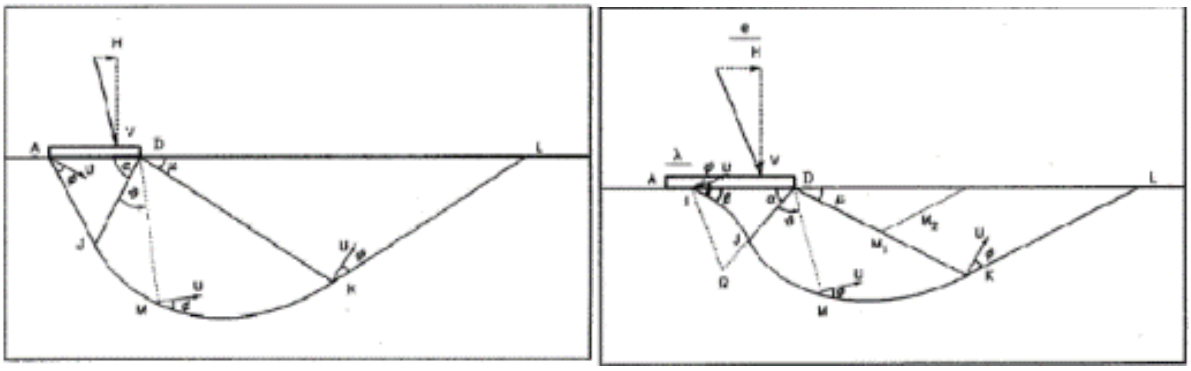

(b) **(c)**

Figure 1.23 (a) Shallow foundation standing on homogenous soil formation subjected to the constitutive Mohr – Coulomb model, **(b)** Kinematic failure mechanism defined by the parameters a and μ, **(c)** Kinematic failure mechanism defined by the parameters a, μ, λ, and β

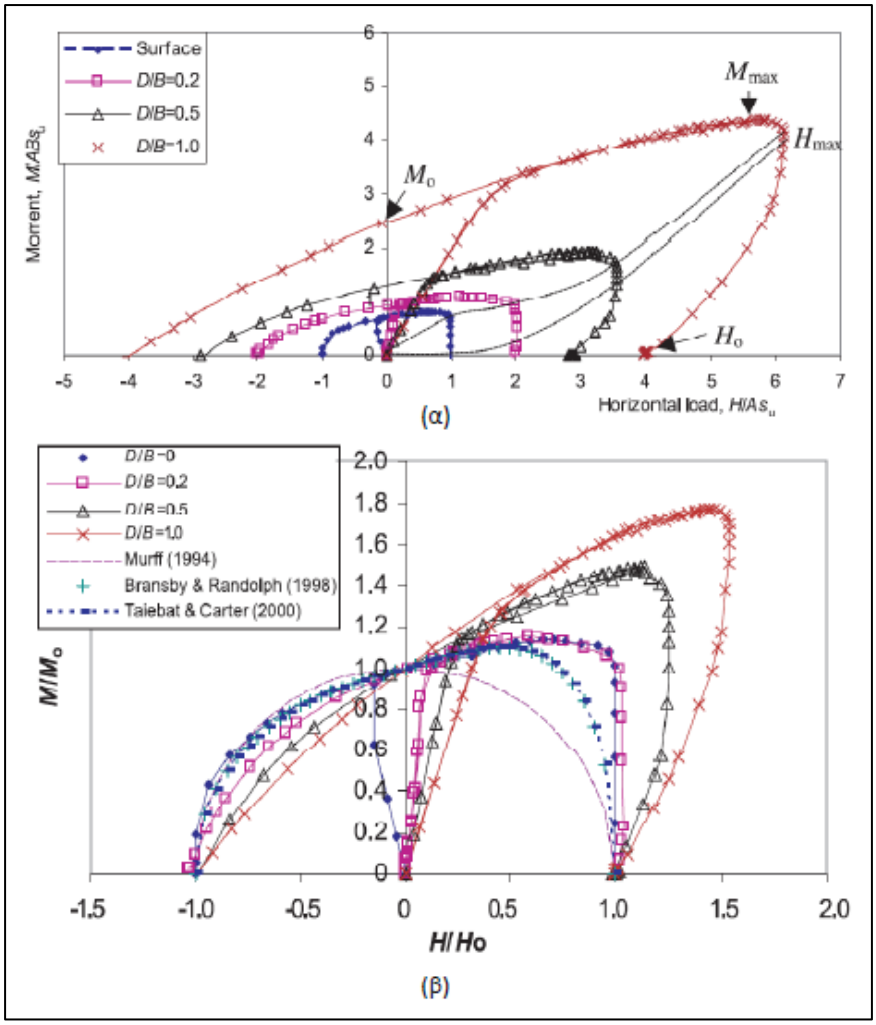

Figure 1.24 Enveloping failure curves for embedded foundations, under H – M (V = 0.0) combined loading. The footing and the surrounding soil are assumed to be fully bonded. Embedded ratios considered: D/B = 0, 0.2, 0.5 and 1.0. **(a)** dimensionless plane of loading **(b)** normalized plane of loading [Yun and Bransby, 2007]

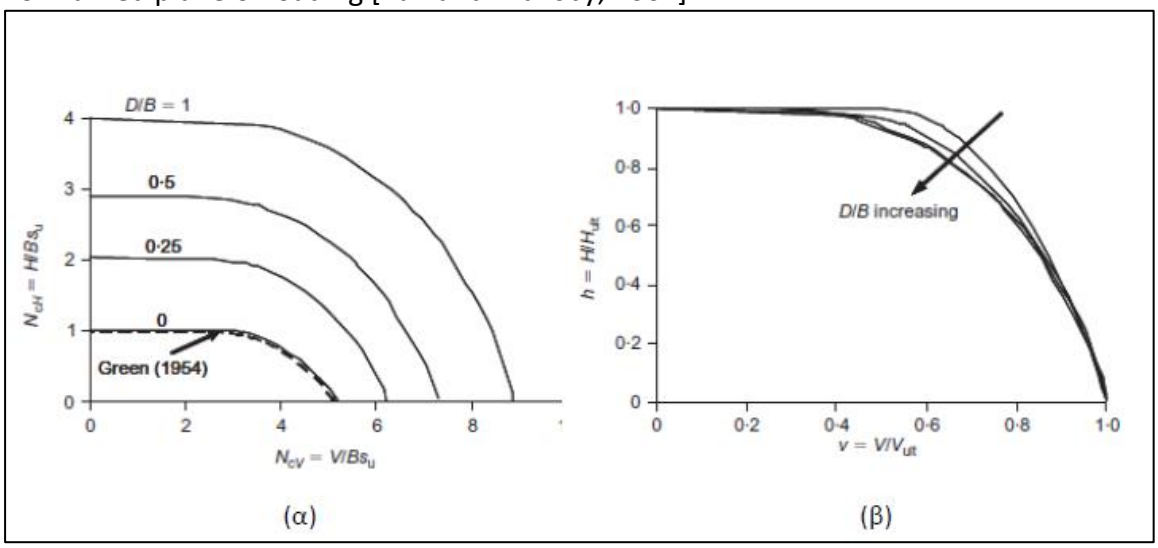

Figure 1.25 Enveloping failure curves of embedded foundations for V – H (M = 0.0) combined loading. **(a)** dimensionless plane of loading, **(b)** normalized plane of loading [Gouvernec, 2008]

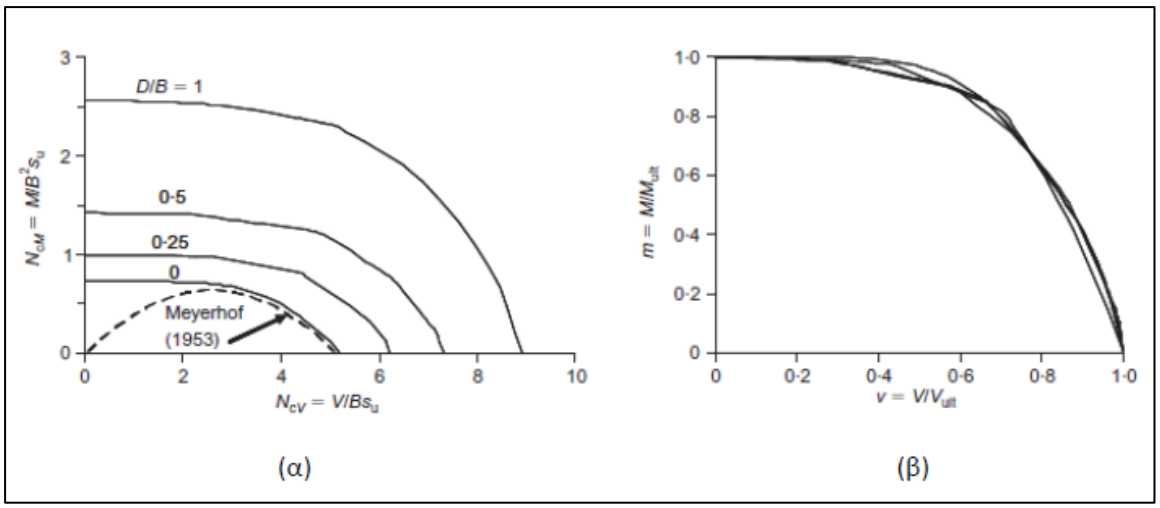

Figure 1.26 Enveloping failure curves of embedded foundations for V – M (H = 0.0) combined loading. **(a)** dimensionless plane of loading, **(b)** normalized plane of loading [Gouvernec, 2008]

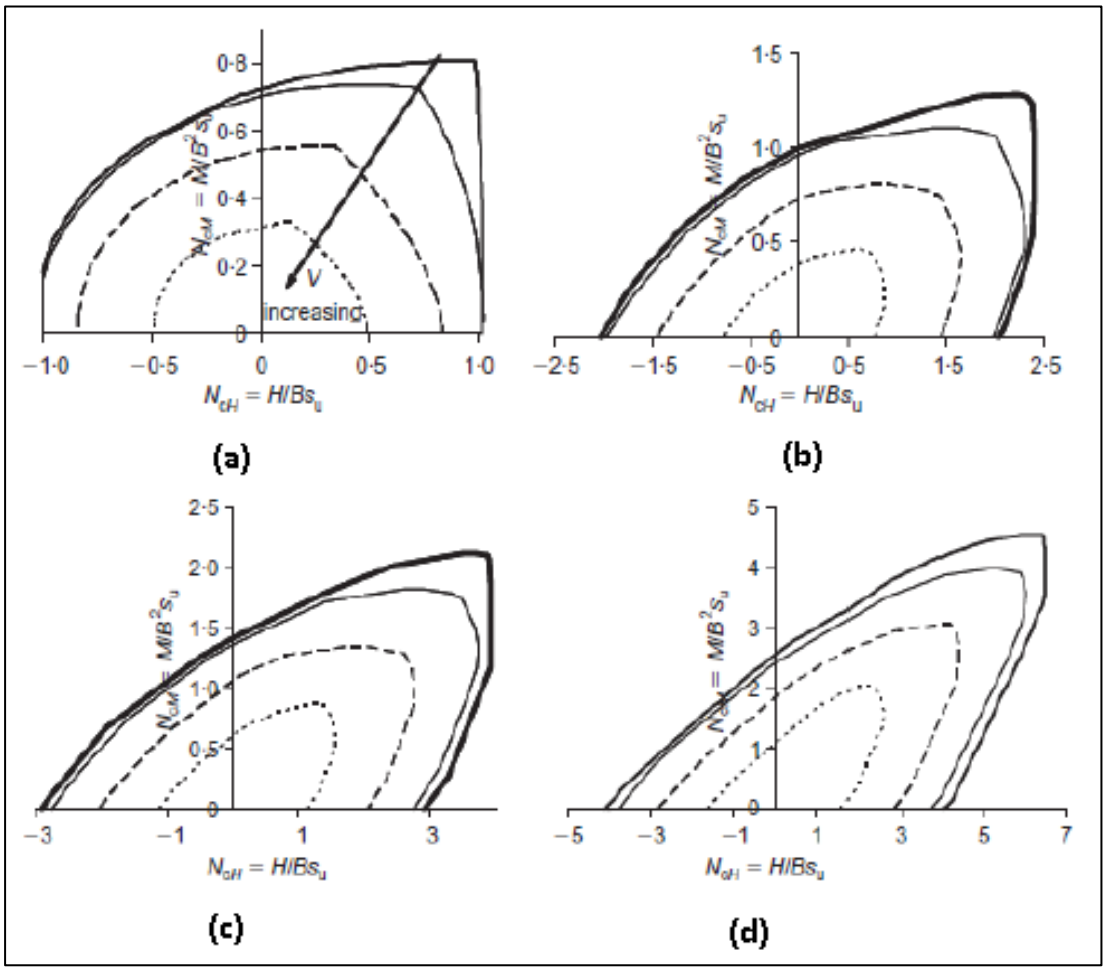

Figure 1.27 Enveloping failure curves of embedded foundations for V – H -M combined loading, considering safety factors V/V_{ult} = 0, 0.5, 0.75 and 0.9: **(a)** D/B = 0.0, **(b)** D/B = 0.25, **(c)** D/B = 0.50, **(d)** D/B = 1.0 [Gouvernec, 2008]

Chapter 2

INTRODUCTION 47

Chapter 2

Experimental Investigation of Rocking Response

INTRODUCTION

In the previous Chapter the necessity of embracing a new philosophy of foundation design, by not restricting our criteria to the pseudo static way of thinking, was extensively discussed. This restriction is still reflected by the current seismic codes which tend to prohibit the application of the "rocking isolation" concept. The mobilization of foundation capacity is not allowed and the plastic hinge is guided to the superstructure, since according to the prevailing opinion, such a behavior is believed to be more controllable, and not to be affected by uncertainties related to soil properties.

Of course the main reason behind this conservatism is the inherent "fear" that mobilization of foundation capacity, either in the form of uplifting or in the form of soil yielding underneath the foundation, may lead to toppling collapse of the structure [Anastasopoulos et al. 2013].

During the last years, some modifications have been incorporated in the building codes, concerning the rocking response of the structures, yet there is still room for further alterations.

As already mentioned in the first Chapter, EC8 clearly prohibits the inelastic response of the foundation, either in the form of uplifting or in the form of soil plastifications. The exact phrasing used in EC8 (Part2, Section 5.8) concerning foundation design is: "*foundations shall not be intentionally used as sources of hysteretic energy dissipation and therefore shall, as far as practicable, be designed to remain elastic under the design seismic action*".

Other building codes however, seem to have been more "receptive" to this new concept. More specifically, in the New Zealand's Transport Agency's Bridge manual [2013], a separate category has been defined for the structures on rocking piers under horizontal seismic load. According to this manual, such a system is characterized as a "special case of ductile structure". The manual provides a clear and integral definition of such a system, identifying the two main characteristics of its response: Firstly, that the footings have the tendency to lift at alternate edges and secondly, that the deformation of the soil and the impact effects provide energy dissipation. However, as stated in the text of the code, "*due to the lack of experimental or practical experience of such a system, a maximum value of ductility* $\boldsymbol{\mu = 3}$ *shall be adopted, unless a larger value can be specifically justified*". This means practically that, the structure shall be designed in such a way, so that the ultimate total displacement at the center of gravity is not larger than 3 times the total displacement at the same spot, at the initiation of rocking. Regarding the displacement at initiation of rocking as D_y (yield), then a ductility factor of $\mu = 3.0$ is defined according to the aforementioned demand. A characteristic illustration of the allowable ductility values on several types of structures is provided in **Figure 2.1**.

The methodology in this manual takes into account that components of the foundation structure or soil might yield and there is also the possibility of rocking or uplift of spread footings on the response and energy dissipation characteristics of the structure. However, the principles of capacity design shall be applied for both the footing and the pier, so as to provide the certainty that any yielding occur in the pier stem, assuming design soil bearing strength. In the case that a plastic hinge is developed at the base of the pier, then special measures have to be taken, to ensure that the column can sustain the possible limited rotation In the interaction between the structure and the foundation during rocking, a careful assessment has to be performed concerning the degradation of the soil strength and the stiffness of the system.

Otherwise put, the response of the system should not include mobilization of the soil bearing capacity, the design shall still follow the conventional capacity concept, and even if rocking is selected as the prevailing response mechanism, a significant conservatism in terms of the ultimate developing displacement is still present in the design philosophy. This fact has been also illustrated by Anastasopoulos et al. 2010, who showed (**Figure 2.6**) that a conventionally designed system may reach a ductility value of approximately 5.0, whereas a

design observing the new philosophy may reach a multiply larger value, sustaining practical no damage.

According to the latest modifications in the Current Foundation Requirements in Canada, they were founded on nonlinear response history analysis, which was conducted on shear wall buildings. The capacities of the shear walls, the foundations, and the soil properties varied, aiming at a generalized conclusion that practically all foundations free to rock experience extensive rotations, which increase as the stiffness of the system decreases.

A number of significant changes have been made to the foundation design provisions in the 2015 Canadian Building Code. First and foremost, there has been a redefinition of the foundations categories, based on their overturning capacity.

- A foundation that is designed for the maximum overturning capacity is expected to remain essentially linear under the design earthquake.
- A foundation designed according to capacity principles is expected to be protected from large inelastic demands in the soil by yielding of.
- The third type of foundation has an overturning capacity less than the one offered by the systems in the superstructure providing resistance to the seismic forces; but more than the minimum overturning capacity.

The traditionally called "*rocking foundation"* in the Canadian codes following the behavior described in the third point, will not be assigned this characterization any more. The reason behind this modification is that a *rocking* foundation refers to foundations free to rotate according to the classical rocking mechanism, which involves a rigid block on a rigid half-space. The behavior of the systems following this mechanism differs significantly from the behavior of foundations which do not have sufficient static overturning capacity to resist the magnitude of a dynamically applied overturning moment. The main argument of the researchers underlying this difference between the two systems is the fact that the rigid block displays rocking behavior when the overturning moment *exceeds* the overturning resistance provided by the block self-weight. Apart from that, it has the ability to re-center when the overturning moment is reduced.

On the other hand, in the case of "rocking" foundations, due to soil deformations and plastifications at the "toe" of the footing, the opposite edge of the footing rises and the foundation rocks *well before* the overturning capacity of the foundation is reached. The term used in the 2015 Canadian Building Code for what was previously called "*rocking"* foundations, is "*not capacity protected"* (NCP) foundations.

In Canada, two force reduction factors are used to determine the seismic loads. $\boldsymbol{R_d}$ is a ductility-based force reduction factor, while $\boldsymbol{R_0}$ is an overstrength-based force reduction factor. The current requirements of the National Building Code of Canada *(*NBCC) are summarized as follows:

(a) The design of the foundations shall observe the principles of capacity design. The transmitted earthquake loads and their consequent effects on the superstructure and the soil shall not exceed the capacities of the soil and rock;

(b) Foundations shall be designed to resist the lateral load capacity of the superstructure. However in the case that the foundations are allowed to *rock*, the design forces for the foundation need not exceed those determined using an $\boldsymbol{R_d * R_o = 2.0}$.

(c) If foundation *rocking* is justified in the response of the system, then the design forces for the system resisting the seismic forces need not exceed the maximum values dictated by foundation rocking.

In other words, soil yielding is not allowed in the response of the system, a ductility factor of $\boldsymbol{\mu \cong 2}$ is considered, when foundations are designed with the ability to rock and again the conventional philosophy of the moment capacity of the foundations being at least equal to the one of the system, is dictated.

As stated in the new provisions, stemming from the results of the analyses, only unrestrained against rotation foundations may be designed as not capacity-protected ones (NCP). The prerequisite for the application of such a design is the provision of proof, that the system and the members not considered part of it can tolerate the increased displacements.

Thus the factored flexural and shear resistances of the footing in NCP foundations must be sufficient to develop the smallest of:

(a) the forces determined using a bearing stress in the soil or rock. For the bearing capacity of the underlying soil a safety factor of $\boldsymbol{2.5}$ shall be applied;

(b) the forces resulting from an applied moment on the foundation equal to the nominal overturning resistance of the superstructure, or;

(c) the forces from design load combinations including earthquake loading calculated using $\boldsymbol{R_d\ R_0}$equal to 1.3. This practically means, that for an overstrength factor $\boldsymbol{R_o = 1.0}$, and a sufficiently flexible structure, a ductility factor of approximately 1.3 shall be applied.

Another characteristic example of building code, demonstrating skepticism against this new concept are the specification standards as published by the department of Transportation of the State of California, U. S. A. (CALTRANS). According to these regulations, the traditional seismic design of bridges in California is taking advantage of the inelastic response of the columns, allowing the formation of plastic hinges [Caltrans SDC 2010]. Despite the fact that according to this design, the structure is safe against collapse, it may require a costly and prolonged restoration. For instance, as a consequence of the deleterious 1995 Kobe earthquake, residual drifts of bridge columns resulted into destruction and replacement of over a hundred bridges [Jeong et al. 2008]. Even in cases of piers which maintained their functionality, residuals drifts larger than $\boldsymbol{1.0}\%$ had to be refurbished for aesthetic reasons and for the public to feel safe when using the bridge. Hence, retrofitting works such as additional casting of concrete and enlargement of the cross sections along the height of the columns, so that they appear straight and cover minor concrete cracks and spalling in the columns, may lead to a cost up to $\boldsymbol{20.0}\%$ of the initial construction budget [Antonellis and Panagiotou, 2013]. To these costs, additional ones have to be included, having to do with potential bridge closure during the period of repairs.

The overall damage is not quantified only in monetary terms, but also in terms of time costs. Delays, due to the post-earthquake inspection and verification of the foundation system, increase the budget significantly as well. While the aforementioned disadvantages and losses support the need for this new philosophy in design, on the other hand the distrust toward the new concept is partly justified, since there is lack of well-established and calibrated methods to study the post-yielding behavior of soil–foundation systems under strong seismic loads. Thus the creation of the right framework of performance-based design, incorporating an effective and credible model, simulating the post-yielding behavior of SFSI systems is necessary.

In order to alleviate the above skepticism, extensive research has been conducted to obtain insights and quantify the main aspects of strongly nonlinear foundation response.

The alternative design involving rocking foundations, decoupling in this way the superstructure from its base, has been introduced [Pecker 2006, Anastasopoulos et al., 2010] and studied analytically in detail and its perks have been pointed out by a number of researchers [Sakellaraki and Kawashima 2006, Apostolou et al. 2007, Deng et al. 2012, Gelagoti et al. 2012, Antonellis and Panagiotou 2014]. According to this concept, the column is attached to the overlying deck with a pin connection and remains nominally elastic [Deng et al., 2012; Antonellis and Panagiotou, 2014].

Sakellaraki and Kawashima [2006] analyzed a bridge with columns on rocking foundations under a single near-fault ground motion record. They proved that the columns sustained practically no or very limited damage. Antonellis and Panagiotou [2014] demonstrated that hypothetical bridges located 3 km from the Hayward fault can be designed using rocking foundations to eliminate column damage after the Maximum Considered Earthquake (MCE) level of seismic excitation.

In spite of the increased number of analytical studies performed on the investigation of this a matter, a key element of those works has been the calibration and validation of the simulation using experimental results. The seismic response of rocking foundations has been studied experimentally using: large scale pseudo-static cyclic tests [Negro et al., 2000], shake-table tests with physical modeling of the soil [Paolucci et al., 2008; Shirato et al. 2008] and without physical modeling of the soil [Saiidi et al., 2002; Espinoza and Mahin, 2008, Hung et al. 2010], and small-scale shake table tests including physical modeling of the soil [Anastasopoulos et al. 2013]. Centrifuge testing has also been an extensively used way of checking experimentally such nonlinear SFSI systems [Deng et al., 2012a; Loli et al., 2014; Kim et al., 2014.

Researchers who performed the tests, without physical modeling of the soil, they either used relatively thin elastic pads to represent soil [Saiidi et al., 2002; Espinoza and Mahin, 2008] or thick neoprene pad simulating a stiff soil [Hung et al. 2010]. On the other hand, centrifuge tests generally do not model physically the reinforced concrete members. Deng et al. [2012] used notched aluminum sections to model the plastic hinges of reinforced concrete columns and Loli et al. [2014] used small scale reinforced concrete elements.

However remarkable the contribution of these aforementioned studies, to the under investigation area of research, they all bear some inevitable disadvantages, which hinder the possibility of ours approaching the problem to its real dimensions. To begin with, all these tests are performed using a scaled specimen, due to the size and weight limitations of the utilized equipment. In addition to that, the backfill soil is taken into account indirectly and in idealized way, thus obstructing the system from demonstrating under real conditions the S – F – S – I effects. Needless to say, that this idealized soil is always in dry conditions, without considering the groundwater in subsurface soils, thus ignoring the possibility of liquefaction and its consequences in rocking foundations. Last but not least, the use of static excitations hardly provides a realistic view of the system's response under dynamic and especially seismic excitations.

For the aforementioned reasons, it came as a natural outcome the fact that a series of pioneering testing should take place: Large – scale shaking table tests of rocking bridge foundations constructed using realistic materials and following realistic methods, were tested under real seismic excitations with and without groundwater in the underlying foundation soil. Such tests represent a significant progress in the experimental data so far available for this type of foundation design and provide insightful information about the behavior of such systems, approaching in this way a little further the reality.

This testing procedure aimed at studying the response of two 460-mm-diameter bridge columns supported on 1.52-m-square shallow rocking foundations on top of clean, well-compacted sand, subjected to unidirectional seismic excitation. The tests were conducted in May 2013 at the outdoor shake table of the Network for Earthquake Engineering Simulations (NEES) at the University of California at San Diego (UCSD) using the largest stiff soil confinement box in the U.S. Three series of test were performed; each series having different ground water table elevation and backfill conditions. The objective of these tests was to demonstrate, based also on accumulated knowledge from previous tests, that bridge columns on rocking foundations can be successfully designed to develop drift ratios of the order of **7**% with limited rotations and settlements. These are the largest shake table tests ever conducted on rocking shallow footings with foundation soil. The tests also produced the largest level of dynamic lateral displacements that have ever been reported for similar scale specimens.

The scope of this Chapter is to present some of the most significant published experimental studies concerning the topic at hand. For the sake of brevity which is dictated by the framework of this thesis, the focus shall be mainly towards studies concerning shake table testing. The target is to select those studies, which provide the full range of data necessary to our acquiring a detailed, analytical view of the investigated phenomenon. In the sequel the results stemming from the selected publications will be compared and contrasted with the investigated experiments, which are the main focus of this thesis. After the literature review, a detailed description of the tests and the utilized equipment is provided.

1. PREVIOUS EXPERIMENTAL STUDIES

1.1Testing on Rocking Foundations

Due to the limitations of this MSc thesis, only a small amount of the published literature will be cited, focusing mainly on studies performed using Shake Table Testing. Of course the published papers on similar works are numerous and all have contributed significantly to this field of research. In further detail we shall delve into presenting similar published experimental with the one investigated herein, in the following paragraphs.

In 1982, Taylor et al., proved that the re – centering effect of a rigid body rocking on a rigid base, applies also to blocks rocking on soil. He provided evidence to support his thesis, by means of 1 – g physical model tests. However, he found that the rounding of the soil surface underneath the footing prevents any sudden elastic collision from happening, as the gap between the footing and soil closes. He explained that the footing practically never rocks on a sharp edge. Later, in 2005 it was Gajan et al., who proved that the dissipation of energy during rocking is dominated by the plastifications occurring at the moving contact between the curved surface of the soil and the flat bottom surface of the footing as the rocking progresses, since the length of the footing being in contact with the soil varies, as the footing rocks.

Negro et al., [2000], performed large – scale shake table tests using as specimens square rocking foundations with dimension of 1.0 m. The safety factor against vertical loading was $FS_v = 5.0$. The footing rested on top of 3.0 m of sand and was embedded by 1.0 m. Two scenarios of soil filling were considered: sand with a relative density $D_r = 45\%$ and $D_r = 85\%$. The loading was cyclic pseudo static and the main results of the test with the dense sand included developed peak footing rotation $\theta_f = 23\ mrads$ and settlement less than $0.02B$, where B is the length of the foundation in the direction of loading.

Gajan et al., [2005] conducted five series of tests on the 9.10 m radius centrifuge at the Center of Geotechnical Modeling at the University of California, Davis. These tests included 40 models of footings supporting shear walls, resting on moderately dense sand under high confining stresses (20g centrifuge experiments), and their objective was to provide insights about the nonlinear load-deformation characteristics during cyclic and earthquake loading. More specifically, parameters such as footing dimensions, depth of embedment, wall weight, initial static vertical factor of safety, soil density, and soil type (dry sand and saturated clay) were systematically altered to provide a more generalized assumption concerning the sensitivity of the "soil–foundation" system to them.

Four series of tests were conducted on dry sand (Dr = 80 and 60%) and one test series was on saturated clay (Cu = 100 kPa). All the specimens were tested on a soil bed prepared in a rigid container each of which included six to ten footing-wall models depending on the testing series. The depth of the sand layer inside the container was 4.0 m, and the thickness of the consolidated clay layer was 1.7 m in clay test series. By altering the

dimensions of the footings (L = 2.5–4.0 m, width, B = 0.4–1.0 m), its embedment depth (D = 0.0–0.7 m), and the total weight of the structure, the tested specimens represented a range of realistic static factors of safety and subjected to slow cyclic and seismic loading. It is noted at this point that the dimension "L" is the one parallel to the direction of rocking (loading direction) and thus it controls through the slenderness ratio the response of the system. **Figure 2.2** depicts the setup of the test providing details about the instrumentation, which was used for the required measurements. The specimens were subjected to vertical push, to slow lateral cyclic push and to dynamic tests. For the needs of the current work, we shall focus our interest on the two latter tests and only the ones referring to the moderately dense sand.

Slow cyclic lateral push tests were conducted on structures with a different height of lateral loading for each series of testing. As a representative result of the moment – rotation (henceforth M – ϑ) relation, **Figure 2.3** is presented, illustrating the moment–rotation, horizontal force sliding, settlement-rotation, and settlement-sliding relationships at the center point of the footing base for one of the lateral push tests on sand (Dr = 80% dry sand, L = 2.84 m, B = 0.65 m, D = 0.0 m, h = 4.9 m, and FS_v = 6.7).

The large area in the hysteresis loops provide evidence of the appreciable amount of energy dissipated by rocking at the interface between the soil and the footing. According to the plots, no reduction in the moment capacity seems to take place as the number of cycles increase; however, deterioration in the rotational stiffness as the rotations progress is visible.

As far as the settlement – rotation (henceforth $w - \vartheta$) relationship is concerned; a significant increasing residual settlement seems to develop underneath the footing. The rate of increase for the settlements seems to deteriorate with the progression of the cycles. This is attributed to the fact that, as the footing settles, its embedment depth D increases, leading to raised overburden stresses and by extension increased vertical stiffness; hence, the reduction in the rate of increase of the settlements. Significant information provided by this plot is also the presence of uplift during the systems' response. The uplift due to rocking accounts for the degradation of the rotational stiffness of the system. As the footing uplifts, a part of it detaches from the supporting soil, thus creating a gap from one side of the footing and causing soil yielding on the other side. The soil plastification contributes further to the increase of uplift. Consequently, rocking response, under high amplitude lateral loading leads to "rounding" of the soil underneath, hence introducing the nonlinearity in the M - ϑ relationship and causing the decrease of rotational stiffness, due to the footing tending to close the opened gap. **Figure 2.4** illustrates the deformed soil surface geometry, due to rocking response of a rigid footing.

Moving on to the horizontal load – sliding plot, it is evident that no softening in the horizontal stiffness takes place and also no significant sliding. The situation alters when the system reaches its shear capacity, when sliding commences. The plot settlement - sliding demonstrates the coupling behavior between uplift and sliding. When loaded in one direction, the footing closes its gap first and then it slides horizontally, while a gap forms on

the other side. The nonlinearity of the system is evident, since as soon as the system starts sliding on one side, a bias is created and residual displacement on one side only develops.

The results stemming from the dynamic tests were in general with agreement to those from the cyclic ones. Referring to the same soil type, as before but for a slightly lower FS_v, the dynamic moment–rotation behavior is also characterized by a softening phase, with an increasing rotation amplitude increases. **Figures 2.5** illustrates the phenomenon according to which, the footing–soil interface shows stiffer response in moment–rotation behavior for small amplitude motions, whereas as the magnitude of shaking increases it shows degradation in rotational stiffness. By the end of shaking, it again shows stiffer response for motions of small amplitude. The maximum amplitude of cyclic rotation observed in the dynamic test (about $20\,mrad.$) was smaller than that applied in the slow cyclic lateral push test (about $60\,mrad.$), proving that the dynamic nature of a seismic excitation might not have as detrimental effects as a static loading. It is worth noticing that the settlement-rotation behavior from the dynamic test does not indicate significant uplift.

Figure 2.6 depicts the M - ϑ relationship, highlighting the backbone curve, i. e. the curve connecting the extreme points of each cycle from the dynamic tests and superimposing it on the slow cyclic moment–rotation plot. The very good fitting of the two plots makes us assume that the M - ϑ relationship during slow cyclic and dynamic can be satisfactorily described also by slow cyclic tests.

Last but not least about this series of testing Gajan et al. pointed out the significant difference in the developing residual settlements between slow cyclic and dynamic tests. The settlements are not only affected by the safety factor against vertical loading, but also by the type of loading. The comparison of the residual settlements between the slow cyclic and the dynamic results proved that the latter were much larger. The cause behind this discrepancy is partially attributed to the settlements of the free field soil, due to dynamic ground shaking (densification effects followed by volumetric reduction). In addition to this reason, they underline that the developing vertical accelerations increase further the accumulating settlements due to the presence of the inertia forces.

Paolucci et al. [2008] and Shirato et al. [2008] performed shake table tests using as specimens 0.5-m-square rocking foundations resting on well-compacted clean dry sand with a vertical safety factor $FS_v = 29$ and $D_r = 85\,\%$. The total height of the soil half space was 2.10 m and the embedment depths ranged from 0.0 to 0.10 m. For D = 0.10 m (D/B = 0.2, close to the embedment ratio used in this study) a peak rotation $\theta_f = 50\,mrads$, a residual rotation equal to $10\,mrads$ and a maximum settlement of $0.012B$ were reported.

1.2 Shake Table Testing for Rocking Bridges

Paolucci et al. and Shirato et al., [2008] performed one of the first large scale 1g shake table tests, by 1g it is meant that the specimen was subjected only to the Earth's

gravitational acceleration field, apart from any other testing loads. The objective of the tests was to provide insight concerning the behavior of shallow foundations subjected to cyclic, static and dynamic, loading. To this end they conducted a series of full-scale shaking table tests at the PWRI (Public Works Research Institute), in Tsukuba, Japan using realistic seismic loads suitable for nonlinear dynamic SSI analyses. The test specimen consisted of a laminar box filled with dry sand compacted in layers simulating in this way nearly homogeneous soil. The relative density of the backfill soil was dry sand with $Dr = 80\%$, mass density $\gamma = 1.60\ t/m^3$ and the angle of internal friction $\varphi = 42.1°$. On the filling soil, which was compacted in layers so as to be considered homogeneous, rested the 0.5m sided square foundation, connected through a short steel beam with two massive blocks, hence having the component a total height of 0.753 m ($h/B\ = \ 1.5$). The superstructure was practically rigid, compared to the soil - foundation system. The test set up is presented in **Figure 2.7**. The static safety factor was estimated via monotonic vertical testing to be $\mathrm{FS_v} = 29$. The writers include argumentation in their published work, claiming that the tested specimen had mechanical properties similar to those of typical design cases.

A series of static tests was conducted, namely: slow monotonic lateral loading, one – sided cyclic lateral loading and two types of reversed cyclic lateral loading. The complete series of static tests is presented in **Figure 2.8a**. **Figure 2.8b** illustrates the applied displacement time histories for the slow cyclic tests. These tests gave the researchers the opportunity to crate the enveloping curves in the M – V plane, and the trajectory of projection of the theoretical failure locus. In this graph the values of maximum horizontal force H developed during seismic and cyclic events were plotted. A significant outcome came from this comparison, since according to the results; there were events, which from the static point of view led the system to failure (there were values of forces H overlapping the enveloping curve). The reality was different nonetheless, since failure did not necessarily occur at all cases when the loads reached the ultimate state.

A variety of strong ground motions were used for the tests, in three stages: The first one included a long duration, sinusoidal-type waveform, with nominal peak acceleration amplitude of 0.50g, followed by the long-duration acceleration history recorded at Schichiho Bridge, Hokkaido, Japan, during the 1993 Hokkaido Nansei Oki Earthquake ($M_W = 7.8$). The model was then subjected to a second sweep wave, after which the structural specimen was raised, the disturbed soil zone in the close vicinity of the foundation was leveled and tampered. Then, the specimen was relocated at the same position, with an embedment depth of 50 mm ($D/B = 0.10$). The shaking table was subjected to the JMA record from the 1995 Kobe Earthquake ($\mathrm{M_W} = 6.9$). **Figure 2.9** provides a collective view of the testing sequence adopted for these tests. The footing toppled only in Case S1 – 5. The model tilted significantly with large pulses and was overturned by a subsequent pulse. Although a similar response was also observed in Case S1 – 4, the side resistance to the footing stemming from a larger embedment depth may have prevented the footing from toppling. The writers comment on the significance of the ground motion intensity, comparing the residual rotation from the Case S1 – 4 and S2 – 2, which both correspond to the JMA excitation with

the only difference being that in the latter the signal was de - amplified by a factor of 0.80. This difference possibly led to markedly smaller residual rotations for the Case S2 – 2. **Figure 2.10** provides a schematic view of the system's condition at the end of each seismic excitation. After the JMA record was applied to the system, the structural model sustained excessive foundation rocking (**Figure 2.10(b)**), and ultimately during the second excitation, with zero embedment, it toppled, as mentioned also above (**Figure 2.10(c)**). Nevertheless, it is clear that the residual rotation of the footing was limited for the same record, after the specimen has been removed and relocated (**Figure 2.10(d)**).

Figure 2.11 shows the time histories of the model responses in the Shichiho and the weakened JMA time histories. The writers used this comparison to prove that the number of cycles has also an effect on the response of the system, since they showed that for the case of Shichiho excitation, which contained multiple cycles of the PGA, the accumulated settlements and rotation was much more intense than in the case of the weakened Kobe excitation. The irreversible vertical displacement at the end of the former case was considerably larger than that at the end of the latter case, despite the similarity between these two cases in terms of maximum accelerations on the ground level, a_g and at the top steel rack, a_1. According to the researchers, the accumulation of the aforementioned plastic deformations is the outcome of the prevailing displacement mode of the footing: the rocking. In fact they managed to prove the dominance of this mechanism, by demonstrating that the total rotational displacement was decomposed practically into the plastic and uplifting rotational components, which contributed to the whole equally. On the other hand, the elastic rotational component was significantly smaller than the former ones. The uplift behavior is illustrated in **Figure 2.12**. The writers, after observing for all cases the characteristic V – shaped curves, reached another important conclusion about rocking: in terms of displacements, the rotational and vertical components in the dynamic response of the system are coupled. The reader can refer to **Figure 2.13** where the residual displacements after each seismic event are presented.

By studying the effective footing length, which remained in contact with the soil throughout the seismic excitations, they concluded that the effective footing length gradually decreased as the sequential time elapsed, which was attributed to the progressive plastification of the underlying soil. In **Figure 2.14** are illustrated yielding phases of foundation–soil interaction as observed during the experiments. The excessive displacements developing in the soil profile underneath the foundation edges resulted in significant distortion of its initially planar shape. The successive strong load pulses in both shaking directions caused "rounding" of the soil surface under the footing. This resulted in an overall degradation of the dynamic foundation impedances, and in turn, elongation of the natural period of the soil–foundation system. A similar evidence of a curved soil surface formation beneath the foundation was also found by Gajan et al. [2005] during centrifuge model tests.

Last but not least, after studying the $M - \vartheta$ loops which resulted from monotonic and dynamic tests, they underlined the similarity in their shape and thus they proposed that

backbone curves for any loading condition can be characterized with the monotonic loading curve.

Rocking isolation has already been applied to the construction of modern bridges e. g. the Rion Antirion Bridge; [Pecker 2005]. Taking this innovative concept one step further, the research community has managed over the last decade to realize that concurrent inelastic soil response, like pure uplifting, also contributes to the structure's decoupling from the ground excitation [Martin and Lam 2000; Pecker and Pender 2000; Faccioli et al. 2001; Gajan et al. 2005; Harden et al. 2006; Pecker 2005; Gazetas et al. 2007; Paolucci et al. 2008; Anastasopoulos et al. 2010a]. To this end, another significant work on the field of rocking isolation was performed by Drosos et al., [2012]. In this study it is investigated by means of shake table testing, whether the mobilization of bearing capacity of the soil as a prevailing response mechanism would act advantageously in the SFSI effects.

The complexity to approach this problem is that, contrary to uplifting, which is easily determined by the system's aspect ratio h/B (h being the height of the center of mass and B being the foundation breadth, parallel to the direction of loading); the nonlinear behavior of the soil cannot be univocally determined. Apart from that, these two mechanisms do interact with each other. The "key factor" controlling the interaction between uplifting and soil yielding is the vertical safety factor: $FS_v = N_{ult}/N$. The objective of the cited study is to investigate by means of 1g shake table testing the role of nonlinear foundation response on the seismic performance of a slender single-degree-of-freedom structure, in order to assess the effect of soil nonlinearity (uplifting and yielding) by comparing the effects of the two factors: h/B and the vertical factor of safety $\boldsymbol{FS_v}$.

In order to investigate the effectiveness of these two mechanisms under the prism of the necessitated conservatism, three different foundations were considered, representing a conservatively designed foundation, a less conservative one, and a significantly under - designed foundation, by giving them respectively large, medium, and small dimensions. This fluctuation in the footings' dimensions provided the chance to study the phenomenon for three distinctive vertical safety factors: 7.3, 3.5, and 2.3, respectively. The scaling laws dictated a reduced-scale physical modeling [Muir Wood, 2004], with a linear geometric scale of 1 : 20 (n = 20). Application of scaling was necessary due to the limitations concerning the bearing capacity of the shake table on one hand, and the internal dimensions of the soil container. It is underlined that the stress field within the soil half space cannot be scaled down, leading unavoidably to scale effects originating from the pressure dependent behavior of soil. A way of alleviating this obstacle is by means of centrifuge model testing. Regardless of that though, the design of the specimens was performed in such a way, as to compensate for these inherent shortcomings of reduced scale. The soil conditions, i. e. a very dense sand stratum ($D_r = 85\%$) were applied in this case study as well. The definition of the problem as well as the geometry of the specimen is presented in **Figure 2.15**. The specimens were tested under static (monotonic and slow-cyclic pushover) loading, and reduced-scale shaking table testing.

The results from the slow cyclic tests are plotted in **Figure 2.16** and led to the following findings:

- An appreciable overstrength is manifested in the slow cyclic M – ϑ curves, compared to the monotonic ones, which is more significant as the FS_v decreases, i. e. the smallest footing demonstrates the largest overstrength. This phenomenon is attributed to the reversal of the role of P-δ effects when the rotation changes sign. Soil densification, may also play an important role. Smaller overstrength values may be observed for the two larger foundations.
- The fact that the smallest footing shows the largest overstrength, reaching approximately the same peak moment as the medium-size foundation, combined with the fact that both have the same slenderness ratio, proves the limited effect of the different FS_v on the system. The researchers propose, in other words, that in such cases, the slenderness ratio h/L is the parameter with the most decisive effect on the rocking response of the system.
- Decreased FS_v leads to increased settlements. Increased FS_v on the other hand (large footing) leads to a prevailing uplifting mechanism of response. This is illustrated by the gradient of the settlement – rotation curves in **Figure 2.16**, which indicates whether the foundation midpoint loses contact with the supporting soil as the foundation rotates, giving evidence on the amount of uplift that takes place during the test. Evidently, the large foundation (of the highest FSv) experiences significant uplifting. This proves that the vertical safety factor indeed controls the interaction between soil plastifications and uplift, since as the FS_v deteriorates, the soil nonlinearity becomes more dominant, leading to increased rate of settlement per cycle and limiting the uplift. This inclination seems to be disrupted in the case of the medium footing, for which we observe that the gradient of settlement reverses after a few cycles of loading, showing upward movement of the foundation midpoint and hence reduction of the minimum soil-foundation contact area, possibly as a result of sand densification (i.e., compaction) under the oscillating footing. As for the smallest footing, the increasingly accumulating settlements are probably another reason for its high overstrength: The footing is not a shallow one anymore, but rather an embedded, hence having an increased vertical stiffness and by extension increased strength.

A variety of seismic motions (artificial and real records) were used in these tests, for brevity reasons though only the results for two levels of sinusoidal artificial accelerograms in 0.15 g and 0.50 g amplitude, characterized as excitations of “moderate” and “severe” intensity respectively are presented in their published work. The sequence of the seismic motions was selected in such way as to study the effect of the maximum acceleration amplitude, A_E, and the excitation frequency, f_E. First, the model was subjected to three sine motions of $f_E = 2\ Hz$, gradually increasing the A_E (0.15, 0.4, and 0.5g). Then, the same excitation sequence, with respect to A_E, was repeated for $f_E = 1\ Hz$.

The results of the sinusoidal motion of $f_E = 2\ Hz$ and $A_E = 0.15\ g$, representing the moderate-intensity seismic excitation and the results of the sinusoidal motion of

$f_E = 2\ Hz$ and $A_E = 0.50\ g$, representing the severe-intensity seismic excitation showed that:

❖ Observing the developing acceleration at the deck – mass (**Figure 2.17**), it was concluded that the smaller the footing, the smaller the dynamic amplification in the developed acceleration. The significant amplification in the case of the large foundation, and the corresponding attenuation for the two smaller ones, is attributed to the frequency dependency of the oscillatory response. In other words, the large foundation as a stiffer system vibrates within an effective dominant period range close enough to that of the input excitation ($f_E = 2\ Hz$), resulting in dynamic amplification of the input motion. In contrast, the effective period of the two smaller foundation oscillators is substantially larger (owing to intensely nonlinear response), resulting in dynamic attenuation of the input motion.

❖ The decoupling from the ground motions is observed also in the case of the severe excitation, when the acceleration time histories of the deck (**Figure 2.17**) are strictly cut off at the value of critical acceleration a_c of each system. The latter is defined statically as the maximum acceleration developed at the mass of the oscillator (representing the bridge deck) which leads the system to its moment capacity:

$$a_c = M_{max}/mgh$$

Some limited isolation effects are observed, even in the case of the large foundation system ($\frac{a_{max}}{A_E} = 0.72$).

❖ It is underlined that for the "moderate" level of seismic excitation, the deck acceleration does not supersede the estimated critical values, which suggests that, at this level of seismic intensity, the response is not affected by the ultimate capacity of the foundation and the related rocking isolation mechanism. This observation is confirmed by the $M - \vartheta$ loops (**Figure 2.18(i)**) according to which the three foundations respond in the nonlinear range but well below their ultimate capacity. The residual settlements for this level of intensity are rather limited up to 2 cm for the larger foundation and between 2.5 and 3.0 cm for the medium and small one.

❖ In **Figure 2.18 (ii)** depicts the moment-rotation and settlement-rotation loops of the three systems for the "severe" level of intensity. Once again, the large foundation experiences the rotational motion of similar or larger amplitude than the two smaller foundations, remaining well within its capacity limits. This is explained, since the advantage of having larger moment resistance and rocking stiffness is outweighed by the almost two - times greater inertial loading, which the large foundation withstands. In comparison with the previously discussed smaller magnitude base excitation, the settlements of all three systems are now significantly larger, reaching a maximum of 3.5 cm for the large and 7 cm for the small foundation.

❖ As far as the deck drifts are concerned, for the moderate seismic excitation the maximum recorded drift reaches the values of 0.27% for the larger foundation and approximately 0.15 % for the two smaller ones.

❖ For the severe seismic excitation, the large foundation pier appears to experience again appreciably larger deck drift (0.62%), which is primarily a result of

foundation rotation for this high excitation level. The corresponding values for the medium and for the small foundations were 0.46 % and 0.54 % respectively.

The researchers comment that at the end of the day, the conservatism reflected on the design of the largest footing, contributes practically only to bounding the settlements to 50% of the ultimate value of the other two.

The sensitivity of the system was investigated against an additional parameter, the predominant frequency of the excitation. In order for the effect of excitation frequency f_E to be studied, the three systems are subjected to a sine excitation of the same acceleration amplitude (0.50g), but of frequency $f_E = 1.0\ Hz$. The reduction of f_E has a drastic effect on the response of the system, as illustrated by the foundation moment-rotation and settlement-rotation curves (**Figure 2.19**).

The first significant difference in comparison to the previous graphs is the apparent gradual degradation of the moment-rotation stiffness in all three cases, which results in a rotational motion three times larger than with the $f_E = 2.0\ Hz$ seismic excitation ($10\ mrad$ instead of roughly $3\ mrad$). It also evident that in this case the effect of the lower excitation frequency overshadows the effect of the FS_V, since even the small foundation (with the minimum FS_V) exhibits sizable uplifting behavior. On the other hand the large one demonstrates a rather bold uplifting behavior. This uplifting-dominated behavior of the small foundation is believed to be the result of soil densification occurring during the preceding seismic excitation cycles.

Having mentioned these differences, the aforementioned assumptions concerning the effect of foundation size on the inertial forces and the resulting displacements, continue to be valid also in the response of this excitation. The only contrast has to do with an overstrength exhibited by the system in this last excitation, mainly because of the settlement acquired during the preceding excitations.

In a similar notion Anastasopoulos et al., [2012] performed a series of reduced-scale monotonic and slow-cyclic pushover tests on an SDOF system lying on a square surface foundation. It is worth commenting at this point, that although the main focus of this literature review is on dynamic experiments, it has been suggested, by the aforementioned work of Gajan et al., [2005] that the performance of a rocking foundation subjected to seismic shaking is fairly consistent with the ‘‘predictions’’ of slow cyclic tests; hence the choice of this publication to be included in this review. The motive behind this work was the inherent fear in rocking systems that they may lead to unacceptable settlements in case of a low static factor of safety $\boldsymbol{FS_v}$. The assurance of an adequately large $\boldsymbol{FS_v}$, which would ensure that rocking is materialized through uplifting rather than sinking, cannot always be offered by the in situ conditions, since the uncertainties of the soil properties are numerous and constitute the main obstacle to accurately simulating the soil formation numerically or experimentally. This difficulty is alleviated partially, by the very nature of rocking being a rather localized phenomenon and thus affecting only the shallow layers of the soil profile. **Figure 2.20** plots the distribution of vertical stresses and the corresponding plastic strains for a lightly loaded ($FS_v = 10$) and a heavily loaded ($FS_v = 2.0$) single degree of freedom

(SDOF) system subjected to monotonic $M-Q$ loading, computed through nonlinear finite element analysis. For this reason shallow soil improvement is considered as an alternative approach to release the design from the jeopardy of unforeseen inadequate FS_v.

For this purpose, this paper studies the rocking response of relatively slender SDOF structures ($h/B = 3.0$), making in this way rocking prevail over sliding. The emphasis was given on the effectiveness of shallow soil improvement stretching to various depths below the foundation. The methodology followed to this end is reduced-scale 1g monotonic and slow-cyclic pushover testing in order to investigate:

(a) the rocking response of a slender SDOF structure under monotonic and slow- cyclic loading, leading the response well into the post – yielding behavior, where the developing moments exceed significantly the capacity.
(b) the effectiveness of shallow soil improvement stretching to various depths below the foundation.

It is underlined that the investigated system refers only to surface or shallow embedded foundations.

The tested specimen was a slender SDOF structure representing a bridge pier with dimensions B = 6 m and h = 18 m. The properties (geometry, mass, stiffness, etc.) were scaled down by utilizing a scale of 1:40. The model was installed inside a rigid 1.6 m long soil container, on top of a sand stratum. The distance of the specimen from the box walls ensured minimized boundary effects. The structure rested on two different scenarios of soil bearing capacity, thus leading to two different testing systems:

- System A: representative of a lightly loaded structure, with a high FS_v and
- System B: representative of a heavily loaded structure, with a low FS_v.

A schematic illustration of the studied SSI system is provided in **Figure 2.21.**

The inherent uncertainty of the exact soil conditions was taken into account by assuming different soil conditions for each of the two systems, which was materialized with altering the $\boldsymbol{D_r}$ of the backfill soil. Three different scenarios for D_r were applied (93%, 65%, 45%).For these three cases of homogeneous halfspace the ultimate bearing capacity of the soil was determined, after static vertical pushover tests, by modifying the mass of the model and by extension the corresponding FS_v. The summary of the finally tested configurations is provided in **Figure 2.21**, it should be mentioned however that the case $\frac{z}{B} = 0.25$ has been omitted from the report, since it was proven to be ineffective.

Concerning the loading protocols, again two different scenarios were considered:

- Type1 load protocol: 14 cycles of increasing displacement δ/δ_R where $\delta_R = 7.50\ cm$ corresponds to the displacement leading to toppling, for the equivalent rigid block. Type 1 should not be considered as a typical earthquake type motion, but rather it should be considered as a set of pulses of different amplitudes mainly aiming to identify the effect of loading amplitude.
- Type 2 load protocol: consists of three sets of ten cycles each. Each set has increased amplitude compared to the preceded one. This loading can be considered as a series of idealized earthquake events (ranging from a small amplitude to a rather

destructive), while it also serves as a means to quantify the effect of the number of cycles. An illustration of the input motions is presented in **Figure 2.22**.

Proceeding to the description of the results, the two homogeneous soil profiles of the two systems were subjected to monotonic and slow cyclic loading. These tests led to the resulting plots presented in Figure 2.23(a) for the lightly loaded system A and in **Figure 2.24(a)** for the heavily loaded system B. The monotonic results do not show any significant difference, from what was already expected. In terms of moment capacity, the systems founded on dense sand (with large FS_v) demonstrate higher normalized moment capacity and overturning rotation compared to the systems founded on medium or loose sand. In terms of settlement, for the specimen on dense sand the response is clearly uplifting-dominated, whereas for the specimen on medium or loose sand soil yielding prevails, distorting the equilibrium of the two systems and accelerating their toppling at lower rotation angles.

Especially the heavily-loaded System B on medium sand, having $FS_v = 2.6$, exhibits an invariably sinking-dominated response, toppling at $\vartheta/\vartheta_R < 0.6$. For all other cases where $FS_v \geq 5$ clearly exhibit uplifting-dominated response. Hence the writers assume logically that a critical value of FS_v would be $2.6 \leq FS_v \leq 5$ beneath which uplifting is not allowed. This assumption is in accord with centrifuge model test results recorded by Gajan and Kutter, [2009].

However, as it will be also commented on in the sequel, FS_v alone is *not* the decisive parameter to determine the dominance or not of rocking. This notion is supported by the results, since it is evident that for all cases of safety factor, except for the one with $FS_v = 14$, for lower rotational amplitudes all foundations are subjected to settlement.

The cyclic results are illustrated in **Figure 2.23(b)** and **Figure 2.24(b)**, for the two investigated systems respectively. The $M - \vartheta$ loops reveal the characteristic S – shaped curves for system A (lightly loaded), whereas the shape of the curves for the latter system is oval. This difference is attributed to the development of concentrated stresses underneath the edge of the footing, when it is subjected to large rotations. This produces localized soil bulging, which results in loss of full contact between the foundation and the soil; hence reducing the effective rocking stiffness of the foundation during unloading and producing this characteristic S-shaped loops. These results are in good agreement with those produced by the previously cited experimental work of Paolucci et al., [2007]. Of course in their case this characteristic was much more vivid, since the achieved $FS_v = 30$!

It is interesting to observe the similarity, which both systems share, since for the low FS_v scenario in both cases a notable overstrength is present during cyclic loading. While in case of the $FS_v = 14$ model, the monotonic dimensionless moment-rotation curve clearly ‘‘envelopes’’ the loops of the slow-cyclic tests, the latter tend to overly exceed it when FS_v is reduced. This phenomenon was also reported by Gajan and Kutter, [2008], who provided the following possible explanations to interpret it:

- The bearing capacity of the soil gradually increases, when it comes to a shallow foundation of a relatively low FS_v. As already pointed out, the consecutive loading

cycles, lead to an "unintended" embedment of the footing, thus leading to a raised vertical stiffness and by extension a raised bearing capacity.

❖ The sand underneath the footing may have been compacted over the successive cycles of loading.

❖ As pointed out also by Drosos et al., [2012], P – Δ effects may have a contributory role to the system, resulting in the exhibited overstrength (Panagiotidou et al., [2012]).

What is remarkable though is the continuously increasing overstrength, for the case of the $FS_v = 2.6$ of System B. Ultimately the monotonic capacity is exceeded by a factor of almost 2, while for the model of $FS_v = 5$, the number of cycles does not seem to have an equally significant effect and the overstrength does not exceed 1.25.

Having stressed out the similarity of the two systems, it is important that their main difference be underlined too. For both systems, the settlement increases substantially with the reduction of FS_v: subjected to theType1 loading protocol, the heavily-loaded System B on medium sand ($FS_v = 2.6$) accumulates almost two times larger settlement compared to the same system on dense sand. Interestingly, even for a remarkably large $FS_v = 14$ (System A on dense sand) a limited, yet non-negligible, rocking-induced settlement is observed. Nevertheless, it should be noted that this observation is totally in accord with UC Davis centrifuge model test results (Gajan and Kutter, [2008]).

Since it is not in the scope of this thesis to delve into the details of the effects of soil improvement, when it comes to rocking systems, for the loading protocol Type 1 the results recorded by the researchers are mentioned laconically. Two different cases of soil improvement are examined for each system: $\frac{z}{B} = 1.0$ and $\frac{z}{B} = 0.5$.

After monotonic tests on system A (**Figure 2.25a**), it was proved the awaited: the moment capacity increases, as the depth of soil improvement grows. The same trend applies also for the toppling rotation, which also has a larger value, as the depth of the improved soil increases. In terms of settlement, again the logical result occurs: In all three cases (homogeneous soil, improved soil by a depth $\frac{z}{B} = 1.0$ and $\frac{z}{B} = 0.5$), for small rotational values, the specimen settles. Of course the range of rotational values for which settling prevails over uplifting is smaller for configurations with larger FS_v. For larger rotational values, where uplifting governs the response, the performance of the models lying on shallow soil improvement is practically identical to the upper-bound case of dense sand (their moment– rotation curves are almost parallel).

Cyclic testing on system A confirmed the previous results concerning the shape of $M - \vartheta$ loops, as well as the system's exhibiting overstrength for lower values of FS_v which is in contrast to the monotonic results, since in absolute values the moment capacity for all systems, is practically the same. All in all, for system A it is assumed that even the shallow improvement of the soil contributes significantly to the system.

Following the same sequence, the monotonic results of system B (**Figure 2.25b**) deviate significantly, when it comes to the shallow depth of soil improvement ($\frac{z}{B} = 0.5$). The

effect of this enhancement is negligible, but on the other hand the deeper soil improvement enhances the moment capacity of the system, approaching in this way the response of homogeneous dense sand. In terms of rotational values, even under ideal soil conditions the response of the heavily-loaded foundation cannot be uplifting- dominated, but is rather accompanied by mobilization of bearing capacity and substantial soil plastification. With limited uplifting taking place, the effective width of the foundation is not reduced as much, and the rocking-induced stress bulb tends to ''penetrate'' deeper. It should be highlighted at this point though, that for system B the achieved FS_v for the ideal homogeneous soil of dense sand is only 5, instead of system's A $FS_v = 14$. In terms of settlements it is evident that all three systems (homogeneous, improved by $\frac{z}{B} = 0.5$ and by $\frac{z}{B} = 1.0$) small rotational values are dominated by settling response. As a result, the behavior of the models on improved sand is almost identical to that on loose sand, revealing an almost negligible effect of soil improvement. Especially for the case of $FS_v = 2.6$ foundation response is sinking-dominated throughout the entire rotation range which is also the case for the soil with the shallow improvement. For the rest of the cases the awaited is recorded: the better the soil, the smaller the rotation at which uplift commences.

Cyclic testing on system B confirms the outcome of the monotonic tests, the observed cyclic overstrength (increasing with the reduction of FS_v), the cyclic moment capacity is almost the same for all soil profiles examined, especially after application of the larger amplitudes of loading when the overstrength has been fully mobilized. The effectiveness of shallow soil improvement in terms of settlement–rotation response is sinking dominated and in order for a significant reduction to be achieved, a deeper $\frac{z}{B} = 1.0$ dense sand crust is required.

It is interesting to cite from this publication, the results from loading protocol type 2, which due to its increasing intensity it may be considered an equivalent seismic excitation. Although the ultimate displacement and hence, rotation amplitude is the same with that of Type1, the fact that strong cycles are preceded by a number of weaker ones, introduces to the response of the system two phenomena: accumulation of settlements and densification of the underlying soil. For both systems, the specimens founded on dense sand and improved soil tend to accumulate settlement only during the initial smaller-amplitude cycles (the first four loading packets fall within the sinking-dominated rotation range), whereas the rate of settlement diminishes with the increase of loading cycles. This decrease is even more pronounced in loose sand, which tends to densify with repeated cycles of loading.

The negligible difference between homogeneous dense sand and improved soil with a crust $\frac{z}{B} = 1.0$ proves that a strengthening to such an extent would not offer significant benefits, in terms of limiting the settlements. However, compared to the results corresponding to the loose sand, the effectiveness of soil improvement is quite impressive, since even with a shallow improvement, the accumulated settlement is reduced remarkably. The results for system A subjected to loading protocol type 2 are presented in **Figure 2.26a**.

On the other hand, and as already commented for loading protocol type 1, soil improvement is not as effective when this severe loading is imposed on system B (having $FS_v = 5$ when founded on dense sand). As shown in **Figure 2.26b**, for system B on loose sand the foundation accumulates almost two times larger settlement than System A. The shallow soil reinforcement is clearly insufficient as the entire loading history falls within the sinking-dominated rotation range. Interestingly, in the case of the deeper improvement sand crust, after the initial four loading packets, the accumulated settlement is reduced and the response tends to approach that of dense sand. Focusing on the last loading packet, with the maximum amplitude, we observe that the performance of the $\frac{z}{B} = 1.0$ improved soil is quite similar to the ideal case of the homogeneous dense sand soil profile. The similarity in the performance of system B founded on dense sand to that of the lightly-loaded System A on loose sand comes as no surprise, since both share the same $FS_v = 5$.

The experimental work described above was taken one step further, by Tsatsis and Anastasopoulos, [2015], who implemented seismic motions to the loading protocol maintaining the physical modeling and the soil configurations exactly the same. The repetition of monotonic tests only confirmed the results presented by Anastasopoulos et al., [2012]. Considering the dynamic response, the critical acceleration a_c has to be defined, since this factor will be a comparison measure in the sequel. As already shown, the maximum acceleration developed at the mass of the oscillator (representing the bridge deck) is the one leading to the moment capacity of the foundation. It is defined as follows:

$$a_c = M_{max}/mgh$$

In **Table 2.1** are presented the critical accelerations for all configurations of systems A and B. Each of the soil conditions considered is presented in further detail in **Figure 2.21**.

The different configurations were subjected to 1g shaking table testing, using a variety of real seismic records and artificial motions as base excitation. In all cases examined, the PGA of the seismic excitations exceed largely the critical acceleration of the systems, forcing them in this way to respond in the plastic (after yielding) and metaplastic regime (after peak conditions are reached, when resistance of the footing decreases due to P–δ effects). **Figure 2.27** provides a collective view of the three loading protocols utilized in this testing series. System A was subjected to testing sequences I and II whereas system was subjected only to sequence III.

Figure 2.28 (i) presents the results for the response of system A, when subjected to the Aegion record, an earthquake of moderate intensity. This excitation contains a strong pulse, the amplitude of which becomes even larger due to dynamic soil amplification (**Figure 2.28 (i)(A)**). Thus, the maximum PGA imposed on the system exceeds significantly the critical acceleration for all cases, forcing the system to respond in a non-linear way for all cases examined. This strong pulse causes the development of a maximum rotation $\vartheta_{max} = 0.01\,rad$ irrespectively of the soil conditions. In terms of residual settlement all configurations lead to similar values, except for the specimen on loose sand, (poor soil conditions), which develops a residual rotation by an order of magnitude larger $\vartheta_{res} = \vartheta_{max}$. In fact it is worth highlighting that the specimen on dense sand has practically zero

cumulative rotation, proving its recentering ability (**Figure 2.28 (i)(B)**). Shallow soil improvement proves to be quite effective in reducing the residual rotation, with the deeper $\frac{z}{B} = 1.0$ crust being more advantageous to the shallow one.

Shallow soil strengthening is also contributory to limiting the accumulated settlement, which under such strongly non-linear foundation response is expected to be significant. The enhancement offered to system by the soil improvement is illustrated in **Figure 2.28 (i)(C)**. It is interesting at this point to compare the results stemming from the seismic excitation with the corresponding ones from the slow cyclic tests. It is evident that although qualitatively the shake table tests confirm the findings of the slow-cyclic pushover tests, from a quantitative point of view, there are very substantial differences. These differences can only be attributed to the dynamic response of the soil, which cannot possibly be captured through cyclic loading. Under dynamic loading, the deformation of the soil underneath the footing is not only caused by the stresses imposed by the rocking foundation (inertia loading) but is also affected by the shear stresses developing within the soil, due to the seismic shaking itself (kinematic loading). Even in the absence of a rocking foundation, the sand would settle because of dynamic compaction, which of course would be much more intense for the case of loose sand ($\boldsymbol{Dr} = \mathbf{45}\%$).

Such a simplified explanation however applicable and suitable for a homogeneous soil unfortunately is inadequate for the configurations with the improved soil. The dense sand crust should not be prone to such effects, underneath this layer however there is still loose sand, which will settle due to dynamic compaction. Naturally, the thickness of the loose sand layer is reduced with the increase of the depth of the improvement crust. Since the amount of soil compaction is proportionate to the thickness of the loose sand layer, the configuration with the shallow crust should lead to larger settlements due to dynamic densification of the soil in comparison to the configuration with the deep crust. The experimental results verify the above simplified approach confirming that the soil with $\boldsymbol{\frac{z}{B} = 0.5}$ strengthening develops settlements deviating more, from the ones in slow cyclic testing. On the other hand, the specimen founded on $\boldsymbol{\frac{z}{B} = 1.0}$ developed settlement deviating less from the corresponding slow cyclic values. This difference is attributed to the fact that the two mechanisms which lead to footing settlement (rocking of the footing and dynamic compaction of the soil deposit under the weight of the footing) act simultaneously and therefore are coupled resulting in less settlement than if they were acting separately. Nonetheless, the results confirm that the differences in the response (compared to cyclic loading) are due to dynamic compaction of the underlying loose sand, since rocking led to the same maximum rotation for all cases!

In an attempt to study the effect of the excitation frequency, the researchers proceeded to testing of system A subjecting it to the deleterious excitation Pacoima Dam, from the earthquake in San Fernando, 1971. The results from this test are summarized in **Figure 2.28(ii).** The response can roughly be divided in two phases:

The first phase, lasting approximately from t =3 to 6s, which includes the long duration (and hence, low frequency) directivity pulse, having an amplitude of 0.6g (see the shaded area in **Figure 2.28(ii)A**). With a very large period $T = 1.2\ s$, this pulse drives both systems well within their metaplastic regime, developing a maximum rotation $\vartheta = 40\ mrad$ (**Figure 2.28 (ii)B**).

The second phase (for t >6 s) is characterized by a multitude of strong motion cycles of even larger amplitude, which is enhanced by the soil amplification, but of substantially smaller period. Under such disastrous seismic excitation, the system managed to survive in the case of dense sand and of $z/B = 1$ soil improvement. Although the differences in θ_{max} are again negligible, there is a substantial difference in $\theta_{res} = 45\ mrad$ for the case of $z/B = 1$ soil improvement, compared to $12\ mrad$ for ideal soil conditions.

As far as the settlement response is concerned, the response of the two different soil configurations deviates significantly. As illustrated in **Figure 2.28 (ii)C**, during the long period directivity pulse, the settlement is minimal in both cases. In fact, the rocking system is mainly subjected to uplifting and the accumulated settlement at t =6 s does not exceed 1 cm. During this phase of response, the $z/B = 1$ crust is proven very effective, exhibiting practically identical behavior to that of the ideal case of dense sand. The performance is markedly different during the second phase, which is characterized by a multitude of strong motion cycles of larger amplitude but of much higher frequency. The settlement mainly takes place during this phase, with the accumulated settlement reaching 8 cm for dense sand and 12 cm in the case of the $z/B = 1$ soil crust. Comparing these results with the ones stemming from the slow cyclic tests for the same value of maximum rotation it is confirmed as for the moderate excitation, that the slow cyclic tests underestimate significantly the awaited settlement. The reasons are the same with those previously discussed, but the accumulation of settlement and the efficiency of shallow soil improvement are clearly affected by the excitation frequency.

To look into the matter of the frequency influence more thoroughly, the researchers tested the lightly loaded system using two idealized 15-cylce sinusoidal motions of the same amplitude with different frequency: f =1 Hz and 2Hz. **Figure 2.29** compares the performance of the two cases of soil improvement with the ideal case of dense sand. It is evident that the "slower" f =1 Hz excitation develops larger ground displacement compared to the "faster" f=2Hz sinus. And since the rotation of the rocking system depends largely on the ground displacement, the rotation amplitude per cycle of the systems subjected to the f =1 Hz sinusoidal excitation is approximately double the respective rotation when the systems are subjected to the f =2 Hz excitation (**Figure 2.29B**).

In terms of settlement response, we observe that the specimen founded on dense sand, is not particularly sensitive to the excitation frequency. However, the view changes significantly, when it comes to the two configurations of improved soil. In these cases the excitation frequency affects largely the response, since it is obvious that, in both cases of shallow soil strengthening, the settlements are much larger for the high frequency excitation than for the low frequency one (**Figure 2.29C**). This very substantial difference is

not only solely attributed to dynamic compaction of the underlying loose sand but is also related to the fact that the efficiency of shallow soil improvement is dependent on the cyclic rotation. In agreement with the results of monotonic and cyclic pushover tests, the efficiency of the crust is found to increase with rotation (the amplitude of ϑ for $f = 1\ Hz$ is almost twice as much for $f = 2\ Hz$). For smaller rotation values the foundation is in full contact with the supporting soil, generating a deeper stress bulb, hence affecting the underlying loose sand layer. When uplifting is initiated the effective foundation width is drastically decreased, reducing the depth of the generated stress bulb, for which case a larger portion of the rocking-induced stresses are obtained by the "healthy" soil material of the crust, improving the performance of the system.

Another dependence investigated by the writers for the lightly loaded system is the one between the number of cycles and settlement. According to their findings, the efficiency of shallow soil improvement is also ameliorated with the number of strong motion cycles. In all cases examined, irrespectively of excitation frequency or amplitude, the settlement per cycle of motion decreases with the number of cycles, thanks to soil densification underneath the footing. In general it is observed, that high frequency excitations have a smaller rate of settlement reduction. On the other hand, the low frequency ($f = 1\ Hz$) excitation leads to a much more intense settlement reduction. In this case, the first two or three cycles are enough to cause substantial dynamic compaction of the soil, and as a result the remaining strong motion cycles are not leading to any substantial additional settlement. The oscillation of a lightly loaded system is of significantly larger amplitude for the low-frequency sinusoidal excitation, and therefore, the first two or three cycles of large rotational amplitude are enough to compact the sand under the footing. On the contrary, the sand is continuously compacted due to small vibrations of the footing when the system is subjected to the f =2 Hz sinusoidal excitation. Moreover, the decreasing trend of settlement accumulation should also be attributed to the rotation accumulation of the systems; as the systems unavoidably accumulate rotation toward the one side, they do not rotate symmetrically rather, they tend to tilt even more. Since settlement development is correlated with the compaction of the sand as the structure returns to its initial position, it is reasonable to assume that settlement accumulation is also affected by the rotation accumulation.

Last but not least concerning system A we highlight also the results proving the decoupling of the ground motion from the super structure as a result of the rocking isolation. To this end **Figure 2.30** is presented with the resulting values of the maximum acceleration recorded at the "deck mass" of the specimen plotted against the PGA of the imposed excitation. It is obvious that the developing maximum acceleration at the deck mass is much lower than the imposed PGA. This phenomenon supports the effectiveness of rocking as a means of isolating the superstructure from the ground motion. The results of the shake table tests are also compared with the previously discussed critical acceleration $\boldsymbol{a_c}$ stemming from static pushover tests.

In all cases examined, during the dynamic loading the footing exhibits a certain degree of overstrength ($a_{max} > a_c$). In fact, this overstrength is more significant as the FS_v value decreases. These conclusions are in full agreement with the results of slow-cyclic pushover tests (Anastasopoulos et al., 2012).

The much lower capacity of system B imposed a restriction to the researchers concerning the loading protocol, hence this system was only subjected to shaking sequence III, which is composed of sinusoidal excitations of frequency f =2 Hz of increasing PGA (from 0.1 to 0.4g). The heavily loaded system lying on loose sand was quite unstable, accumulating rather substantial rotation and settlement and toppled for $PGA = 0.4g$. In the case of the shallower soil crust, System B toppled for a slightly higher value of PGA. Further increase of the improvement depth to $z/B = 1$ led to a much more stable performance, and almost identical response with the ideal case of dense sand, even for the maximum imposed PGA.

In terms of settlement, the deeper $z/B = 1$ soil improvement led to a substantial improvement. A more shallow $z/B = 0.5$ crust was not as effective. The efficiency of the crust started improving for larger acceleration amplitudes, when uplifting started to dominate the response, but soon after that the system collapsed. Based on this result, it is safe to conclude, confirming the results extracted also from Anastasopoulos et al, [2012], that such a shallow $z/B = 0.5$ improvement is not enough for such heavily loaded systems. On the other hand, the deeper z/B=1 soil crust proved to be quite effective, with the settlement being roughly 25% larger compared to the ideal case of dense sand.

An interesting finding about this system is its much higher efficiency in decoupling the motion from the superstructure. In stark contrast to the lightly loaded System A, where overstrength was apparent, the measured acceleration a_{max} were much lower than the corresponding critical acceleration a_c. The fact that for all four soil profiles a_{max} increased with the excitation PGA is attributed to soil densification and to the fact that the pier was gradually tilting toward the one side resulting to increased a_{max} on the opposite side. Quite interestingly, although System B did not reach its ultimate moment capacity, the response was profoundly non-linear as revealed by the accumulation of rotation in all cases examined. This phenomenon led to a rather intense attenuation of the seismic motion for all four soil profiles examined.

In an attempt to shed more light to such de-amplification effects, **Figure 2.31** compares the performance of the heavily loaded System B with the lightly loaded system A. The comparison is performed for seismic excitation with an f =2 Hz sine having a PGA of 0.2g. It is remarkable the fact that system B in spite of having significantly lower moment capacity, it performs better. More specifically, the lightly loaded system was exhibited higher settlement for all cases except for the ideal soil conditions. The differences are attributed by the writers to the following factors:

- This particular excitation is the first of shaking sequence I, whereas for the heavily loaded system B, it is preceded by two other excitations, which means that some densification may have already taken place.

- The loose sand representing poor soil conditions is of lower relative density in the case of the lightly loaded system (Dr =45% as opposed to 60%), thus having larger margin to be compacted.
- Although the seismic excitation is the same, being much stiffer, the lightly loaded system is excited much more: its lower natural period is closer to the dominant period of the seismic excitation. In stark contrast, the heavily loaded system is much more flexible, and becomes even more flexible as soon as it enters the plastic regime. Due to such non-linear SSI, significant degradation of the system's effective stiffness takes place, leading to a substantial increase of its effective period, which in turn leads to de-amplification. As a result, the heavily loaded system proves to be more resilient to this particular seismic excitation than the lightly loaded ones.

Naturally, overall the lightly loaded systems are much less vulnerable, as also revealed by the cases in which the heavily loaded systems toppled.

Last but not least, after comparison of the two systems with the same FS_v (the lightly loaded system lying on loose sand and the heavily loaded system lying on dense sand), it is found that the two systems exhibit remarkably different behavior. The heavily loaded system accumulates less settlement and the rotation amplitude of its oscillation is notably smaller. This proves that the FS_v alone cannot describe the dynamic response of two systems subjected to the same excitation. As shown in other studies (Kourkoulis et al.,2012), the response of two rocking systems of the same FS_v and aspect ratio h/B subjected to the same excitation can be similar provided that there is the appropriate analogy in the stiffness of the foundation soil. In this case, the loose sand deposit proves to be relatively less stiff for the lightly loaded system leading thus to increased rotation and settlement accumulation.

A research study performed by Anastasopoulos et al., [2010] used as an example a simple but realistic bridge structure to illustrate the efficacy of this new concept being indeed a pioneering and effective one for design. They demonstrated by means of nonlinear Fe analyses that the ductility capacity of the new design concept is an order of magnitude larger than the capacity of the conventional design. This is the main advantage of "utilizing" progressive soil failure as demonstrated in **Figure 2.32**. In terms of the seismic response of the system, after conducting nonlinear dynamic time history analyses, using an ensemble of 29 real accelerograms it was shown that for large intensity earthquakes, exceeding the design limits, the performance of the new design scheme was proven advantageous, not only avoiding collapse but hardly suffering any inelastic structural deformation. According to the results of the analyses, the system experienced in some cases increased residual settlement and rotation. This shortcoming, as the researchers comment, is "a price to pay" for the advantageous effect of the strongly inelastic response of the foundations and must be properly evaluated in the design. **Figure 2.33** presents some of the results provided by the dynamic analyses.

The numerically approach was accompanied by shake table testing performed by Anastasopoulos et al., [2013], in order to be verified also experimentally that this new

concept is indeed beneficial for the structures. The model used for the numerical simulation is presented in **Figure 2.34(a)**, illustrating both the conventional and the new design philosophies.

Figure 2.34 (b) presents the comparison between the prototype and the testing component. It is interesting to mention at this point, that a modification in the geometry of the footings had to take place, in order for the scale effects to be alleviated. According to the researchers, the significant discrepancy in the induced strength on the soil, between the prototype and the model, would lead to an overestimation of the soil bearing capacity. Thus the similitude between the real structure and the specimen managed to be preserved by incorporating the same factor of safety against vertical load as well as the same ratio of the lateral loading of the foundation over its corresponding capacity (M/M_{ult} and Q/Q_{ult}) following data in the design of the specimen. These two conditions were satisfied by preserving the factors of safety for vertical (FS_V) and combined-seismic loading (FS_E) in the model the same as in the prototype. Of course the limitation of avoiding any overestimation of the soil bearing capacity, would lead to a reduction of the foundation area. But doing so in both directions would violate the third requirement concerning the preservation of the slenderness ratio h/B, which controls the rocking response. Thus a modified shape was adopted for the footings, achieving a reduced area by decreasing only the out of plane foundation dimension L.

Two testing specimens were constructed for the needs of the tests: one representing the conventional design and the other representing the rocking – isolation design. **Figure 2.35** provides the dimensions of the two specimens, which in both cases consisted of strip foundations supporting cantilever columns resting on a dense sand soil stratum ($D_r = 85\%$) and were constructed by applying the appropriate scaling laws on the corresponding conceptual prototype. The same scaling laws were applied, as the ones mentioned in Drosos et al., 2012. For these tests, two different scenarios of FS_v were taken into account: $FS_v = 3.3$ and $FS_v = 6.9$.

The input motions used in the experiment covered a wide variety of earthquake scenarios, ranging from medium intensity excitations, what we consider in the various building codes as "design earthquake" (e.g. the Aegion record), to strong motions like Gilroy and ultimately to extremely strong motions, dramatically exceeding the design, like Rinaldi and Takatori, which are considered as some of the most deleterious excitations recorded.

To illustrate the improved performance of the rocking isolated system, the researchers compared the maximum acceleration which can possibly develop at the deck mass in order to assess the performance of the two designs for the three aforementioned levels of motions. In the first case of moderate motions, i. e. “design earthquake”, it was shown that the large conventionally designed foundation can sustain $a_c = 0.40\ g$ taking into account also the observed cyclic over- strength. Due to its substantially lower moment capacity, the smaller foundation of the rocking-isolated system can sustain significantly lower acceleration: $a_c = 0.20\ g$, if cyclic overstrength is accounted for. Interestingly, in both cases of this excitation event the measured acceleration is quite lower than the

corresponding $\boldsymbol{\alpha_c}$ value, implying that none of the two foundations reached its ultimate moment capacity.

Yet, the response of both systems shows a great difference from what is known as linear-elastic regime, demonstrating in this way the presence of hysteretic material (**Figure 2.36**). It is worth mentioning that the elastic stiffness, as it was calculated from the cyclic relation of lateral force - displacement of the conventionally system was estimated approximately 217 MN/m whereas the effective one was only 26% of the elastic value. The rocking system demonstrated a similar drop in the transient stiffness, estimated about 24%, with the elastic stiffness to be equal to 92 MN/m.

In the same work the researchers provide an illustration of the seismic performance of the two systems, by reporting the drift ratio time histories. The results showed that for moderate seismic shaking (Aegion) both systems demonstrate approximately the same maximum drift $\delta \approx 8\,cm$. Nevertheless, in terms of residual drift, the conventionally designed system seems to re-center entirely, whereas the rocking - isolated one ends up with a residual drift of about 2 cm, which is attributed to the residual rotation of the foundation.

For strong motions (Gilroy) the increase of seismic demand is reflected on the response of both systems, which now clearly mobilize their ultimate moment capacity. This is evident also in the $M - \vartheta$ cyclic curves (**Figure 2.37**). The larger conventionally designed foundation reaches its ultimate moment capacity, but without exhibiting substantial nonlinearity (**Figure 2.37a**). On the other hand, the smaller foundation experiences strongly nonlinear response, as evidenced by its oval-shaped $M-\vartheta$ loops. As it was awaited and is also illustrated in the $w - \vartheta$ curves (**Figure 2.37a**) the conventional system experiences substantially lower rotation and uplifting-dominated response compared to the rocking-isolated system which accumulates settlements upon each cycle of rotation. The latter system results in a residual settlement of about 3.2 cm, three times larger than the conventional one. Of course the advantageous performance of limited rotations for the conventional system comes at the cost of developing higher inertia forces. The rocking isolated system develops a bending moment at the base of the pier bounded by the inferior moment capacity of the footing, whereas the conventional system has the possibility to develop moments exceeding its capacity, thus sustaining flexural cracks at the base of the pier. Naturally, its ductility capacity is the deciding factor of the system's ultimate survival. In terms of the recorded drift ratios, the rocking-isolated system experiences substantially larger maximum deck drift δ ≈ 10 cm, as opposed to roughly 6 cm of the conventional system. The residual values are 2.4 cm and 1.9 cm respectively for the two systems, values in both cases considered tolerable by the writers of the study.

When the motions of the maximum intensity were applied on the system, both systems mobilized fully their ultimate moment capacity. In fact, the conventional system developed larger acceleration compared to its estimated α_c. The only factor which can account for this improvement is the soil densification. After all, these excitations were applied on the system after a sequence of already four motions. The $M - \vartheta$ loops of **Figure**

2.38 confirm the strongly nonlinear response of both foundations. Contrary to the previously discussed case of strong motions, both foundations exhibit similar maximum rotation, despite their substantial differences in terms of moment. Again, the conventionally designed foundation experiences lower residual rotation compared to the rocking-isolation alternative. Moreover, according to the $w - \vartheta$ curves, the larger conventionally designed foundation exhibits uplifting-dominated response, enhanced by the previously discussed densification from preceding shaking events. Its residual settlement reached the value of 5.8 cm (**Figure 2.38a**). On the other hand, almost double was the value of accumulated settlement for the rocking – isolated system. Residual drift ratio of around 3% developed on the rocking isolated system, whereas the conventional one exhibited slightly larger value. The maximum drift ratios recorded were 2.7% and 3.9% for the two systems respectively.

One of the fears, which cause doubt against the efficacy of rocking – isolated systems is the fact that although the performance of a rocking-isolated structure may be advantageous, after sustaining a strong earthquake the damage to the system will be in the form of permanent deformation: settlement and rotation. These accumulated displacements, even in the cases of being within tolerable limits, cannot be easily alleviated. For this reason, an additional aspect was investigated in the currently discussed experimental study: the performance of a rocking isolated system subjected to consecutive earthquake excitations. This was materialized by applying the injurious Takatori, 1995 seismic record, considering three different scenarios:

(a) The seismic excitation is imposed on the "virgin state" soil-foundation structure model, i. e. a newly built and undisturbed system. In this case Takatori is the first shaking event.

(b) The seismic excitation is imposed on a *non-symmetrically* "weakened" model, having already sustained several real records of increasing severity. In this scenario Takatori is applied after all other real records (Aegion, Lefkada, Gilroy, and Rinaldi).

(c) The seismic excitation is imposed on a *symmetrically* "weakened" model, having already sustained a sequence of symmetric multi-cycle artificial (sinusoidal) excitations of increasing severity. Takatori is again applied after all of them have been induced to the system.

The performance of the rocking-isolated system subjected to the three scenarios is summarized in **Figures 2.39a**, **b** and **c**, in terms of $M-\theta$ and $w-\theta$ response, and deck drift time histories respectively.

The results prove that the rocking system avoids toppling collapse in all three shaking scenarios. As far as the first scenario is concerned, the $M-\theta$ cyclic curves presented in **Figure 2.39a** reveal strongly inelastic foundation response, accompanied by substantial accumulation of settlement (28 cm).

The residual settlement seems to be rather limited in the case of the rocking-isolated system having already sustained a number of previous non symmetric real shaking events. In this case the accumulated settlement is reduced by almost 50% (**Figure 2.39b**). According to the results of the third scenario, when symmetric multi-cycle sinusoidal motions have

preceded the Takatori record, the residual settlement is reduced even more, reaching the value of approximately 7 cm (**Figure 2.39c**). The researchers attribute this improvement in the response to the soil densification taking place during the preceding shaking events. As the sand becomes denser, the behavior of the foundation becomes more-and-more uplifting-dominated, as opposed to its sinking-dominated "virgin-state" response. The partial embedment of the foundation due to the multitude of the preceding multi – cycle events, accounts also for the soil improvement.

In terms of rotational response of the system, in the first scenario after the Takatori record the system exhibits a residual rotation of $24\ mrad$, a value which is double in the second scenario, when the system has previously sustained non-symmetric shaking events. Contrary to this trend, in the third scenario the accumulated permanent rotation remains practically the same (**Figure 2.39**). This apparent dissimilarity is directly dependent on the inherent characteristics of the seismic excitation. In Scenario 3, the preceding symmetric (sinusoidal) shaking events strictly produced settlement without permanent rotation, whereas the shaking history of Scenario 2 includes non-symmetric seismic motions (real records), which tend to accumulate settlement and rotation. In this way, due to the nonlinearity of the system a bias is created on the side of the accumulated rotation, thus when the already tilted system is subsequently subjected to the Takatori record, P–δ effects contribute even further to the accumulation of rotation in the direction of initial tilting, leading to increased permanent rotation. These results are confirmed also by the results of the deck drift time histories, according to which, in Scenario 1 the residual drift reaches 37 cm, dramatically increasing to 70 cm when the system has already sustained non symmetric shaking events in Scenario 2. Again, changing the trend, after the third scenario the residual deck drift is reduced to 29 cm.

Based on the aforementioned experimental works of shake table testing, it can be inferred that the main shortcoming is the reduced scale, which has to be adopted. In spite of the fact that a small scale test would mean limited stresses, the problem is in reality more complex. The fact that there is a significant dead load, the weight of the superstructure, which the soil skeleton has to bear, the representative friction angle φ has to be determined. The friction angle on the other hand is a function of the confining stress (Bolton, 1986). The stress field developing in the backfill soil cannot be reproduced in a scaled manner. Small scale effects lead to lower stresses than the real ones, which leads to overestimation of the friction angle φ and by extension of the soil strength. In the same manner, other parameters such as the shear modulus, also dependent on the applied field of confining stress, cannot be accurately determined from shake table tests results.

Another inherent disadvantage in this methodology of testing has again to do with the necessary scaling, which has to be applied on the specimen, in order for the testing to be feasible. As already mentioned in the published works of Anastasopoulos et al., [2013] and Drosos et al., [2012], this need may lead to a modified geometry in the design of the specimen, deviating from the geometry of the prototype. However consistent the design might be, by observing the slenderness ratios and the safety factor against vertical loading,

this modification introduces uncertainties in the overall behavior of the system, which can constitute only a simplified approach of the real problem.

Last but not least, as it will also be discussed in the following Chapter it is rather difficult to reproduce the theoretical input motion of the real earthquake excitation with the shake table. This difficulty was also stressed out by Shirato et al., [2008]. Thus the inherent uncertainties in this kind of testing are significant and for this reason it is necessary to turn to validating methodologies, such as comparison with other similar experimental works or analytical results, to verify that the outcome of the experiment reflects indeed the investigated phenomenon.

The reader is encouraged to obtain a more spherical view on the sector of shake table testing by studying the following works: Sakellaraki et al., [2005], Mergos and Kawashima, [2005], Espinoza and Mahin, [2006] and Hung et al., [2010 as well.

1.3 Centrifuge Testing for Rocking Bridges

Having stressed out the weaknesses of the shake table as a methodology of testing, it is obvious that the close-to-real scale accomplished by this method has its advantages as well. On the other hand a remarkable contribution to the published literature concerning experimental studies of rocking response for bridges' footings originates from centrifuge tests. The decisively lower cost of such tests, as well as the possibility to achieve more precise results in terms of the developing soil stress field, avoiding scaling effects, have made centrifuge tests a rather competitive application in the current area of research. Geotechnical centrifuge modeling uses centrifugal acceleration to increase the self-weight stresses in a small model to equal the self-weight stresses in a large prototype. If a soil model containing the same soil as the prototype is spun at centrifugal acceleration of $\boldsymbol{N}$ times the prototype gravity, the vertical stress in a soil layer at depth h in model scale is identical to the vertical stress in the prototype soil layer of depth $\boldsymbol{N \times h}$. Because soil properties such as the yield strength and shear modulus depend on the confining stress, the centrifuge facility improves the ability to accurately model the soil properties. The principles of dynamic centrifuge modeling for soil-footing-structure interaction research were explained by Morris [1981].

Gajan and Kutter, [2008] conducted centrifuge tests of single bridge columns founded on shallow rocking foundations under dynamic excitation and demonstrated that rocking foundations have a non-degrading M - ϑ behavior, and the analytically predicted moment capacity is verified by the experimental results. They introduced the ratio A/A_c, where A is the area of the footing, and A_C is the minimum soil-footing contact area that supports the vertical load during rocking. They showed that re-centering, energy dissipation and settlement behavior of rocking footings are better correlated to the critical contact area ratio, A/A_c, where A is the area of the footing and A_c is the minimum soil-footing contact

area supporting the vertical load during rocking. In the following Chapter more information are provided for the definition of the $\boldsymbol{L_c}$.

Deng and Kutter, [2012] presented results of centrifuge model tests exploring the behavior of rocking shallow foundations embedded in dry sand, investigating a variety of factors of safety for vertical bearing. The results of slow (quasi-static) cyclic tests of rocking shear walls and dynamic shaking tests of single-column rocking bridge models were performed. Results are studied in terms of moment–rotation and settlement–rotation of the system.

To this end, two series of model tests (named LJD01 and LJD03) performed in the centrifuge facility of UC Davis at centrifugal acceleration of 49 g were performed. The LJD01 test series featured slow (quasi-static) cyclic tests on five shear wall models with small (S), medium (M), and large (L) footing dimensions as indicated in **Figure 2.40**. The models in LJD03 series were subjected to several dynamic shaking tests using a shaker mounted on the centrifuge. The specimens rested on Dry Nevada sand. The backfill soil had relative densities varying from 73% (dense) to 38% (loose). The peak frictional angles of the soil in the zone affected by the footing were estimated using the procedures in Salgado, [2008]. **Figure 2.40** lists soil characteristics and the key mechanical and geometric properties of the structural models.

Gajan and Kutter, [2008] concluded that the settlement caused by foundation rocking may be significant if the L_f/L_c value is small. To limit settlement, L_f may be increased, but this in turn increases the moment capacity because M_{c_foot} is linearly proportional to L_f and may result in conventional elastic foundations. Another approach is to decrease settlements by improving the ground under the footing. One idea for ground improvement that seems practical is to create a region of improved ground under each edge of the rocking foundation where the bearing pressure is the highest during rocking. Consequently, circular concrete pads under the edges of the footing were used. Their dimensions were 25mm in diameter and 50mm in height in model scale, or 1.23m in diameter and 2.45m in height in prototype scale. The measured axial load capacity of the pads was estimated to be 60–70% of the structural weight. However, no evidence of pad failure was observed during centrifuge tests. The concrete pads are envisioned to limit the settlements by distributing the edge loads over the pad area. **Figures 2.41(a)** and **(b)** show the elevation view of the models supported by the pads, and **Figure2.41(c)** shows the plan view of the embedded concrete pads.

When an embedded footing rocks, soil can potentially fall into the gap that forms during each of the footing uplift cycles. The centrifuge model footings were backfilled with clean dry sand, which probably tends to ravel into the gap more than many moist and silty sands used in construction practice. To limit the amount of sand raveling under the footing, which would it makes the interpretation of the settlement mechanism more complicated; thin layers of oil-based modeling clay were stuck to the side walls of the footing of almost models. In this way the sand was successfully in restricted from flowing under the footing;

however, the phenomenon was not entirely prevented. The placement of thin modeling clay layers is illustrated in **Figure 2.42**.

The lateral sliding of the footing was not significant compared with the displacement of the shear wall at the loading elevation in this study because the footings were embedded and the moment-to-shear ratios (H/L_f) were relatively high. Gajan and Kutter, [2009] showed that, when the $H/L_f > 1.0$, rocking dominates over sliding.

The results are presented first for the slow cyclic tests, distinguishing the cases of high and intermediated ratio L_f/L_c.

Concerning the former case, Gajan and Kutter, [2008] characterized the settlement versus footing rotation during each cycle using the results from slow-cyclic tests and dynamic shakes, and correlated the settlement per cycle with the amplitude of rotation for $1.50 \leq \frac{L_f}{L_c} \leq 15.0$ varying between. To find the settlement/uplift mechanisms for the cases with larger L_f/L_c ratios, shear-wall models SC-1, MC, and LC with $L_f/L_c = 14.5, 30.2, \text{and } 44.5$, respectively, were designed for slow-cyclic tests (see **Figure2.40** for model details). The relative density of the ground soil was 73%.

Figure 2.43(a) shows the correlation of rocking moment versus footing rotation of the LC model. The predicted M_{c_foot} is drawn as two dash lines in **Figure 2.43(a)**. Obviously, M_{c_foot} was non-degrading and matched the predicted capacities very well, consistent with the findings of Gajan and Kutter, [2008]. The moment versus rotation loops display "pinched", S-shaped hysteresis curves. The curves have initial rocking stiffness higher than that of the models with smaller footing length. This is reasonable because the initial rotational stiffness is proportional to the L_f. The phase of plateau in the moment versus rotation curves was reached when the footing started to rock about the critical contact area. The residual rotation was less than 1% after three cycles of 4% amplitude, showing the benefit of a rocking footing in limiting the residual rotation. Three representative phases of the rocking footing are labeled and sketched qualitatively in **Figure 2.43(c)**. The footing was initially flat and in full contact with the soil; as the lateral load increases, the structure rotates about one edge of the footing. The rocking moment reaches the moment capacity as the rotation reaches approximately 0.5%, when the soil-footing contact reaches the critical contact area (A_C). The phase where the rocking footing stands on the critical soil-footing contact area and the moment remains constant at the moment capacity M_{c_foot} is marked as "2" in **Figures 2.43(a)** and **(b)** and sketched in **Figure 5(c)**. The soil profile phases from these cyclic tests are also consistent with the sketches in Paolucci et al., [2007], which recorded pressure at the foundation base using shake-table experiments. **Figure 2.43(b)** shows the curves of the footing settlement versus the footing rotation, in which the positive vertical axis means uplift. The high cyclic stress on the moving contact between the soil and footing is expected to cause settlement and curving of interface soil. Instead of settlement, however, the footing actually ended up with residual uplift in this experiment (see the direction of the residual settlement in **Figure 2.43(b)**). It is possible that dilation of the soil under the footing caused by bearing failure might contribute to reducing settlements.

Additionally, despite our efforts to reduce sloughing of sand under the rocking footing, the primary mechanism of residual uplift appears to be the falling of sand into the gap under the footing rocking, as illustrated in **Figure 2.42(a)**. Comparing the uplift of these models implies that higher L_f/L_c ratio led to larger uplift. **Figure 2.42(b)** shows the excavated footing of model LC. The curved colored sand profile underneath the footing indicated the curved contact interface resulting from the rocking footing. The clay sheets on the sides separated from the footing, and the adjacent Nevada sand fell into the gaps beside and underneath the footing. **Figure 2.42(b)** confirms the hypothetical mechanism of uplift. The sand falling into the gap would hinder the complete re-centering; subsequent compression of the falling sand may contribute to increasing the width of the hysteresis loops.

As far as the results for the ratios with ratio L_f/L_c of intermediate values ($L_f/L_c < 10.0$) are concerned, they stem from tests, in which the specimens were placed on loose sand ($D_r = 44\%$). The two structural models are identical, but SC/I were supported on concrete pads. The rocking moment versus rotation of two models are shown in Figures 2.44(a) and 2.45(a). The settlement versus rotation curves of the footings are shown in **Figures 2.44(b)** and **2.45(b).**

As shown in **Figure 2.44(a)**, the hysteresis loops are less "pinched" — the unloading stiffness is nearly linear and not S-shaped as it is in **Figure 2.43(a)**. Large energy dissipation is indicated by the significant hysteresis shown in **Figure 2.44(a)**. The hysteresis may be explained by the low L_f/L_c ratio of the SC-2 footing. Imagine an extreme case of a footing on a rigid foundation with $L_f/L_c = 1.0$. The load deformation hysteresis would be just straight lines because there is no energy dissipation involved in this hysteresis. On the other hand, if the ground is soft, and L_f/L_c is a certain small number, then larger hysteresis will be observed in the moment versus rotation curves. The moment capacity of the curves in **Figure 2.44(a)** almost reaches the predicted M_{c_foot}, although there is a small error, which may come from the error in estimating L_C. Again M_{c_foot} did not degrade even after three 4% cycles.

As observed in **Figure 2.43(b)**, the settlement versus rotation curve indicated that, as we load the footing, it rocks (or rotates) and uplifts with an open gap forming at one side; while unloaded, the footing subsides back, but a net settlement occurs because of the compaction and shearing of the soil underneath. Each rocking cycle causes similar cumulative settlement. The settlement during the last three 4% cycles was $0.043\ m$, which is considered to be significant but not excessive for a bridge foundation.

The moment versus rotation hysteresis of the model SC/I in **Figure 2.45(a)** is similar to that of SC-2, except for the small kinks caused by the presence of the concrete pads while the footing was unloaded. The effects of these pads are conceptually sketched in **Figure 2.45(c)**. The pads at the edges of the footing might be lower than the pads at the center of the footing because of the concentrated loads on the footing edges after many cycles. The footing on the concrete pads had an effective L_f/L_c ratio larger than the footing directly on the same ground, because the pads would distribute the stress from the structure, as shown in phase "1" in **Figure 2.45(c)** in which most of the weight on the footing is taken by the pad

underneath it. According to the predicted value, M_{c_foot} of SC/I should be larger than M_{c_foot} of SC-2; this hypothesis is confirmed by comparing the respective moment capacities shown in **Figures 2.44(a)** and **2.45(a)**. The footing base hit the central pads during the unloading process, resulting in the kink in the moment–rotation curves; this phase is marked as "2" in **Figure 2.45(c)**. The footing settlement versus rotation curves in **Figure 2.45(b)** show a smaller permanent settlement for the enhanced SC/I model. The settlement during the last three 4% cycles was 0.020 m, which represents a reduction of more than 50% compared with the settlement of SC-2.

SDOF models SF and ISF were subjected to a series of earthquake motions of various amplitudes and frequency contents that are available in Deng et al., [2012]. This section presents results from a motion consisting of asymmetric velocity pulses. The input motion and selected plots are compiled in **Figure 2.46**.The motion has an intermediate intensity with the $\mathbf{55}\ \boldsymbol{cm/s}$ peak velocity pulse and about 1-s pulse period. Time histories of deck drift angle, which are the ratio of lateral deck drift to the height of the deck relative to the footing base, are plotted in **Figure 2.46(a).**

Time histories of the vertical displacement of the footing center are shown in **Figure 2.46(b)**. Cumulative settlement from previous shakes is kept as the baseline. The permanent settlement of SF during this pulse motion was $12.9\ mm$, which is 18% larger than the $10.5\ mm$ settlement of ISF. These settlements are quoted at prototype scale and are both quite small. Note also that the settlements are smaller than the cyclic vertical displacements. The settlement was reduced as concrete pads were used, although the effect was not as obvious as it was in the slow cyclic loading tests. It should also be noted that settlements may be caused by factors besides rocking (e.g., free field settlement caused by cyclic shear stress), and these factors might not be controlled by the concrete pads.

The rocking moment versus footing rotation hysteresis of SF and ISF are depicted in **Figures 2.46(d)** and **(e)**. Considerable 2% plus peak-to-peak footing rotation was mobilized by this motion; however, the residual rotations of both rocking footings were found to be negligible. This fact reiterates the recentering benefits of rocking foundations in seismic events. A slimmer rocking moment versus rotation hysteresis for footings with concrete pads was observed in the dynamic shaking tests, which is similar to the pattern in previous slow-cyclic tests. The experimental moment capacity of SF matched very well with the theoretically predicted, M_{c_foot} marked in **Figure 2.46(d)**. The experimental rocking moment capacity ($23\ MNm$) of ISF indeed was greater than that predicted.

Figures 2.46(f) and **(g)** show the settlement versus footing rotation curves, respectively. Although the curves are not very smooth because of the complexity of the nonlinear dynamic systems, they clearly show the pattern similar to that of slow-cyclic tests. The amount of transient uplift is proportional to the footing rotation.

Deng et al. [2012] investigated further the rocking response of rocking – isolated foundation, focusing even further on the bridge structure. To this end they conducted three

series of centrifuge testing at the 9-m centrifuge at University of California, Davis. The test series have the following notations: LJD01, LJD02 and LJD03.

In the LJD01 and the LJD03 test series, the specimens consisted of scaled models from a single-column double-span bridge in central California.

The LJD01 test series involved the interaction between nonlinear columns and rocking foundations of single-degree-of-freedom (SDOF) bridge models. The LJD02 test studied two full bridge systems scaled from a two-column two-span prototype bridge in southern California, one implementing the new design principles stated in the previous section and another one following the requirements in the Seismic Design Criteria.

One of the important factors limiting the use of rocking foundations is the perception that they might tip over. Motivated from this inherent fear and in an attempt to investigate the tip-over mechanism of a rocking system, LJD03 test was intended to cause collapse by repeating strong shakes and to enable comparison of the collapse mechanisms for systems with rocking foundations to the mechanisms for a yielding column on a fixed-base foundation.

Figure 2.47 presents the test series, physical model codes, their critical model properties, soil densities, and bearing capacity factors of safety. The foundation base shear that mobilizes the moment capacity of the rocking footing and the base shear that mobilizes the moment capacity for a column were distinguished in the models so the yielding would be controlled between the footing and the column. If Cr < Cy, the footing is prone to rock before the hinge forms in the column; for the fixed-base bridge models the opposite situation is expected. If the two coefficients are close to each other in some cases, plastic behavior may occur in both the columns and the footings.

Tests LJD01 and LJD03 were performed in a gravitational field of 40g, whereas the test LJD02 was performed in a gravitational field of 49g. The model bridges were built upon homogeneous dry Nevada Sand. Peak friction angles for the sand beneath the footing were approximately 36° (LJD01 and LJD02) and 33° (LJD03). The relative densities (Dr) of Nevada Sand were $73\%, 77\%$, and 38%, respectively. The primary reason for use of $Dr = 38\%$ soil was to achieve a relatively low factor of safety ($FSv = 11$ in LJD03 test) for rocking-foundation models. The LJD01, LJD02 tests and Gajan and Kutter, [2008] have shown that rocking foundations performed well on dense sand, but little data are available for rocking foundations on loose sand. Therefore, loose sand was used in the LJD03 test.

For test LJD01 Two SDOF models (SD and MD) were considered (**Figure 2.48a**). The difference between these two specimens was the size of the footings, with the SD model having small-sized spread footings and the MD model having medium-sized spread footings. In this way they attempted to investigate the effects of the size of rocking foundations on the behavior of bridge systems. Both models had the same notched columns and deck mass.

The models for the LJD03 series, displayed in **Figure 2.48b-d**, are based on the same prototype bridge. Especially the 4CSF model was designed to explore the idea of the deck being supported on multiple columns might be more stable than a deck mass supported on a single-column. **Figure 2.49 (a)** shows the prototype bridge for the LJD02 test in the

longitudinal direction and **Figure 2.49 (b)** shows the elevation view of the bridge models with either rocking or conventional foundations in the transverse direction. The two models were identical except for the size of the footings, which were dimensioned so they would have different yielding mechanisms. Teflon pads were mounted onto the bottom of model deck plates and rested on a steel tube that represented the abutment. Physical hinges consisting of short lengths of threaded rod with negligible moment capacity were designed at the top of the columns. **Figure 2.50** shows the three-dimensional setup of the models and a picture in the container.

Both artificial and historical seismic motions were utilized in the tests, which were scaled and filtered appropriately to avoid frequencies and amplitudes that were outside the capability of the centrifuge and shake table equipment.

As far as the results are concerned, the deck drift time histories showed in general that the maximum total drift ratio of the rocking-foundation bridge in terms of the column rotation plus the footing rotation was greater than that of the hinging-column bridge, but the residual total drifts of the two bridge system were almost the same. The “rocking-foundation bridge” exhibited less but still significant column yielding even though the system was designed to rock before the column yielded. This indicates that the column of the rocking bridge was weaker than the design value, possibly attributed to the deterioration of the strength of the aluminum (i.e., the model column material) because of welding. So in effect, the rocking bridge suffered both rocking and hinging deformations.

The rocking footing, however, was able to absorb some of the ductility demand to protect the column. **Figure 2.51(a)** and **(b)** show the rocking moment versus rotation hysteresis of the rocking - foundation bridge system and the hinging column bridge system in the LJD02 test series. The theoretical rocking moment capacity and the experimental initial rocking stiffness are also indicated. **Figure 2.51(c)** and **2.51(d)** show the column moment versus rotation hysteresis, and for comparison, the moment versus rotation loops of the columns under cyclic loading tests. The dash lines in **Figures 2.51(c)** and **2.51(d)** are measured from cyclic loading tests on the same columns. The moment capacity of small rocking footing did not show any degradation even after two full cycles, and the large hysteretic loops dissipated a great amount of seismic energy. The maximum moment fits well with the predicted moment capacity. It was also observed that the foundation started to yield when the rotation was greater than approximately 2 mrad. As shown in **Figure 2.51(b)**, the large footing was capable of resisting the plastic hinging moment on the column. The acting moment on the large footing was well below its moment capacity. The large-footing bridge had to rely on other bridge parts, that is to say the column in this case, to dissipate the earthquake energy. **Figure 2.51(d)** indicates that the large hysteretic loops of the column dissipated most the earthquake energy, which is expected to occur when an elastic foundation is designed. The overall view of the results led the researchers to assume that the small footings reduced the ductility demand on the columns as well as the permanent drift of the deck. A column experienced a larger ratio of (permanent drift)/(peak

drift) than a rocking footing did. The double-column frame could also prevent the deck from accumulating permanent drift.

As far as the results from the LJD03 tests are concerned, it is worth mentioning, that SDOF systems and the 4-column system had almost the same performance based on the residual deck rotation; however, the small-footing system (SF) had slightly larger peak rotation than the 4CSF. The LF (large footing and hinging column) exhibited the highest residual deck rotation and was the worst among the three structures. Large residual deformation of the column at the notch section was observed when the conventional elastic foundation was designed; an example was shown in **Figure 2.52(a).** In contrast, the rocking footing showed very small permanent rotation as indicated in **Figure 2.52(b)**. The disturbed ground surface around the footing edges in **Figure 2.52(c)** was good evidence of significant footing rotation.

The moment attributed to vertical axial load of the deck (i.e., P _ Δ moment) plays different roles in the rocking foundation and fixed-base system. The P _ Δ moment adds to the restoring force when the footing rocks and uplifts; in contrast, it adds to the loading component when a column on a fixed foundation yields, causing instability of the system. The latter was the case for the column of the model LF with conventional foundation: the large deformation of the column due to the transient P - Δ moment accounted for 20% of its ultimate moment capacity and led to cumulative rotation toward one side until the column collapsed.

The writers mention that for as long as the excitations were small (first four events), the response of all specimens in the LJD03 test was practically the same. However, as the shakes became stronger, plastic hinge formed rapidly in the column of LF, and LF collapsed after three strong events. Plastic hinges also formed at the edge of the footing, but the footings were able to withstand the strong shaking with small permanent rotation. In an attempt to explore the tipover of rocking footings, repetitive pulse-like motions were applied to the rocking systems after the hinging-column collapsed. After several pulse-like motions, the rocking footings of SF and 4CSF ended up with less than 40 mrad permanent drifts.

Last but not least, this work managed to unveil an inconsistency as far as the settlements are concerning, compared to the published work of Gajan and Kutter, [2008]. They, characterized the settlement versus footing rotation during each cycle using the results from slow cyclic tests and dynamic shakes, and correlated the settlement per cycle with the amplitude of rotation and the ratio of A/A_C. So far the methodology worked fine, since Deng at al., [2012] proved through their experimental work that as a flat spread footing rocks, the contact area between the soil and footing reduces and this leads to limited localized bearing failure that in turn leads to progressive settlement. Based on understanding the rocking mechanism, and based on the authors' experiments, settlements are considerable if the ratio of A/A_C is small (e.g., < 5 or 10). If the ratio of A/A_C is large (e.g., > 10), the settlements tend to be very small. However useful for understanding the mechanism, the approach of Gajan and Kutter, [2008] was, it proved difficult to apply in

practice because it requires a priori estimation of the number and amplitude of cycles of footing rotation. Furthermore, their approach implies that the amplitude of settlement increases linearly with the amplitude of rotation. In LJD03, the authors observed that sometimes small rotations caused settlement and large rotations caused residual uplift, which is contrary to implications of Gajan and Kutter [2008].

In the framework of centrifuge tests, an experimental study performed by Loli et al., [2014] tested a bridge pier founded on rocking footings and compared it with the same pier being founded on foundation designed conventionally. The experiments took place in the University of Dundee.

This study aimed at providing experimental verification of their numerical findings suggesting that although a conventionally designed reinforced concrete (RC) pier on an adequately large shallow foundation would suffer structural failure of the RC column and collapse in an earthquake sufficiently exceeding its design limits, rocking motion of an alternative under-designed foundation would allow the same pier to survive even extreme shaking scenarios. To this end, it was necessary to realistically model the various attributes of nonlinear response of both the structural element (RC column) and the soil foundation interface, therefore necessitating the use of the following:

(1) A new scale model reinforced concrete capable of replicating stiffness, strength, failure mode, and post-failure response of the bridge pier.

(2) The University of Dundee (UoD) centrifuge earthquake simulator (EQS) to accurately replicate nonlinear soil behavior and provide repeatable replication of historically recorded earthquake motions.

A series of centrifuge tests were performed to investigate and compare the performance of the two RC model bridge piers, having the same structural section in each case, but each representing one of the two considered design approaches, namely, a conventional design and a rocking isolation design. This paper focuses mainly on the dynamic response of the two structures stemming from a variety of shaking scenarios using real historical ground motions.

For the materialization of the tests a scaling factor of 1:50 was applied, in order for the stiffness, strength, failure mode, and post-failure response of the bridge pier i. e. the various aspects of nonlinear response to be simulated in a pragmatic way. The nonlinear response of the soil (and soil – foundation interface) was rationally simulated by means of centrifuge testing, conducted in 50g gravitational field, which, as already mentioned, prevents scaling effects from distorting the results. In this scale the reinforced – concrete elements as well as the soil behavior were appropriately simulated. Previous works have implemented artificial way to guide the inelastic deformations within the superstructure (e. g. using notches on the piers made of aluminum, Deng and Kutter, [2012]), something which of course has certain limitations:

- The exact location of the plastic hinge is determined a priori, thus not allowing any moment redistribution within the section

❖ The relationship of axial load – moment in an aluminum structure differs from that in an RC concrete structure, thus not representing correctly the redistribution of the axial load within the section

❖ Under cyclic loading, the deterioration of moment capacity will not be visible, if "fuses" in the form of notches or artificial hinges are introduced in the specimen.

Thus the innovation in this work lies in the fact that the scaling was introduced in the construction of the specimen, by using an appropriately geometrically scaled steel reinforcing cage embedded within a cementitious material and by including in the testing set up the entire soil–foundation–structure system as a whole. In this way, the correct foundation behavior could be modeled simultaneously with a structure having fidelity of response closer to that of a larger scale structural element test than had been achievable to date.

Figure 2.53 illustrates the conceptual prototype of a modern bridge pier designed in accordance with Eurocode specifications for RC structures and seismic actions. The pier is founded on a shallow, 10-m thick, layer of medium density sand with a square (B × B) footing. Two different footing dimensions are studied, representing the two design alternatives. **Figure 2.54** summarizes the two foundation designs listing: static and seismic loads (Q_E, M_E), design seismic actions (Q_{Ed}, M_{Ed}), and ultimate shear and moment capacities (Q_u, M_u) and the factors of safety for static vertical loads (FS_V) and seismic loads (FS_E).

Only the conventional foundation complies with this requirement (hence having $FS_E > 1$, as opposed to the rocking foundation which has $FS_E < 1$). Combined with the limitations on the maximum allowable eccentricity ratio ($e = M/N < 2B/3$), this overstrength requirement leads to the conventional foundation being significantly larger. **Figure 2.55(a)** displays a photo of the mass-column foundation assembly indicating key dimensions. Dynamic centrifuge model testing was carried out in the 3.5-m diameter beam centrifuge of the UoD. A schematic cross section of the model including key dimensions and instrumentation is shown in **Figure 2.55(b).** The 200-mm deep soil layer was prepared by air pluviation of dry fine Congleton silica sand to achieve a uniform relative density $D_r = 60\%$.

As far as the testing protocol is concerned, an interesting approach is implemented, since two loading scenarios are tested: one with the induced seismic excitations having an increasing intensity, and the other with the induced seismic excitations having a decreasing intensity. The testing program is presented in **Figure 2.56**.

The response results from the earthquake Scenario A prove what has already been noticed: the rocking pier experiences invariably lower acceleration than the conventional pier. This advantage, known as rocking isolation, is the result of the difference in the ultimate moment capacity of the two designs (**Figure 2.54**): the ultimate moment capacity of the RC column section is larger than the ultimate moment capacity of the rocking foundation. This advantage becomes more significant as excitation intensity increases and the ultimate capacities are mobilized. Hence, upon shaking with the L'Aquila record, the maximum transient demand experienced by the rocking pier is half the demand on the

conventional pier. By calculating through the ultimate moment capacity the critical acceleration, we observe that this value coincides with the measured peak mass acceleration only in the very first shaking event using the Aegion record. Thereupon, overstrength effects, associated with soil densification during shaking, lead to some considerable increase in this value, which yet remains substantially lower than the peak demand on the conventional pier. Such overstrength effects, which lead to some considerable increase of $M_u$and α_c due to preceding loading cycles, have been identified in the past experimental studies and documented in (Drosos et al., [2012] and Anastasopoulos et al., [2013].

The two design alternatives, both relying on inelastic response, differ only in the component where the inelastic deformation is directed to. The adequacy of these nonlinear components ('fuses') may refer to their strength, ductility, cumulative damage resistance, and energy dissipation capacity. The effectiveness of the designated 'fuses', either the RC column section for conventional design or the soil–foundation interface for the rocking design, is of critical importance for the survivability of the system. Direct comparison of the two piers' 'fuse' response is highlighted by comparing the family of hysteresis plots depicted in **Figure 2.57**. **Figure 2.57(a)** shows the response of the RC column during the three first earthquakes of Scenario A in terms of shear load (Q=mα) versus the flexural component of drift (δ_{col}). It can be seen that the conventional pier column marginally mobilizes its lateral load capacity during the Aegion earthquake resulting in minimal plastic flexural deflection. Subsequent loading with the stronger Lefkada motion causes an important number of excursions into the nonlinear regime, accumulating substantial permanent deformation at the column base. Nevertheless, designed according to modern code requirements, the pier column possesses adequate confinement and, hence, ductility to sustain such a significant number of loading cycles with no apparent deterioration of strength, yet at the cost of considerable permanent deflection $\delta_{col} \approx 30\ cm$ ($\frac{\delta_{col}}{h} \approx 0.3\%$). However, having experienced this damage, the pier column appears unable to sustain further excitation with the equally strong L'Aquila motion, which exhausts its ductility capacity causing rapid deterioration of strength after a couple of cycles and eventually collapse. On the other hand, the column of the rocking pier responds, as expected, practically within the linear-elastic regime throughout the entire sequence. **Figure 2.57(b,c)** summarizes the performance of the two foundations in the moment rotation and settlement rotation domains. Verifying its design, the conventional foundation responds linear elastically with increased rotational stiffness, in comparison with the monotonic backbone curve, owing to densification of the underlying soil. By contrast, the rocking foundation presents a broad moment–rotation hysteresis receiving comparatively larger rotational demand. Nevertheless, rotational movement is kept within tolerable margins. As far as the settlements are concerned, downwards movement prevails resulting in considerable settlement of the foundation from the first earthquake ($\approx 5\ cm$, which is equal to the total settlement of the conventional foundation over the complete scenario), this being the main shortcoming of the rocking design. Foundation settlement increases drastically in response

to the multiple shaking cycles of the Lefkada record, leading to a considerable amount of settlement (w≈14cm) by the end of the third earthquake. Nevertheless, despite the increased settlements, the rocking pier appears to have a crucial advantage over the conventional pier: not only does it avoid collapse but it also exhibits a particularly effective and ductile 'fuse' mode of response, as its rocking foundation sustains a large number of loading cycles with no apparent deterioration of strength.

In spite of the conventionally designed structure collapsing at the third seismic excitation, Test 1 was continued by applying two additional very strong motions, the Rinaldi and the Takatori records. Remarkably, despite having been subjected to a sequence of three earthquakes with intensity equivalent to, or exceeding, its design earthquake and having suffered considerable foundation deformation, the rocking pier survives the excess demands imposed by the Rinaldi motion. Displacements, in both horizontal and vertical directions, are naturally increased substantially ($w_{res} = 27\ cm,\ \delta_{tot} = 45\ cm$), but the response is judged as satisfactory as the pier remains stable after such a deleterious sequence of earthquakes. The realistic reproduction of flexural failure in the case of the conventional pier (**Figure 2.58(b)**) is worth observing, where the plastic hinge length is approximately equal to the column width, as expected in practice. Note, also, that after hitting the horizontal LVDT during the L'Aquila motion, the pier was found to have collapsed in the out-of-plane direction (**Figure 2.58(a, b)**). After being subjected to the entire sequence of Scenario A (five earthquakes), the rocking pier rotated significantly (**Figure 2.58(c)**) with evident foundation uplift, yet with its RC column remaining practically intact (**Figure 2.58(d)**).

The results of the earthquake scenario B are demonstrated in **Figure 2.59**. The comparison of the hysteretic responses recorded during the first excitation, which in this case is the Rinaldi record, shows strongly nonlinear behavior of the RC column or the foundation in the case of the conventional design or the rocking design, respectively. It is worth observing that this first strong motion pushes the response of the conventional column (**Figure 2.59(a)**) well within its nonlinear regime consuming more than half of its theoretical ductility capacity. The following lower magnitude earthquakes add up to the total ductility demand and the column is observed to be 'on the verge of failure' by the end of the shaking sequence, having exhausted its theoretical ductility margins. On the other hand, the rocking foundation exhibits good energy dissipating behavior with no deterioration of foundation capacity (**Figure 2.59(b)**). Furthermore, it is important to observe that, as with horizontal displacements, there is negligible additional settlement of the rocking foundation due to the post- Rinaldi earthquake loading (**Figure 2.59(c)**). Due to both specimens having survived the seismic sequence testing was continued by applying the deleterious Takatori motion. The writers underline again the resilience of the rocking isolated system, since it managed to survive twice the Takatori motion, whereas the conventionally designed structure toppled after the first application of the motion. **Figure 2.60** shows images of the conventional pier model after testing, showing the significant structural damage at the base of its RC column, in this case, in the plane of shaking. Again,

the damage pattern (hinge length, crack formation, and compressive spalling) implies realistic modeling of the actual response of RC elements.

The latest research work of Hakhamaneshi and Kutter, [2015] examines the effect of the ratio $\frac{A_c}{A}$, the footing shape and embedment on re-centering. Two shapes are studied for the footings: rectangular and H-shaped.

As shown in **Figure 2.61** length L and width B of a rocking footing are the length in-plane and perpendicular to the plane of rocking respectively. To characterize the shape of a rocking footing two parameters: b/L_c, $\frac{A_{rect}-A}{A_{rect}}$ are introduced. For rectangular footings $b = B$. For an H-shaped footing, $b = t_f$, where t_f is the thickness of the flange, as defined in **Figure 2.62** and the parameter $MAR = \frac{A_{rect}-A}{A_{rect}}$, called "Missing Area Ratio" describes the footing shape. For a rectangular footing, $MAR = 0$ whereas for an H-shaped footing with a negligibly small "web" and "flange", $MAR = 100\%$. **Figure 2.62** illustrates the definition of b and the MAR.

The researchers conducted slow cyclic lateral tests at the Center for Geotechnical Modeling at UC Davis, using the 1m radius centrifuge. All experiments were performed at centrifugal acceleration of 35g, and the specimens were placed on a uniform soil layer of medium dense Nevada sand with relative density of 80%. The bearing capacity of the underlying soil is controlled by the ratio of "critical contact", i. e

$$\rho_{ac} = \frac{A_c}{A}$$

where, A_c represents the minimum area of the footing required to support the vertical load when the soil bearing capacity is fully mobilized on the contact area and A is the total area of the base of the footing. The testing set up is illustrated in **Figure 2.63**.

In fact, Gajan and Kutter [2008] and Deng et al., [2011] showed that for rocking rectangular footings, when they are loaded along the length of the footing. The critical contact length L_c is directly related to the critical contact area: $L_c = \frac{A_c}{B}$. The value of L_c represents the minimum area of the footing required to support the vertical load when the soil bearing capacity is fully mobilized on the rectangular contact area. With the knowledge of bearing capacity q_b one can analytically determine L_c for rectangular footings by

$$L_c = \frac{P}{q_b B}$$

The main loading protocol involved application of several loading packets, each with three cycles of sinusoidal displacement. The amplitudes of successive loading packets increased by approximately a factor of 2 until the applied displacement was 6% of the height, $\boldsymbol{H}$.

Two series of tests were conducted:

The first series of experiments included testing of sixteen different soil-foundation-superstructure models. The shape and embedment of the footings were systematically varied, while the moment-to shear ratio remained constant.

More specifically, eight footings were placed on the surface of the Nevada sand backfill soil and were designed to have a relatively large ratio $\rho_{ac} = 0.2 \div 0.33$ (relatively low FS_v). Afterwards, the same footings were embedded into the sand and the axial load on the footings was reduced, so as to achieve lower values of the ρ_{ac} ratio ($\rho_{ac} = 0.091 \div 0.125$). **Figure 2.64** summarizes the properties of the sixteen footings tested in the first series of experiments.

From these tests, the following conclusions concerning the effect of footing shape on the settlement and uplift, re-centering and energy dissipation were drawn:

Concerning the moment – rotation and settlement - rotation response, **Figures 2.65** and **2.66** present plots of the moment – rotation hysteretic loops as well as settlement – rotation curves for selected embedded and surface footings respectively. Two rectangular and three H-shaped footings are plotted in each Figure. The rocking moment is normalized by the moment capacity for rocking on rigid base ($PL/2$). The rocking moment capacity, calculated by the following expression, is shown by a horizontal line. The agreement between the experimental and calculated moment capacity in **Figures 2.65** and **2.66** is remarkable.

The embedded footings had ratios $\rho_{ac} = 0.09 \div 0.13$, which led to substantial uplift on the unloaded side of the footing during large rotations. Surrounding soil can fall into the gap created, leading to foundation uplift. Thus negative values of settlement and reduction in the embedment are apparent phenomena in **Figure 2.65**. The effect of soil raveling into the gap is more pronounced for cases of cohesionless soils. The value of the developing uplift in each cycle of rotation varies with footing shape. The loss of embedment leads to smaller bearing capacity and to smaller moment capacity. A notable, yet not significant, reduction in the moment capacity is shown **in Figure 2.65**, especially for the footing with the greatest residual loss of embedment.

The surface footings had a comparatively larger ratio ρ_{ac}, due to the larger value of L_c. The settlement rotation plots demonstrate the accumulation of permanent settlement (left axis) and increasing embedment (right axis) with increasing cyclic rotations. The accumulation of permanent settlement depends on the shape of the footing. As a surface footing settles, the foundation becomes embedded, leading to an increase in the bearing capacity and an increase in the passive pressure from the sides. Thus, settlement leads to a modest increase in the moment capacity, which is shown in **Figure 2.66**. The H-shaped footing settles most and consequently shows the largest increase (about 10% to 15%) in its moment capacity.

As a footing settles or uplifts the rate of settlement (or uplift) decreases. This is a characteristic of both embedded and surface footings, shown in **Figures 2.65** and **2.66** accordingly. At this point the researchers propose that there is a value of “critical embedment”, for which the mechanisms of settlement and uplift counterbalance each other. For this value of embedment, the foundation would not experience further permanent settlement or uplift.

The conclusions concerning the effect of the footing shape are presented in a summary, since this aspect is outside of the scope of this thesis. The outcome of the first series of testing lead the researchers to conclude that for rectangular footings the effect of the shape is characterized by the ratio b/L_c, where b is the width of the footing, whereas for H-shaped footings the shape is characterized by both the missing area ratio MAR and b/L_c. The researchers found that under the same critical contact ratio ρ_{ac}, wider rectangular rocking footings, i. e. footings with higher b/L_c ratio, settle less than narrow rocking footings. For a rectangular footing with large b/L_c, the soil deformations associated with the localized bearing failure would be expected to be primarily in the plane of rotation as indicated by the arrows in **Figure 2.67**. In this case, the researchers estimate that about 50% of the displaced due to bearing failure soil of the strip-shaped loaded area gets pushed back under the footing, whereas the other half gets pushed away from the footing, accounting for settlement. As b/L_c decreases, the out-of-plane soil displacements associated with bearing failure increase and a reduced fraction of the displaced soil would be pushed back into the gap under the footing. If other factors, e. g. ρ_{ac} are let constant while varying the footing shape, due to a greater proportion of soil being pushed away from the footing, one may expect greater displacements for rocking of long-narrow (small b/L_c) rectangular footings, than for short wide rectangular footings.

In other words, due to less lateral confinement around the rocking edge and the 3D nature of failure mechanism for narrow footings, a larger fraction of soil displaced by bearing failure at the loaded edges is pushed out from underneath the footing; hence larger settlements are expected for narrow footings. In the case of wide rectangular footings, lateral confinement reduces out -of-plane soil displacements and settlements. For an H-shaped footing, it is observed that footings with larger MAR suffer larger settlements, which can be attributed to the smaller lateral confinement around the rocking edge (flange).

As far as the effect of the footing shape on the re-centering ability of the rocking footing is concerned, Deng et al., [2014] defined the re-centering ability of a rocking footing (R_d) using the following expression:

$$R_d = 1 - \frac{z}{d}$$

where, z is the residual rotation of the footing upon complete unloading (moment=0) and parameter d is the maximum footing rotation for the corresponding hysteresis loop. In the case of a foundation rocking on a rigid surface, ($\rho_{ac} = 0$), a perfect re-centering of the footing occurs, leading to $R_d = 1$ ($z = 0$). On the other hand, if the axial load P is equal to the foundation's bearing capacity ($\frac{1}{\rho_{ac}} = FS_v = 1.0$), then the applied moment does not cause the creation of a gap, and no recentering occurs (fully compliant soil). This would lead to $R_d = 0$ ($z = 1.0$). Deng et al., [2014], proposed an empirical correlation for R_d as a function of the ρ_{ac}, as shown in the following expression:

$$R_d = \frac{1}{2.6\rho_{ac} + 1}$$

This formula does not take into account the influence of the footing shape or the amplitude of the cyclic rotation on re-centering. **Figures 2.68** and **2.69** plot the re-centering ratio against the amplitude of cyclic rotations, for the embedded and surface footings accordingly. These Figures capture the effect of sand falling into the gap, the effect of footing shape and the variation of re-centering ratio with amplitude of cyclic rotations.

The general notion is that factors hindering the re-centering of the rocking footing, lead to an increase in the damping ratio and an increase in the amplitude of residual settlement or uplift. For surface and embedded footings, the widest rectangular footing ($\frac{b}{L} = 1.55$) had the greatest re-centering behavior, the smallest damping ratio and the lowest potential for residual uplift or settlement. The H-shaped footings with large MAR, have the poorest re-centering behavior, the largest damping ratios and the greatest potential for residual settlement or uplift.

The footings with the highest values in the b/L ratios (wide surface footings) showed almost constant re-centering ratio at different rotation amplitudes. For the other surface footings and all the embedded footings, the re-centering ratio decreases as the amplitude rotation increases. Deng et al., [2014] and Antonellis et al., [2014] have also reported a reduction of re-centering ratio with increase in amplitude of rotation re-centering.

The second series of testing they utilized one footing as a specimen, which was placed at different embedment. In this way they aimed at studying the effect of initial embedment on the residual settlement and / or uplift. **Figure 2.70** presents the properties of the models for test series 2.

These test series aimed at illustrating the concept of a critical embedment. The footing was embedded by three different depths, while the axial load on the footing remained unchanged. The time history showing the progression of the normalized by the footing length embedment (e/L) for the three experiments, is presented in **Figure 2.71**. The Figures in this plot suggest that a foundation-superstructure system may reach a single value of ultimate embedment, regardless of its initial embedment. At critical embedment, the uplift due to soil falling under the footing balances the settlements due to local bearing failure and hence this might be useful design embedment target. However difficult the accurate prediction of the critical embedment depth may be, still as a concept it is considered useful for understanding the mechanisms of residual settlement and uplift.

The results of the centrifuge tests showed in general that for footings embedded in sand with a small ρ_{ac} rocking results in residual uplift. This outcome could be attributed to the sand falling into the gap, which cyclically opens and closes as the footing rocks. The magnitude of normalized residual uplift is greater for footings with small b/L_c, especially at large amplitudes or rotation. The test results of the embedded H-shaped footings showed that as the MAR increases, the residual uplift increases accordingly.

The experiments suggest that the factors leading to large residual uplift or residual settlement also lead to larger damping ratio and loss of re-centering ability. H-shaped footings with large missing area ratio suffered the most settlement for surface footings, most uplift for embedded footings, the highest damping and the least re-centering ability.

On the other hand, wide rectangular footings (with large B/L and large b/L_c) produced the least potential for settlement for surface footings, least potential for uplift of embedded footings, the lowest damping and the best re-centering ability.

The researchers point out that it is not possible to correlate settlement uniquely to the $\boldsymbol{\rho_{ac}}$or the footing shape because the tendency for settlement also depends on other factors such as embedment, and possibly to the amplitude of sliding compared to the amplitude of rotation. As depth increases, the uplift mechanisms (dilation and soil raveling, sliding or being scraped into the gap under the footing) become more important and the settlement mechanisms (bearing failure and densification) become less significant. The researchers are led to a hypothesis that there is some value of critical embedment at which the settlement mechanisms balance the uplift mechanisms. Despite of this concept being useful, they conclude that the critical depth of embedment cannot be predicted, due to a variety of factors (soil type and moisture conditions) involved.

In order to obtain an overview of the results stemming from all presented experimental work so far, the reader is encouraged to refer to Appendix A, which includes tabularized the outcome in terms of maximum and residual rotation and of maximum settlement. Especially the settlement is also presented normalized as a percentage of the footing width, in order to overcome the problem of different geometries and sized being compared.

Several other experimental studies have been conducted using centrifuge testing (Ugalde et al., [2010], Knappett et al., [2011], al – Dafae and Knappett [2014], Storie et al., [2015], etc.), which the reader is prompted to study, for a more global view of the described problem.

2. COMPARISON OF THE TWO METHODS

As mentioned also earlier, centrifuge testing requires appropriate scaling, aiming at simulating with accuracy the prototype stress field. However, the realistic view gained by this feature, is outweighed by the unrealistic modeling of the specimen. Usually, in order to avoid scale effects in the used materials (e. g concrete), aluminum is utilized as a munfacturing material for the footing and the pier. However, this introduces inaccuracies, as seen in Deng et al., [2012] and underlined by Loli et al., [2014], since the relationship of axial load – moment in an aluminum structure differs from that in an RC concrete structure, thus not representing correctly the redistribution of the axial load within the section.

Contrary to centrifuge testing, 1-g shake tables offer the chance of testing larger specimens and for this reason check the performance of realistic materials and construction methods. Of course the limitations included, have mainly to do with geometry (low height) and with the developing stress field. In spite of these difficulties, nonetheless, in recent years shake table testing is becoming a choice as a methodology of testing by steadily growing number of researchers, as the facilities offer the possibility of testing in large to full

scale, also for geo-structure specimens using large shake tables. Examples of such works include tests on retaining walls using a 2.8 m-high rigid container (Ling et al. [2005]; Ling et al. [2009]; Ling et al. [2012]), investigations of liquefaction and lateral spreading using a 6 m-high laminar container (Thevanayagam et al. [2009]; Dobry et al. [2011]), and soil-structure interaction studies using a 5 m-high rigid container and two 6 m-high laminar containers (Sato et al. [2000]; Kagawa et al. [2004]; Suzuki et al. [2008]; Motamed et al. [2009]; Motamed et al. [2013]). The obvious advantage of such tests is the significant accuracy which can be obtained in the stress conditions by using realistic materials and specimen construction methods, let alone the use of a specimen in a 1:1 scale.

3. DESCRIPTION OF THE TESTS

After having extensively described the published experimental studies using testing as a means of demonstrating the favorable effects of "rocking isolation", this section focuses on the tests which are the main subject of this thesis. The following description is founded on the paper composed by Antonellis et al., [2015] in order to present the results of the series of shake table tests which took place on the Large High Performance Outdoors Shake Table (henceforth LHPOST) of the Network for Earthquake Engineering Simulation at the University of San Diego and investigate the behavior of two shallow 1.5-m-square rocking foundations supporting two 460-mm-diameter columns. These tests are considered a pioneering attempt in the area of rocking foundations – testing, since an applied scale of 1:1 has never been applied before.

The test include full scale simulation of two bridge piers founded on shallow foundations, one aligned with the seismic excitation and the other skewed by 30˚. Both piers were founded on a very dense sand stratum, with a total depth of 3.40 m, inside the Large Soil Confinement Box (henceforth LSCB), which was attached on the LHPOST. The specimens are subjected to six consecutive historical seismic excitations, which result in peak drift ratios up to 13.8%. For peak drift ratios up to 6.9%, the rocking foundations performed satisfactorily, demonstrating residual drift ratios between 0.5% and 0.9%, depending on the backfill conditions. Due to the soil being sufficiently compacted, only minimal settlements were reported and no structural damage.

The tests lasted three consecutive days, each day testing a different configuration. The difference lied mainly in the existence and the elevation of groundwater in the backfill soil. Naturally, other factors acted during testing as well, which affected the performance of the system during the second and the third day; some having to do with the response of the system, and others with the sequence of construction in between testing days. More specifically, during Test Day 1 the backfill soil consisted of very well compacted sand, completely dry with only a minimum moist of approximately 5% ($w_c \approx 5\%$). During Test Day 2 there underground water in the backfill soil reached a level of 1.20 m below the footing. The percentage of moisture in the soil was slightly reduced ($w_c \approx 2\%$), and the sand was

looser compared to the previous day. In Test Day 3 the aforementioned indications are alleviated by casting concrete of weak strength below the footings, whereas the underground water is only 0.6 m below the footings. The plan view and the elevation vie of the test set up are represented in **Figures 2.72(a)** and **(b)** respectively.

It is underlined at this point, that for the purposes of the present thesis and due to the increased complexity of the problem for Days 2 and 3, only Test Day 1 is investigated in the current work. Nevertheless, the following information regarding the presentation of the experiments, concern all 3 days of testing, so that the reader has a full view of the tests at hand.

3.1 Test Setup

The LHPOST as well as the LSCB constitute the main parts of equipment used for the test set up. The technical specifications for both of these pieces of equipment are provided in a following section. The Shake Table works as the base of fixity for the stiff structure of the Confinement Box, which is composed of high-strength precast concrete panels and an exterior steel support frame (Sander et al. 2013, Fox et al. 2014). The detailed design of the test set up is presented in **Figure2.72 (a)** and **(b).**

The geometry of the specimens was defined in accordance with the full scale specimen tested by Schoettler et al., 2012. In that case the specimen was fixed at the base, with a column of 1.20 m diameter and a seismic weight of 2.32 MN. Appropriate structural scaling laws (Espinoza and Mahin 2008) were applied to maintain similar working stress at the base of the column. In compliance with this restriction, a scale factor of 1/S, where S = 3.0 is applied leading to a diameter of 0.46 m for the column and a seismic weight on top of it of 0.25 MN. According to the detailed design of the test set up, both specimens are placed inside the LSCB on a stratum of 3.35 m well compacted sand. The square footings of 1.52x1.52x0.51 are slightly embedded with and embedment depth of 0.66 m. The two footings have a different orientation, one being aligned with the direction of the motion and the other being skewed by 30˚.

The total height h from the base of the foundations to the center of gravity of the mass equals to 3.03 m, which leads us to conclude that the total height of the pier is

$$h = (3.03 - 0.51) = 2.52\ m.$$

Another conclusion extracted from the measurements (h = 3.03 m and B = 1.52 m) of the structure is the slenderness ratio, which is equal to:

$$\frac{h}{B} \cong 2.0$$

This, according to Kutter et al., [2009] characterizes a slender structure, prone to rocking response and insignificant sliding.

On top of the column are attached three mass blocks, which represent the total seismic mass of the deck. These blocks are placed on top of steel beams supporting a load stub, which is the supporting system of the seismic mass. For this practical reason, the

column does not have a uniform section in all its height. In fact, the top 0.60 m of the column have a broad square cross section of 0.61x0.61 m, which is supported by the steel beams in the four sides and bears the seismic mass.

Apart from this implementation in the design, special care was taken that overturning be avoided, so that the LSCB walls will be protected against a possible overturning of the specimens and collision with them. To this end a special system of a total weight of around 10 kN was implemented, which consisted of hollow square steel structural tubing cast and was grouted into near each corner of each footing, extending upwards above the footing. The tubes were rigidly connected to steel beams which extended horizontally outwards from the footings. A system of tapered timber beams (**Figure 2.74 (b)**) is fixed to the steel beams and has dimensions which allow the "restraining system" to touch the sand surface when the footing rotations reach values of 10 to 15% depending on the soil elevation, footing settlement, and precision of sand leveling beneath the tapered wood beams.

It is worth mentioning that this mechanism is activated only on the 3rd Day of the tests and during the last motion ("Motion 9", see also **Table 2.2**). **Figure 2.73 (b)** shows a crane placing the assembled aligned specimen inside the LSCB. The direction of the motions is parallel to the East – West axis of the setup, i. e. parallel to the longitudinal axis of the LSCB. A full view of the tested setup is depicted in **Figure 2.74.**

3.2 Construction Sequence

Initially the inner walls of the LSCB were covered with two coatings of PVC geomembrane liner and protection nonwoven geotextile, in order to prevent the water, from flowing out.

By means of a crane and a hopper the backfill material of clean sand fills the LSCB. The loading of the sand proceeds gradually with a step of 0.20 m each time. As a next step, the 0.20 m of loose sand is compacted to about 0.15 m. Compaction is performed using the appropriate equipment. Only in the neighboring area of the footings and for construction reasons only, is the backfilling and compaction of the soil in the vicinity of the footings performed manually **Figure 2.73(c).** It should be noted at this point, that during compaction the sand is wetted to achieve a target relative density $Dr > 80\%$, in order for the densification of the soil material during shaking to be minimized. The LSCB is filled with the clean sand up to a height of 3.35 m from the platen of the shake table.

The assembly of the components is completed outside the LSCB and they are placed in their foreseen position by a crane. After the completion of each day's tests, the components are removed from the LSCB, the soil level is restored to its initial value, and the sand is re-compacted manually, before the specimens are placed again in the LSCB for the continuation of the next day's tests.

This construction sequence plays a major role in the performance of the two components. To begin with, the process of re-compaction between the first and second test day leads to loss of moisture from the mass of the backfill. Thus, the water content in the sand close to the footings on Test Day 2 is found to be about only 2% immediately after the completion of the tests, as opposed to 5% measured for Test Day 1.

This phenomenon influences the response of the rocking foundations, since the significantly reduced moisture leads to reduction of the apparent cohesion of the sand, which was artificially acquired thanks to the maceration of the backfill soil. Consequently, when large rotations occur, the sand falls in the gap between the soil and the footing during the rocking movement of the footing.

For this reason, on Test Day 3 the tests took place, with the alteration of casting weak strength concrete around the perimeter of the footings **Figure 2.73 (d).** This modification successfully prevented the accumulation of sand under the footing and increased slightly the moment capacity of the rocking foundation.

3.3 Material Properties

For a detailed description of the exact material properties used in the experiment, the reader is prompted to study the published paper by Antonellis et al., [2015] "Shake Table Test of Large-Scale Bridge Columns Supported on Rocking Shallow Foundations". As long as the material properties required for the scope of this work are concerned, it is worth mentioning that the concrete used for the footings and the piers has a specified compressive strength of 41.3 MPa and maximum aggregate size of 9.5 mm.

During Test Day 1, the compressive strength of the concrete at the foundations as well as at the piers is measured and found equal to 42.1 MPa 30.3 MPa respectively. However this data has no special significance for the analyses performed in this study, since as it is stated in the test report and also mentioned in the sequel of the present text, both of these elements remain within their elastic regime and thus the material "Concrete" is considered to be an elastic one.

The material of the backfill consists of a standardized soil: Carroll Canyon type II ASTM C33 washed concrete sand, classified as poorly-graded medium sand, with the dry unit weight to range between 14.4 kN/m^3 and 17.7 kN/m^3. After 16 sand cone tests at different stages of the construction the relative density of the built soil profile $\boldsymbol{Dr}$ was found to be approximately 90% ($\boldsymbol{Dr = 90\%}$). Based on the angularity of the sand, the constant volume friction angle is assumed to be 33°.

3.4 Testing Protocol

A total of six historical earthquake excitations are induced to the two specimens. On the 3rd Day of the tests three motions in addition to the six were included. **Table 2.2** presents the testing protocol including the details of each excitation as well as the

corresponding scaling amplification factors, used for each ground motion. The imposed PGA is recorded at the walls of the rigid confining box, which coincides with the reproduced signal of the shaking table. In accordance with the scaling in the length of the specimens, the duration of the induced excitations had to be scaled down as well. Therefore, the justification for the influence of the length scaling on the testing components is provided by the duration scaling, accomplished by a multiplication with the factor:

$$\sqrt{\frac{1}{3}} = \mathbf{0.577}.$$

As far as the intensity and some qualitative characteristics of the used motions are concerned, useful information is provided by the distance from the rupture plane. The Pacoima Dam (Motion 4), Takatori (Motions 5 and 6), and Parachute Test Site (Motions 7, 8, and 9) were recorded at a distance equal to 7.0, 1.5, and 1.0 km from the fault rupture plane and included strong pulses. The Parachute Test Site excitations were used only during the 3rd Day of testing.

Two levels of severity are identified in the sample of the available excitations: Motion 3 (Imperial Valley, El Centro) is categorized as a Design Earthquake (DE), whereas Motion 5 (Kobe, Takatori) is identified as the Maximum Considered Earthquake (MCE). The target drift ratios according to which the scale factors for the DE and MCE are selected are 3% and 6% respectively. The desired amplitude of the induced ground motions was determined by means of numerical simulations using a nonlinear Winkler type model for the foundations (Antonellis and Panagiotou, [2014]).

The Pacoima Dam record was filtered with a low-pass, 5 Hz cut-off frequency, resulting in a reduction of the maximum possible force, which the LSCB could withstand. According to numerical analysis, this modification on the ground motion had no significant effect on the performance of the rocking foundation systems.

As already mentioned, Motions 7, 8, and 9 are used only in Test Day 3. In **Figure 2.75** are presented the linear acceleration and displacement spectra (3% damping ratio) for Test Day 3 of the recorded soil acceleration at a location near the center of the LSCB and at the foundation base elevation. This image confirmed to the researchers that the input and the recorded motions did not differ significantly. Moreover, the respective spectral values stemming from the recorded motions, during the three days of testing, range within a bound of no greater than 10% discrepancy.

4. TESTING EQUIPMENT

The UCSD Englekirk Structural Engineering Center is located about 15 km east of the main campus at the Camp Elliot field site in San Diego and contains a network of large-scale equipment, including the LHPOST (**Figures 2.76** and **2.77**) for controlled seismic and blast

testing of structural components and systems. An expansion to its capabilities, permitting large to full scale testing of geo – structure specimens, is provided by the LSCB (**Figure 2.77**).

4.4 The Large High Performance Outdoors Shake Table of UCSD

The Large High Performance Outdoors Shake Table, (mentioned also as LHPOST) where the aforementioned tests take place, has been designed with the capacity to reproduce strong near fault earthquake excitations, in order to test structural and study SFSI (soil – foundation – structure – interaction) systems. The capacity and the size of the facilities are such, that full or very large scale of testing is feasible. (**Figure 2.76**).

The NEES (Network for Earthquake Engineering Simulation) facilities at the UC San Diego are utilized to check the performance of components related to the Critical Infrastructure Protection (CIP), which manifest structural and geotechnical challenges. Potential fields of research include:

- ❖ the effects of passive and semi-active energy dissipating systems on building response;
- ❖ large-scale testing of dynamic soil-foundation-structure interaction;
- ❖ seismic response of nuclear waste dry storage casks, including soil-structure interaction and the interaction between casks;
- ❖ loss estimation of buildings, including the interaction between their components;
- ❖ seismic response of full-scale wood-frame construction including school buildings;
- ❖ response of building diaphragms, where the presence of a distributed mass constrains the testing to be performed solely under dynamic conditions;
- ❖ assessment of liquefaction mitigation mechanisms;
- ❖ seismic response of tall wind turbines, high-voltage towers and industrial chimneys; and
- ❖ the study of the complex interaction between interconnected components of electrical substations, such as high-voltage transformer-bushing systems. (*Source: http://nees.ucsd.edu/facilities/*)

The LHPOST has initialized its operation since October 2004 and is directed as a National Science Foundation (NSF). With the close collaboration among different locations equipment of NEES is available and the NEES headquarters, NEES at UCSD offers the possibility of “tele – participation” to distant researchers, providing them in this way with the technical support they need as well as with access to the shaking table. Although the LHPOST is not the largest shake table in the world, it offers since December 2009 the possibility of motion in the six degrees of freedom and it is in terms of its velocity capability, frequency range and stroke margins, the largest shake table outside of Japan. As operating facilities, the LHPOST at UC San Diego contributes decisively to the testing capabilities of the existing testing facilities in the United States.

After a long series of shake table tests, the LHPOST has performed numerous large scale tests. These tests required uncommonly strong ground excitations to be performed and resulted in a better understanding of the dynamic response of the structures as well as in the improvement of the seismic codes. **Figure 2.78** presents the operational components of LHPOST facility, which are also enumerated below.

The LHPOST consists of a steel platen 7.6 m wide by 12.2 m long which has the ability to move. *Nr. 1* in **Figure 2.78** corresponds to the platen, platen which weighs about 144 ton. The platen is surrounded by a reaction block made of reinforced concrete (*Nr. 2*) on which are attached two dynamic actuators with a combined horizontal force capacity of 6.8MN (*Nr. 3*). *Nr. 4* depicts the sliding system consisting of six vertical actuators, on which the platen is fixed. The restraining system protecting the LPOST against the development of overturning moments is represented by *Nr. 5*. This system consists of two nitrogen-filled hold-down struts. Last but not least, *Numbers 6* and *7* show two pairs of slaved hydrostatic pressure-balanced bearings which serve as a swerve restraining system and the cover plates which protect the actuators respectively.

The following table provides a complete list summarizing the specifications of the shake table. Parameters such as frequency range, stroke margin of the actuators, peak acceleration and velocity etc. are crucial to the capacity of the shake table. Due to the large scale and thus high demand of the tests and research applications, the following parameters were designed in such a way as to abide by the applied testing needs.

More specifically, concerning the selection of a peak table (ground) acceleration of a little more than 1g, was based on the study of a large number of strong ground motions, all of which seemed to have an upper limit of approximately 1g. In addition to the parameter of acceleration amplitude, the nature of the ground motion as a near fault excitation or an ordinary one (far from the source) had to be considered. As it is known from numerous sources in literature (Mavroeidis and Papageorgiou, [2003], Makris and Black, [2004], Baker [2007]), the effects of the near fault ground motions are controlled to a great extent by the peak ground velocity parameter. In this case this parameter is the peak table velocity. Due to the necessity of the LHPOST being able to simulate precisely near fault excitations, a peak table velocity of 1.80 m/s was selected by taking into account a group of representative near-fault records used extensively in numerical earthquake engineering research. It is worth noticing that when the Large Soil Confining Box is mounted on the table, an additional amplification is developed, with the peak velocity on the soil surface exceeding the value of 1.80 m/sec*.*

Last but not least, the force capacity of the actuators as well as the maximum overturning moment which the moving platen can withstand, were selected by taking into account a group of potential large or full-scale specimens. Another factor which resulted in this selection, was the assumed mass of the platen including elastic and inelastic dynamic amplification effects (230 ton), as well as the assumed effective height of the specimen (10.0 m) and dynamic similitude requirements. *(Source: http://nees.ucsd.edu/facilities/shake-table.shtml).*

4.2 The Large Soil Confinement Box (LSCB)

The geometrical stability, which a soil skeleton can demonstrate without lateral structural support is rather limited, hence the necessity for lateral confinement when it comes to testing of geo-structure specimens.

An initial attempt to fulfill this need, was a smaller laminar shear box, which was fixed on the LHPOST to assess the dynamic performance under seismic loading of 1.80 m-high retaining walls [Ahn and Cheng, 2013]. The elevation of such specimens as well as the stress field they create in the soil profile, are only the minimum in the range needed for most field applications. Therefore, for the sake of similitude between the test and reality, a larger container is needed to investigate geo-structures closer to prototype size.

Apparently, the addition of the LSCB in the UCSD Test Center enriched the efficiency of the facilities, providing the opportunity of carrying out performance seismic tests, sometimes in full-scale, for large geo-structures. The LSCB has an open roof and a total height of 7.60 m. As far as the plan dimensions are concerned, they are modifiable, in order for the box to adapt to the shape and size of different specimens. Therefore, a smaller structure to be tested can be assembled in the 'narrow configuration' with interior dimensions of 4.6 m × 10.1 m, whereas the 'wide configuration' offers the area size of 5.8 m × 10.1 m. Structural diagrams are provided in **Figure 2.79** a and b.

The LSCB is attached on the footprint of the LHPOST. It has smooth interior walls consisting of precast concrete panels and an exterior galvanized steel support frame.

The design of the SLCB fulfills the following objectives:

- Maximize allowable specimen height
- Maximize specimen acceleration
- Minimize out-of-plane deflection of longitudinal (side) walls
- Minimize specimen friction against longitudinal walls
- Maximize specimen friction at the bottom boundary
- Derive all support reactions from table
- Allow for variable width (modular) assembly
- Avoid resonance within the operating frequency band of the LHPOST
- Minimize total weight
- Minimize cost

The load case leading the design of the LSCB, i. e the worst –case loading condition, is the one where the box is filled with a saturated backfill soil with a unit weight of 20.4 kN/m^3, subjected to a lateral acceleration of 0.7g. The minimum natural fundamental frequency of the empty LSCB is 30 Hz. The main concern is that the design of the LSCB should ensure that plane strain conditions prevail during dynamic loading. For this reason, the side walls (along the longitudinal direction), have a rather limited out-of-plane deflection of only 6 mm assuming a liquefied soil (20.4 kN/m^3) and lateral pressure distribution. On the other hand, the walls along the transversal direction are designed to withstand apart from the lateral pressures, also the entire inertial load of the specimen (i.e.,

assuming frictionless side and bottom boundaries). In order for the LSCB to have the capacity to withstand such forces, bolted steel frames combined with high strength precast concrete panels constitute the interior walls of the LSCB.

The large size of the structure, allows for relatively simple boundary conditions:

- The upper surface of the LHPOST accommodates the fixities of the LSCB. On this surface 16 transverse steel angles are directly bolted so as to prevent any slippage at the lower boundary. This ensures that the movement of the LHPOST is directly and without any distortion transmitted to the base of the LSCB.
- The longitudinal walls (and depending on need, one or both of the transversal as well) of the LSCB are covered with three layers of low density polyethylene sheeting in order to maintain very low friction coefficient along the interface. This ensures better approximate plane strain conditions.

The fixation of the LSCB on the LHPOST is materialized by means of 76 post-tensioned rods, each with a force capacity of 880 kN. These rods are inserted through steel base plates under the columns and through the middle of the concrete panels (i.e., over full height) to provide maximum stiffness for interior walls of the structure.

The assembly of the LSCB is carried out by bolting the precast reinforced concrete panels to the exterior steel frame in order to enhance the resistance of the panels to out-of-plane bending. Both concrete and steel components are then post-tensioned to maintain fixity to the table and to increase the composite shear and bending stiffness of the structure.

4.3 LSCB Structural Performance

Empty Condition

Before the LSCB is filled with soil the following dynamic test takes place, so as to be confirmed that the LSCB does not resonate within the normal operating frequency range of the LHPOST (0 – 20 Hz). White noise motion is applied at three levels of root mean square acceleration amplitude (0.07g, 0.14g, and 0.21g), whereas impulse motion is applied at two levels of peak acceleration amplitude (0.1g and 0.6g). The response of the box is monitored using an array of uniaxial and multiaxial accelerometers attached at various locations around the structure. Biaxial accelerometers (orthogonal horizontal directions) are mounted to the exterior faces of the transverse walls at all four corners and at three elevations from the table surface. Vertical accelerations are also measured at the top of each corner to indicate potential rocking of the LSCB. Uniaxial accelerometers are mounted at the mid-span of each of the four walls at the upper two elevations to measure out-of-plane accelerations relative to the corners. Uniaxial accelerometers are also placed at the center of some critical unsupported panel areas.

The performance of the empty LSCB under dynamic excitation observes the design limitations and fulfills its goals. The accelerometer array indicated that amplification of the

table motion was highest at the top of the transverse walls and, as such, these measurements were used to develop frequency response functions (FRFs). A FRF is the ratio of power density between output and input signals (e.g., acceleration or displacement) in the frequency domain. According to these results, the LSCB experiences essentially rigid body motion in the low frequency range. Moreover, it is proved that the resonant condition of the box is outside the working frequency range for the LHPOST and is unlikely to influence the response of geo-structure specimens contained in the LSCB.

The foregoing response measurements indicate that the empty LSCB has a fundamental natural frequency in the longitudinal direction of shaking of 22 to 23 Hz and displays strong linearity in its vibrational response up to 18 Hz. These results also indicate that the LSCB maintains excellent rigidity for frequencies up to 10 Hz. Since the optimal behavior occurs within the dominant frequency range for most earthquake motions, the LSCB is well-suited for seismic testing of large geo-structures. For motions with significant energy content in the high frequency range (15 – 20 Hz), LSCB deformations should be monitored closely during testing or a low-pass filter can be used to avoid corruption of specimen response due to resonant deformations of the box.

Full Condition

Testing the LSCB in full condition demonstrates that the peak in the FRF remain visible near 22 Hz and indicate that stiffness of the LSCB itself does not degrade throughout the excitation.

FIGURES OF CHAPTER 2

	System A	System B
Poor Soil Conditions	0.072g	0.065g
Shallow Improved Soil Crust z/B = 0.5	0.117g	0.065g
Deep Improved Soil Crust z/B = 1.0	0.130g	0.085g
Ideal Soil Conditions	0.162g	0.095g

Table 2.1 Critical acceleration for each soil configuration of the two systems: the lightly loaded one, system A and the heavily loaded one, system B. *(Tsatsis and Anastasopoulos, 2015)*

No.	Station	Earthquake Location, Year	M_w	R_{rup}, (km)	Amplitude Scale Factor	Imposed Peak Ground Acceleration (g)	Recorded peak ground Acceleration (g)
1	Gilroy #1	Loma Prieta, CA, 1989	6.90	9.60	1.00	0.47	0.55
2	Corralitos	Loma Prieta, CA, 1989	6.90	3.90	0.80	0.33	0.40
3*	El Centro #6	Imperial Valley, CA, 1979	6.50	1.40	1.10	0.35	0.39
4¥	Pacoima Dam	Northridge, CA, 1994	6.70	7.00	0.80	0.43	0.54
5	Takatori	Kobe, Japan, 1995	6.90	1.50	0.50	0.36	0.39
6¤	Takatori	Kobe, Japan, 1995	6.90	1.50	1.00	0.74	0.79
7₹	Parachute Test Site	Superstition Hills(B), CA, 1987	6.50	1.00	1.00	0.43**	-
8₹	Parachute Test Site	Superstition Hills(B), CA, 1988	6.50	1.00	-1.00	0.46**	-
9₹	Parachute Test Site	Superstition Hills(B), CA, 1989	6.50	1.00	1.10	0.47**	-

* Design Earthquake

¥ Filtered at 5 Hz (low - pass)

¤ Maximum Considered Earthquake

₹ Test Day 3

** Records used only in Test Day 3

Table 2.2 Ground motions used in the experimental program. The recorded PGA refers to the free field acceleration in the middle of the confining box, at the foundation level.

Size	7.6 m × 12.2 m
Peak acceleration: bare table, 400 ton payload	4.2 g, 1.2 g
Peak velocity	1.8 m/s
Stroke	±0.75 m
Maximum gravity (vertical) payload	20 MN
Force capacity of actuators	6.8 MN
Maximum overturning moment: bare table, 400 ton specimen	35 MN-m, 50 MN-m
Frequency bandwidth	0 — 33 Hz

Table 2.3 Technical Specifications of the LHPOST at the UCSD
(*Source: http://nees.ucsd.edu/facilities/shake-table.shtml*)

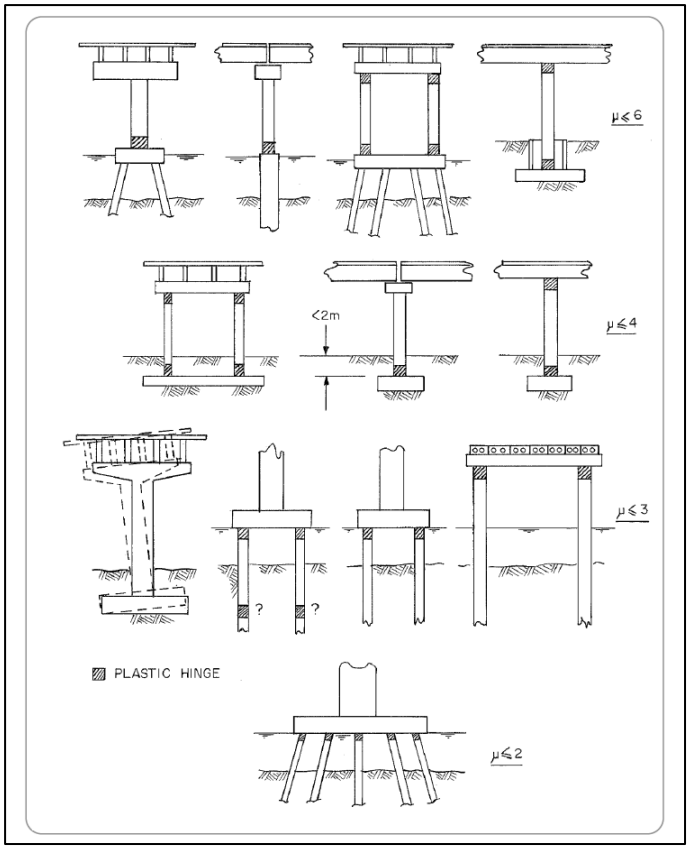

Figure 2.1 Examples of maximum values of μ allowed according to New Zealand standards for bridges. (*Source: The NZ Transport Agency's Bridge manual SP/M/022 Third edition, Effective from May 2013*)

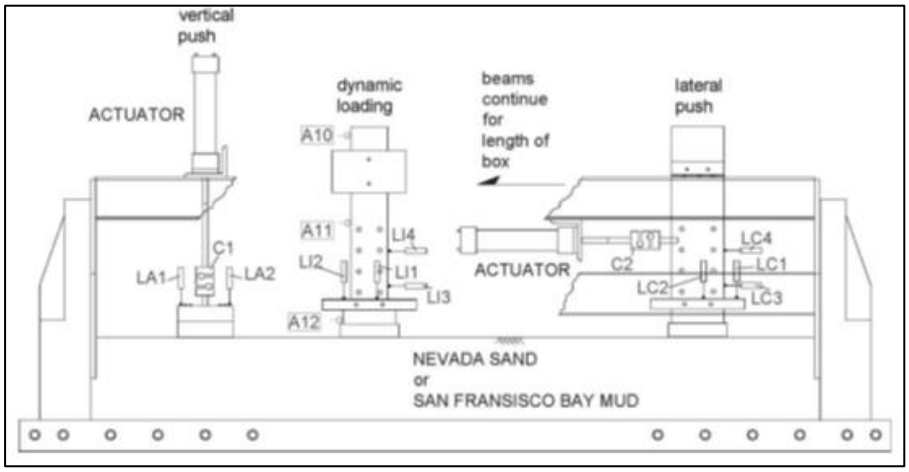

Figure 2.2 The Container of the specimen along with annotations describing the test setup and applied instrumentation for vertical push, slow cyclic lateral push and dynamic testing. The soil bed in the container was divided into six to ten stations and tests were conducted in each station separately. *(Gajan et al., 2005).*

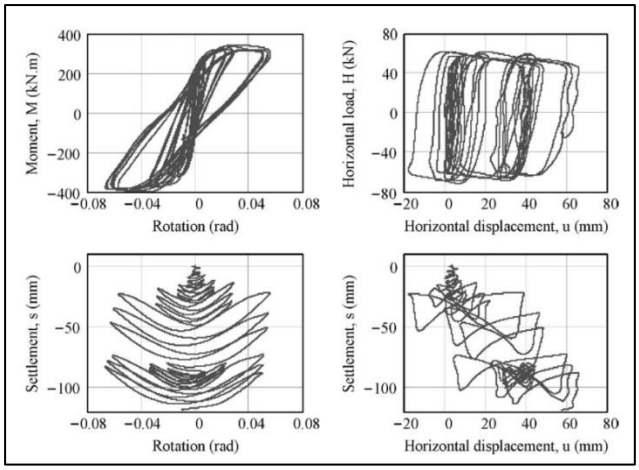

Figure 2.3 Results concerning slow cyclic lateral push test for the soil: Dry Sand ($Dr = 80\%$). The dimensions of the footing were: $L = 2.84\,m$, $B = 0.65\,m$, $D = 0.0\,m$, $FS_v = 6.70$. The lateral load was applied on a height of $\mathbf{4.9\,m}$ (the results refer to the base center point of the footing). (*Gajan et al., 2005).*

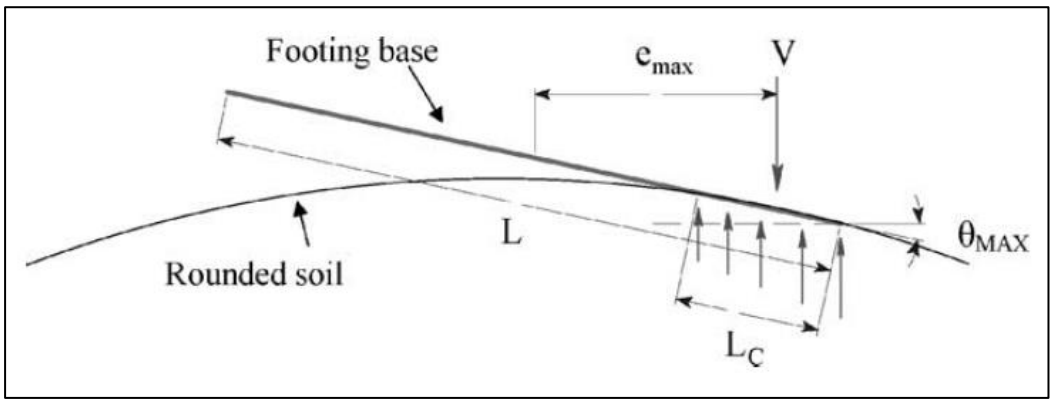

Figure 2.4 Rounding of the interface between the soil and the footing during rocking. The deformed soil surface introduces geometrical non linearity to the problem, which is visible in the $M - \vartheta$ response. *(Gajan et al., 2005)*

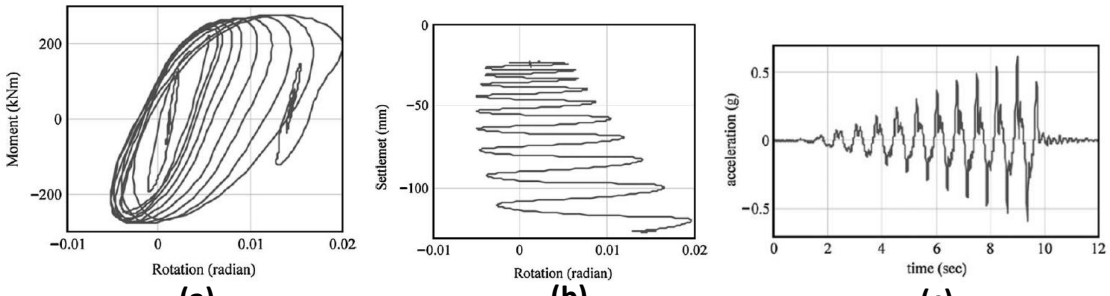

Figure 2.5 Results concerning dynamic testing for the soil: Dry Sand ($\boldsymbol{Dr = 80\%}$). The dimensions of the footing were: $L = 2.84\,m$, $B = 0.65\,m$, $D = 0.0\,m$, $FS_v = 5.30$. (*Gajan et al., 2005).*

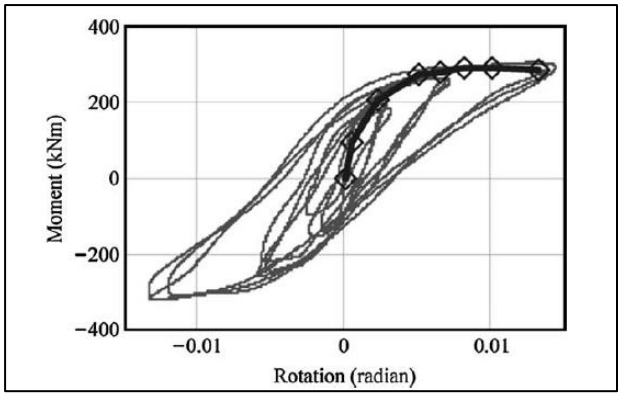

Figure 2.6 Superposition of the dynamic $M - \vartheta$ results with the corresponding ones from the slow cyclic tests. The results refer to the specimen Dry Sand ($Dr = 80\%$). The dimensions of the footing were: $L = 2.84\ m$, $B = 0.65\ m$, $D = 0.0\ m$)

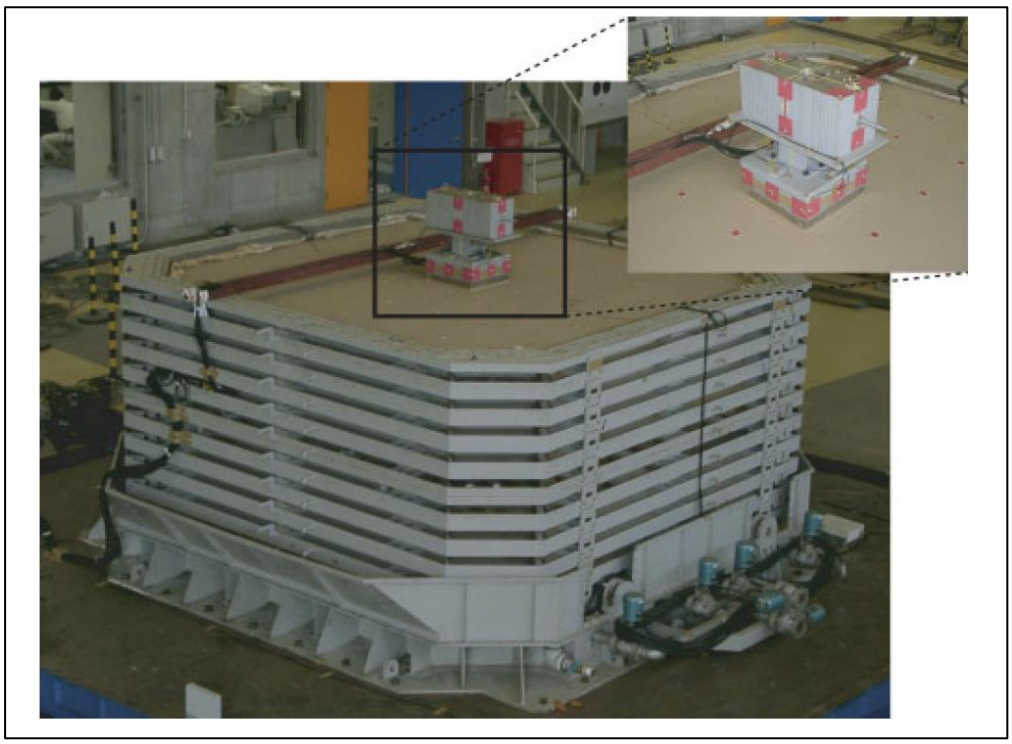

Figure 2.7 Picture of the experimental set-up, including the test model. *(Paolucci et al. 2007)*

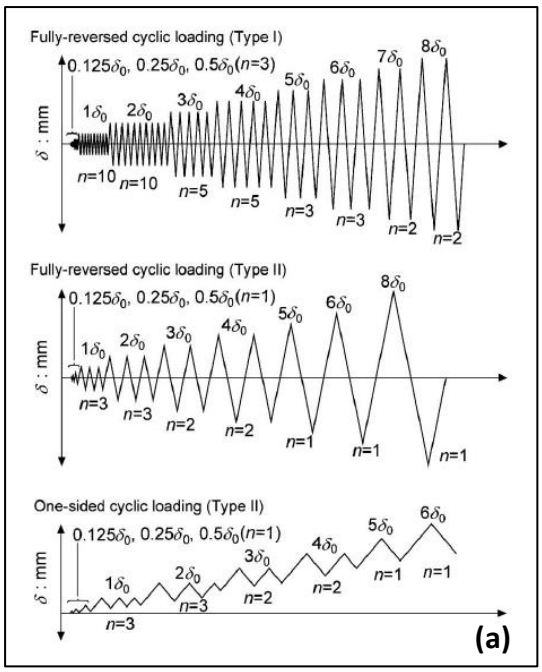

Case identifier	Loading pattern	Relative soil density	Lever arm length, L^*
C1	Monotonic loading	80%	1300 mm (Tall column)
C2	One-sided cyclic loading with Type II pattern	80%	1300 mm (Tall column)
C3	Fully-reversed cyclic loading with Type II pattern	80%	1300 mm (Tall column)
C4	Monotonic loading, followed by one-sided cyclic loading on the reversed-side	80%	900 mm (Short column)
C5	Fully-reversed cyclic loading with Type I pattern	80%	900 mm (Short column)
C6	Fully-reversed cyclic loading with Type II pattern	80%	900 mm (Short column)
C7	Monotonic loading	60%	900 mm (Short column)
C8	Fully-reversed cyclic loading with Type I pattern	60%	900 mm (Short column)
C9	Fully-reversed cyclic loading with Type II pattern	60%	900 mm (Short column)

* The length from the base of the footing to the loading point

(b)

Figure 2.8 (a) Applied slow cyclic displacement time histories. δ_0 is the displacement level at which the maximum moment developed at the monotonic lateral tests. **(b)** Slow cyclic experimental program. *(Shirato et al. 2008)*

Case identifier	Earthquake motions and notes on the preparation	Planned maximum acceleration	Observed maximum acceleration on table	Embedded depth
S1–1	Sweep wave	50 gal	112 gal	0 mm
S1–2	Shichiho wave	386 gal	601 gal	0 mm
S1–3	Sweep wave	50 gal	106 gal	0 mm
S1–4	(Remove the model, recompact the soil surface, and settle the model again)→Kobe wave	812 gal	712 gal	50 mm
S1–5	(Remove the model and settle it at a different position 1 m west from the original position) →Kobe wave→(Remove the model and soil deposit)	812 gal	726 gal	0 mm
S2–1	Sweep wave	50 gal	110 gal	10 mm
S2–2	Weakened Kobe wave	650 gal	557 gal	10 mm
S2–3	Sweep wave	50 gal	113 gal	10 mm

Figure 2.9 Shake Table experimental program *(Shirato et al. 2008)*

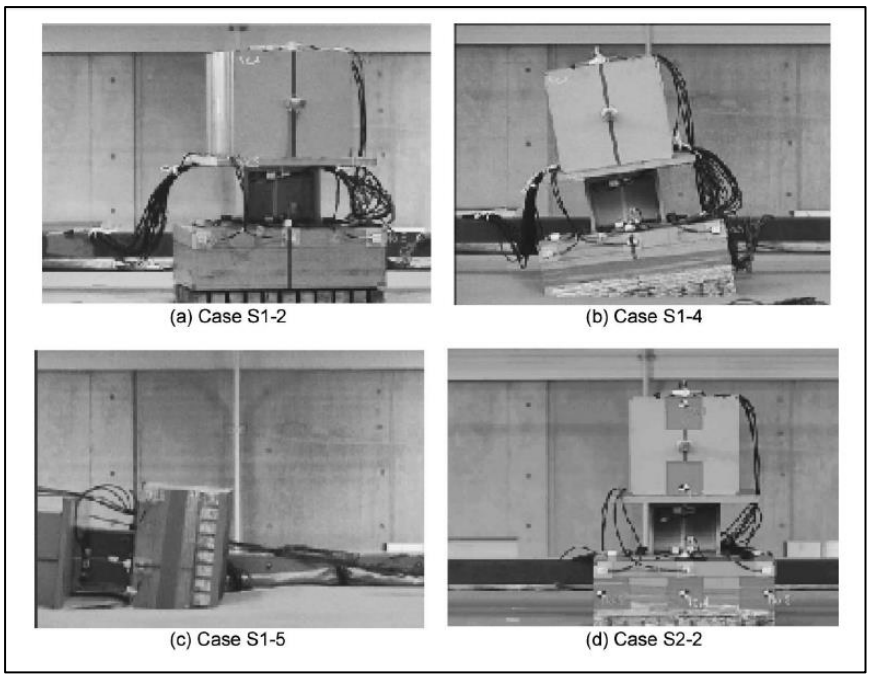

Figure 2.10 Snapshots depicting the condition of the footing after each of the excitations. *(Shirato et al. 2008)*

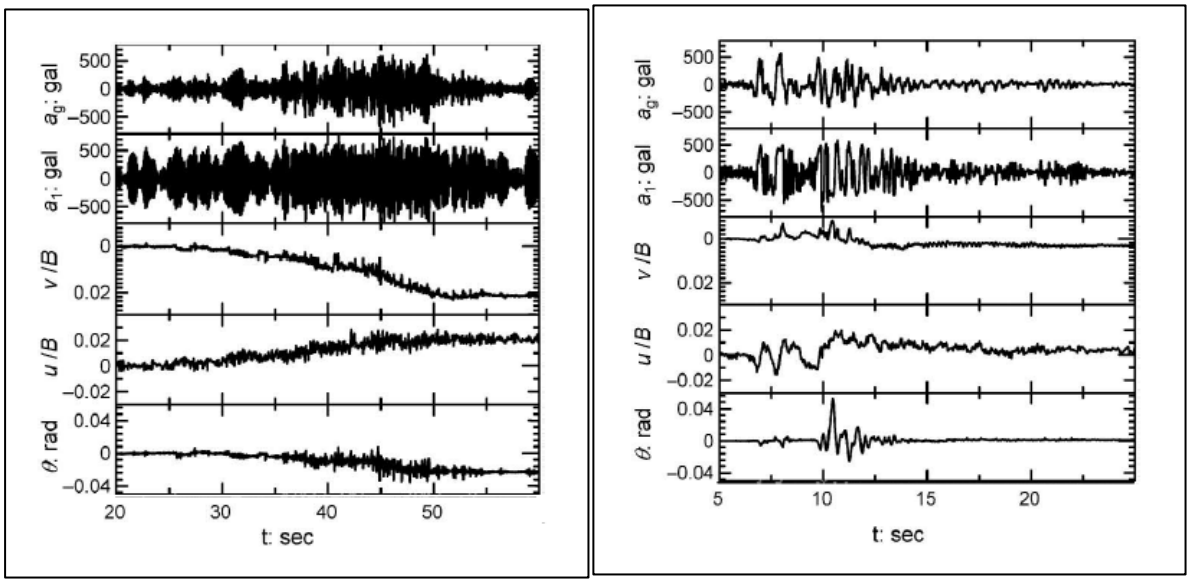

Figure 2.11 Time histories of acceleration at the ground surface, a_g, acceleration at the center of the top steel rack, a_1, and settlement, sliding and rotation of the footing, v, u, and ϑ respectively. Cases S1 – 2 (left) and S2 – 2 (right). *(Shirato et al. 2008)*

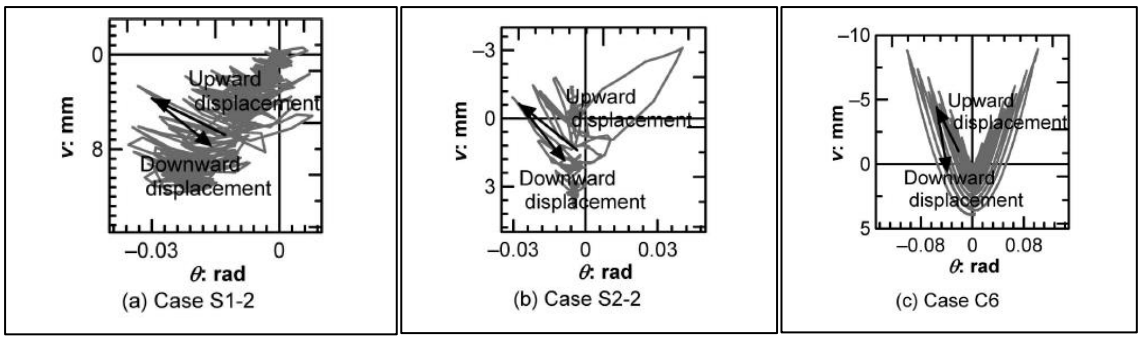

Figure 2.12 Rotation – Settlement plots for Cases S1 – 2, S2 – 2 and C6. *(Shirato et al. 2008)*

Table II. List of residual displacement at the end of seismic loading experiments.

	Residual displacements		
Case	Vertical (mm)	Horizontal (mm)	Rotation (rad)
1-2	−10.6	10.0	−0.023
1-4	−17.6	−101.6	−0.161
1-5		Toppled	
2-2	−6.0	3.5	−0.01

Figure 2.13 Residual displacements at the end of the Hokkaido excitation (Case 1-2), after the JMA record (cases 1 – 4 and 1 – 5, the only difference between them is that in the former case the specimen was embedded by 50 mm and in the latter the embedment was zero), at the end of the JMA record, after the relocation of the specimen. *(Paolucci et al. 2007)*

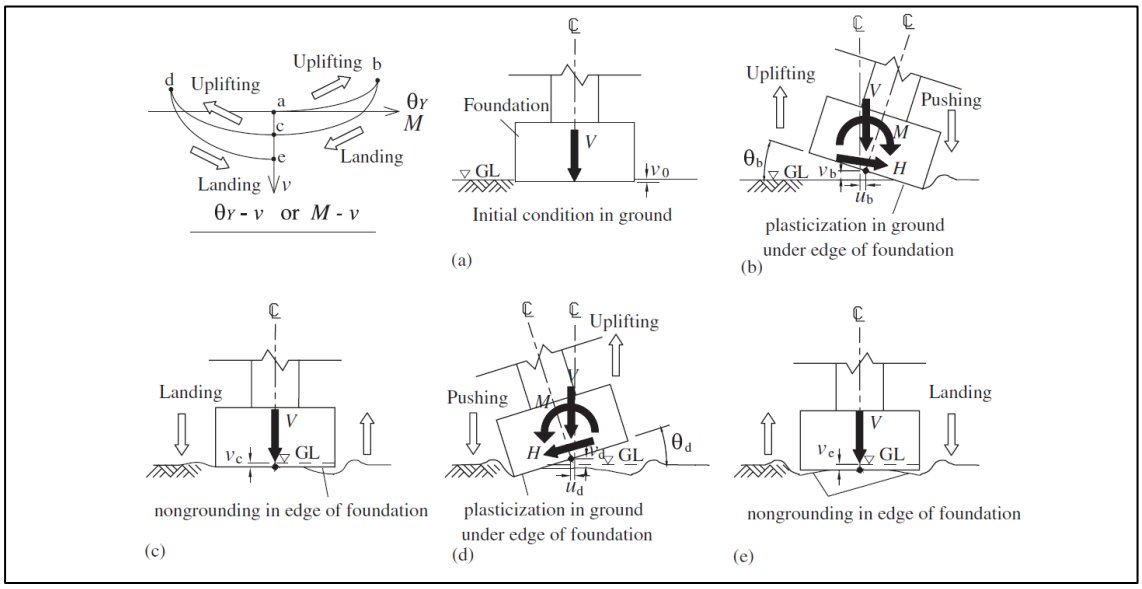

Figure 2.14 Schematic presentation of yielding phases of foundation–soil interaction as observed from shaking table experiments: **(a)** initial vertical settlement; **(b)** soil yielding during rocking in one direction; **(c)** decreased contact width beneath the foundation at the end of first yielding phase; **(d)** subsequent soil yielding in the other rocking direction; and (e) decreased contact width beneath the foundation at the end of second yielding phase. In the upper left side of the Figure, is presented the schematic vertical settlement vs rotation plot resulting from the previous phases. *(Paolucci et al. 2007)*

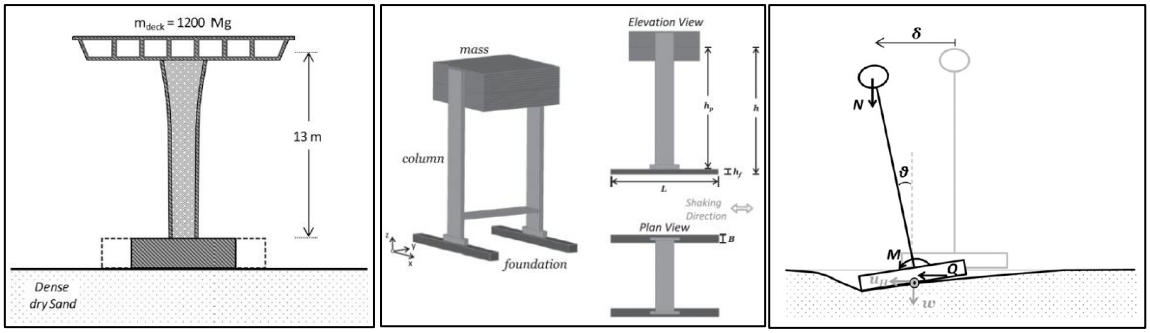

Figure 2.15 (a) Problem definition: idealized bridge pier on shallow foundations of varying dimensions; **(b)** Geometry of the foundation-structure model, showing the notation for loads and displacements, and **(c)** simplified rigid-structure model *(Drosos et al., 2012)*

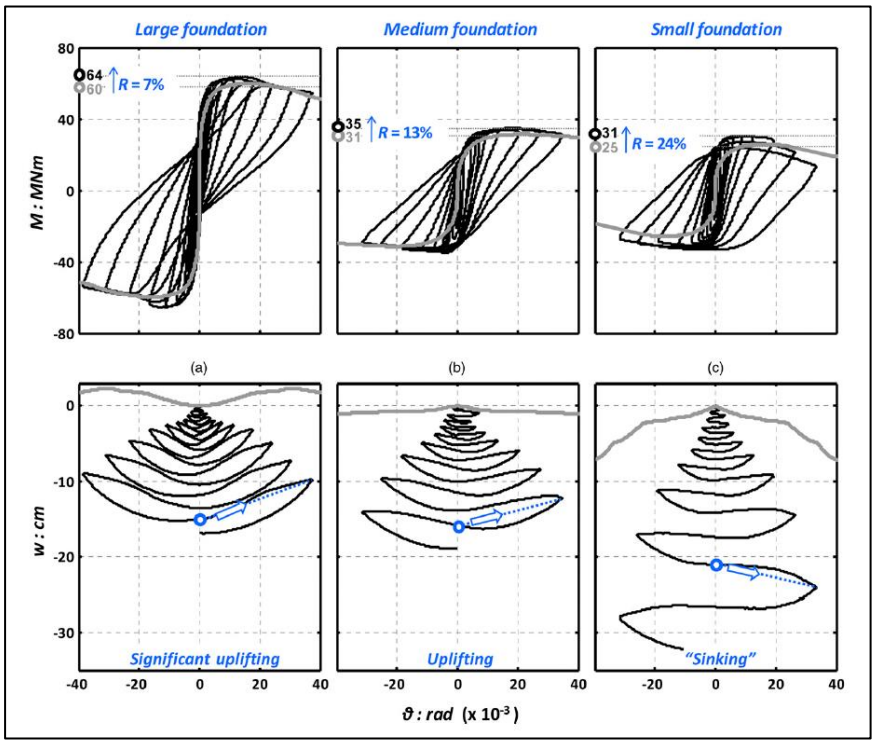

Figure 2.16 Monotonic (gray line) and slow-cyclic (black line) lateral pushover test results in terms of moment-rotation and settlement-rotation foundation response: **(a)** large foundation (FS_V =7.3); **(b)** medium foundation (FS_V =3.5); **(c)** small foundation (F_{SV} =2.3). The settlement refers to the foundation midpoint. *(Drosos et al., 2012)*

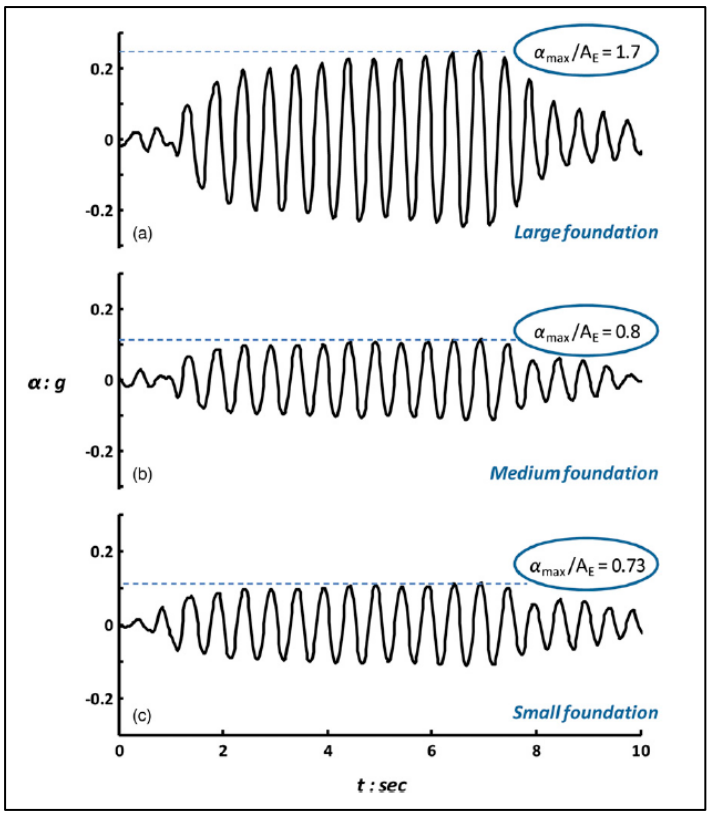

(i)

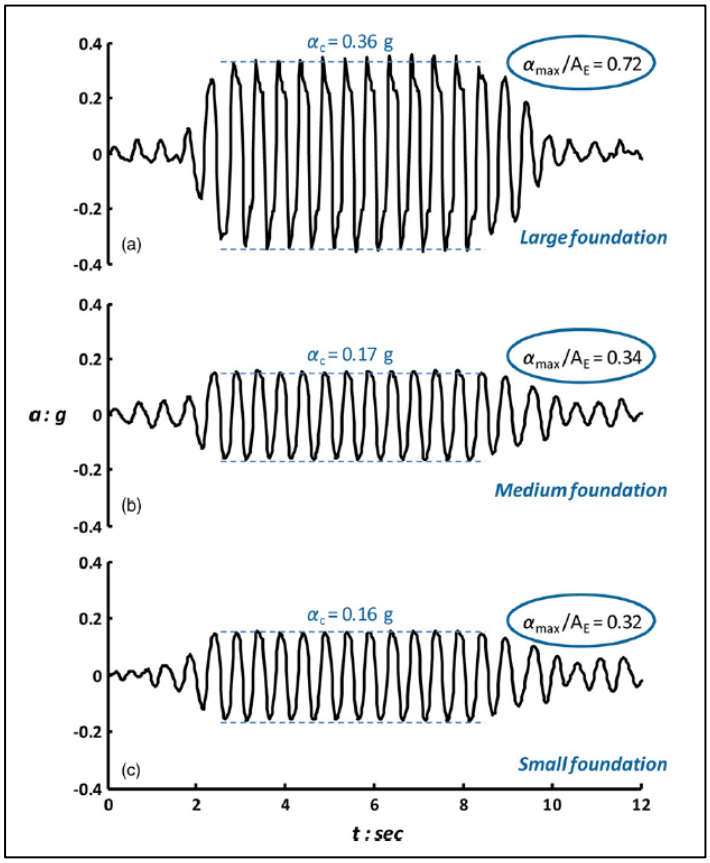

(ii)

Figure 2.17 Acceleration time histories recorded at the level of the deck (center of mass) for base excitation with a **(i)** 12-cycle 2-Hz sine of 0.15g acceleration amplitude and **ii)** a 12-cycle 2-Hz sine with 0.50g acceleration amplitude for the **(a)** large foundation ($FS_V = 7.3$); **(b)** medium foundation ($FS_V = 2.5$); **(c)** small foundation ($FS_V = 2.3$). *(Drosos et al., 2012)*

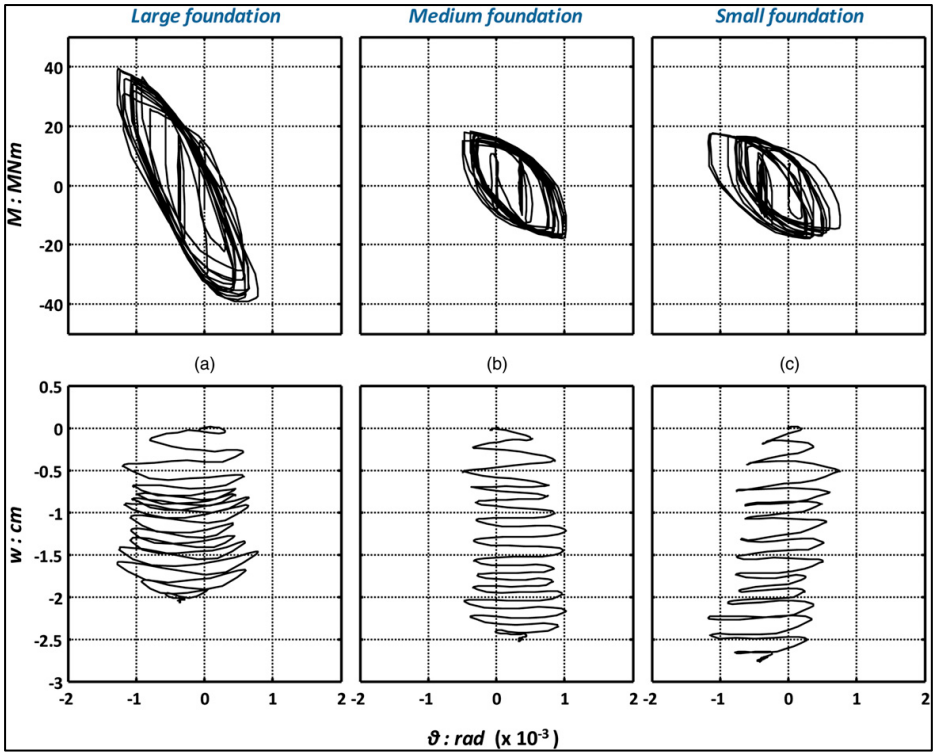

(i)

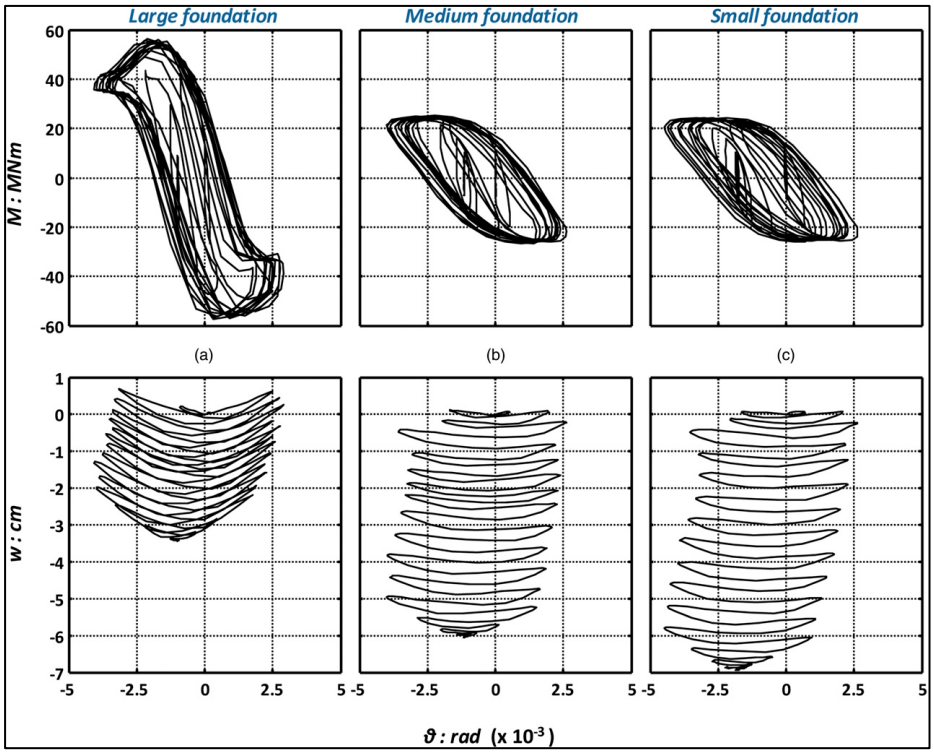

(ii)

Figure 2.18 Foundation response to base excitation of a **(i)** 12-cycle 2-Hz sine with 0.15g acceleration amplitude and **(ii)** of a 12-cycle 2-Hz sine pulse with 0.50g acceleration amplitude; evolution of moment-rotation and settlement-rotation hysteretic response for **(a)** large foundation ($FS_V = 7.3$); **(b)** medium foundation ($FS_V = 2.5$); **(c)** small foundation ($FS_V = 2.3$). *(Drosos et al., 2012)*

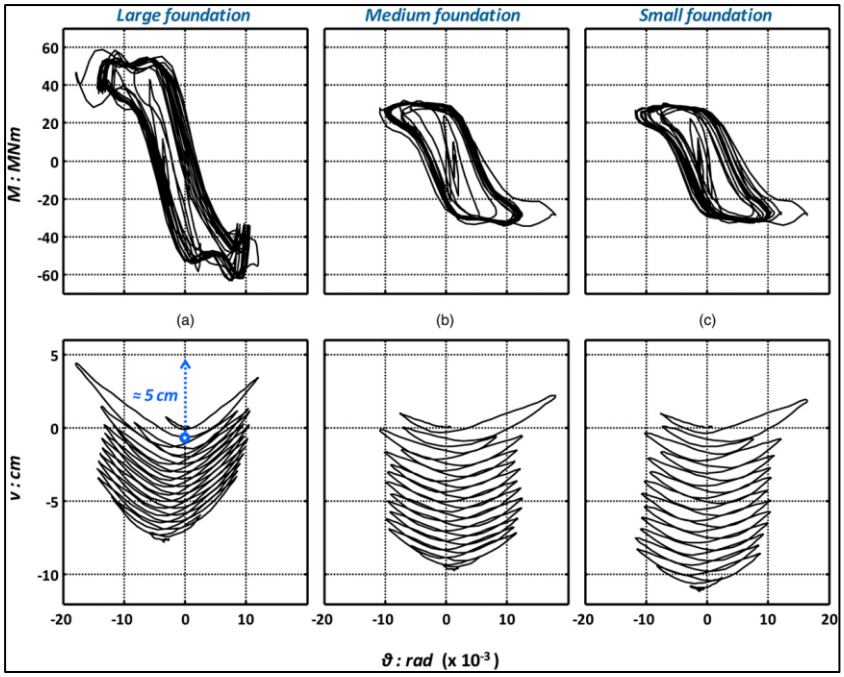

Figure 2.19 Foundation response to base excitation of a 12-cycle 1-Hz sine with 0.50g acceleration amplitude (sin120.50g); evolution of moment-rotation and settlement-rotation hysteretic response for **(a)** large foundation ($FS_V = 7.3$); **(b)** medium foundation ($FS_V = 2.5$); **(c)** small foundation ($FS_V = 2.3$). *(Drosos et al., 2012)*

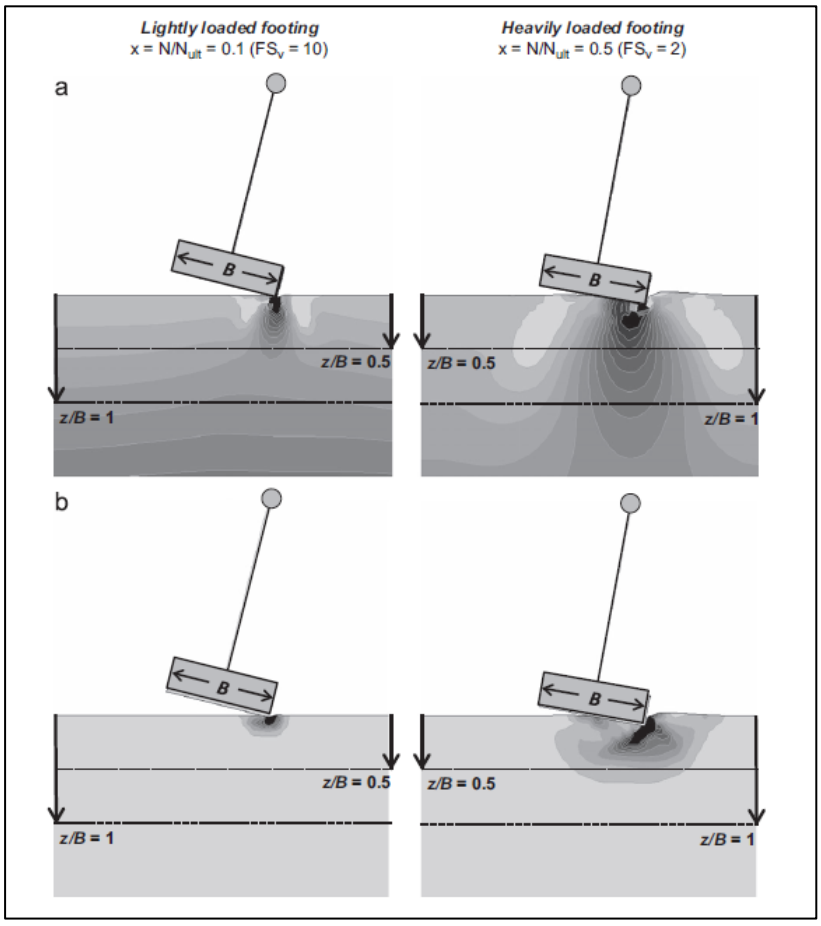

Figure 2.20 Illustration of the shallow nature of the rocking mechanism. Numerical simulation of a lightly-loaded ($FS_v = 10$) and a heavily-loaded ($FS_v = 2.0$) footing: **(a)** contours of vertical stresses and **(b)** plastic strain. In the case of the lightly loaded system, the soil at depth $z/B > 0.5$ is not affected and plastic deformation is constricted to a depth even smaller than $0.5B$. In the latter case, the rocking mechanism is deeper, with the vertical stresses being substantially affected at depths $z/B \leq 1.0$, and plastic deformation being contained at $z/B \leq 0.5$.

(Anastasopoulos et al., 2012)

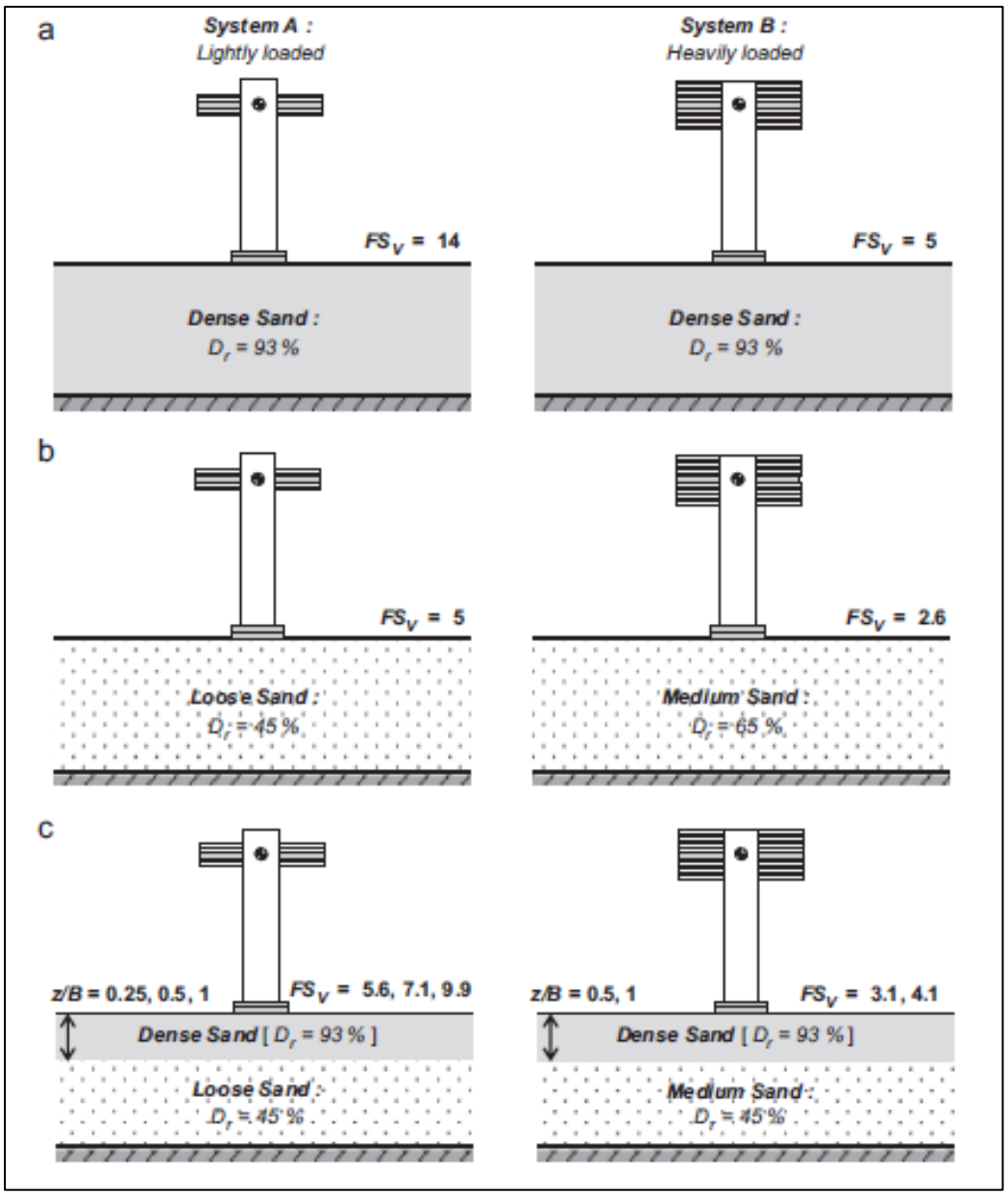

Figure 2.21 Schematic illustration of the studied soil-structure systems. Two configurations are investigated, one referring to a lightly loaded system (left), and one referring to a heavily loaded (right) founded on: **(a)** dense sand, representing the reference case of ideal soil conditions; **(b)** medium and loose sand, representing poor soil conditions; and (c) soil improvement with a shallow soil crust of dense sand, of varying depth ($z/B = 0.25 - 1.0$). *(Anastasopoulos et al., 2012)*

	System A		
	Configuration	N_{ult} (kN)	FS_v
Ideal soil conditions	Dense sand (D_r=93%)	4.83	14.1
Poor soil conditions	Loose sand (D_r=45%)	1.70	5.0
Soil improvement	z/B=0.25 on top of loose sand	1.95	5.6
	z/B=0.5 on top of loose sand	2.45	7.1
	z/B=1 on top of loose sand	3.40	9.9

	System B		
	Configuration	N_{ult} (kN)	FS_v
Ideal soil conditions	Dense sand (D_r=93%)	4.83	4.9
Poor soil conditions	Medium sand (D_r=65%)	2.48	2.6
Soil improvement	z/B=0.25 on top of medium sand	3.03	3.1
	z/B=0.5 on top of medium sand	3.73	3.7
	z/B=1 on top of medium sand	3.96	4.1

Figure 2.21 Summary of measured bearing capacity of the B = 15 cm square foundation, for homogeneous (dense,medium,and loose sand) and two-layeredsoilprofiles (denses and crust on top of medium or dense sand). *(Anastasopoulos et al., 2012)*

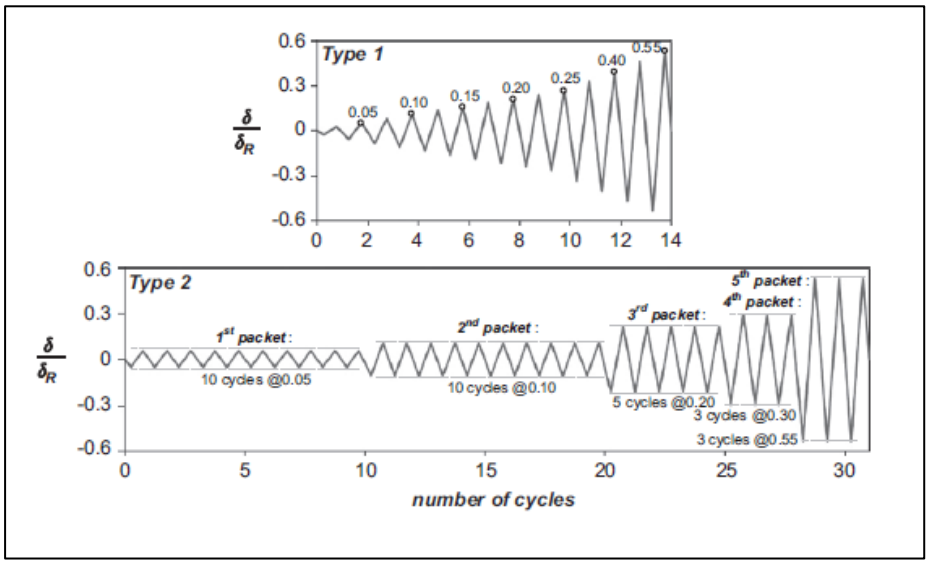

Figure 2.22 The two displacement protocols used for cyclic loading tests, normalized to the toppling displacement δ_R of the equivalent rigid block (forthe B = 15 cm foundation used in the tests, $\delta_R = 7.50\ cm$). *(Anastasopoulos et al., 2012)*

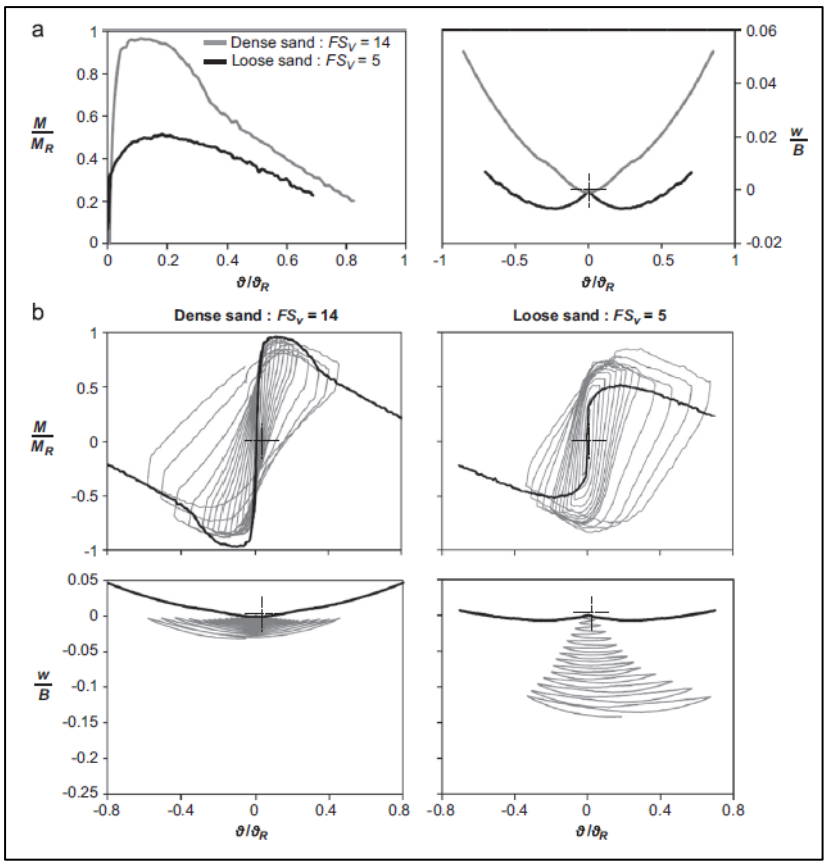

Figure 2.23 Moment–rotation and settlement–rotation response of the lightly loaded System A on dense and loose sand subjected to displacement-controlled: **(a)** monotonic loading and **(b)** cyclic loading (with Type 1 protocol). Moment and rotation are normalized to the overturning moment $M_R = 0.026\,kNm$ and toppling rotation ϑ_R of the equivalent rigid block ($\vartheta_R = \frac{b}{2h} = 0.167\,rad$); settlement is normalized to the width B of the footing. *(Anastasopoulos et al., 2012)*

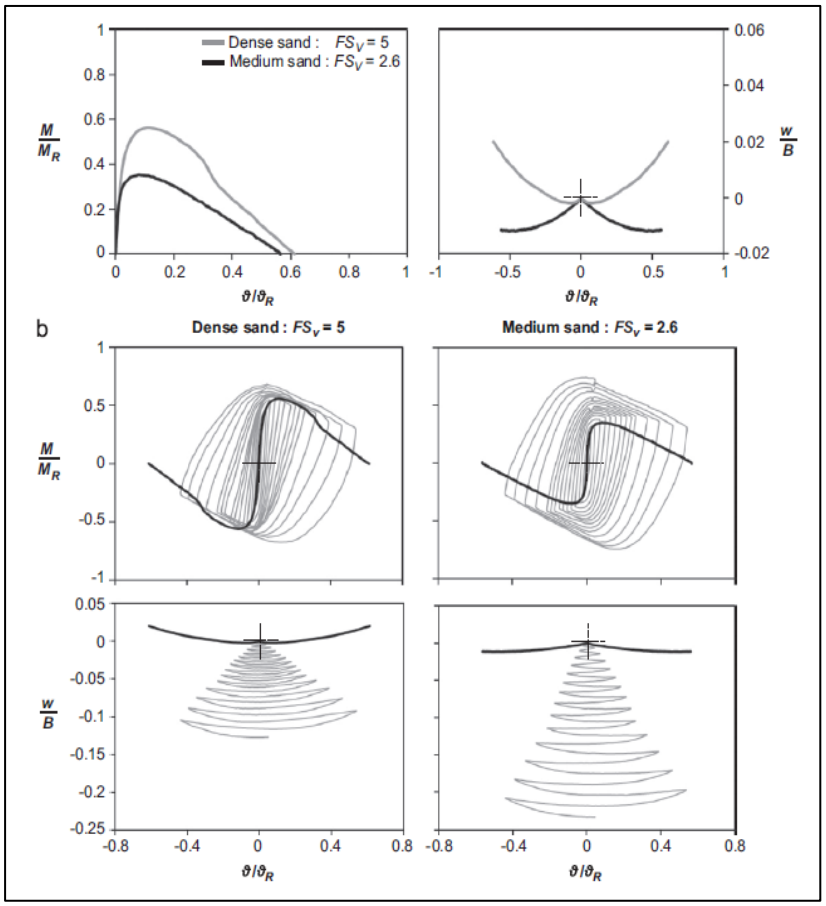

Figure 2.24 Moment–rotation and settlement–rotation response of the heavily loaded System B on dense and medium sand subjected to displacement-controlled: **(a)** monotonic loading and **(b)** cyclic loading (with Type 1 protocol). Moment and rotation are normalized to the overturning moment $M_R = 0.075\,kNm$ and toppling rotation ϑ_R of the equivalent rigid block ($\vartheta_R = \frac{b}{2h} = 0.167\,rad$); settlement is normalized to the width B of the footing. *(Anastasopoulos et al., 2012)*

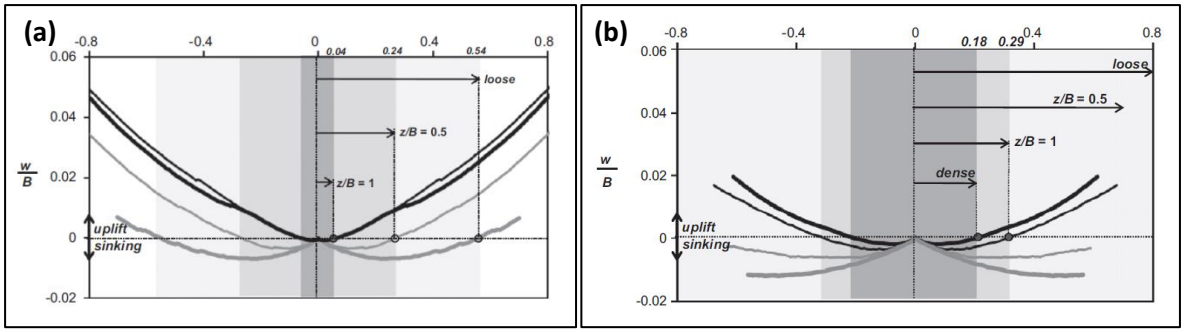

Figure 2.25 Effectiveness of soil improvement in terms of settlement–rotation response (highlighting sinking-dominated response for each case). **(a)** lightly loaded system A and **(b)** the heavily loaded system B subjected to monotonic loading. *(Anastasopoulos et al., 2012)*

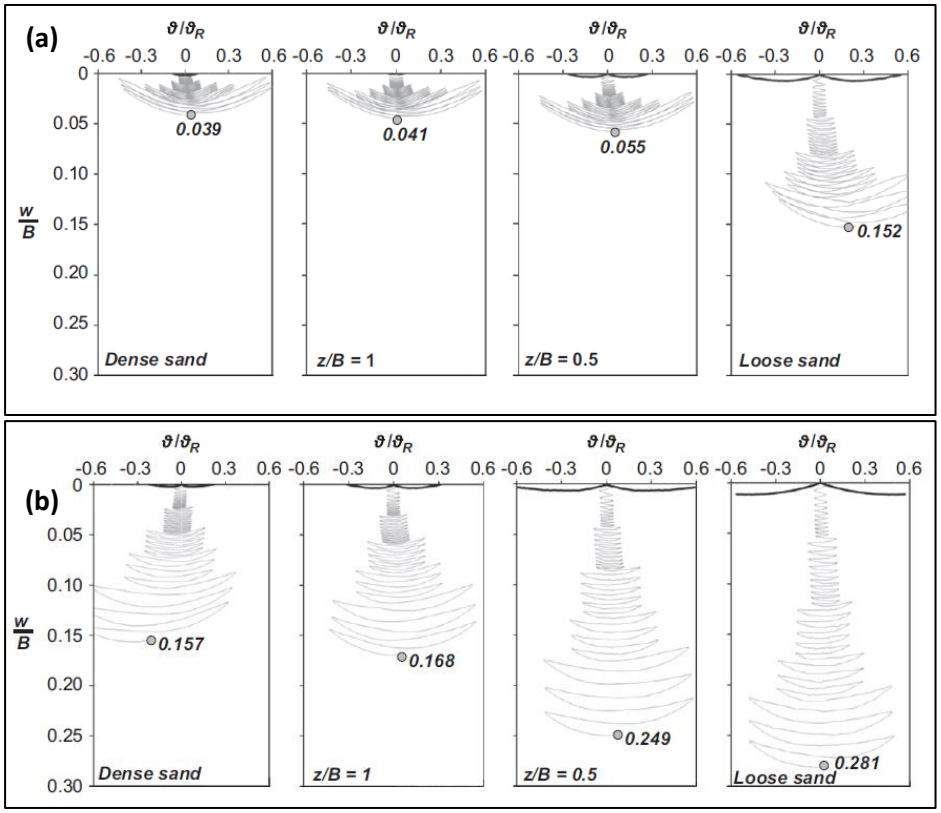

Figure 2.26 Effectiveness of soil improvement forType2 loading protocol. Settlement–rotation response: **(a)** for the lightly loaded System A, and **(b)** for the heavily loaded System B. *(Anastasopoulos et al., 2012)*

Sequence I		Sequence II		Sequence III	
Excitation	**PGA (g)**	**Excitation**	**PGA (g)**	**Excitation**	**PGA (g)**
sin 2 Hz	0.2	Aegion	0.39	sin 2 Hz	0.1
sin 2 Hz	0.4	Kalamata	0.4	sin 2 Hz	0.15
sin 1 Hz	0.2	Lefkada 2003	0.2	sin 2 Hz	0.2
sin 1 Hz	0.4	JMA	0.4	sin 2 Hz	0.25
Pacoima Dam	1.25	Rinaldi	1.14	sin 2 Hz	0.3
Sakarya	0.36	Takatori	0.36	sin 2 Hz	0.35
Lefkada 2003	0.43			sin 2 Hz	0.4

Figure 2.27 The three seismic shaking sequences of the shaking table tests. *(Tsatsis and Anastasopoulos, 2015)*

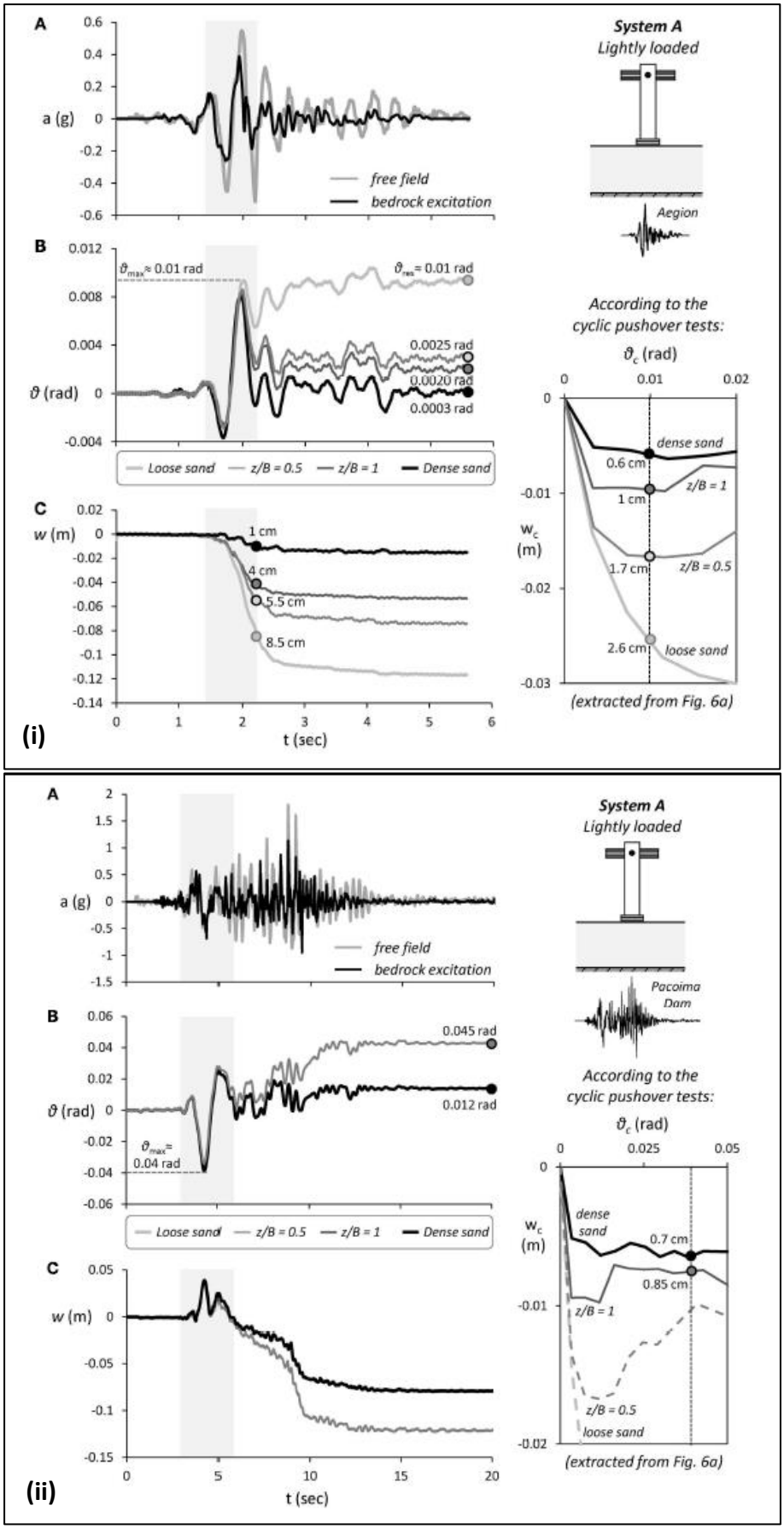

Figure 2.28 Seismic performance of System A subjected **(i)** to moderate seismic shaking using the Aegion record and **(ii)** to seismic shaking using the Pacoima dam record as excitation–comparison of shallow soil improvement with poor (loose sand) and ideal (dense sand) soil conditions. Time histories of **(A)** free field and base excitation, **(B)** foundation rotation,and **(C)** settlement. An extract from the slow-cyclic pushover tests results is included illustrating the settlement per cycle w_c as a function of cyclic rotation amplitude ϑ

(Tsatsis and Anastasopoulos, 2015)

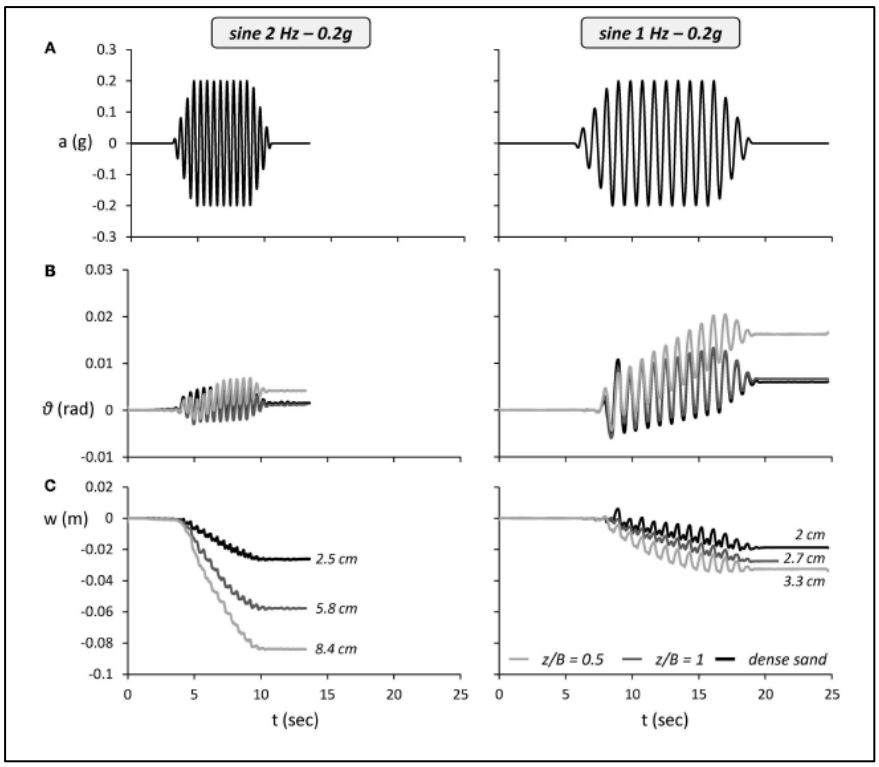

Figure 2.29 The effect of excitation frequency on the efficiency of shallow soil improvement. Comparison of shallow soil improvement with ideal soil conditions for the lightly loaded System A subjected to seismic shaking using two 15-cylce sinusoidal excitations of frequency f =2 Hz (left) and f =1 Hz (right). Time histories of **(A)** free field and base excitation, **(B)** foundation rotation, and **(C)** settlement. *(Tsatsis and Anastasopoulos, 2015)*

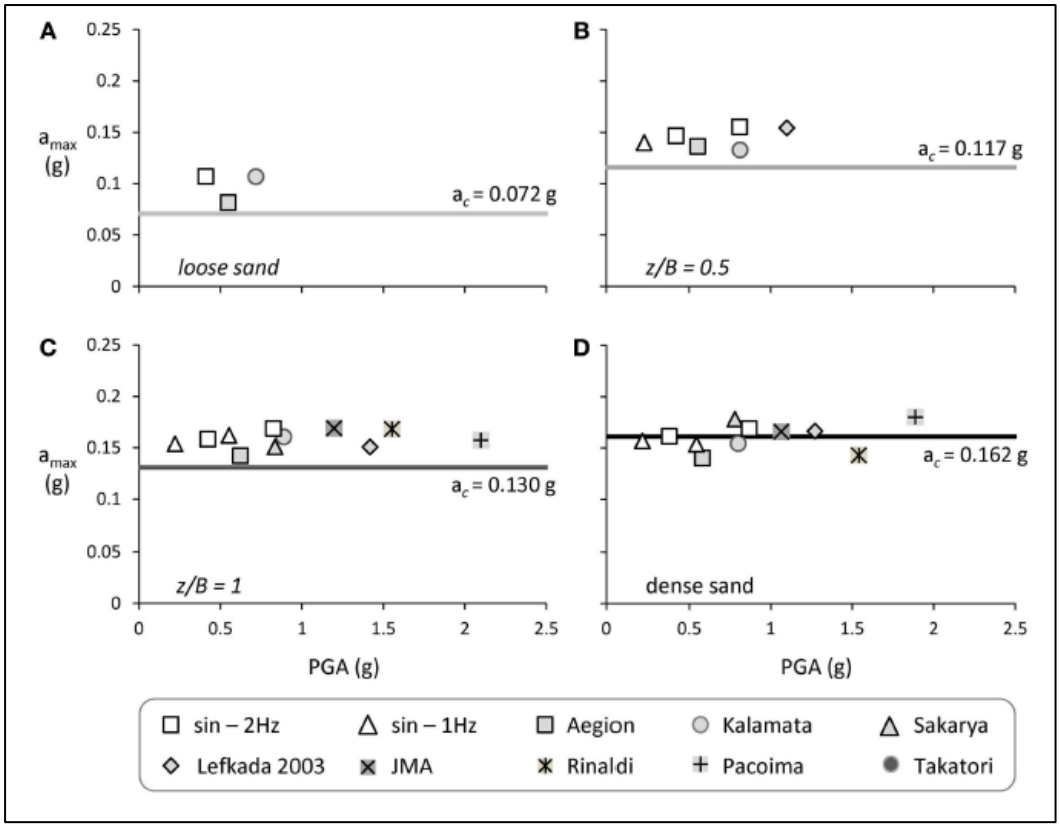

Figure 2.30 Synopsis of the performance of the lightly loaded System A subjected to seismic shaking sequences I and II. Maximum acceleration a_{max} at the oscillator mass as a function of PGA: **(A)** loose sand-poor soil conditions; **(B)** $z/B = 0.5$; **(C)** $z/B = 1$; and **(D)** dense sand-ideal soil conditions. *(Tsatsis and Anastasopoulos, 2015)*

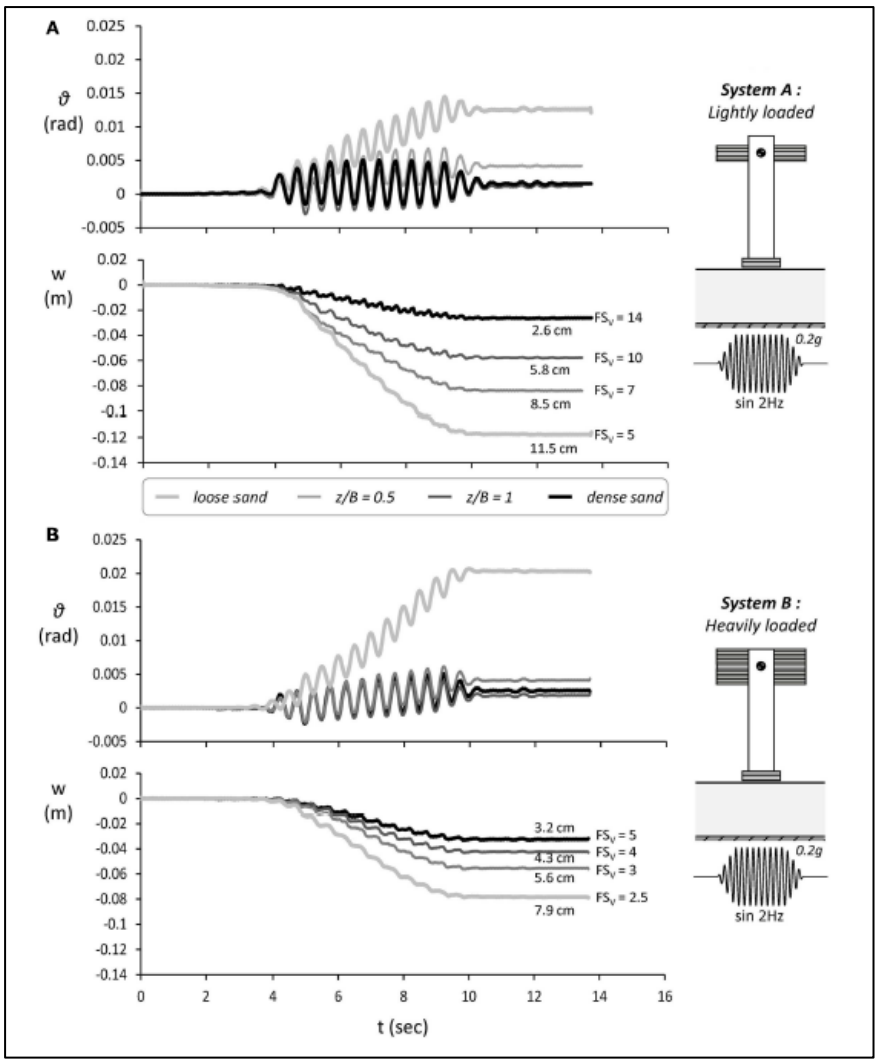

Figure 2.31 The effect of "de-amplification" due to strongly non-linear SSI. Time histories of rotation ϑ and settlement w for all soil profiles examined, subjected to an f =2 Hz sine of PGA=0.2 g. Comparison of **(A)** lightly loaded System A; with **(B)** heavily loaded System B. *(Tsatsis and Anastasopoulos, 2015)*

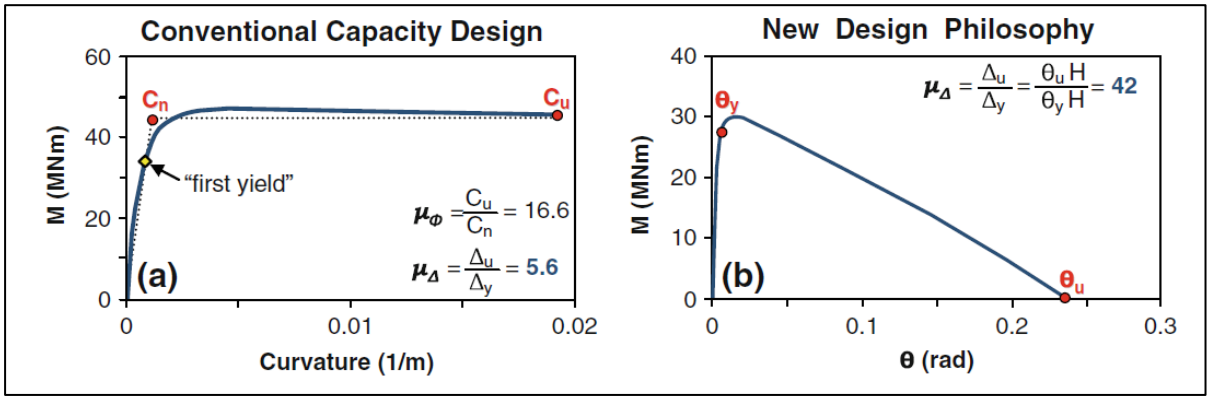

Figure 2.32 (a) Static Pushover analysis for the conventionally designed system. The ductility capacity in terms of curvature $\mu_\Phi \approx 16.60$, whereas the ductility capacity in terms of yielding displacement $\mu_\Delta \approx 5.60$. **(b)** The same analysis performed for the new design concept leads to a displacement yielding ductility capacity $\mu_\Delta \approx 42$. The difference in this approach lies in the fact that the ductility in this case is related to the rotation of the foundation, due to the soil plastification; leading to a value almost an order of magnitude larger.

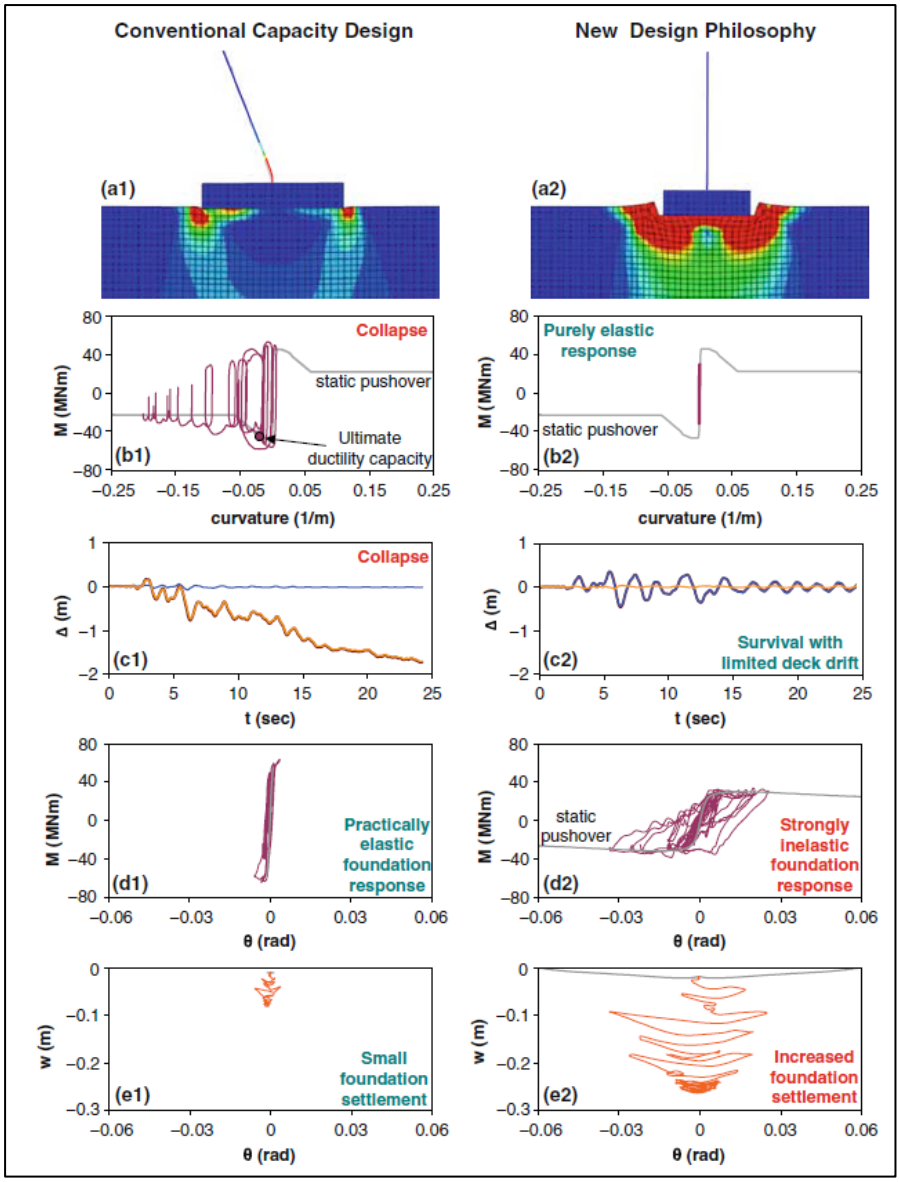

Figure 2.33 Comparison of the results for the Takatori, 1995 motion between the two alternative approaches. **(a)** The deformed mesh is depicted superimposing the plastic strains and thus indicating the location of the plastic hinge: in the base of the pier in the first case; in the foundation soil in the second. **(b)** Bending moment–curvature response at the pier base. The ductility demand for the conventional design exceeds the design would lead to collapse. Contrary to that the pier designed according the new approach remains elastic. **(c)** The drift time history for the conventional pier indicates collapse, since its response is governed by flexural failure. The maximum drift of the new design concept is large (mainly due to foundation rotation), but the system survives with insignificant residual drift. **(d)** $(M-\theta)$ response of the two foundations indicates an elastic behavior for the conventionally designed one contrary to a purely inelastic behavior characterizing the one representing the design of the new approach. **(e)** $(w-\theta)$ response shows that the settlement of the conventional system is minor, whereas the new design experiences a large $(24\ cm)$ settlement. *(Anastasopoulos et al. 2010)*

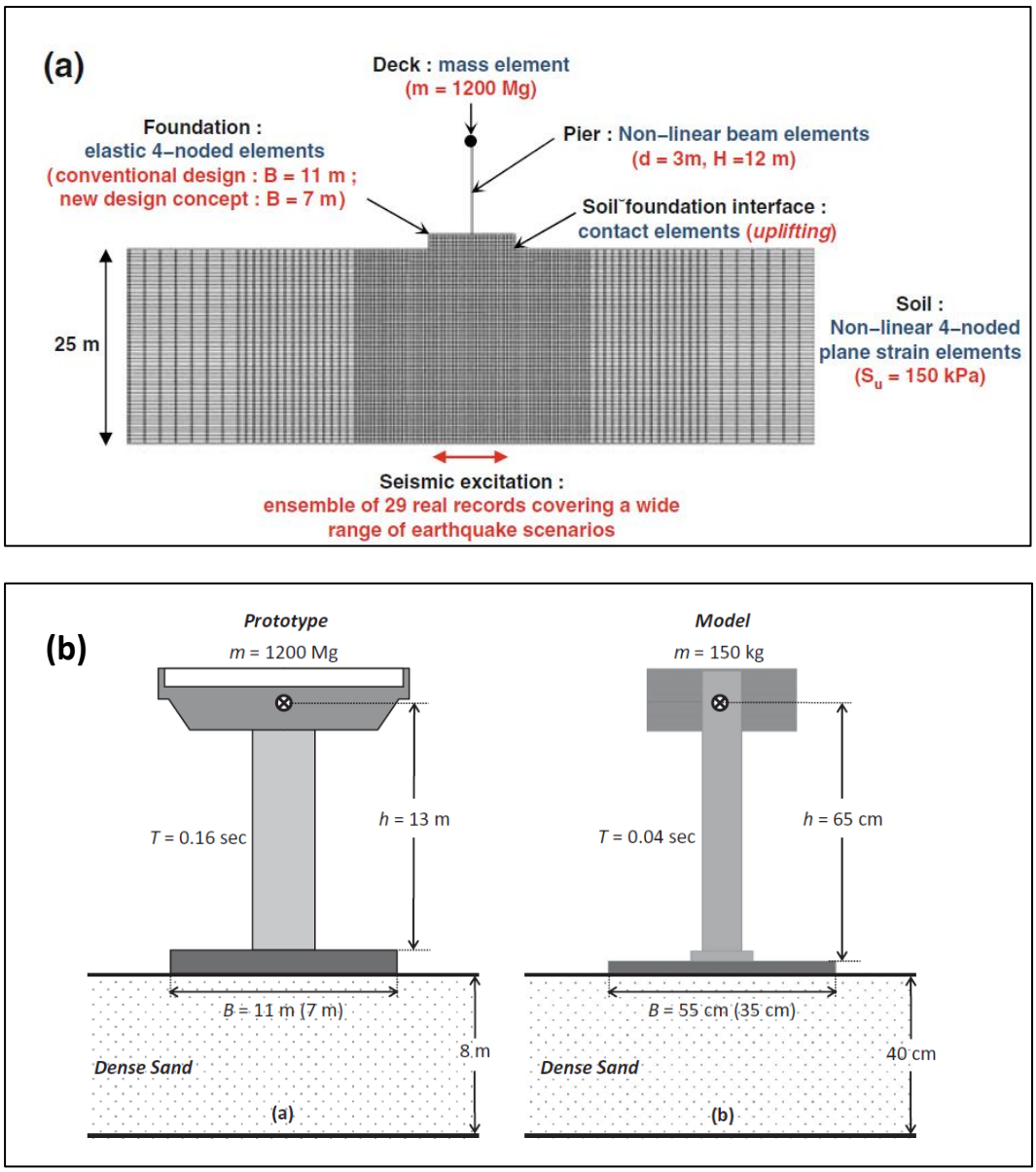

Figure 2.34 (a) Overview of the finite element modeling assuming plain strain conditions and considering material inelasticity for both the soil and the superstructure and geometric non linearity, due to P – Δ effects and uplifting. **(b)** Problem definition depicting the conceptual prototype of an idealized stiff bridge pier lying on dense sand; and the corresponding shaking table model (in 1 : 20 scale). *(Anastasopoulos et al., 2010 and 2013)*

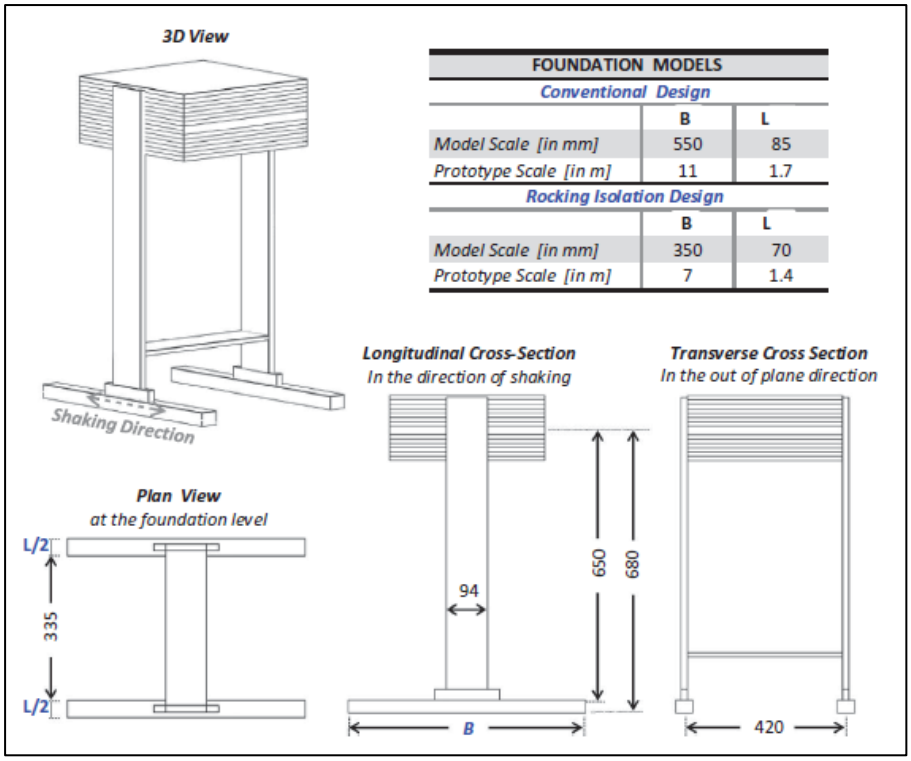

Figure 2.35 Geometry of the configuration for the two specimens tested on the shaking table (all model dimensions in [mm]) *(Anastasopoulos et al., 2013)*

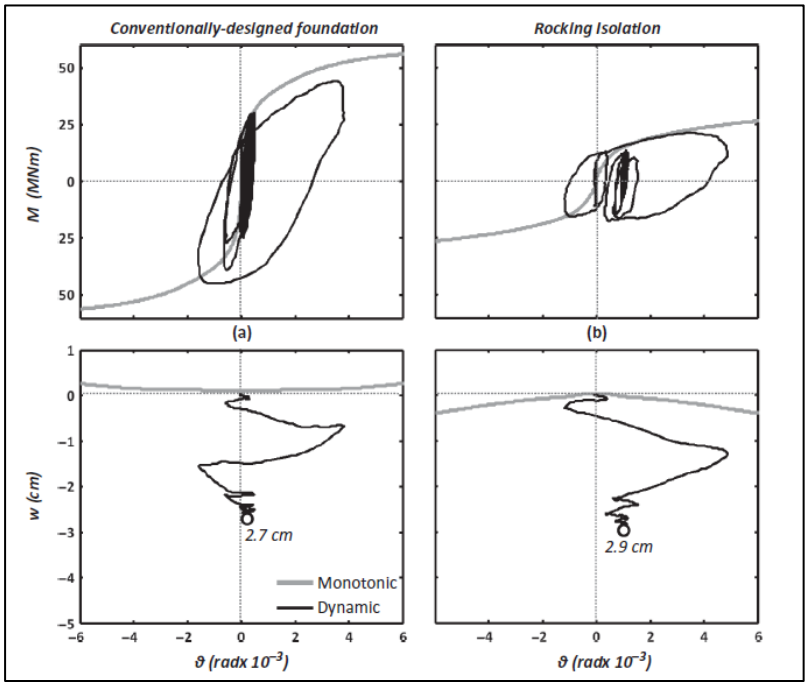

Figure 2.36 Foundation performance for *moderate* seismic shaking (Aegion). Moment–rotation (M–θ) and settlement–rotation (w–θ) response for: (a) system on conventionally designed B = 11 m foundation, compared to **(b)** rocking isolated alternative with underdesigned B = 7 m foundation. *(Anastasopoulos et al., 2013)*

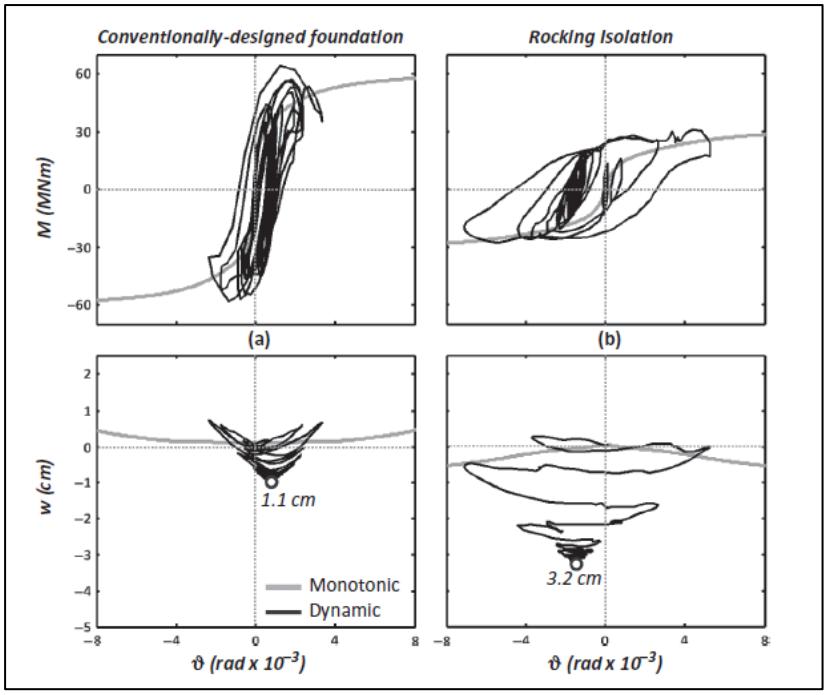

Figure 2.37 Foundation performance for *strong* seismic shaking (Gilroy). Moment− rotation (M−ϑ) and settlement–rotation (w−ϑ) response for: **(a)** system on conventionally designed B = 11 m foundation, compared to **(b)** rocking isolated alternative with underdesigned B = 7 m foundation. *(Anastasopoulos et al., 2013)*

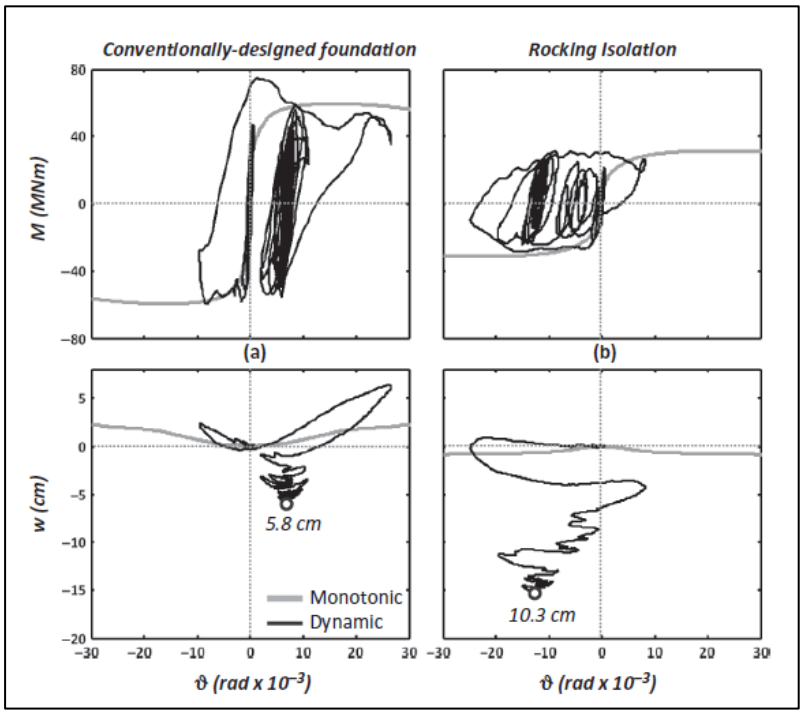

Figure 2.38 Foundation performance for *extreme* seismic shaking (Rinaldi). Moment–rotation (M−ϑ) and settlement–rotation (w−ϑ) response for: **(a)** system on conventionally designed B = 11 m foundation, compared to **(b)** rocking isolated alternative with underdesigned B = 7 m foundation. *(Anastasopoulos et al., 2013)*

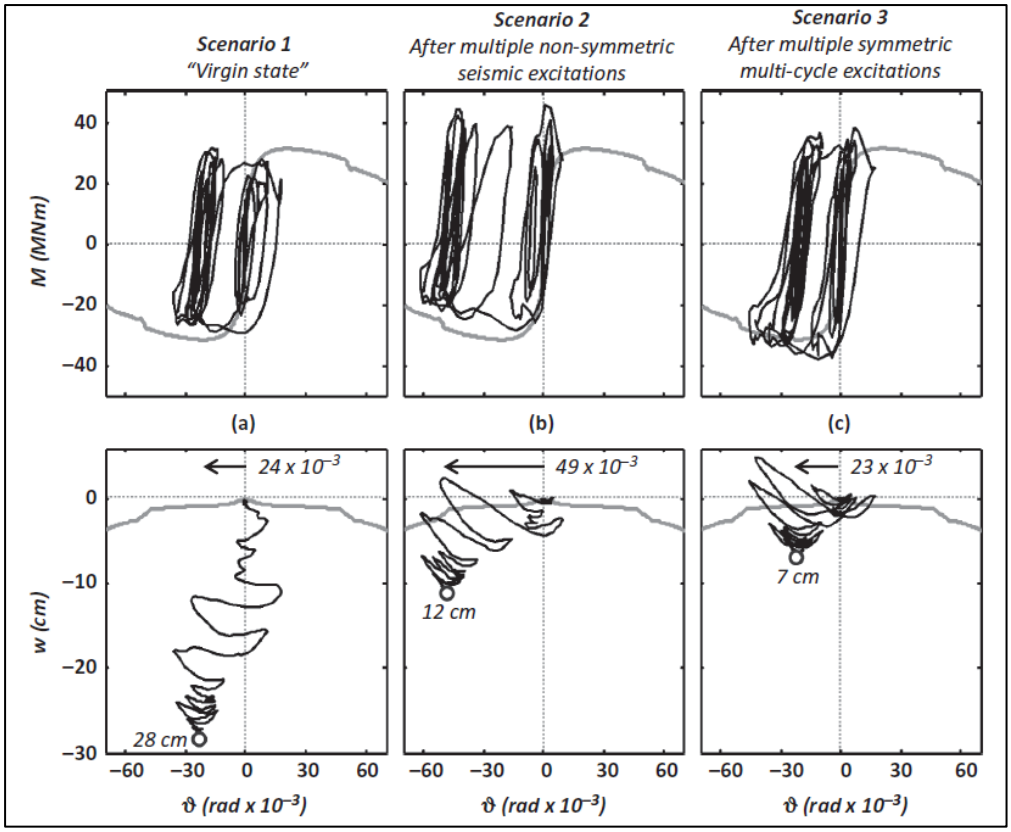

Figure 2.39 Moment–rotation (M–ϑ) and settlement– rotation (w–ϑ) response for the rocking isolated pier during shaking with the Takatori (Kobe, 1995) record: **(a)** "virgin state"; **(b)** after multiple non-symmetric seismic excitations (real records, characterized by directivity effects, hence unsymmetrical excitations); and **(c)** after multiple symmetric multicycle (sinusoidal) excitations. The dynamic performance (black lines) is compared to the horizontal pushover response (grey lines) on undisturbed soil. *(Anastasopoulos et al., 2013)*

Model names	SC-1	MC	LC	SC-2	SC/I[ii]	SF	ISF[ii]
Test series	LJD01	LJD01	LJD01	LJD01	LJD01	LJD03	LJD03
Loading type	Slow cyclic	Slow cyclic	Slow cyclic	Slow cyclic	Slow cyclic	Dyn.	Dyn.
Supported on concrete pads?	No	No	No	No	Yes	No	Yes
Total load, Q (kN)	7017	9056	1.073e4	7017	7017	6192	6192
Footing length, L_f (m)[i]	6.70	9.76	12.20	6.70	6.70	7.35	7.35
Footing width, B_f (m)	4.28	6.24	7.79	4.28	4.28	4.70	4.70
L_c (m)	0.46	0.32	0.27	0.83	n/a	0.73	n/a
L_f/L_c	14.6	30.5	45.2	8.0	n/a	10.1	n/a
FSv	14.8	29.6	43.7	9.0	n/a	11.0	n/a
M_{c_foot} (MN·m)	21.9	42.7	64.0	20.7	n/a	20.5	n/a
Soil relative density, D_r	73%	73%	73%	44%	44%	38%	38%
Peak friction angle, ϕ(°)	36.6	36.4	36.2	33.4	n/a	32.7	n/a
Embedment, D (m)	2.24	2.24	2.24	2.24	2.24	2.24	2.24
Loading height, H (m)	13.54	12.12	12.12	12.12	12.12	n/a	n/a
Moment-to-shear ratio, H/L_f	2.02	1.24	0.99	1.81	1.81	n/a	n/a

Figure 2.40 Properties of centrifuge models in prototype scale. Notes: **(i)** L_f = Footing length in the loading direction; **(ii)** L_c and FS_V values were not evaluated for models supported by concrete pads. *(Deng and Kutter, 2012)*

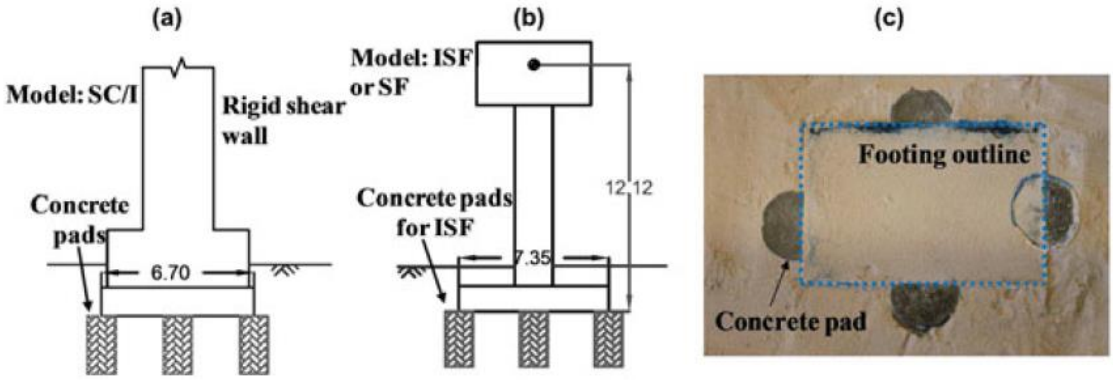

Figure 2.41 Layout of the concrete pads as a way to reduce the settlements: **(a)** the shear wall model for slow cyclic tests, **(b)** the SDOF model for dynamic tests, and **(c)** a plan-view photograph of the pads. Dimensions are in meters in prototype scale. *(Deng and Kutter, 2012)*

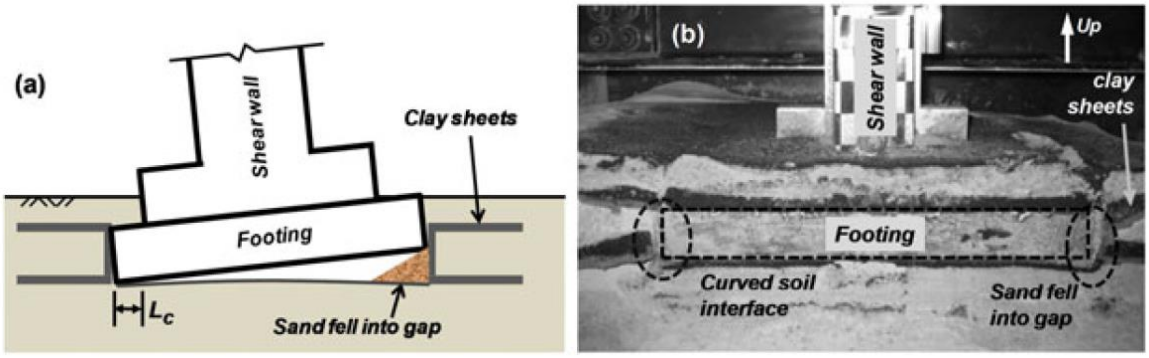

Figure 2.42 (a) Illustration of the sand falling into the gap for the cases with a high L_f/L_c ratio; note that the rotation angle and the fallen sand wedge are exaggerated for illustration purposes; and **(b)** post-test elevation - view photograph of the excavation beside the LC foundation. *(Deng and Kutter, 2012)*

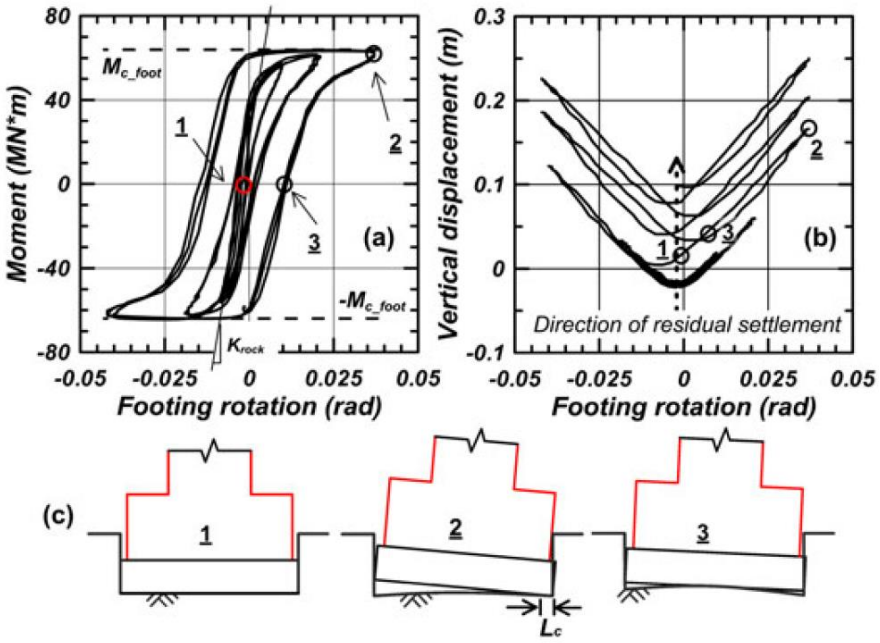

Figure 2.43 (a) Rocking moment versus footing rotation; **(b)** footing vertical displacement versus footing rotation; **(c)** conceptual sketches for the model during different phases of loading cycles. These curves were from the test results of model LC with $L_f/L_c = 44.5$. *(Deng and Kutter, 2012)*

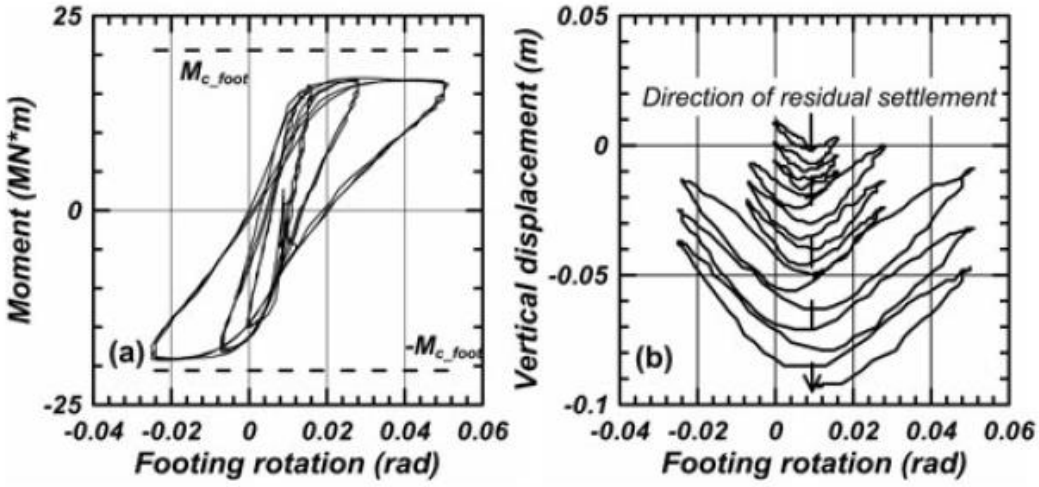

Figure 2.44 (a) Rocking moment versus footing rotation; **(b)** vertical displacement of the footing versus footing rotation. These curves were from the test results of SC-2 with $L_f/L_c = 8$ *(Deng and Kutter, 2012)*

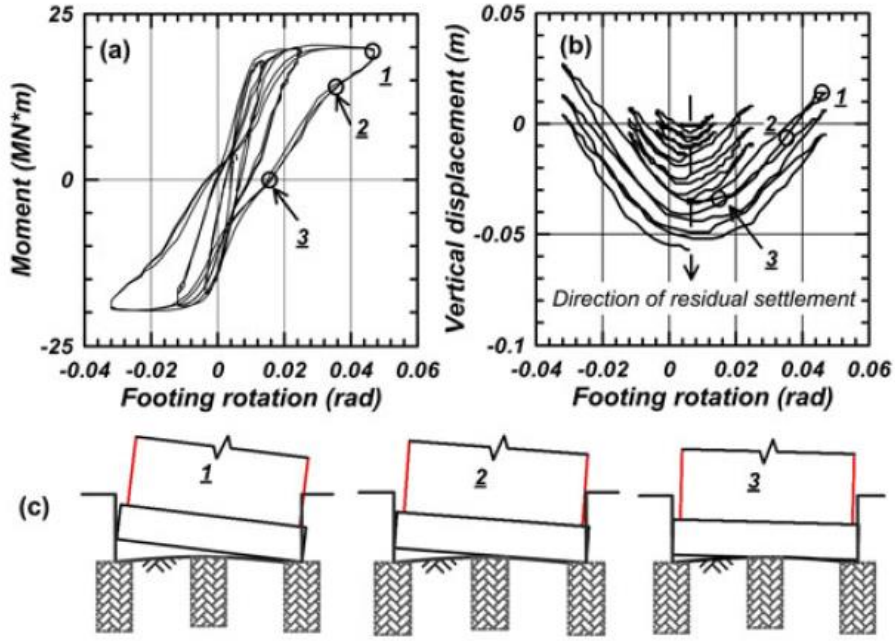

Figure 2.45 (a) Rocking moment versus footing rotation; **(b)** vertical displacement of the footing versus footing rotation; **(c)** conceptual sketches for the model during different stages of the loading cycle. These curves were from the test results of model SC/I. *(Deng and Kutter, 2012)*

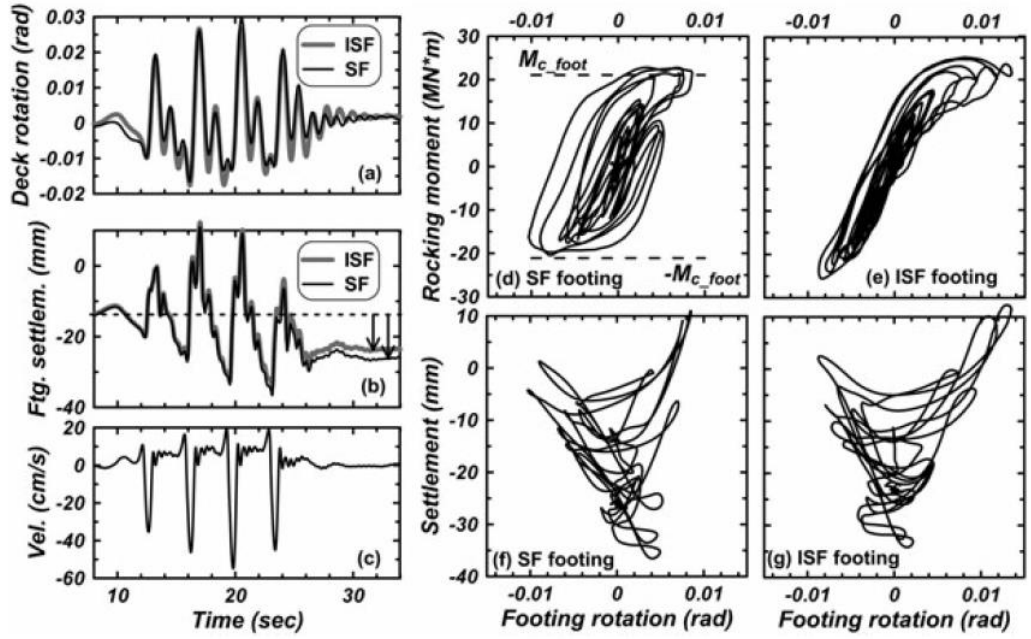

Figure 2.46 Results of the model SF and ISF subject to an asymmetric pulse motion (amplification factor =1.0): **(a)** deck rotation angle of SF and ISF; **(b)** footing settlement histories; **(c)** velocity time history of the input; rocking moment versus footing rotation of **(d)** SF and **(e)** ISF; and settlement versus footing rotation of **(f)** SF and **(g)** ISF. *(Deng and Kutter, 2012)*

Test series	Model code[a]	L_f (m)	B_f (m)	Initial D_r [b]	Initial FSv[c]	A/A_c	M_{c_foot} (MN·m)	M_{c_col} (MN·m)	C_r [d]	C_y [e]
LJD01	SD	6.70	4.28	73%	15	14	17.52	15.29	0.303	0.321
	MD	9.76	6.24	73%	30	30	25.53	15.29	0.533	0.321
LJD02	North Bridge	5.04	5.04	77%	29	30	8.82	10.0	0.184	0.283
	South Bridge	7.56	7.56	77%	53	55	16.45	10.0	0.348	0.283
LJD03	SF	7.35	4.70	38%	11	10	20.5	111.4 (elastic)	0.353	—
	LF	12.20	7.79	38%	26	23	49.0 (fixed-base)	15.29	—	0.315
	4CSF	7.35	4.70	38%	11	10	20.5	111.4 (elastic)	0.353	—

Figure 2.47 Configuration of the Centrifuge Test Series.
[a]SD = SDOF model with a small footing in LJD01; MD = SDOF model with a medium footing in LJD01; SF= SDOF model with a small footing in LJD03; LF = SDOF model with a large footing in LJD03; 4CSF = system model with 4 columns and 4 small footings in LJD03.
[b]Dr = relative density of the soil.
[c]FSv = factor of safety for vertical bearing capacity of the soil calculated by conventional bearing capacity equations for shallow foundations.
[d]Cr = base shear coefficient for rocking foundations.
[e]Cy = base shear coefficient for hinging columns. *(Deng et al., 2012)*

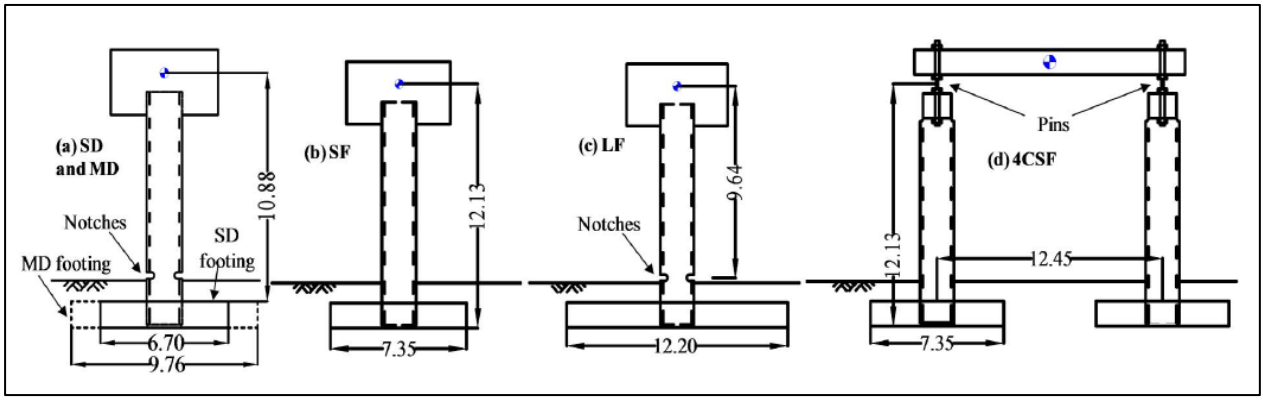

Figure 2.48 Models manufactured for test series: (a) LJD01 (a); (b–d) LJD03 LJD03. Dimensions are given in meters. *(Deng et al., 2012)*

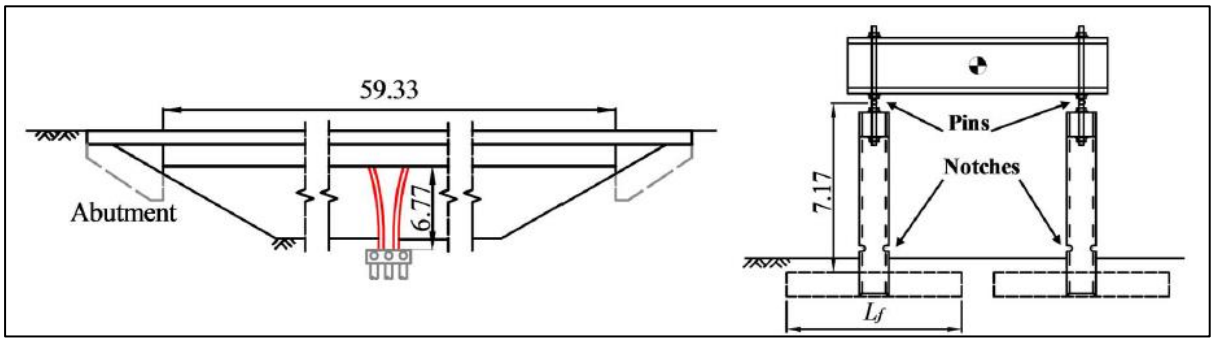

Figure 2.49 (a) A longitudinal view of the prototype bridge for LJD02 test series; **(b)** an elevation view of the bridge model in transverse direction (note: L_f = 5:04 m for rocking bridge and L_f = 7:56 m for hinging-column bridge). *(Deng et al., 2012)*

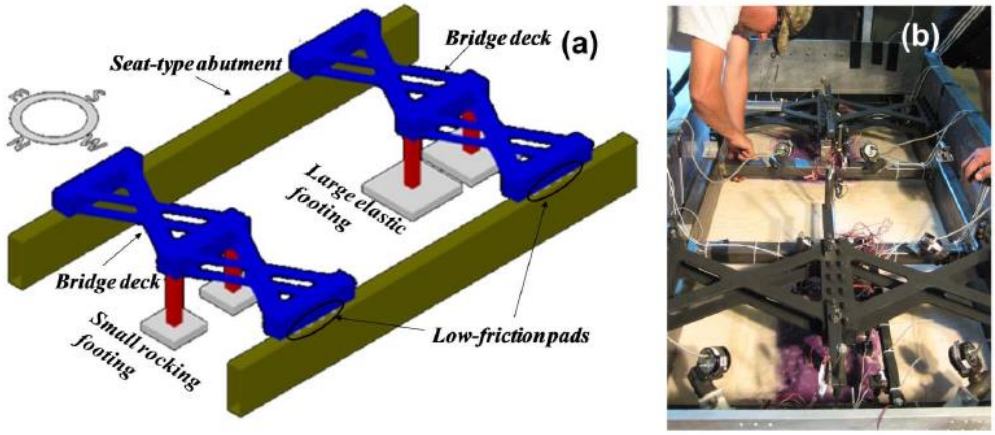

Figure 2.50 Experimental setup of LJD02 test series: **(a)** 3D view; **(b)** models in container. The shaker on the centrifuge shook the whole box in the N-S direction. *(Deng et al., 2012)*

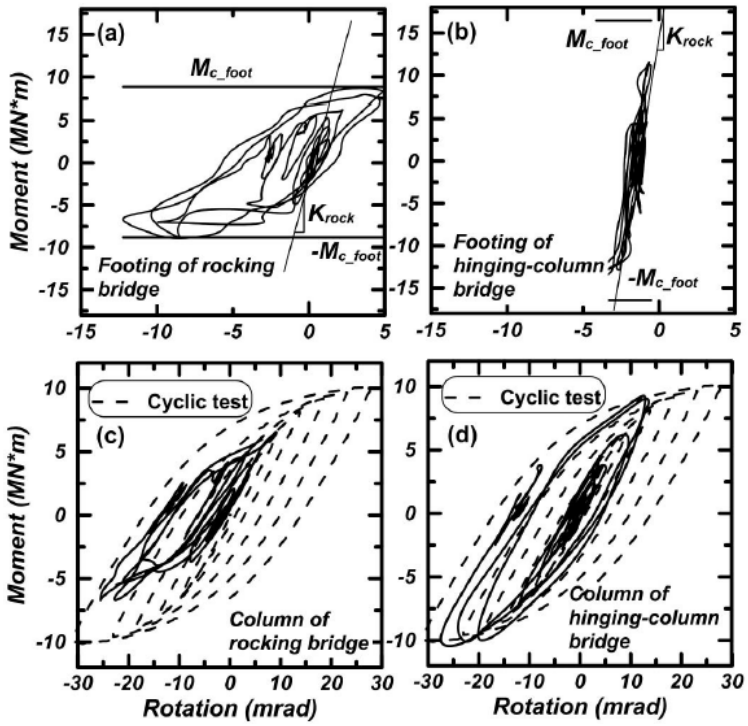

Figure 2.51 Moment versus rotation of: **(a)** footing of rocking-foundation bridge; (b) footing of hinging-column bridge; **(c)** column of rocking foundation bridge; **(d)** column of hinging-column bridge. *(Deng et al., 2012)*

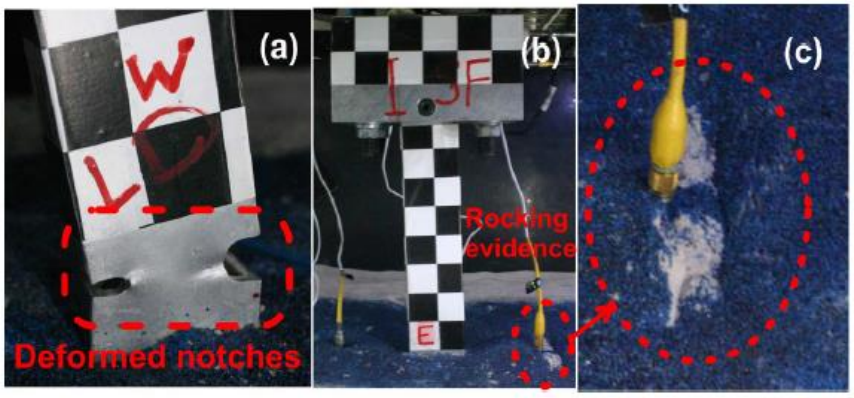

Figure 2.52 Photos taken after San Fernando event in LJD03 test: **(a)** the hinging-column of the model LF; **(b)** the rocking-foundation of the model SF; **(c)** zoom-in view of the disturbed ground because of rocking-foundation

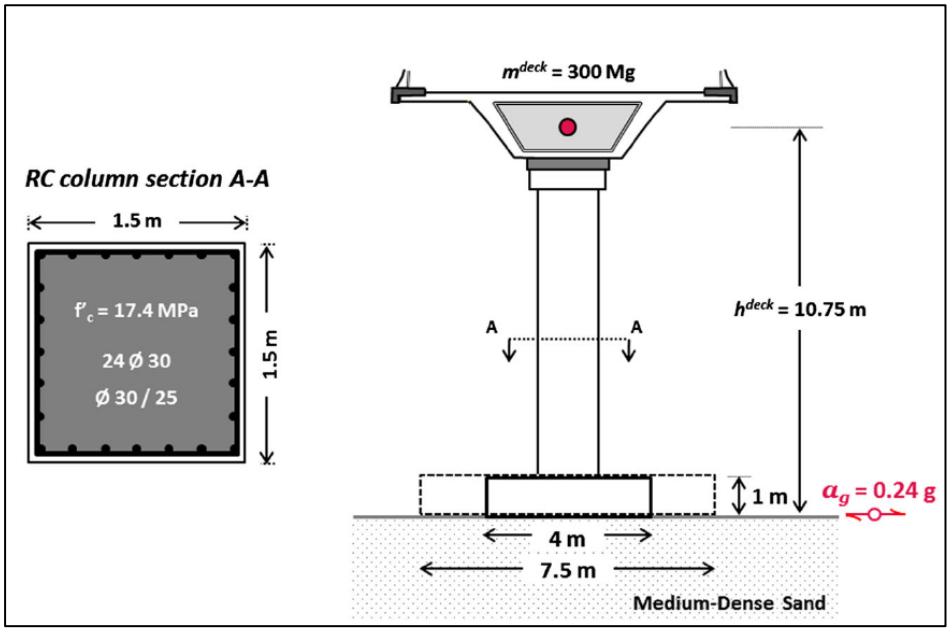

Figure 2.53 Schematic definition of the studied problem. *(Loli et al., 2014)*

Property	Unit	Conventional	Rocking
Breadth	B:m	7.5	4
Total vertical load	N_{tot}:MN	4.9	4
Seismic shear load	Q_E:MN	0.7	0.7
Seismic moment load	M_E:MNm	7.3	7.3
Design shear action	Q_{Ed}:MN	0.7	0.7
Design moment action	M_{Ed}:MNm	7.3	7.3
Ultimate shear capacity	Q_u:MN	1.2	0.5
Ultimate moment capacity	M_u:MNm	12.9	4.8
Factor of safety in vertical loading	FS_V	18	3.5
Factor of safety in combined (seismic) loading	FS_E	1.77	0.66

Figure 2.54 Foundation design: summary of actions and factors of safety (FS). *(Loli et al., 2014)*

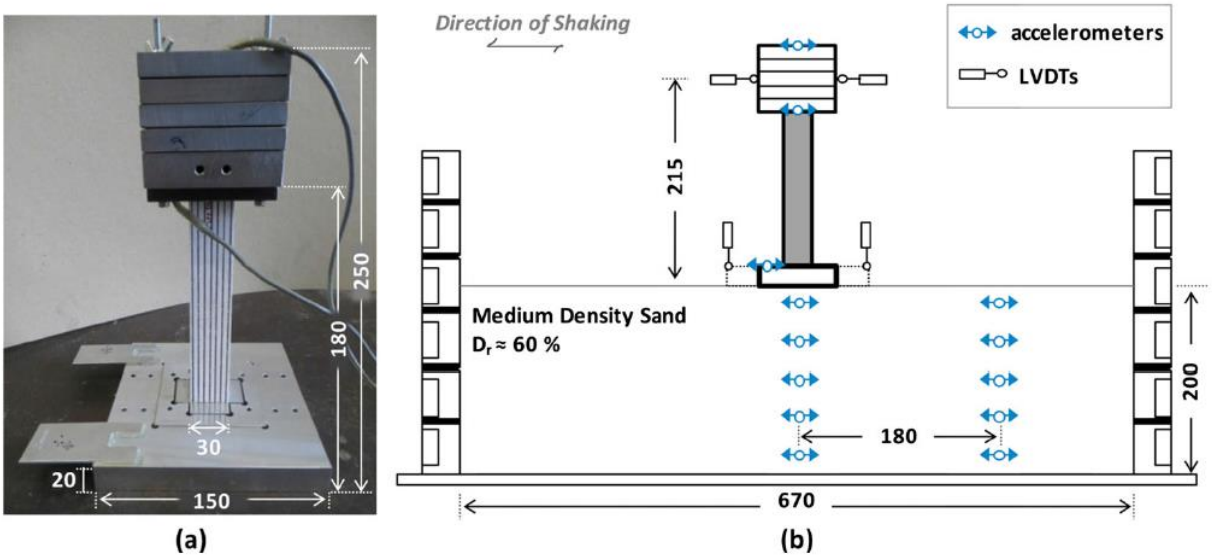

Figure 2.55 Experimental setup:**(a)** photo of the pier model assembly (mass, RC column, and foundation) and attached accelerometers indicating characteristic dimensions and **(b)** schematic cross section of the model within the laminar box showing instrumentation. All dimensions are in millimeters (model scale). *(Loli et al., 2014)*

Test	Pier design		Motion protocol					
1	Rocking isolation	A	Aegion	Lefkada	L'Aquila	Rinaldi	Takatori	—
2	Conventional design		Aegion	Lefkada	L'Aquila	—	—	—
3	Rocking isolation	B	Rinaldi	Aegion	Aegion	L'Aquila	Takatori	Takatori
4	Conventional design		Rinaldi	Aegion	Aegion	L'Aquila	Takatori	—

Figure 2.56 Testing program: sequence of seismic excitations. Earthquake Scenario A: the ground motions are in order of increasing intensity. Earthquake Scenario B: the ground motions are in order of decreasing intensity. *(Loli et al., 2014)*

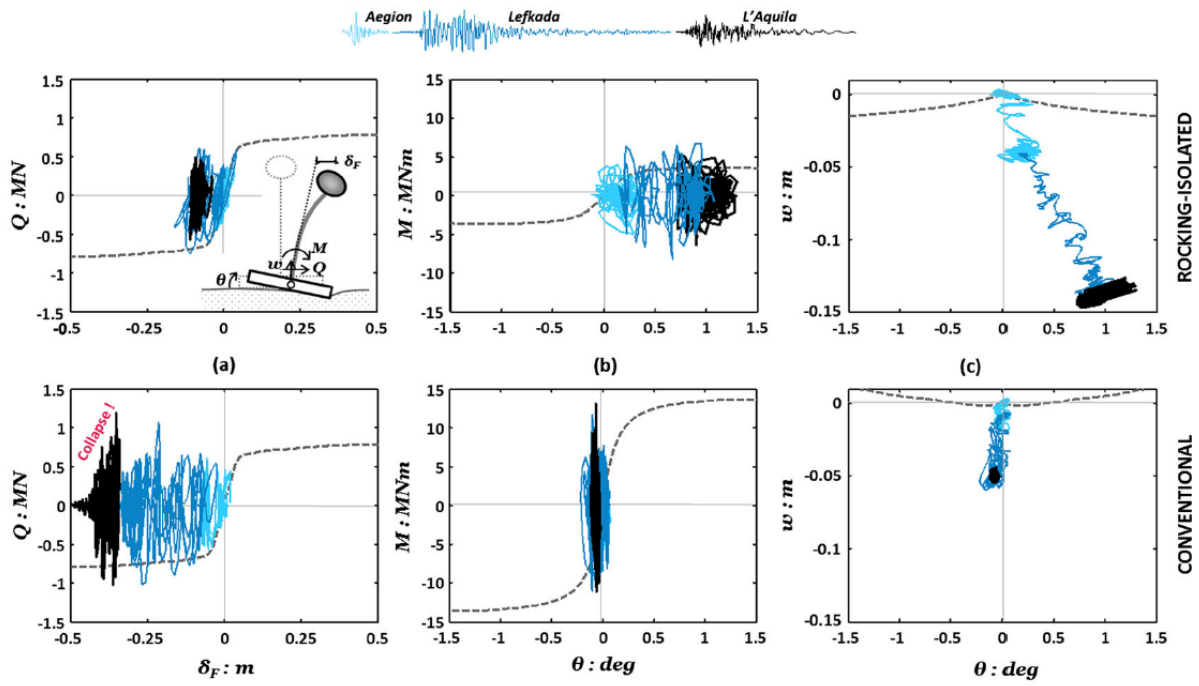

Figure 2.57 Rocking (top) versus conventional (bottom) pier hysteretic responses: **(a)** Q–δcol with reference to the base of the RC column; **(b)** foundation M–ϑ; and (c) foundation w–ϑ for Earthquake Scenario A. *(Loli et al., 2014)*

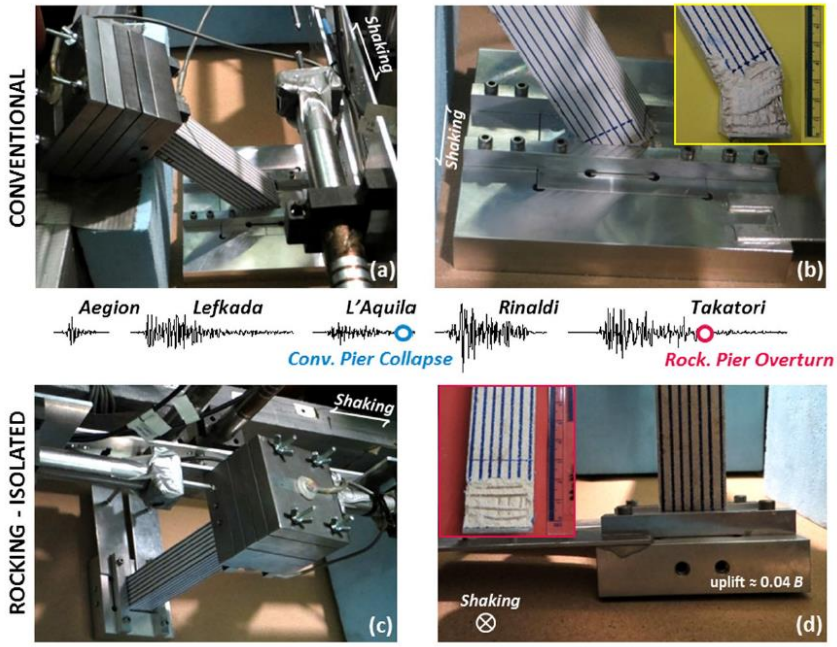

Figure 2.58 Photos of the bridge models after Tests 1 and 2 (Scenario A): **(a)** failure of the conventional pier after the first three medium-strong intensity motions and **(b)** the damage at the pier base compared with **(c)** the rocking pier subjected to the same motions plus two additional very strong motions, focusing on **(d)** foundation uplift. *(Loli et al., 2014)*

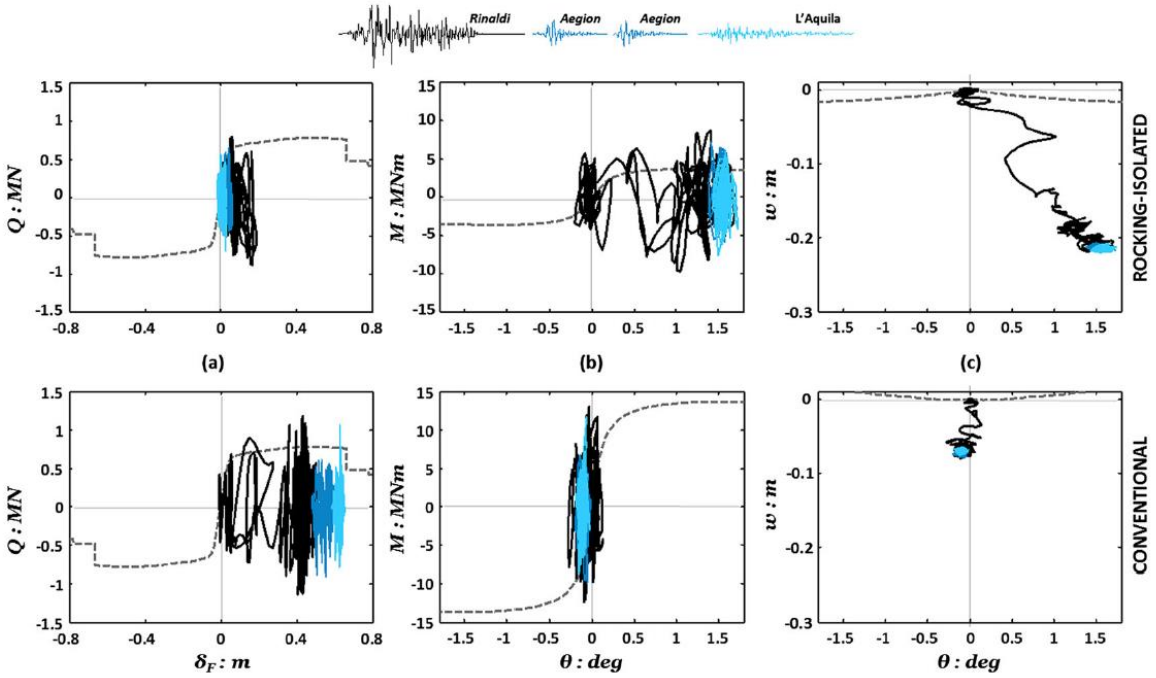

Figure 2.59 Rocking (top) versus conventional (bottom) pier hysteretic responses: **(a)** Q–δ_{col} with reference to the base of the RC column; **(b)** foundation $M-\vartheta$; and **(c)** foundation $w-\vartheta$ for Earthquake Scenario B. *(Loli et al., 2014)*

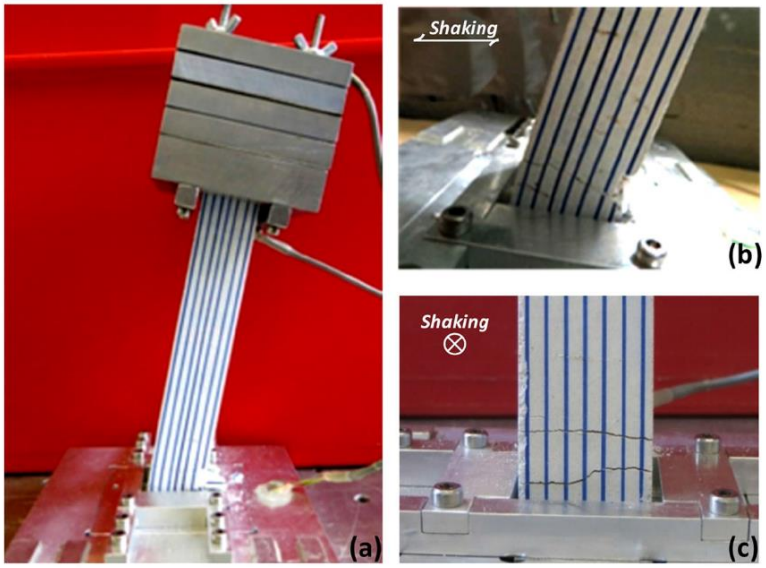

Figure 2.60 Photos of the conventional pier after Test 6 indicating the damage induced by shaking with Earthquake Scenario B followed by one additional very strong motion (the Takatori record): **(a)** view of the entire pier model **(b)** in-plane and **(c)** out-of-plane views of the column–foundation joint. *(Loli et al., 2014)*

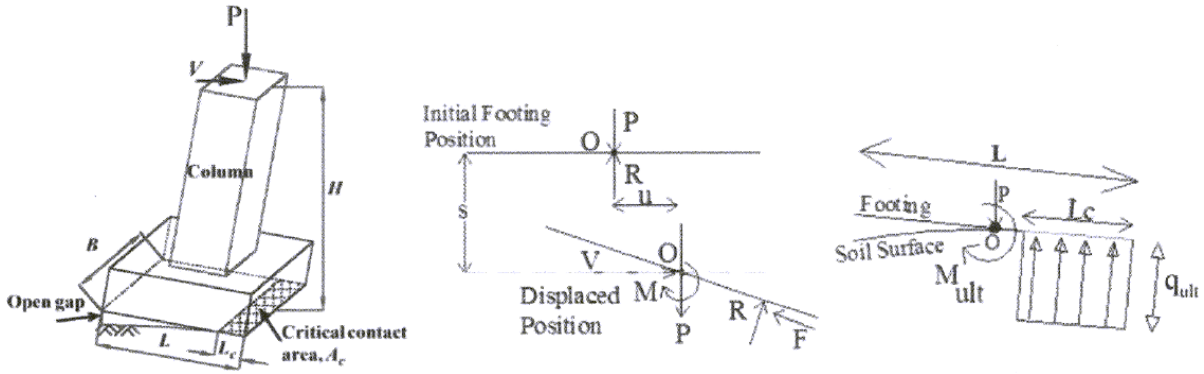

Figure 2.61 Rocking shallow foundation under vertical load (P), lateral load (V) with definition of critical contact area (A_c) and critical contact length (L_c) *(Hakhamaneshi and Kutter, 2015)*

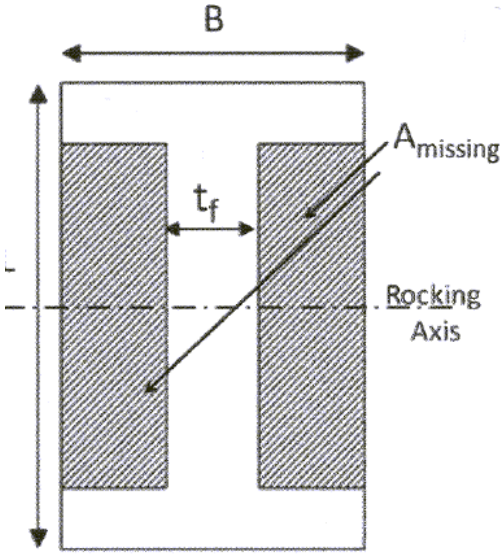

Figure 2.62 Footing shape parameters for rectangular and H-shaped rocking footings *(Hakhamaneshi and Kutter, 2015)*

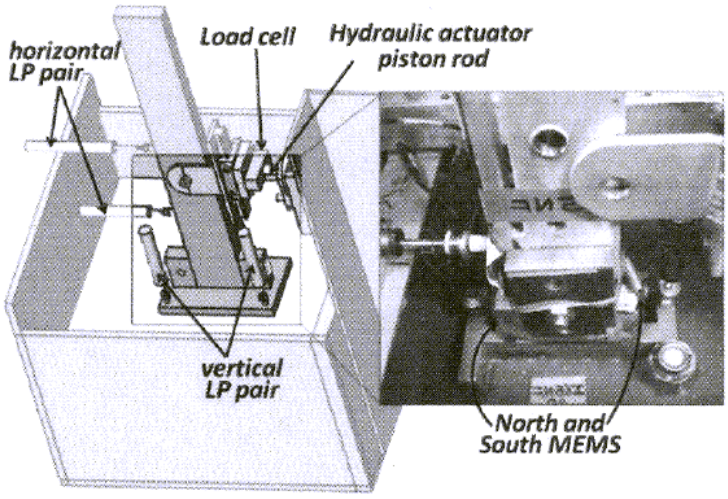

Figure 2.63 MAHS test series configuration and sensor layout. *(Hakhamaneshi and Kutter, 2015)*

Test Name	L (mm)	B (mm)	t_w (mm)	t_f (mm)	b (mm)	D (mm)	ρ_{ac}	Footing Notation
1.4_e_R_0.6	150	90			90	32	0.114	Rect_0.6
1.45_e_R_1.55	110	170			170	32	0.115	Rect_1.55
1.57_e_R_0.14	210	30			30	32	0.102	Rect_0.14
1.5_e_H50_0.11	150	75	26	17	17	32	0.098	H50NF
1.5_e_H50_0.17	150	75	19.5	25	25	32	0.105	H50NW
1.5_e_H35_0.13	150	75	39	20	20	32	0.109	H35NF
1.5_e_H35_0.26	150	75	20	39	39	32	0.109	H35NW
1.5_e_H65_0.09	150	75	16	13	13	32	0.091	H65NF
2_s_R_1.55	110	170			170	0	0.25	Rect_1.55
1.6_s_R_0.14	210	30			30	0	0.233	Rect_0.14
1.4_s_R_0.6	150	90			90	0	0.244	Rect_0.6
1.5_s_H35_0.26	150	75	20	39	39	0	0.286	H35NW
1.5_s_H35_0.13	150	75	39	20	20	0	0.294	H35NF
1.5_s_H50_0.17	150	75	19.5	25	25	0	0.323	H50NW
1.5_s_H50_0.11	150	75	26	17	17	0	0.323	H50NF
1.5_s_H65_0.09	150	75	16	13	13	0	0.385	H65NF

Figure 2.64 Footing properties. The length scale factor to convert results to prototype scale is 35. Values are reported in model scale. *(Hakhamaneshi and Kutter, 2015)*

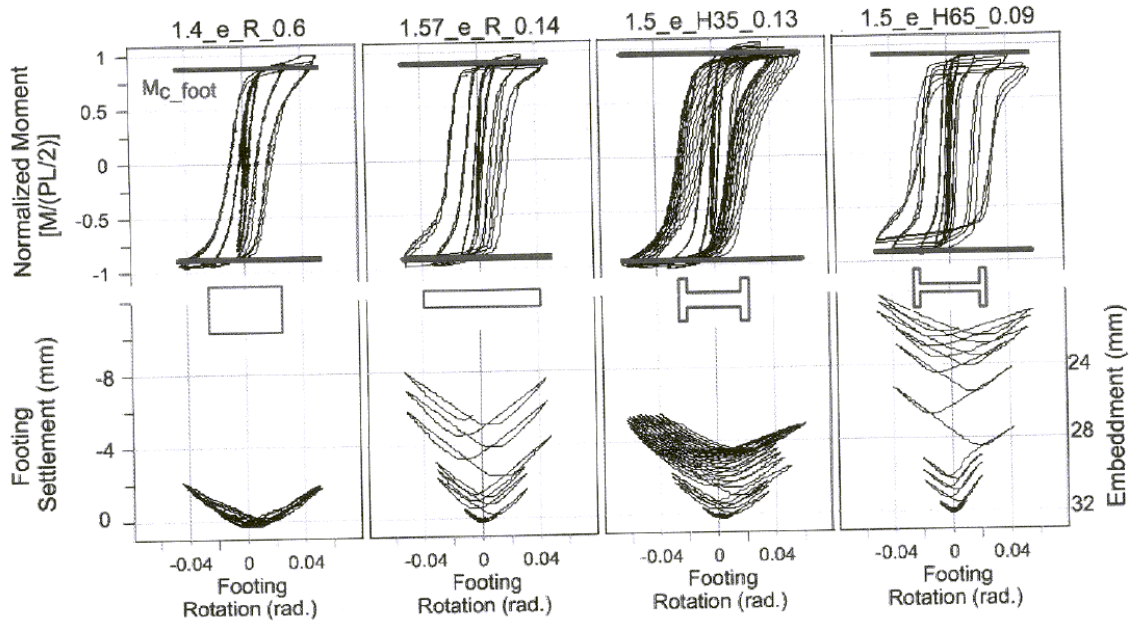

Figure 2.65 Moment vs. rotation and settlement (left axis) of embedment (right axis) vs. rotation for embedded footings, 0.091<ρa_c<0.125. *(Hakhamaneshi and Kutter, 2015)*

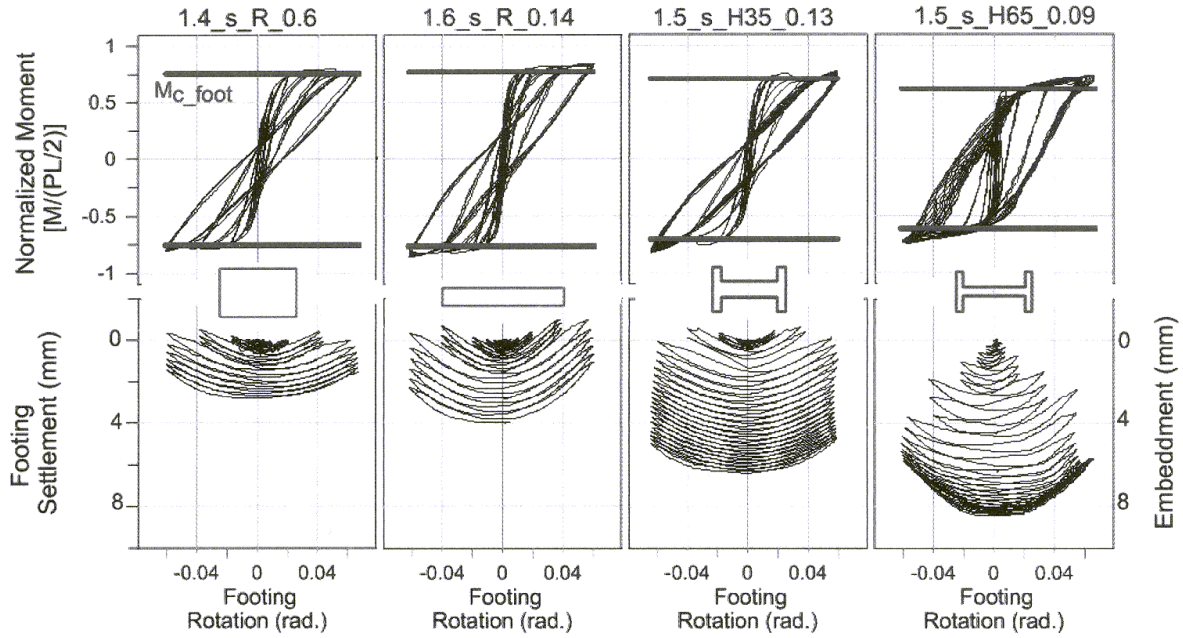

Figure 2.66 Moment vs. rotation and settlement vs. rotation for surface footings, 0.2<$\boldsymbol{\rho_{ac}}$<0.5. *(Hakhamaneshi and Kutter, 2015)*

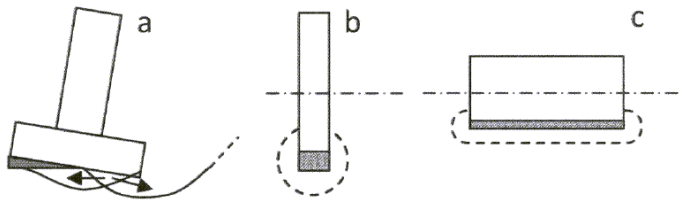

Figure 2.67 Settlement mechanism for long-narrow and short-wide footings. *(Hakhamaneshi and Kutter, 2015)*

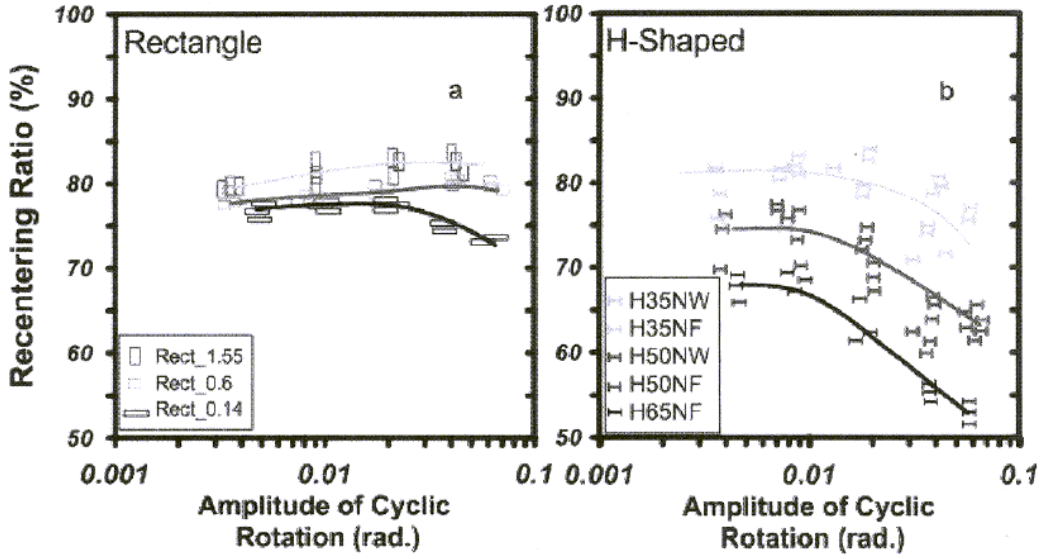

Figure 2.68 Recentering ratio vs. amplitude of cyclic rotation for 0.2<ρ_{ac}<0.5. (a) Surface rectangular footings and (b) surface H-shaped footings. *(Hakhamaneshi and Kutter, 2015)*

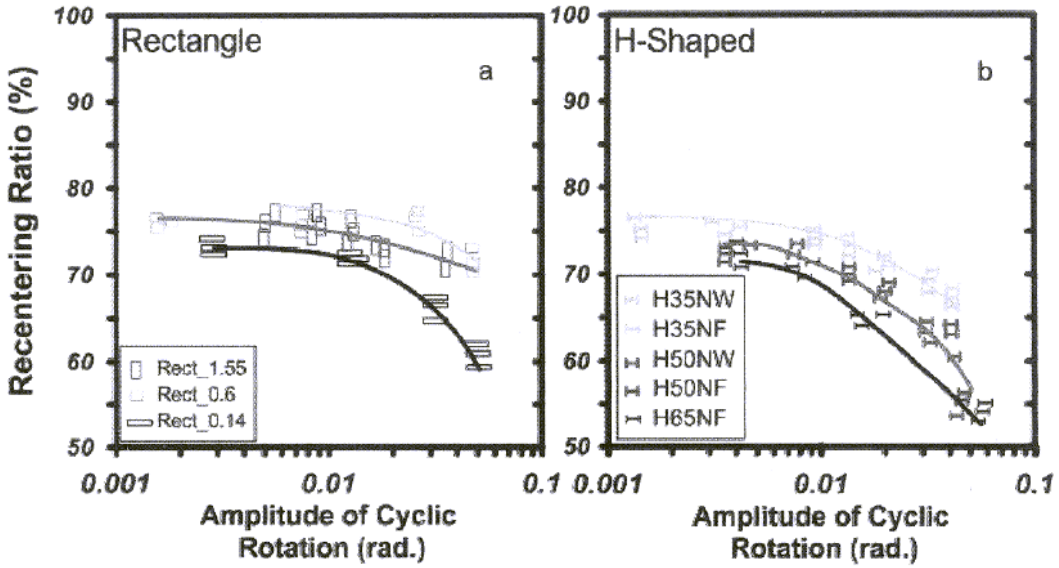

Figure 2.69 Recentering ratio vs. amplitude of cyclic rotation for 0.091<ρ_{ac}<0.125. (a) MAHS Embedded rectangular footings and (b) MAHS embedded H-shaped footings. *(Hakhamaneshi and Kutter, 2015)*

Test Name	L (mm)	B (mm)	D (mm)
1.55_s_R_0.6	150	90	0
1.55_c_R_0.6	150	90	20
1.55 e R 0.6	150	90	10

Figure 2.70 Test Series 2 - Footing properties. *(Hakhamaneshi and Kutter, 2015)*

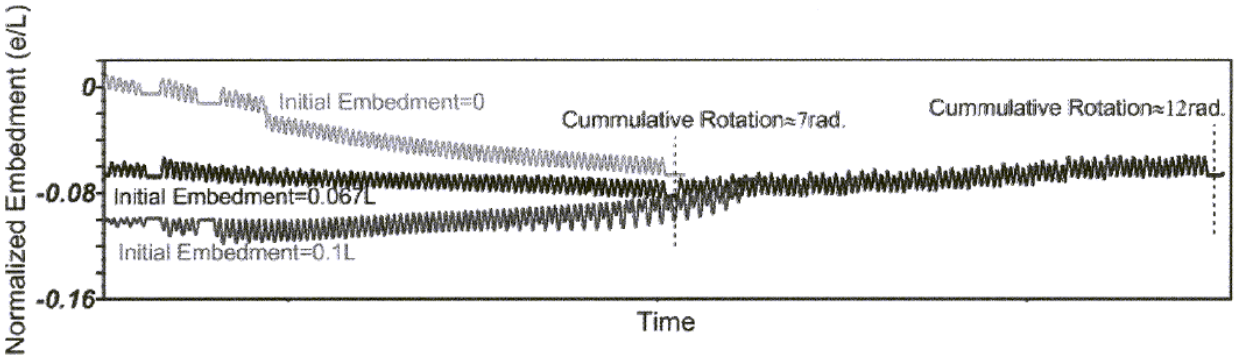

Figure 2.71 Evolution of embedment while many large cycles of rotation are applied to identical footings with different initial embedment. *(Hakhamaneshi and Kutter, 2015)*

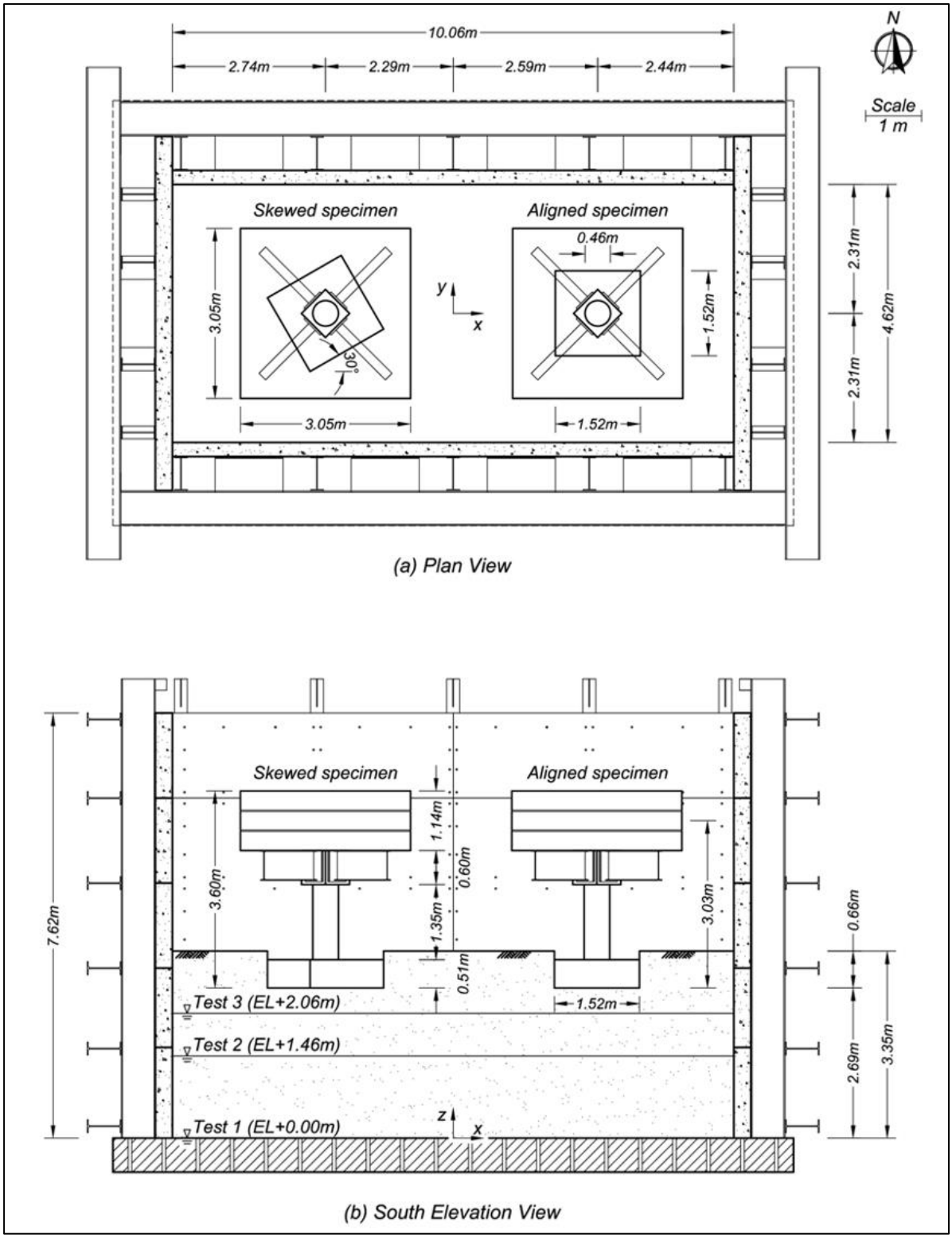

Figure 2.72 Basic geometric characteristics of the LSCB, the soil, and the bridge column specimens. The direction of shaking is along the East - West direction. **(a)** Plan view of the testing set up is represented, showing the exact location of the aligned and skewed specimens. **(b)** Elevation view of the test configuration depicting the soil, the water elevation for the different test days, and the elevation of the specimens. *(Antonellis et al., [2015])*

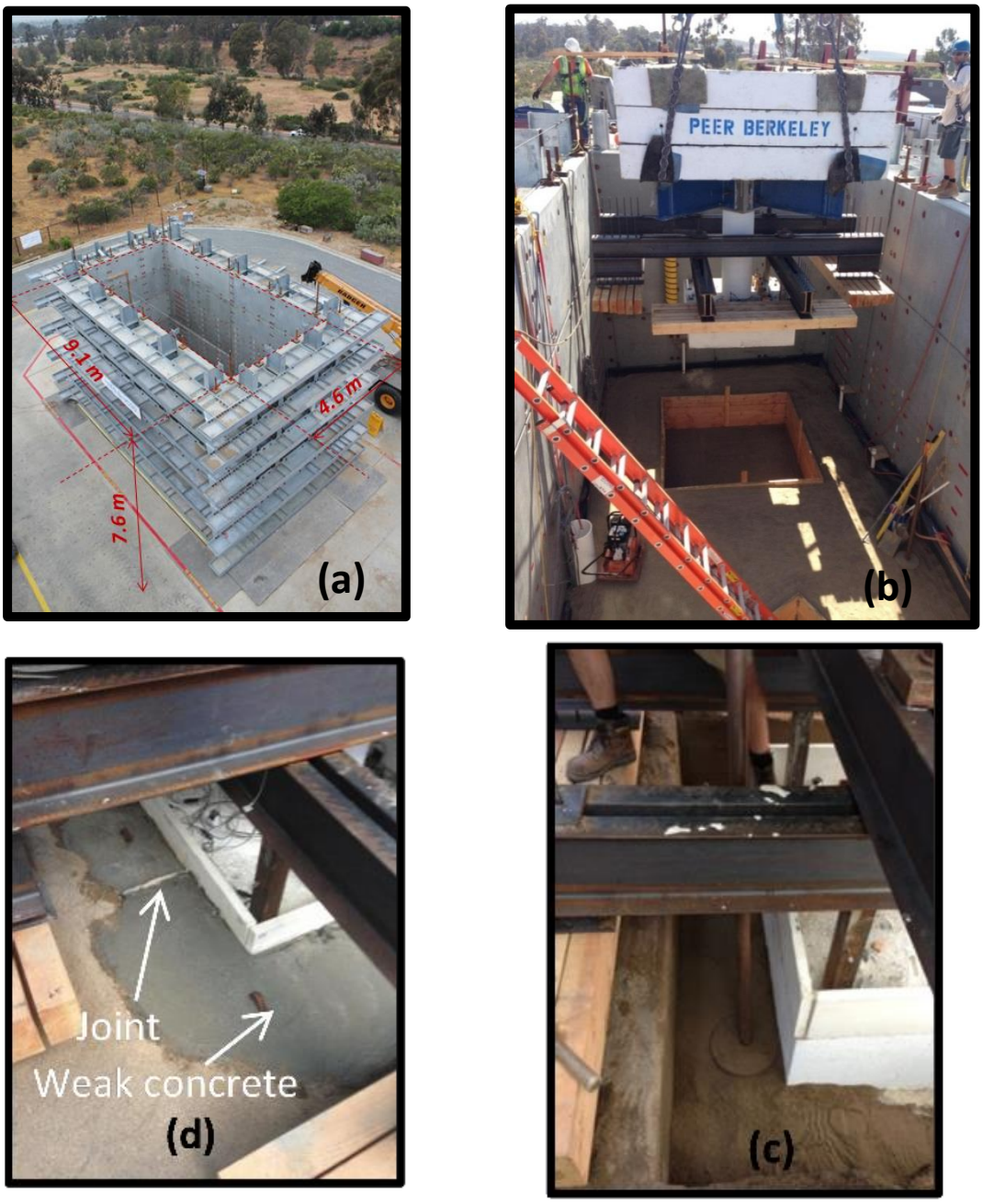

Figure 2.73 Photos of **(a)** the large soil confinement box (empty), **(b)** the placement of the aligned specimen before Test Day 1, **(c)** the backfilling and hand compaction of the sand in the vicinity of the foundation (Test Days 1 and 2), and **(d)** construction details around the footings for Test Day 3 only. *(Antonellis et al., [2015])*

Figure 2.74 (a) Full view of the tested set up **(b)** system of tapered timber beams fixed to the steel beams allow the "restraining system" to touch the sand surface when the footing rotations exceed values of 10 to 15%. *(Fox et al. [2014])*

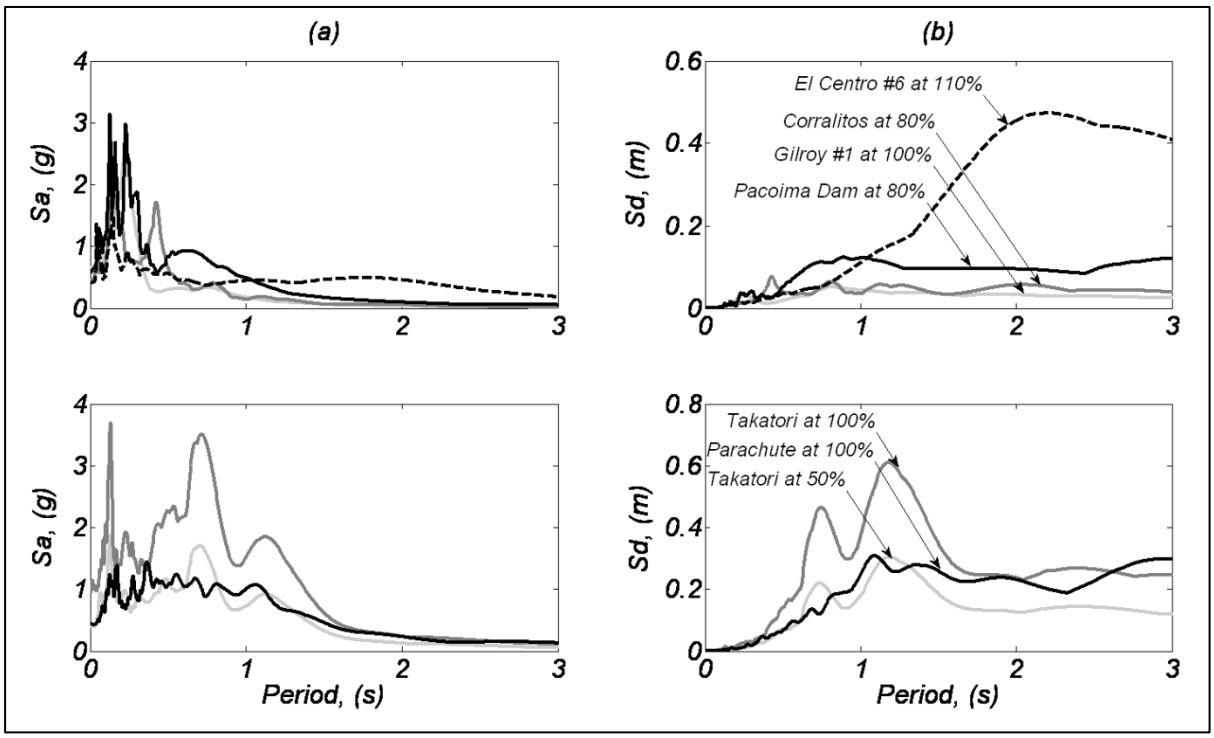

Figure 2.75 Linear elastic **(a)** acceleration and **(b)** displacement spectra for the recorded soil free field acceleration at the elevation of the base of the foundation in the direction of shaking (damping ratio ζ = 3%). *(Antonellis et al., [2015])*

Figure 2.76 The LHPOST at the University of California, San Diego. (*Source: http://nees.ucsd.edu/facilities/shake-table.shtml*)

Figure 2.77 LSCB at UCSD Englekirk Center side view *(Fox et al. [2014])*

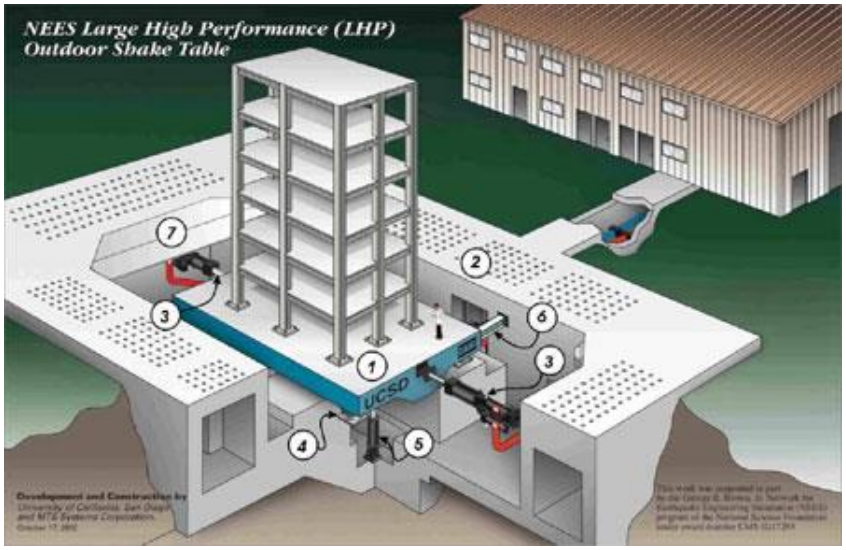

Figure 2.78 Operational components of the LHPOST at the UCSD. (*Source: http://nees.ucsd.edu/facilities/*)

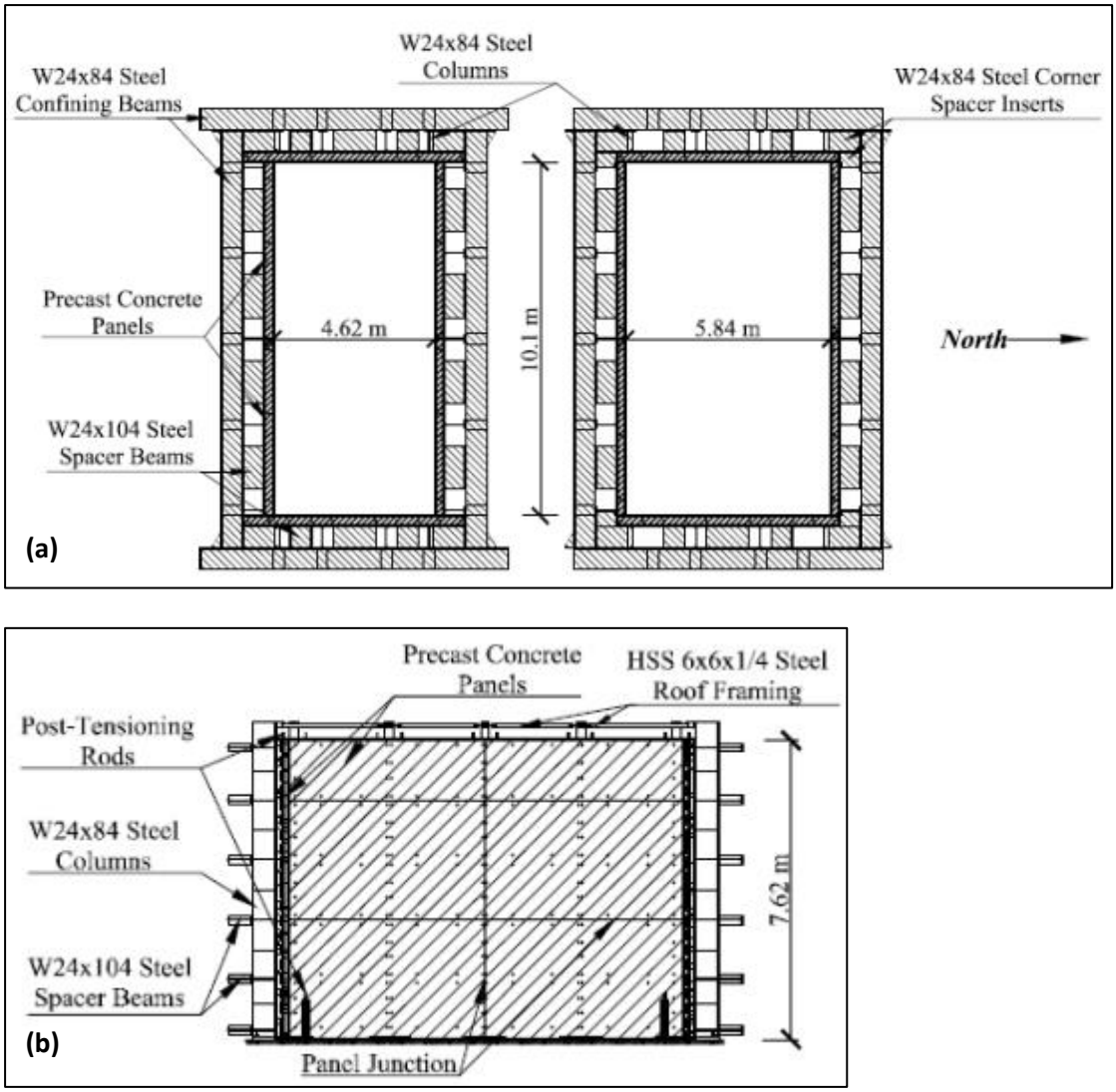

Figure 2.79 Structural diagrams of LSCB: **(a)** plan view (narrow configuration), **(b)** plan view (wide configuration), **(c)** profile view (longitudinal axis). *(Fox et al. [2014])*

Chapter 3

Chapter 3

Evaluation of Experimental Data and Simulation Assumptions

INTRODUCTION

In the previous Chapter we tried to provide an overview of the published experimental work on rocking isolation. An extensive description of the latest large scale shake table tests was also included. In this Chapter the main focus are the results recorded in Test Day 1, for the aligned footing. A comprehensive study is included which aims at interpreting the recorded response. The interpretation of these results is the guide for a consistent numerical simulation of the problem. Based on this judgment the assumptions for the numerical simulation of the problem are explained.

By means of nonlinear static and dynamic analyses the calibration of the model is performed, so as to validate its behavior against the exhibited response during the

experiments. Some conclusions are drawn from this procedure as well, concerning the consistency of the two methods: analysis and experiment. After all, as already pointed out, these two methodologies act in a way of cross-checking each other. After the FE simulations is validated against the experimental results, follows the presentation of the results for the skewed specimen.

Apart from the numerical investigation of the problem, an analytical approach, by means of pseudo static method is incorporated, so as the reader acquires a more spherical view of the investigated issue.

1. INTERPRETATION OF THE EXPERIMENTAL RESULTS

The large scale shake table tests performed in the large shaking table at the University of California, San Diego lasted three days. During the first day the system consisted of the two piers, founded on rocking footings, one of which was aligned with the direction of shaking and the other was skewed by 30˚. No water was included in the backfill soil this day.

Aiming at understanding the behavior of the tested system, we focus our attention on the results produced only for the aligned specimen. Due to the inherent limitations of testing in general (predetermined number of well-functioning devices used for instrumentation, limited amount of time, construction difficulties etc.) combined with the large scale adopted in the experiment (scale 1:3), the possibility to fully cover the response of the system is not realistic. However, a significant effort has been performed and the researchers extract from the tests the following data:

- Footing rotation: Defined as the peak primary footing rotation, measured about a horizontal axis normal to the primary shaking direction.
- Moment of the system: Defined as maximum dynamic footing moment demand, normalized by the rocking moment capacity of rigid base ($0.5P_{static}L$), with unimportant high frequency noise filtered out.
- Recorded horizontal acceleration in the primary shaking direction: measured at the walls of the confining box, utilized also as an input motion for the FE analyses.

The list with the utilized excitations is provided in **Table 2.2** and plots of the original records are provided in **Figure 3.1**. It is highlighted at this point that there is acknowledged difficulty in reproducing a seismic motion accurately with the shaking table. Apart from that, due to a defective accelerometer attached on the platen, the time history acceleration recorded by this accelerometer, cannot be trusted.

Indeed, after comparisons between the theoretical input and the one the shaking table, it was clear that this reproduction was not accurate enough. Apart from that, the recorded acceleration at the free field of the box (**Figure 3.2**), led to unrealistic comparison with the reproduced signal of the platen. Ultimately, it was found that the acceleration as it was recorded on the walls of the confining box was in much better agreement with the

recorded acceleration in the free field and thus it was decided by the researchers to define as base acceleration the one recorded at the walls of the confining box. From these accelerograms stem the values of imposed PGA in **Table 2.2**.

The study of the results follows and is performed observing the sequence of the consecutive excitations, so as to make clear the progressive change in the response, as each excitation succeeds the previous one. It is noted that the results are presented in a uniform scale, shedding light in this way to the gradual alteration in the response of the system. Nonetheless, for the first three seismic excitations, a larger scale is provided too, making visible in this way the details of the response. The results are studied in terms of $M - \vartheta$ and $w - \vartheta$ loops. Both settlements and rotations are provide in the text for each excitation separately, without taking into account any residual settlements and / or rotations from preceding excitations. The reader my find the accumulating values presented in the corresponding graphs. These plots provide insights concerning the macroscopic performance of the system, i. e. its maximum moment, rotation, and settlement. The plots showing the degradation of K_R, the rotational stiffness, as rotation progresses, provide valuable information concerning the *characteristic* stiffness of the system, which is ultimately on of the most integral factors controlling the response. Naturally, the rotational stiffness of the system reveals also information about the secant shear modulus of the system. Last but not least in the presented results are included the plots of the recorded acceleration at the walls of the confining box as well as a comparison of their elastic spectra against the corresponding ones of the recorded acceleration at the free field (elevation of foundation). It is clarified at this point that the *original* excitations have a longer duration, however only the significant pulses are studied herein, after having confirmed of course that the corresponding acceleration spectra remain unaltered by this modification in the duration of the motions.

1.1. Gilroy Array #1, (Loma Prieta, 1989)

Figure 3.3b presents the $M - \vartheta$ loops produced from the first seismic event. Macroscopically speaking, one would claim that the response of the system is practically elastic, since no permanent rotation is visible. As mentioned before, however, this scale may be misleading, since in a scale by an order of magnitude smaller, the response is clearly inelastic. The view in **Figure 3.3a** supports this notion. The loops are “broadened”, providing evidence of existing hysteretic damping. The backbone curve is also incorporated in the plot. The maximum rotational value recorded is approximately $3\ mrad$.

The most significant proof of the existing nonlinearity of the system is provided in **Figure 3.9a**. This plot and the respective ones which follow in the sequel, show the degradation of the rotational stiffness of the system, as rotation progresses. Each point is a loop, from which the rotational stiffness has been calculated. It is obvious that the system initiates its response at a very high elastic stiffness, which however lasts only a little. This is explained by the lack of points in the neighborhood of the corresponding “elastic” values.

On the other hand, there is significant accumulation of points in much lower values of K_R, almost 90% reduced!

In terms of settlements, in the uniform scale they are barely visible (**Figure 3.3d**), in the large scale though, a very limited settlement of about $0.6\ mm$ is recorded. Of course in this order of magnitude settlement is negligible, but for the sake of comparison all values are mentioned in detail.

The free field acceleration recorded in the middle of the box, at the elevation of foundation, is presented in **Figure 3.3e**, whereas **Figure 3.3f** plots a comparison of the elastic acceleration spectra of the input acceleration and the one recorded in the free field. Let's remember at this point that the box is rigid, and thus a movement like a solid body does justify the lack of any significant amplification in the response of the system. Nonetheless, there is noticeable exceedance of the input spectral values, in the range of high frequencies, which leads us to believe that the rather stiff soil formation filters the motion, intensifying the values at very low periods.

1.2. Corralitos, (Loma Prieta, 1989)

A similar behavior to the one described above is demonstrated also in this excitation. There is extraordinary difference in the plot of $M - \vartheta$ (**Figure 3.4a** and **b**) when presented in the magnified and the uniform scaled. The rotational amplitude is almost doubled, reaching a value of $5\ mrad$. We observe that the increased rotational values are accompanied by a rise in the achieved moment of the system. This leads us to believe, that the overall stiffness of the system has not changed significantly yet. The backbone curve is also incorporated in the plot.

To provide further evidence on that, the view in **Figure 3.9b** shows clearly that the elastic rotational stiffness of the system is very close to the one recorded in the previous event. Again, the system responds with its elastic stiffness only for some individual cycles, whereas the stiffness and by extension the shear modulus characterizing the system, are of much lower value. In fact, there is higher concentration of points in the area of low stiffness, compared to the previous event, which indicates that the system gradually becomes softer. This difference however is not that striking yet.

The similarity in the behavior is also noticed in terms of $w - \vartheta$ response. In the uniform scale (**Figure 3.4d**) the settlements are barely visible, a view which changes strikingly in **Figure 3.4c**, according to which the settlement reaches a maximum value of $1.0\ mm$. Again the value is considered negligible. It is worth noticing that t the curves start taking more clearly the characteristic V-shaped form, revealing the dominance of uplifting response. This is going to be even more obvious in the following events.

As reported also for the excitation of Gilroy Array, the comparison of the spectral values in **Figure 3.4f** reveals the rigidity of the box, on one hand; on the other hand, there is a clear surpass of the input values, in the range of high frequencies, again indicating the dynamic amplification of the soil formation.

1.3. El Centro, (Imperial Valley, 1979)

This excitation is a milestone in the sequence of the tested seismic events. Although one might comment on the fact that both the imposed and the recorded PGA are within a similar range, there is a remarkable difference in the response of the system during this event, noticeable in both the $M - \vartheta$ loops and the $w - \vartheta$ curves.

As far as the former is concerned, again we comment on the significance of the utilized scale, when plotting a graph, since an inappropriate scale may lead to false conclusions. Having said that, even in the reduced scale there is an obvious indication revealing the influence of a strong pulse affecting the response of the system. In the plotted graphs, this pulse creates the largest hysteretic loops forcing the system to exhibit a maximum rotation of about $9\ mrad$. The nonlinearity of the system is strongly underlined in this plot. The illustrated backbone curve in **Figure 3.5a** is much "smoother" than the previous ones, revealing the softening behavior of the system. It is worth mentioning however, that the maximum developing moment is again increased compared to the previously exhibited values.

To shed more light in this aspect of the response, we focus our interest in the plotted distribution of the rotational stiffness values as they fluctuate with the increasing rotation (**Figure 3.9c**). Observe that the elastic stiffness is again "felt" by the system only for singular cycles, whereas there is an astonishing concentration of rather low (almost by 90%) values in a range of also rather low rotations. This constitutes a change in the previously discussed $K_R - \vartheta$ plots. In the previous cases the significant degradation of the stiffness, was exhibited, as awaited, in large rotational values. Now the view is different, proving that the system has started demonstrating a more softened behavior, being dictated by a decreased rotational stiffness value.

Moving on to the settlement response, as shown in **Figure 3.5c**, the maximum vertical displacement reaches the value of $0.7\ mm$. Observe the shape of the curve, reveals an uplifting dominated response, since the residing settlements are insignificant. The maximum uplift is however limited, reaching the value of approximately $1.3\ mm$. The impact of the large pulse is evident here as well, since the response of the system is clearly non symmetrical, as the pulse pushes strongly the system toward one side. Observe however, that no accumulated rotation is noted, proving the recentering ability of the system.

As far as the recorded accelerogram is concerned, the deleterious pulse causing the aforementioned characteristics in the response is shaded in **Figure 3.5e**. This strong cycle has a period of $T_P = 0.36\ sec$ and amplitude $0.39g$. The amplification caused by this pulse is exhibited also in the spectral values of both, the input and the recorded accelerations (**Figure 3.5f**). In accordance with the previously reported results, the dynamic soil amplification is present also in this case.

1.4. Pacoima Dam, (Northridge, 1994)

From this point on, the plots are presented only in uniform scale, since the exhibited response values are significantly larger. Indeed, starting with the moment – rotation response depicted in **Figure 3.6a** the system exhibits for the first time maximum moment over $200\ kNm$ followed by a maximum rotation by an order of magnitude larger than before: $28\ mrad$. Observe that there is again one large loop, providing evidence of a strong pulse in the acceleration time history.

The clearly softened behavior of the system is confirmed by **Figure 3.9d** in which we observe that the elastic rotational stiffness of the system is remarkably, almost by 70%, decreased. It is worth noticing in this case as well, the extremely abrupt way, in which the dive in the rotational stiffness values occurs. Only for a few cycles does the system respond with this rotational stiffness, since it is again visible that there is a much higher concentration of cycles, in which the system behaves with its effective characteristics (shear modulus).

The response of the system in terms of settlement response has altered also significantly, since the clearly V-shaped $w - \vartheta$ curves reveal a striking $1\ cm$ uplift over a maximum settlement of $2.4\ mm$. The corresponding graph is presented in **Figure 3.6b**. Observe that the curves have a slight eccentricity, which leads us to assume that the system does not rock about a zero rotational angle, but rather it accumulates rotation toward one side. An a typical inelastic system, from now on it is expected that the system has obtained "bias" toward the side, where the accumulated rotations

The currently discussed seismic record is very well known for a high amplitude directivity pulse it contains. It has already been stressed out that elasto-plastic systems are extremely vulnerable in low frequency pulses. The shaded area in **Figure 3.6c** indicates the disastrous cycle of $T_P = 0.70\ sec$, which causes on one hand this impressive rotation to the system and on the other hand the aforementioned striking uplift. Observe that the period of this pulse is double than the one addressed for the El Centro motion. Thus, is proved the susceptibility of the system to large period cycles, since for the Pacoima Dam motion the rotation was increased by an order of magnitude (almost thrice higher). The effect of this strong cycle leaves its mark also in **Figure 3.6d**, where the comparison of the input and recorded acceleration elastic spectra is presented. Observe the effect of soil dynamic amplification in the area of low periods, in this case as well.

1.5. Takatori, 50%, (Kobe, 1995)

This seismic record is also a rather notorious one, known for its deleterious effect, which has been exposed and underlined several times in past research works. This excitation has only been scaled down by 50%, whereas its frequency content remained intact. By studying the recorded accelerogram (**Figure 3.7c**), we can locate two strong pulses of significant period and amplitude. The first one, shaded with grey, has $T_P = 0.70\ sec$

approximately and the second one follows shaded with purple, having lower amplitude and $T_P = 1.17\ sec$. The two distinguished peaks in the corresponding period values in the comparison of the elastic spectra show the effect of these two pulses in the acceleration spectral values of both the input and the recorded motion (**Figure 3.7d**).

Bearing in mind the preceding descriptions, the presented results are the awaited ones. To begin with, the $M - \vartheta$ loops shown in **Figure 3.7a** exhibit several broad cycles, proving a highly inelastic response, providing to the system a significant amount of hysteretic damping. The impact of the strongest pulse ($T_P = 0.70\ sec$) is evident, since it causes the largest loop, forcing the system to respond demonstrating a maximum rotation of $55\ mrad$, double that the recorded rotation during the previous motion. The maximum moment recorded remains in the area of $200\ kNm$. The inelasticity of the system is further proved by **Figure 3.9e**. The system practically responds almost exclusively with its effective rotational stiffness, already from small rotational values.

The $w - \vartheta$ curves have a more vivid V-shape and reveal a maximum uplift of twice as much as the one recorded during the Pacoima Dam motion. The uplift of $2\ cm$ is accompanied by accumulating settlements of $2.8\ mm$. The eccentricity in the center about which the rocking occurs, is evident also in this plot. As awaited, the system clearly shows a bias in its response, demonstrating larger displacements toward the side of accumulated rotations.

1.6. Takatori, 100%, (Kobe, 1995)

The frequency content of this excitation shall not be further discussed, since the only difference from the preceding one is that in this case the motion is used in its full amplitude. By studying the moment – rotation response, plotted in **Figure 3.8a**, we come across a rather distorted shape. It is obvious that the system suddenly, after the effect of an extremely intense cycle, sustains permanent rotation and continues responding in this deformed position. Note that the permanent rotation is recorded on the same side, where previously the rotations accumulated. The maximum recorded rotational value is almost $102\ mrad$ and the residual rotation is about $22\ mrad$. Other than that, it is worth commenting on the fact that the maximum developing moment reaches almost the value of $300\ kNm$, significantly larger than the respective recorded value in the previous motions.

The severity of this record is reflected clearly in **Figure 3.9f**, according to which the characteristic rotational stiffness of the system has diminished. Even the quasi elastic value, i. e the stiffness of the system for the first small rotational amplitudes, has dropped remarkably in comparison with the corresponding values during the Pacoima Dam and Takatori (50%) motions.

Figure 3.8b presents the settlement – rotation response, illustrating the aforementioned rotational behavior. The curves progress in two stages: the first one before the severe pulse, when rocking occurs about almost zero rotational angle, and the second, when rocking response occurs about a residing rotation of about $22\ mrad$. the impact of

the strong pulse forces the system to demonstrate an astonishing uplift of nearly $4\ cm$, whereas the maximum recorded settlement is approximately $0.5\ mm$.

At this point it is necessary to comment on a particular characteristic appeared on the $M - \vartheta$ graphs of the last three seismic records. Observe the change in the slope of the loops, when they reach their peak. At these points a noted overstrength makes its appearance, something which is visible almost exclusively in the largest loop of the response. A practical explanation is provided to account for this peculiar behavior. After careful observation of the videos recorded during the shake table tests, there was significant flow of sand material underneath the footing as the footing rocked. This is evidence enough to explain where the aforementioned overstrength comes from: As the footing rocks, as soon and the strong pulse occurs, it pushes the system so vividly, that a significant uplift occurs, thus permitting an appreciable amount of soil to fill the opened gap. As the footing continues its rocking movement, heading toward recentering and rotating to the other side, it finds increased resistance to complete its rotational motion, thus exhibiting the observed overstrength.

In the case of Pacoima Dam, which was the first seismic event leading to a clearly unsymmetrical response; we observed a slight eccentricity as far as the center of rocking is concerned. This eccentricity, caused by the impact of the strong large period pulse of the excitation, is accompanied by this characteristic change in the slope of the $M - \vartheta$ loops. Apparently, the effect of the falling sand material underneath the footing affected the response of the system, during this excitation. The same applies also for the next seismic event, Takatori (50%). The $M - \vartheta$ loops are excessively broadened due to this plasmatic overstrength, whereas the response continues being unsymmetrical, with residing rotational angles other than zero.

Especially for the last case of Takatori motion (100%) this pulse is so severe, that the accumulation of soil underneath the footing caused an irreversible rotation to the whole system, which from that point on continued working on this deformed condition. The phenomenon of the soil material accumulation underneath the footing during rocking has been addressed in other experimental works as well, (Deng and Kutter, [2012] and Deng et al., [2012]), stressing out similar effects. All in all, it is evident that this phenomenon hinders recentering of the system and increases the width of the hysteresis loops.

2. ASSUMPTIONS FOR THE SIMULATION

In order for us to be able to study the behavior of the system at hand, it was necessary to proceed with its numerical simulation. To this end the Finite Element Code "ABAQUS", is utilized. The target is the creation of a 3D numerical model, simulating the experimental set up as it was built. Below follows an analytical presentation of the simulation.

2.1. Geometry and Boundary Conditions

In terms of geometry, the experimental set up is simulated in a scale 1:1. In order to minimize the computational cost, only half of the actual system is included in the model. This means that the aligned and skewed specimens are checked in separate sets of analyses. Rocking in its nature is a rather local phenomenon, something which is also conspicuously proved by the deformed mesh of the analyses. For this reason it is assumed that there is no significant interaction to be accounted for between the piers. A snapshot of the model geometry is provided in **Figure 3.9**.

Appropriate boundary conditions have been considered, simulating plane - strain conditions, since this was the case for the boundaries created by the rigid confining box. For the analyses concerning the aligned footing, the motion is applied at the base and the transversal sides of the model. The longitudinal sides of the model are allowed to move only parallel to their direction. In this way we achieve the simulated motion of the model to resemble the one of the rigid box, during the experiments.

For the analyses concerning the skewed model, the motion is applied to all sides of the model, and is analyzed by 30˚ in two components, accounting in this way for the angle of the skewed footing. Moreover, an appropriate kinematic constraint has been implemented between the central nodes of the model and the peripheral ones, so as to move like a diaphragm. The application of the motion to all sides of the model ensures again that the model moves like the rigid box during the investigated experiments.

The lumped mass structure with the square footing depicted in **Figure 3.9** represents the bridge-pier foundation system. The pier is modeled with elastic linear beam elements of circular section, $D = 0.46\,m$, while the deck is represented by a mass element. Foundation is modeled with elastic solid 8-noded continuum elements (C3D8).

2.2. Soil Simulation

Soil is a sand stratum modeled with non-linear solid 8-noded continuum elements (C3D8). Two scenarios are taken into account concerning the constitutive model which characterizes the soil behavior. In the first case an equivalent von Mises model, described in Gerolymos et al., [2006] is utilized and in the second case the conventional Mohr – Coulomb failure criterion is tested. In both cases the soil is not homogeneous, but rather, its elastic modulus follows a parabolic distribution with the depth. The reason behind this check for both constitutive models is only to confirm their efficacy in our problem. In an effort to calibrate the numerical simulation so that it demonstrates behavior similar to the behavior of the “real” system, it is necessary to confirm whether one of these two models provides better results, and thus reflects more accurately the governing soil conditions during the experiments.

Initially, the elasto - plastic soil behavior is described with an extended von Mises yield criterion with non-linear kinematic hardening and associated plastic flow rule.

According to the extended pressure-dependent von Mises failure criterion (**Figure 3.10a**) is combined with nonlinear kinematic hardening and the associated plastic flow rule. This assumption is not valid for sand, the volumetric behavior of which largely depends on dilation. The evolution of stresses is defined as:

$$\sigma = \sigma_0 + \alpha$$

where σ_0 is the value of stress at zero plastic strain, assumed to remain constant. The parameter α is the "backstress" which defines the kinematic evolution of the yield surface in the stress space. The function F defines the pressure independent yield surface:

$$F = f(\sigma - \alpha) - \sigma_0$$

Where $F = f(\sigma - \alpha) - \sigma_0$ equivalent Mises stress with respect to the backstress α.

Given the associated plastic flow, the plastic flow rate is $\dot{\varepsilon}^{pl} = \bar{\varepsilon}^{pl}\frac{\partial F}{\partial \sigma}$, where $\bar{\varepsilon}^{pl}$ is the equivalent plastic strain rate.

The evolution law of the model consists of two components:

1. a nonlinear kinematic hardening component, which describes the translation of the yield surface in the stress space and is defined by the superposition of a purely kinematic term and a relaxation term (which introduces the nonlinear behavior), and

2. an isotropic hardening component, which describes the change of the equivalent stress defining the size of the yield surface σ_0 as a function of plastic deformation.

The isotropic hardening component defines the evolution of the size of the yield surface as a function of the equivalent plastic strain $\bar{\varepsilon}^{pl}$

$$\sigma_o = \sigma_0 + Q_\infty\left(1 - e^{-b\bar{\varepsilon}^{pl}}\right)$$

where Q_∞ and b are model parameters, defining the maximum change of the size of the yield surface and the rate of this change with $\bar{\varepsilon}^{pl}$, respectively. For $Q_\infty = 0$, the size of the yield surface remains constant and the model reduces to a nonlinear kinematic hardening model.

The evolution of the kinematic component of the yield stress is described by the expression:

$$\dot{\alpha} = C\frac{1}{\sigma_o}(\sigma - \alpha)\bar{\varepsilon}^{pl} - \gamma\alpha\bar{\varepsilon}^{pl}$$

Where C is the initial kinematic hardening modulus [$C = \sigma_y\varepsilon_y = E = 2(1+\nu)G_o$] and γ is a parameter determining the rate of decrease of the kinematic hardening with increasing plastic deformation.

The preceding equation is based on Ziegler's [1959] kinematic hardening law, in which the "recall" term $\gamma\alpha\bar{\varepsilon}^{pl}$ has been added to introduce the nonlinearity in the evolution law (Lemaitre and Chaboche, [1990]). **Figure 3.10b** illustrates the evolution of the two hardening components (kinematic and isotropic) for multiaxial loading. According to the evolution law governing the kinematic hardening component, the "backstress" α must be contained within a cylinder of radius $\sqrt{\frac{2}{3}}\frac{C}{\gamma}$.

Since the yield surface remains bounded, this implies that any stress point must lie within a cylinder of radius $\sqrt{\frac{2}{3}}\sigma_y$. At large plastic strains, any stress point is contained within a cylinder of radius $\sqrt{\frac{2}{3}(a^s + \sigma^s)}$, where σ^s is the equivalent stress defining the size of the yield surface at large plastic strain and a^s is the magnitude of α at saturation.

In the case of sand, the shear strength depends on the confining pressure and the friction angle φ. This pressure-dependency is incorporated in the model by defining the yield stress at saturation as a function of octahedral stress and the friction angle, as follows:

$$\sigma_y = \sqrt{3}\left(\frac{\sigma_1 + \sigma_2 + \sigma_3}{3}\right) sin\varphi$$

where σ_1, σ_2, and σ_3 represent the principal stresses. Accordingly, parameter γ can be expressed as:

$$\gamma = \frac{C}{\sqrt{3}\left(\frac{\sigma_1 + \sigma_2 + \sigma_3}{3}\right) sin\varphi - \sigma_0}$$

Parameter σ_0, which controls the initiation of the nonlinear behavior, is defined as a fraction λ (typically ranging from 0.1–0.3) of the yield stress σ_y:

$$\sigma_0 = \lambda\sigma_y$$

Figure 3.11 summarizes the parameters incorporated in the formulation of the proposed model.

As a second option the soil behavior is described with an elasto – plastic constitutive model, following the failure criterion of Mohr – Coulomb. In contrast with the aforementioned model, this one takes into account the dilatancy of the sand, but due to its bilinear law, it entails an underestimation of the hysteretic damping, provided by the cyclic soil behavior, in the range of small deformations, since in this range the soil behaves as an elastic material. On the other hand, for large shear deformations, the Mohr – Coulomb model tends to largely overestimate the damping offered by the cyclic soil behavior. Apart from that, there is no foresight in this model for the gradual degradation of the initial shear modulus and the increase of damping ratio as the shear deformations increase.

All in all, this constitutive model, neither does it simulate accurately the cyclic behavior of the soil, nor does it consider gradual reduction of the initial shear modulus G_o as the shear deformations increase. Yet, it would be an omission not to test the arithmetic model's behavior with this failure criterion as well. The exact values applied to the soil properties will be discussed in the sequel, for both scenarios.

The foundation is connected to the soil with special contact elements allowing for realistic simulation of possible uplifting of the foundation. The coefficient of friction is large enough so that sliding at the soil footing interface is prevented ($\mu = 0.7$). In each case material nonlinearity, emerging from the soil non-linear behavior and geometrical nonlinearities (P-Δ effects and uplifting) are taken into account.

2.3. Material Properties

The pier and the footing are assigned the material of "concrete", which is simulated as an elastic material with E = 30 GPa and ν = 0.20. The behavior of the material as an elastic one is prescribed in Antonellis et al., [2015], where it is clearly stated that the design of the column "ensured elastic response of the concrete column during rocking".

The simulation of the soil behavior, as mentioned above, is performed utilizing two approaches. Regardless of that though, one of the fundamental parameters, which needs to be determined, so that the right approach is adopted in the simulation of the backfill soil, is the initial elastic shear modulus, Go or G_{max}. Due to lack of experimental data, this parameter is determined by means of *reverse engineering*. To this end it is possible to prescribe this value by finding first the elastic rotational stiffness of the system. It is known that the equivalent stiffness in rocking is determined as the slope of the secant modulus of the appropriate $M - \vartheta$ monotonic response (pushover) curve.

$$K_R = M/\vartheta$$

For a footing bonded onto a homogeneous elastic halfspace, K_R is determined by the following expression by Gazetas [1991]:

$$K_R = \frac{3.60 * G * B^3}{1 - \nu}$$

This expression applies to a square footing, where B is the half the breadth of the footing parallel to the direction of loading.

Of course in most cases, where the soil formation follows an inelastic behavior and the SFS system has as well nonlinear nature, the aforementioned formula cannot be used, as soon as the system has entered its plastic region. In our case the non-linearity of the system stems almost exclusively from the separation of the footing from the supporting-ground surface (negligible sliding). In addition to that, the factor of safety against vertical loading $F_{sv} = 24$ dictates a purely uplifting – dominated response, but since the backfill consists of sand material and not clay, the nonlinearity plays an important role in the response of the system (Anastasopoulos et al., 2014).

Our interest focuses on the $M - \vartheta$ plots of the first two seismic excitations imposed on the system. It has already been commented on, that the scale of presentation may lead to false assumptions, thus these plots are provided also in a magnified scale (**Figure 3.3a**, **b** and **Figure 3.4 a**, **b**). It is obvious from the graphs in the uniform scale, that the response of the system is practically elastic. Of course after taking a look at the magnified scale, there is obviously non linearity present, which is evident also from the degradation of the rotational stiffness as the rotations progress (**Figure 3.3 g** and **Figure 3.4 g**).

Nevertheless, the non-linearity alone, demonstrated in the aforementioned plots, does not lead us to the assumption that the system has entered the plastic regime. We shall provide proof supporting this notion as follows.

According to Adamidis et al., [2013] and Anastasopoulos et al., [2014] a system with a high FS_v tends to be much stiffer in terms of its initial rotational stiffness (for very small

rotational values) compared to another system, with a lower FS_v, although the exact opposite is observed in terms of their moment capacity: a heavily loaded system has higher moment capacity than a lightly loaded one).

According to a comprehensive numerical parameter study, for a variety of rectangular and a circular foundation plans by Gazetas et al,. [2013] the following approximate relation is provided:

$$K_R \approx K_{R,elastic} * \psi(F_S) * \chi\left(\frac{\vartheta}{\vartheta_S}, FS_v\right) \quad \textbf{(3.1)}$$

In our case the purely-elastic stiffness referring to a square footing of width 2B is given by the following formula:

$$K_{R,elastic} = \frac{3.60 * G * B^3}{1-\nu}$$

The function $\psi\,(Fs\,)$ accounts for the initial yielding of the soil under solely vertical forcing (i.e., before any moment is applied) and is determined from the formula:

$$\psi\,(Fs\,) \approx 1 - \frac{0.8}{FS_v}$$

The parameter ϑ_S is the characteristic angle, at which uplifting initiates in lightly-loaded foundations *($FS_v > 10$)*. The validity of the following formula has been tested through trial and error for all other values of FS_v so that all the results plot within very narrow bands (Gazetas et al. 2013).

$$\vartheta_S = \frac{NB}{4 * K_{R,elastic} * \psi(FS_v)}\left[1 - 0.22\left(1 - \frac{1}{FS_v}\right)^2\left(\frac{B}{L}\right)^{0.2}\right]$$

Where, *B* = 2*b* for a square footing.

Finally, the χ function is given graphically in **Figure 3.12** in terms of ϑ/ϑ_S, with the static FS_v as a discretely-varying parameter.

It has to be underlined at this point, that the aforementioned relations have been extracted for a "typical clay" material, exhibiting the behavior which would fit well to the G – γ curve provided by Vucetic and Dobry [1991] with the utilization of PI = 30. Since the material at hand is very dense sand, with a relatively high confining stress at the elevation of interest ($125.5\ kPa$), it is assumed that the aforementioned expression be applied also in our case, without introducing significant inaccuracies. It is however an approximation in our solution.

Based on all aforementioned information, we study the cycles of the $M-\vartheta$ response corresponding to quasi-elastic response i. e. to very small rotation ϑ. For the first seismic excitation, Gilroy Array, the elastic rotational stiffness is calculated: $K_{R,elastic} \approx 420\ MNm/rad$ corresponding to a $G_o \approx 190\ MPa$.

It is observed that the quasi elastic rotation recorded during this motion is approximately $0.06\ mrads$. Interestingly, the characteristic angle ϑ_S for the investigated problem is estimated:

$$\vartheta_S = 0.2\ mrads$$

By applying the same procedure also for the second and third seismic excitations, Corralitos and El Centro, we reach the same conclusion: the system seems to behave in its elastic regime, despite the nonlinearity of its response. The results from these three excitations are summarized in Table 3.1.

From the graphs provided in **Figure 3.12** the resulting value of χ is equal to unity, which leads to the conclusion from the equation (3.1):

$$K_R \approx K_{R,elastic}$$

Following the aforementioned approximation, it is concluded that the initial shear modulus of the soil formation is:

$$G_{max} = 190\ MPa$$

However justified this value may be it is not of significant importance to us, since it is a value which is "felt" by the system only momentarily. Indeed, a detailed look in the progression of the $M - \vartheta$ loops verifies that the system practically responds with its secant modulus and be extension its effective rotational stiffness, for which of course the aforementioned formula cannot be applied.

For this reason, through a trial and error procedure, a value of:

$$G_o = 67\ MPa$$

which is almost one third of the "real" elastic value is selected. Our interest is focused at a depth right underneath the footing, since rocking affects only a shallow layer of the underlying soil. For this reason, the selected G_o refers to the depth of interest, were the confining stress is approximately $125.5\ kPa$.

Other than that, the specific gravity of the soil formation, as well as its peak friction angle are in agreement with the given values from the test report ($\gamma = 16\frac{kN}{m^3}, \varphi = 43^\circ, \nu = 0.30$). Especially for the case of the Mohr – Coulomb simulations, the dilation angle is assumed to be $\psi = 13^\circ$.

2.4. Soil Calibration

As already mentioned the sand used in this experiment is the Carroll Canyon type II ASTM C33 washed concrete sand. This material according to the literature has never been tested, in order for its exact mechanical properties to have been determined. Not being an experimental soil material introduces an inherent difficulty in determining its mechanical properties and in "understanding" its behavior. For this reason it is logical to assume that having determined the initial shear modulus of the soil formation is only a first step in the effort to reproduce the soil conditions in the confining box.

As a second step it has to be confirmed that the simulated soil behaves as typical sand under cyclic loading, which means that the system's secant $\boldsymbol{G}$ decreases in a controllable way, as the shear deformations progress. This leads us to the need of calibrating the aforementioned parameter $\boldsymbol{\lambda}$ of the von Mises constitutive model, for the specific soil to be simulated.

The calibration is performed by means of nonlinear dynamic analyses with the FE code "ABAQUS": Initially a hypothetical value is assumed for $\boldsymbol{\lambda}$. A single soil element confined in the depth of interest, is subjected to shear cyclic loading, of specific amplitude. The results provide us with hysteretic loops of shear stress against shear deformation, from which the damping ratio as well as the $G_{effective}$ are estimated. A typical graph depicting the hysteretic behavior of the soil element subjected to shear cyclic loading, is provided in **Figure 3.13**. The resulting values of $G_{effective}$ and damping ratio for the various amplitudes of shear deformation are plotted on the Ishibashi – Zhang, [1993] G – γ and ξ – γ curves, checking in this way the discrepancy from the targeted values. If the fitting is satisfactory, the value of λ is decided, otherwise a new value is hypothesized and the procedure is repeated. As shown in **Figure 3.14a**, for a selected value of $\lambda = 10$, and $G_o = 67\ MPa$, the achieved fitting in the targeted curves is satisfactory. The distribution of the elastic modulus of the soil formation with the depth is presented in **Figure 3.14b**.

Based on this assumption of the $G_o = 67\ MPa$, the secant G is applied as the shear modulus for the Mohr – Coulomb simulation. Thus we select a value of $G_{secant} = 22.30\ MPa$, which corresponds to one third of the selected G_o of the equivalent von Mises criterion.

3. VALIDATION OF THE NUMERICAL SIMULATION

According to Gajan et al., [2005] as a rocking system, founded on shallow foundations is dynamically excited, it accumulates vertical displacement which causes an involuntary embedment to the footing. In this way the further progression of the settlements is obstructed. If the footing area and vertical load remain constant as embedment increases, the tendency for horizontal sliding should decrease. Although the footing base friction remains constant, additional passive pressure is mobilized at the toe of the footing, for increasing embedment, providing more resistance to sliding. Thus the theoretical moment capacity, is calculated as:

$$M_{MAX} = \frac{L * V}{2} * \left(1 - \frac{1}{FS_v}\right) + P_p \frac{D}{3} + 2p_0 k \frac{D}{3} - P_a \frac{D}{3} \qquad \textbf{(3.2)}$$

In the same work they showed that the uplift of the footing, as rocking commences, leads to partial detachment of the footing from the supporting soil, thus creating a gap from one side of the footing and causing soil yielding on the other. The soil plastification contributes to further increasing the uplift. Consequently rocking response under high amplitude lateral loading, leads to "rounding" of the underlying soil. Following the same notion, the curved shape of the soil surface at the footing–soil interface enhances the uplift response reducing even more the footing–soil contact area.

The same occurs to a rocking system, during moment loading: the footing begins lifting off on either side of its contact, and progressively creates a curved soil surface

beneath the footing. As a result, the length of contact between the footing and soil decreases as the structure's rotation increases and as the curvature of the soil surface becomes more significant. The contact length not only reduces, but also moves along the length of the footing as the structure rocks, causing a nonlinear bearing pressure distribution in the soil beneath the contact length. The changing location of the resultant bearing pressure distribution with the rotation of footing, dictates the moment–rotation behavior.

To maintain stability (i.e. a factor of safety of 1.0 against bearing failure), for a given soil-footing system, a limiting minimum value of footing–soil contact length may be calculated. This contact length is defined as the critical contact length (L_c). The ultimate moment can be obtained when the contact length at one edge of the footing reaches its critical contact length. Considering the free body diagram at critical overturning illustrated in **Figure 2.4**, and assuming that the resultant of the bearing pressure acts at the center of the critical contact length, for a surface footing, the maximum moment is given by:

$$M_{MAX} = \frac{VL}{2}\left[1 - \frac{L_c}{L}\right] \quad \textbf{(3.3)}$$

where V is the total vertical load on the soil-footing contact and L is the footing length in the rocking direction, and L_c is the critical contact length. In fact, Equation (3.3) is similar to Equation (3.2) for surface footings, where active, passive and side soil pressures are not present.

It can be shown, using conventional bearing capacity equations, that for surface footings when $L_c \geq B$:

$$\frac{L_c}{L} = \frac{1}{FS_v} \quad \textbf{(3.4)}$$

Hence the moment capacity is not sensitive to soil properties if $L_c \,/\, L << 1$. It is sensitive to the relatively well know quantities of footing length and the vertical load on the footing. Equation (3.3) is simply based on statics and again is a derived hypothesis before it is validated by physical model tests. It is necessary that this hypothesis be verified not only by physical model tests, but also numerically.

3.1. System Moment Capacity

According to the test report by Antonellis et al., [2015], the moment capacities of the two foundations are determined based on the resistance provided by the underlying soil (Gajan and Kutter, [2008]) and the passive and frictional resistance at the leading side(s) of the footings. For the aligned footing, moment capacity is determined as:

$$M_{c,foot} = \frac{Q * B}{2} * \left(1 - \frac{A_c}{A}\right) + P_p * \frac{D}{3} + k * P_p * \frac{B}{2}$$

where Q is the applied vertical load at the base of the footing, B is the side dimension of the footing parallel to excitation axis, P_p is the passive earth force, D is the embedment depth and k is the concrete-soil friction coefficient, corresponding here to two-thirds of the constant volume friction angle, φ_{cv}. The term $\frac{A_c}{A}$ is discussed in the sequel.

The calculated moment capacity of the aligned foundation is $229\ kNm$ and $252\ kNm$ for the skewed.

The next step in the adopted methodology is the validation of the numerical simulation against the performed experiments. In order for the numerical model to be validated, nonlinear static and dynamic analyses have taken place, utilizing the FE code "ABAQUS".

By means of static nonlinear pushover analysis, the moment capacity of the aligned and skewed system is verified taking into account the soil – structure interaction. This analysis has been performed considering both the von Mises constitutive model and the Mohr – Coulomb failure criterion for the aligned specimen, whereas for the skewed specimen only the von Mises constitutive model is utilized.

For the aligned specimen the results are plotted in terms of lateral force against the imposed displacement in **Figure 3.15a** for the equivalent von Mises constitutive model and **Figure 3.15b** for the Mohr – Coulomb failure criterion.

In the former case, with the "von Mises" approach the achieved moment capacity of the system is found:
$M_{cap} = 173.30\ kNm$ corresponding to a $P_{ult} = 57.21\ kN$,
whereas in the latter case, with the "Mohr – Coulomb" approach the achieved moment capacity of the system is found:
$M_{cap} = 219.76\ kNm$ corresponding to a $P_{ult} = 72.53\ kN$.
The discrepancy from the corresponding results in the test report is: 32% and 4.2% respectively.

For the skewed specimen the von Mises constitutive model gives results, which are in good agreement with the targeted values. The moment capacity of the system is found: $M_{cap} = 211\ kNm$ corresponding to a $P_{ult} = 69.6\ kN$. The discrepancy from the targeted value of $252\ kNm$ is approximately 16%. **Figure 3.18** presents graphically the progression of the pushover analysis in terms of lateral force – displacements, until the stage when the analysis reaches a plateau.

3.2. Natural Period of the System

The theoretical fixed base fundamental period of the test specimens for uncracked concrete is:

$$T_{FIXED} = 0.29\ sec$$

This value has been calculated considering a fixed based single – degree – of – freedom pier with the same geometry as the one of the tested specimens. In other words:

$$K = \frac{3EI}{h^3}$$
$$I = \frac{\pi D^4}{64}$$
$$h = 2.52\ m$$
$$M = 25.5\ Mgr$$
$$D = 0.46\ m$$

For system identification purposes in the framework of the herein investigated experiments, white-noise motions were used before and after every earthquake ground motion. The white-noise input motion had duration of 300 s and 0.05-*g*-root-mean-square (RMS) amplitude of acceleration. As shown in **Figure 3.16** the initial natural period of the system for the first day of the experiments, is measured:

$$T_{SSI}^{aligned} = 0.60\ sec \text{ and } T_{SSI}^{skewed} = 0.50\ sec,$$

for the aligned and the skewed specimen respectively.

The natural period of the system accounting for the SSI effects, is verified by utilizing the results provided by the pushover analyses. In **Figure 3.17 a** and **Figure 3.17 b** the natural period of the aligned system is depicted against the imposed lateral displacement. Observe that close to failure, the natural period tends to an infinite value. This behavior is expected of course; since at this point the system tends to overturning and thus its stiffness becomes negligible. The estimated initial natural period of the system, in both soil simulation approaches, is in excellent agreement with the experimental results, since the natural period from the pushover analyses is found to be also:

$$T_{SSI} = 0.60\ sec$$

Figure 3.19 a and **Figure 3.19 b** provides a view of the deformed mesh, showing with contouring the soil plastifications, at the failure stage of the nonlinear static pushover analyses. Observe the rather limited affected area for the case of Mohr – Coulomb, where the plastifications are much more local than in the case of von Mises criterion. In the latter case the failure mechanism is obvious and fully developed.

Following the same procedure, we estimate the natural period of the skewed system. From **Figure 3.18** and for the elastic branch of the graph, it is estimated that the natural period from the pushover analyses reaches the value of:

$$T_{SSI} = 0.50\ sec$$

which is in agreement with the calculated value in the test report. **Figure 3.20(a)** provides a plot of the deformed mesh of the nonlinear static pushover analysis for the skewed specimen, showing with contouring the soil plastifications, at the stage of plateau **Figure 3.20(b).**

In an effort to get a better understanding of the interaction between the two footings and the underlying soil, we examine further the results stemming from the nonlinear static pushover analyses. **Figure 3.21 (i)** provides a plot showing with contours the distribution of maximum vertical traction at the same applied displacement for the aligned (**Figure 3.21 (a)**) and the skewed specimen (**Figure 3.21 (b)**). The displacement value for

Figure 3.21(i) corresponds to the stage of plateau (right before the decreasing branch), in both cases. Observe that the effective area for the aligned footing is approximately: $\frac{B^2}{10}$ whereas for the skewed is slightly larger: $\frac{B^2}{6}$. For this reason we conclude that the average effective stress for the former case is slightly larger compared to the latter, given that the vertical load in both cases is the same. On the other hand we notice that the maximum developing stress is almost twice as high for the skewed footing compared to the aligned.

The same plots are presented in **Figure 3.21 (ii)** for **(a)** the aligned and **(b)** the skewed footing and refer to the initial (quasi elastic) values of vertical traction. It is noted that the value of maximum vertical stress is developed approximately at the same total imposing displacement, thus the results from the two footings are comparable. **Figure 3.21(iii)** presents again the distribution of maximum vertical traction, at an intermediate stage, when the developed rotation of both footings is approximately $10\ mrads$. As it will be discussed below, this rotational value does not lead to uplift neither of the two footings, hence we would expect a slightly milder stress concentration. However, the view is different, since it is obvious that although the effective traction are distributed to comparable areas, the maximum stress for the case of the skewed footing are restricted to a rather limited area, hence leading to 0.65 MPa the skewed and 0.50 MPa the aligned footing.

Figure 3.22 presents the comparison of the maximum developing stress as it progresses with increasing displacement (the same for the aligned and skewed footing). It is clearly shown that the skewed footing strains the underlying soil in much more intense way, leading the system to develop almost twice as high vertical stress as the aligned one. This view is corroborated by the plots presented in **Figure 3.23**. The plots include the results from the nonlinear static pushover analyses performed with the equivalent von Mises constitutive model. **Figure 3.23a** and b illustrates the $M - \vartheta$ relation for the aligned and skewed footing respectively. Observe that the skewed footing demonstrates slightly higher moment capacity, which can be attributed on one hand to the fact that the skewed footing is characterized by a slightly larger width: $B_{eff} = B/\sqrt{\frac{3}{2}} = 1.76\ m$ and on the other hand it is possible that the confinement offered by the soil at the edge of the embedment, instead of the side, enables more effective contribution of the embedment (resistance) to the response of the footing, hence adding strength to the system.

Figure 3.23c compares in $w/B - \vartheta$ terms the response of the aligned (orange line) and the skewed (blue line) footing. The settlement is normalized to the width of the footing in order for the results to be comparable. As already explained, the effective width of the footing is different in the two investigated cases: aligned and skewed by 30˚. Thus, the settlement values are divided by $B = 1.52\ m$ for the former and by $B = 1.76\ m$ in the latter case. Observe that the skewed footing has clearly a tendency for further settling compared to the aligned one, since the imposed rotation required for uplift is larger for the skewed footing compared to the aligned. Two factors account for this behavior:

❖ The skewed structure is characterized by a slightly lower slenderness ratio, since as mentioned before; the effective with of the footing is slightly larger (1.76m instead of 1.52m). Thus the same imposed displacement leads to smaller developing rotation for the skewed than the aligned footing.

❖ As shown in **Figures 3.21 (i)** and **(iii)** there is tremendous concentration of stress in the underlying soil of the skewed footing, during almost the whole range of imposed displacements. Despite the fact that the effective areas of both footings are comparable, the extremely localized maximization of vertical traction in the case of the skewed structure causes the footing to practically penetrate the underlying soil, thus leading to an overall sinking tendency. Observe that this tendency does not necessarily make its present as soon as uplift commences, but as already discussed, even for a lower rotational value (**Figures 3.21 (iii)** for which both footings settle, again the vertical traction imposed on the underlying soil by the skewed footing surpass the ones of the aligned.

Figure 3.23d confirms that the imposed rotation on both systems is the same, with the aligned having a little lower stiffness and thus leading to slightly higher rotation, for the same imposed displacement. Of course, as discussed previously, the response of the two systems on the same imposed rotation is strikingly different. This behavior: more sinking dominated for the skewed specimen compared to the aligned one is expected to be met also in the results of seismic analyses.

3.3. Soil Bearing Capacity

For the estimation of ultimate bearing pressure and bearing capacity factors the researchers have utilized classical equations (Salgado, [2008]), depth factors (Brinch Hansen, [1970]), shape factors (Vesic, [1973]) and inclination factors (Meyerhof, [1963]). For both cases, the corresponding peak friction angles are practically same and equal to 44.3˚. Peak friction angle was estimated from Bolton's [1986] empirical equation for triaxial compression conditions with assumed fitting parameters of $Q = 10$ and $R_Q = 1$. The representative mean effective stress is determined from De Beer, [1965]. The ratio of the bearing capacity in purely vertical loading to the static vertical load $FS_v = 23.9$, for both specimens based on a peak friction angle of 42.1˚.

Taking the aforementioned methodology by Gajan et al., [2005] one step further, the critical contact area of the footing is defined as the area which must remain in contact with the underlying soil to support the vertical loads acting on the soil-footing interface. According to Deng and Kutter, [2012], when the critical contact area ratio, $A/A_c > 8$, residual rotations are small and settlements are less than $0.01B$ for cumulative rotations up to $150\ mrad$. On this precept is founded the design of the footings. The critical contact area, *Ac*, is determined as described by Deng and Kutter [2012], following an iterative procedure, overlooking the influence of apparent cohesion in the sand due to moisture. For the skewed footing, the triangular shape of the critical contact area and its rectangular idealization for bearing capacity estimation was based on Highter and Anders [1985]

equations for two-way eccentricity. The critical contact area ratios, A/A_c, before Test Day 1 are equal to $\frac{A}{A_C} = 11.30$ for the aligned and $\frac{A}{A_C} = 13.50$ for the skewed footing.

At this point we have to comment on the evident discrepancy between the *calculated* $FS_V = 24$ and the one proposed by Gajan et al., [2005] regarding the soil bearing capacity in rocking expressed as $\frac{A}{A_C}$. This significant difference may be attributed to the overestimation of the bearing capacity by the analytical expressions, when the friction angle has values so high (over 40˚). Only as an indicative value it is mentioned that the analytical expression by Meyerhof estimates a safety factor of $FS_V = 30$.

In an effort to calibrate the arithmetic simulation also in terms of bearing capacity, nonlinear static pushdown analyses have been performed. For these analyses, again both soil simulation scenarios were taken into account.

For the constitutive model of the equivalent von Mises, the bearing capacity is found:

$P_{ult} = 3500\ kN$, leading to an $FS_V = 12$.

On the other hand, the failure criterion Mohr – Coulomb seems to lead to a much higher bearing capacity, reaching the value of:

$P_{ult} = 15000\ kN$, leading to an $FS_V = 50$.

In **Figure 3.24a** the failure mechanism for the von Mises constitutive model and in **Figure 3.24 b** is shown the failure mechanism for the Mohr – Coulomb criterion. For both cases we notice that the mechanism has not developed fully due to boundary limitations. The arising issue at this point is the following: The proximity of the boundaries in the case of Mohr – Coulomb is also tampering the failure mechanism, apart from preventing its full development. Due to the transverse boundaries being restrained in the transverse and vertical direction, the tendency of the soil to “push” laterally is also obstructed. Thus it comes as a logical assumption that the Mohr – Coulomb failure criterion in the case of push down analysis overestimates the safety factor in vertical loading. On the other hand, the von Mises constitutive model seems to underestimate it. At this point it has to be highlighted, that the “omission” of the dilatancy from this failure criterion, as a key parameter controlling the soil behavior, influents significantly the results in the push down tests. The obstructed tendency of the soil to swell due to external loading provides strength to the soil skeleton. Hence it is logical for the case of the equivalent von Mises constitutive model to underestimate the bearing capacity of the soil formation, since the sand dilation is not accounted for. Further discussion concerning the simulated bearing capacity versus the one achieved in the experiments, follows in the sequel.

4. ANALYTICAL VALIDATION OF THE EXPERIMENTAL SETUP

Bearing in mind the advantages (correct simulation of the geometry and stiffness of the system) and shortcomings (simulated bearing capacity) of the numerical model, as they are revealed by the static nonlinear push-over and push-down analyses, the next step is to check the behavior of the FE simulation, against the same seismic loading, which was utilized in the shake table tests. In this way we gain valuable insight about the weaknesses of the arithmetic model, concerning its overall dynamic behavior.

As already mentioned, the input of the analyses coincides with the recorded accelerogram at the walls of the confining box. The box is rigid, thus this selection offers a dual advantage; first the accurately reproduction of the base motion, due to its rigidity, and secondly the bypass of the inaccurately recorded motion by the shaking table. It is underlined at this point that the six consecutive excitations utilized in the experiments are imposed as successive seismic loading in the same sequence also in the arithmetic model.

Taking advantage of the geometric simplicity of the aligned specimen, we examine the results only for the aligned model in terms of $M - \vartheta$ and $w - \vartheta$ curves as well as in terms of the system's rotational time history, in order to calibrate further our numerical simulation. It is decided to investigate the correctness and consistency of the arithmetic simulation macroscopically, by checking the response of the system, rather than focusing on the superstructure. After all, in the majority of the published literature dealing with similar experiments (refer to Chapter 2) the same philosophy is adopted adopt as a way of approaching the problem.

Each seismic motion is investigated separately, which means that the response values from each seismic event do not include the residual values from the preceding excitations. The corresponding results produced for each soil simulation scenario (von Mises approach and Mohr – Coulomb approach) are plotted next to each other, so that the comparison is easier and more direct. Each graph presents simultaneously both the experimental and the analytical outcome, so that the validation of the arithmetic simulation is more accurate. It is underlined that the scale for each set of graphs corresponding to the same excitation is the same, so that the comparison is more effortless. On the other hand, *different* scale has been utilized when plotting the results of different excitations, so that a clearer and more detailed view of the results is preserved.

Starting with the first excitation, the Gilroy Array motion, we notice a satisfactory fitting of the $M - \vartheta$ loops and the rotational time history. The consistency in terms of hysteretic loops confirms that the selection of the secant G is logical, whereas the good agreement in time history terms assures us that the dynamic and inertial characteristics of the system are also consistent with the corresponding ones in the experiment. The only parameter which seems to follow a different behavior than the tested system is the settlement. Already from the first motion there is evident uplift during the tests, whereas in the case of the analytical response the vertical displacements seem to accumulate. The discrepancy in absolute terms is not exaggerated, since in both cases the settlements are of

the same order of magnitude. In fact in the scale of millimeters, settlement is considered negligible, thus even though there is a significant difference in the results; we consider this inconsistency to be of minor importance.

For the same motion, the Mohr – Coulomb failure criterion is again in good agreement with the experimental results in terms of the stiffness of the system. However, there is significant difference in the breadth of the loops, i. e. the provided by the system hysteretic damping. The developing rotations seem to be almost twice as high as the ones during the experiments, whereas a slightly worse fitting is observed for the rotational time history. As for the measured settlements, they are in rather good agreement with the ones in the experiments. The results for the Gilroy Array motion stemming from both the von Mises and Mohr – Coulomb simulation are provided in **Figure 3.25a**, **b** and **c**.

The outcome of the analyses for the second seismic motion (Corralitos) is provided in **Figure 3.26 a**, **b**, and **c**. Again we notice a surprisingly good agreement in the moment – rotation loops between the experimental and the analytical results, with only a minor discrepancy in the maximum measured moment. The rotational values are also consistent with the respective ones produced in the shake table tests. We notice the altered effective mechanism in the simulation describing the progression of the settlements. In the case of the FE analyses, the settlements seem to accumulate ('sinking" response), whereas during the experiments the behavior is uplifting dominated.

This situation is significantly different in the case of the Mohr – Coulomb criterion. The response in this case is strikingly similar to the one observed in the confining box. The purely uplifting dominated response is exhibited at a cost of almost twice as high rotations as the targeted ones, whereas in terms of the frequency content of the motion, the results are considered satisfactory. The hysteretic loops are again much smaller than the experimental ones, revealing a system behavior much more elastic than it was in the tests.

Figure 3.27 shows the outcome of the analyses for the El Centro seismic motion, which is the third consecutive excitation. As far as the von Mises simulation is concerned, apart from a slight overrun in the value of maximum moment, the $M - \vartheta$ loops fit very well to the experimental ones. Interestingly, despite the "sinking" behavior which is evident in this case too, the settlements are much more limited for this excitation, half the value of the Corralitos' settlements. Such behavior is underlined also in a number of experimental works, some of which have been cited also in Chapter 2 (Drosos et al., [2012], Anastasopoulos et al., [2012], Tsatsis and Anastasopoulos [2015]). In this excitation there is a long period pulse, which according to the literature, acts in favor of limiting the accumulation of settlements for two reasons:

- Due to the vulnerability of the rocking systems in long period pulses, the uplifting is more intense. Consequently, the limited accumulation of settlements is attributed to the shallower stress bulb generated for larger rotation values, since the foundation is in limited contact with the supporting soil.

❖ The strong long period pulses cause rapid compaction of the underlying sand, as the specimen re-centers, thus diminishing the further accumulation of settlements, as the motion progresses.

Of course in our case, neither of the constitutive models simulates the dynamic densification of the sand. Therefore this improvement in settlement accumulation is attributed to the first point described above. Again, the rotations are in very good agreement with the targeted ones. Notice that at the end of the motion, the specimen does not re-center completely, but rather it ends up with an irreversible rotation.

The view in the Mohr – Coulomb results is less promising, since we observe clearly almost triple developing rotations, than the ones recorded experimentally. The loops are again narrower, something which explains the significantly amplified rotational values. On the other hand we cannot overlook the remarkably better behavior, clearly uplifting dominated, in terms of settlements demonstrated in the simulation for the MC failure criterion.

Moving on to the fourth seismic excitation (**Figure 3.28**), the one of Pacoima Dam, it is evident that ABAQUS cannot reproduce the effect of the falling soil material underneath the rocking footing. Thus no change in the slope of the $M - \vartheta$ loops is noticed in the arithmetic simulation results. This is the only deviation of the analytical outcome compared to the experimental one, in terms of rotations and moments. Of course there is again the inconsistency of the settlement behavior, which is "sinking" dominated. However, observe that the maximum settlement in this excitation is almost as high as the one measured during the second excitation, which was less severe and shorter in duration. This leads us to assume that the settlements are again limited comparing with the ones measured for the first two excitations. The explanation of this phenomenon has again to do with the frequency content of the excitation, since the Pacoima Dam record contains a strong low frequency pulse, thus forcing the footing to excessive uplifting. Observe that there is accumulated rotation (toward the negative rotational values) at the end of the motion, which will play crucial role in the next two motions.

The most remarkable characteristic in **Figure 3.28** concerns the analytical results stemming from the Mohr – Coulomb analyses. Observe in the $w - \vartheta$ curves the remarkable effect of dilation, leading to significant swelling of the soil and by extension to significant uplift. The rotational values are once more overestimated in the arithmetic model and the hysteretic loops are again much narrower.

The outcome of the fifth excitation is presented in **Figure 3.29**. This is the first excitation, for which the shape of the $M - \vartheta$ loops for the von Mises soil simulation is significantly different from the one reflecting the experimental results. Obviously, the inability of the specimen to completely re-center at the end of the third and fourth excitations has a significant effect on its response in the Takatori motion (de – amplified by 50%). The inconsistency lies in the fact that during the experiments such major plastic rotation is not witnessed until the last motion. Nonetheless, this difference has to do mainly with the simulated soil being much more compliant, with decreased bearing capacity,

compared to the backfill soil in the confining box. Apart from this shortcoming, the frequency content of the rotational response, as well as the rotational values are in fairly good agreement with the achieved experimental values.

The view provided by the Mohr – Coulomb simulation seems again disadvantageous comparing to the former one. The dilation causes further swelling of the soil, leading in this way in positive vertical residual displacement (elevation of the specimen). The much larger rotations are demonstrated only on one side, apparently the one which has been further plasticized. Neither the fitting of the $M - \vartheta$ loops nor the agreement in terms of rotational time history presents a satisfactory view.

Figure 3.30 a, **b** and **c** illustrates the results from the last motion (Takatori at 100%). As commented before, in the arithmetic simulation the intense soil plastification of the underlying soil, which has rapidly progressed during the preceding motion, determines the fate of the structure, leading it to collapse. The toppling occurs during the second long period pulse of the excitation. This outcome is only a natural and awaited consequence of the system's exhibited behavior so far: The largely softer soil, lacking in the beneficial contribution of the dilation, is plasticized earlier than it happens during the experiments. On the other hand, as we already saw, the experimental results are quite encouraging, since the structure survived all strong motions. Regardless of the ultimate failure of the system in the arithmetic simulation, it has to be underlined, that for as long as the structure oscillates, its rotational response in rather good terms with the one recorded during the experiments (**Figure 3.30c**).

The Mohr – Coulomb simulation results, included in **Figure 3.30** however continue showing a behavior deviating from the experimental one. In this case the structure survives all six of the consecutive excitations, but it comes at a cost: The most significant characteristic in this response is again the detrimental effect of sand dilation, causing a plasmatic uplifting in the structure due to soil swelling. Moreover, we notice a difference in the "sensitive" direction of the system, but this alteration has plainly to do with the fact that the preceding excitation leads to residual rotation toward the other side, than the "sensitive" one for the experimental system. Observe that the residual rotation in the case of the Mohr – Coulomb simulation (approx. $1.2\ mrad$) is much lower than the one recorded during the experiments (approx. $27\ mrad$). This shows once more that the simulated soil formation follows a much more elastic behavior, comparing to the experimentally achieved soil conditions. Last but not least, the rotational time history is in fairly good agreement with the experimental one.

A more comprehensive illustration showing the progression of the seismic motions in terms of soil plastifications is provided in **Figure 3.31**. In this illustration are presented snapshots of the plastification magnitude in the underlying soil, at the moment when the strong pulse of each seismic excitation occurs. For the first three strong motions (Gilroy Array, Corralitos and El Centro corresponding to **3.31a**, **3.31b** and **3.31c**), the view is provided scaled up ten times. Observe that any significant plastification is developed in a very local area underneath the footing. The soil does not fail, but rather follows the imposed

motion. **Figures 3.31 d**, **e** and **f** are shown in real scale and correspond to the last three earthquake motions, i. e Pacoima Dam, de – amplified by 50% Takatori and Takatori at 100%. Already from the El Centro motion there is asymmetry in the developed plastifications, a view which only deteriorates as the successive seismic excitations follow. Note that for the last two motions, a snapshot has been implemented for each one of the two strong pulses acting. The second strong pulse in the Takatori at 100% motion is the one leading the system to collapse.

The evident asymmetry underlying the nonlinear nature of the system's response is shown also in **Figure 3.32a** and **b**. Two snapshots of the plastification magnitude are implemented at the end of the fourth and the fifth seismic motion respectively. The "weak" side of the system has been determined and at this side ultimately occurs the toppling of the structure.

4.1. Evaluation of the Arithmetic Model Calibration

In these paragraphs a discussion is presented, concerning the effectiveness of the calibration being consistent with the tested system. This evaluation is performed by means of comparing the response of the arithmetic model with the response of the experimentally investigated system. Additionally, since the two constitutive models utilized as alternative ways to simulate the backfill soil, lead to a quite different behavior, an evaluation also in these terms is performed.

To begin with, the general view provided by the arithmetic simulation following the equivalent von Mises constitutive law, shows a rather good agreement in terms of stiffness, moment, and rotations. The frequency content of the exhibited motion in the arithmetic simulation reveals consistency with the experimental results. A complete view showing the progression of rotations during the total time of the tests and the simulation, is presented in **Figure 3.33 (i) a** and **(ii) a**. It is obvious comparing these two graphs that until the fourth excitation, the progression of rotations is almost identical with the one during the tests. Of course, the slightly earlier occurrence of plastification in the supporting soil of the analyses and its slightly quicker progression, introduces a discrepancy in the residual rotation values. Bearing in mind that the simulated soil formation seems to be more compliant than the one in the confining box, this deviation from the experimental results is understandable. Needless to say however, that after such a deleterious sequence of strong seismic motions, during which the agreement is very good with the targeted results, the control of the exact moment, when soil is excessively plasticized does not matter. It is safe to assume that from the dynamic and inertial point of view the FE simulation is accurate enough, when we take into account that during testing, especially in a large scale, there are always uncertainties which distort the results. These uncertainties can neither be known beforehand, nor can they be introduced in the FE simulation.

The main inconsistency of our system against the tested one is the mechanism dictating the progression of settlements. In **Figure 3.33 (i) b** and **(ii) b** the different

governing mechanisms dictating the progression of settlements are presented. In the former case, reflecting the results of the tests, it is obvious that the response of the system is uplifting dominated, whereas the analytically extracted response is sinking dominated. The straightforward explanation for this evidently sinking behavior, is the underestimation of the FS_V (safety factor against vertical load). Indeed, as mentioned before, the effective $FS_V = 12$ for the von Mises simulation is practically half of the claimed effective value during the experiments. Of course the *analytically estimated* FS_V, mentioned in the test report is only a rough approach, probably overestimating the FS_V, which is yet unknown. The overestimation is stemming from the fact that for large friction angles, the analytical expressions calculating the safety factor, lead to unrealistically high values. On the other hand, according to numerous experimental works, the determination of the *exact* bearing capacity of the soil is performed by means of push down tests. Since such tests were not included in the testing protocol, there is no assurance that the value estimated by the analytical expressions is accurate; especially for such a high value of friction angle (43°). On the other hand, of course the underestimation of the calculated FS_V in our arithmetic model is indeed a shortcoming, which only worsens the problem.

Another key factor affecting the response of the soil formation in terms of the developing settlements is the sand dilation. As already mentioned this factor has not been accounted for in the von Mises constitutive law. In more detail this issue is presented in the next paragraph: "Evaluation of the two Constitutive Models".

Regardless of the aforementioned shortcomings of the arithmetic simulation, as it has been already excessively discussed in the previous Chapter, the mechanism dictating the progression of settlements, does not solely depend on the FS_V. This means that we have to "dig deeper" in order to identify any other reason behind this significant discrepancy. The densification of the underlying soil as a factor minimizing the settlements during the experiment, cannot be of any compelling importance, since according to the test report the achieved $D_r \cong 90\%$, was the targeted compaction result, so as to avoid effects of dynamic densification.

The only factor acting significantly in favor of restricting the system's settlements is the flowing of soil material underneath the rocking footing. As it has been extensively discussed in the previous chapter and specially stressed out by Hakhamaneshi and Kutter, [2015], the slight embedment of the footing contributes significantly to enhancing the uplift mechanisms (dilation and soil raveling, sliding or being scraped into the gap under the footing) and to restricting the settlement mechanisms. Apart from the contributing effect of the embedment on the response of the system, the effect of soil raveling into the creating gap is pronounced in the testing report of the herein investigated tests by Antonellis et al., [2015]. Thus negative values of settlement and reduction in the embedment are apparent phenomena in the response of the studied system.

Since the aforementioned phenomenon is not possible to be implemented in the FE code, we accept this discrepancy, as the main weakness of our model. At this point though, it has to be underlined that in absolute values the produced settlements by the arithmetic

simulation are not prohibitive, in terms of design limitations. To be more specific, the maximum measured settlement value is approximately $2.50\,cm$, without taking into account the last motion leading to toppling the structure. This value is an acceptable one, and thus even with this shortcoming, the simulation results show in overall terms a satisfactory behavior.

4.2. Evaluation of the Two Constitutive Models

As mentioned before, this evaluation provides us with the opportunity to compare and contrast the two constitutive models used for the arithmetic simulation. A first look at the results leads us to believe that the two failure criteria are in competition with each other:

The von Mises constitutive law provides better results in terms of the system's hysteretic damping, stiffness, and rotations, whereas the Mohr – Coulomb provides significantly better results in terms of settlements. In fact, only the latter constitutive model offers the system the chance to respond with dominating uplift.

Of course a closer look changes the aforementioned idea. The von Mises criterion is much more effective, since in the first four seismic excitations the fitting of the response graphs is quite satisfactory, given that there are always uncertainties in the tested system to account for minor discrepancies between the arithmetic simulation and the experiment. The only inconsistency with this approach has to do with the different mechanism governing the progression of settlements. As already mentioned, this has to do with the omission of the dilation parameter from this constitutive law. As already stressed out, the omission of the sand dilation as a key factor affecting the response of the soil, greatly influences the results. To understand this we need to approach the problem in a microscopic scale, i. e in terms of soil element. Normally, as the element responds under cyclic loading and enters its plastic region, the plastic flow vector is not normal to the enveloping curve (τ – σ or γ – ε terms). This means that the soil element withstands shear as well as volumetric deformation. Of course in the case of very dense sands ($D_r = 90\%$), which is the case in the herein investigated results, this volumetric deformation is reflected in the "swelling" of the soil element, creating the characteristic V – shaped loading – unloading curves. This constitutes the advantageous contribution of the dilation, when it is accounted for in the simulation of the soil formation, which responds under cyclic loading. In the case of the sand being loose ($D_r = 25\%$), the shear deformations are accompanied by accumulated settlements (volumetric deformations with a positive sign, since the volume of the soil formation decreases).

In the equivalent von Mises constitutive law, the relative density of the sand is taken into account indirectly through the high friction angle, i. e through the strength of the soil element. However, the weakness of this model is that in terms of deformations, the lack of the dilation parameter leads to the only deformations imposed on the soil element being

shear ones, thus "losing" the beneficial contribution of "uplift" offers by the volumetric deformation of the soil elements.

Another consequence of this weakness has to do also with the underestimation of the achieved FS_V. Since there is no effect of obstructed volumetric deformation ("swelling"), which would offer significant strength to the soil skeleton, the bearing capacity of the underlying soil is largely decreased.

Macroscopically, this leads us to conclude that although in terms of strength, the simulation *should be* accurate compared with the described soil conditions in the confining box, in terms of deformation, there are *inherent* weaknesses in the constitutive law.

The Mohr – Coulomb approach seems to simulate a more "elastic" soil formation, much less compliant, depriving the system of hysteretic damping. This is the reason why the rotational values are overestimated compared to the ones recorded during the tests. At this point we have to underline, that from the "design" point of view, higher uplift values are rather critical to the superstructure, since they lead to significantly larger displacements (drifts). On the other hand, the total measured settlement may as well be an acceptable design value. For this reason the comparative advantage of minor to negligible settlements provided by the Mohr Coulomb failure criterion is not of real importance to our problem. Another characteristic of this criterion is its taking into account the dilatancy of the sand. The mechanism of sand dilation is already explained, in an effort to point out the weakness of the von Mises constitutive law.

Of course in such high friction angle values the dilatancy is also rather significant. Although one would expect advantageous results, the reality is rather disappointing. The problem is that, although under static conditions the soil formation does indeed exhibits a consistent behavior approaching the real soil behavior, under cyclic loading the situation is much different. After the completion of each cycle, there is residual increase of the element's volume, thus leading to strikingly intense uplift, due to constantly accumulating soil swelling. This plasmatic uplift along as well as the decreased hysteretic damping are indications of a failure criterion which is not appropriate for cyclic loading. An illustration of the distortion in the results caused by the Mohr – Coulomb approach is presented in **Figure 3.34**. In terms of the progression of rotational time history (**Figure 3.34 (i) (a)** and **(ii) (a)**), it is evident the change in the frequency content in the last three earthquake motions. Apart from that the maximum rotational values are multiple times larger than in the experiment. **Figure 3.34 (i) (b)** and **(ii) (b)** shows again the overall inconsistency between the arithmetic simulation and the tests. It is evident that the accumulated swelling of the soil, as the cyclic dynamic loading progresses leads to an accumulated uplift which cannot be rational as an outcome reflecting the reality, and for this reason it cannot be accepted.

Based on the aforementioned it is concluded that the equivalent von Mises criterion prevails over the Mohr – Coulomb.

5. ANALYTICAL RESULTS FOR THE SKEWED FOOTING

The numerical model is modified accordingly, in order to simulate the response of the skewed specimen as well. In the experimental set up the footing is askew by 30˚. In ABAQUS instead of rotating the footing, the imposed seismic excitation is analyzed by 30˚ in two components. Following the same notion as before, only the results in terms of $M - \vartheta$ and $w - \vartheta$ curves as well as in terms of the system's rotational time history are studied. It is underlined at this point that the $M - \vartheta$ graphs present the correlation between the maximum developing moment at the top of the oscillator and the rotation measured about a horizontal axis normal to the primary shaking direction. The target is to check whether the calibration performed for the aligned footing, is valid also for the skewed one. Of course, based on the conclusion concerning the higher efficacy of the equivalent von Mises constitutive model, the nonlinear dynamic analyses for the skewed specimen are performed only for this soil simulation approach. The comparison between the response of the aligned and the skewed specimen helps us draw significant conclusions, concerning the dynamic behavior of these two systems.

Starting with the analysis results from the first excitation, a rather well fitting is observed in terms of $M - \vartheta$ loops and rotational time history, presented in **Figure 3.35a** and **c**. Observe that in both cases: experiment and analysis, the structure practically fully re-centers. The most significant difference between the two responses has to do with the developing settlements, being excessively larger (almost thrice) than the measured ones for the aligned model (**Figure 3.35b**).

Observe that by comparing the experimental results for both footings, there is clear resemblance in the shape and maximum values of moment and rotation. On the other hand, when comparing the settlements, the footing responding under biaxial excitation, seems to develop less settlements than the aligned one.

The view does not change significantly in the second excitation. Again, there is rather good agreement between the analytical and the experimental results in terms of moment – rotation response and rotational time history (**Figure 3.36b** and **c**). at this point our attention focuses on the reduced developing moment during half of the strong pulse of the excitation. We observe that as the pulse commences towards its first peak, the system follows this motion, reaching the maximum value of approximately $150\ kNm$. As the motion of the pulse progresses toward s its second peak value on the opposite side, the system manages to exhibit only a value of $130\ kNm$. There is a negligible difference in the residual rotation, at the end of the movement, which is more visible in **Figure 3.36b**. The accumulation of settlements again is more excessive in the case of the biaxial motion, than in the uniaxial one.

When comparing the test results, for both footings, again the response is remarkably alike in terms of developing moment and rotation. Observe that in the first and second excitations, the recorded uplift for the aligned footing is higher than the respective one for the skewed. This probably has to do with the geometry of the rocking system. As already

discussed in the previous chapter, it has been proved experimentally (Drosos et al., 2012) that the rocking response is mainly dependent on the slenderness ratio $\frac{h}{B}$. In the case of the footing being excited biaxially, the effective B is not its side but rather is its diagonal. Thus the slenderness ratio in this case is lower and as a less slender structure, especially when the motion is not that severe (there is not any significant low frequency pulse) the uplift is limited.

The analytical results concerning the El Centro excitation are presented in **Figure 3.37a**, **b** and **c**. The fitting of the analytically developed $M - \vartheta$ loops is not that satisfactory in this case. This is mostly attributed to a vividly unsymmetrical response of the arithmetic model, contrary to the clearly symmetrical motion of the tested specimen. As mentioned also for the previous motion, again we observe that during the action of the main pulse of the excitation, the system manages to reach its moment capacity only on one side of its response. Interestingly, this side happens to be the opposite one, than in the case of the previous motion. In spite of this difference, the residual rotation at the end of the motion seems to be in good comparison between the simulation and the experiments. The fairly good fitting of the rotational time history reveals that the frequency content of the arithmetic model is consistent with the frequency content in the developed motion during the experiments.

After comparing the experimental results for both the aligned and the skewed systems again there is evident resemblance in the response in all aspects. Observe that for the case of the aligned footing the response seems to be more symmetrical compared to the aligned.

The fitting of the $M - \vartheta$ loops produced by the FE analyses is further deteriorated as it is shown in **Figure 3.38 a**. Although the frequency content of the response is in very good agreement with the one in the motion during the experiments, the measured rotation as well as the developing moment, in the arithmetic simulation, is significantly underestimated. Apart from that, the already discussed trend of accumulating settlements being largely overestimated is visible also for this record, leading to twice as much sinking as in the case of the aligned footing (**Figure 3.38 c**).

The aligned and the skewed footings during testing responded similarly also during this motion. The moment – rotation and settlement – rotation graphs reveal this similarity in the behavior of the two systems. Observe that the uplift is significant in both cases and not just for the aligned footing, as it was commented for the first and second excitations. This is attributed to the harmful long period pulse of the Pacoima Dam record, exciting the structure by forcing it to develop large rotations. It is worth noticing the symmetry in the response of the skewed system as opposed to the aligned one, which has already started showing evidence of soil plastification on one side of the footing.

The comparison of the analytical results between the aligned and skewed footing for the fifth motion (de – amplified Takatori by 50%) in terms of $M - \vartheta$ response, are quite similar, but deviate significantly from the experimental outcome. The reason behind it, as was mentioned also in the evaluation of the analytical results for the aligned specimen, is

the intense plastification of the underlying soil at the moment when the strong long period pulse of the motion is imposed on the system. This phenomenon results in residual rotation, deviating significantly from the respective one recorded during testing, since according to the experimental results, the specimen manages to re – center almost fully at the end of this motion as well. Apart from this outcome, another significant difference is the decrease in the strength of the system, judging from the evidently lower developing moment values. **Figure 3.39a** provides an illustration of the aforementioned description. In **Figure 3.39b** is evident yet again the sinking response of the numerically simulated footing, as opposed to the uplifting dominated response of the tested specimen. The rotations seem to fit well in terms of frequency content in the experimentally produced rotational time history (**Figure 3.39c**).

As for the comparison of the two systems according to the experimental results, again the response is quite similar, whereas it is evident once more that the skewed specimen responds more symmetrically than the aligned. Observe how significant has become the uplift at this stage for the skewed specimen. This is characteristic of the major effect, which has the frequency content of the motion, on the rocking response of the structure.

Comparing the two systems for the last excitation, Takatori at 100%, it is apparent in **Figure 3.40 a**, **b** and **c** that the structure in our FE model topples. As mentioned also in the evaluation of the results for the aligned specimen, the extensive plastification which is imposed by the previous motion largely affects the response of the system: The soil is largely deformed and thus, as soon as the second strong pulse of the motion occurs, the soil cannot provide any support to the structure, which is forced to rotate excessively, and thus the structure collapses.

On the other hand the experiments show in both cases, the aligned and skewed system, that the structure survives this deleterious sequence of strong seismic excitations, only with a noticeable irreversible rotation at the end of the motion.

To sum up from all characteristics, which are revealed from the comparison of the aligned and skewed specimen not only in analytical but also in experimental terms, the most important fact worth highlighting is the obvious resemblance in the dynamic response between the aligned and the skewed footing. Of course it is of major importance that the specimen is rectangular. In this way there are no major differences in its geometry along the two directions, in which it is excited. After all, during the first motions the fact that the base of the equivalent rigid box was not equal to the footing's side but rather to the footing's diagonal, did make a difference in its response, by bounding the developing rotations.

The excessively accumulating settlements, which are twice and sometimes thrice as high as the ones measured by our simulation for the aligned specimen, are attributed to the much higher soil plastification, at the edges and sides, where the footing imposes pressure through its rocking response. This phenomenon has been stressed out also for the case of the pushover analyses of the skewed specimen. More specifically, during motion 2 the system sustains the first major pulse, forcing it to develop a maximum rotation of about

$5mrads$. As we already saw from the pushover analyses, this rotational value does not suffice to lead the system to uplift, however, the concentration of vertical traction, being larger in value and much more concentrated in distribution than in the case of the aligned footing, lead to single-sided penetration of the soil by the footing. This rotation due to settling is irrevocable and already has deformed the underlying soil, by pushing it backwards. As soon as the second half of the pulse occurs, the system responds by further sinking, but is unable to develop equally large rotation to the other side. The greatest amount of energy is expensed in an effort to push downwards the curved underlying soil in order to re-center. The same happens during the occurrence of the pulse in motion 4 (maximum rotation of about $8\,mrads$), but the side where the penetration occurs is the opposite one. Observe that as long as the maximum developing rotation increases is only natural that the area imposing the maximum vertical traction decreases, thus leading to much more acute penetration of the soil and thus much more excessively settling response. It is worth mentioning that Deng and Kutter, [2012] have also interpreted the mechanism of settlement accumulation in a similar way. Thus by the end of these motions, both sides in the effective width of the footing are excessively plasticized due to significant vertical deformation. Thus as soon as the fourth motion commences, bearing the deleterious pulse of the Pacoima Dam record (maximum developing rotation of about $13\,mrads$), this phenomenon is magnified: the footing sinks on its edges even further, hence leading to a much higher rate of settlement accumulation.

If we combine the harmful response of the skewed footing with the fact that the simulated soil is already more compliant than it “should” and is also lacking the beneficial contribution of dilatancy, then it is understandable why the arithmetic model exhibits such an intensely sinking response compared to the response exhibited by the skewed footing during testing, which evidently is uplifting dominated. Apart from the apparently higher strength of the soil in the confining box, the effect of the soil material flowing underneath the footing, again enhances the footing response, by obstructing the progression of settling. This effect is also underlined in the testing report by Antonellis et al., [2015] as well as by the latest publication of Hakhamaneshi and Kutter, [2015]. A more thorough investigation of the response in biaxial excitation and the consequential interaction between the footing and the underlying soil is presented in the next Chapter.

A more comprehensive illustration showing the progression of the seismic motions in terms of soil plastifications is provided in **Figure 3.41**. In this illustration are presented snapshots of the plastification magnitude in the underlying soil, at the moment when the strong pulse of each seismic excitation occurs (snapshots bearing the notation (i)). Note for the first three strong motions (Gilroy Array, Corralitos and El Centro corresponding to 3.41(i)(a), 3.41(i)(b) and 3.41(i)(c)), the view is provided scaled up ten times. Observe that any significant plastification is developed in a very local area underneath the footing. The soil does not fail, but rather follows the imposed motion. **Figures 3.41 (i)(d), (i)(e)** and **(i)(f**) are shown in real scale and correspond to the last three earthquake motions, i. e Pacoima Dam, de – amplified by 50% Takatori and Takatori at 100%. For the last two motions, a

snapshot has been implemented for each one of the two strong pulses acting. The second strong pulse in the Takatori at 100% motion is the one leading the system to collapse.

Moreover, for each snapshot presenting the magnitude of the developing plastifications, a Figure showing the distribution of the vertical displacements underneath the footing are implemented (snapshots bearing the notation (ii)). The vectors of vertical displacement reveal the character of the response, which is exhibited by the skewed footing. Observe that the footing does not rock solely between the edges of its diagonal, but rather its response resembles the one performed by a twisting coin, spinning along its circumference. This means that apart from its edges also its sides participate in the response. The uplift is significant already from the second seismic excitation (**Figure 3.41 (ii) (b)**), where it is clear that the settlement on the one side of the footing is much larger than on the other side. Observe that in almost all cases *both* edges of the footing settle, which confirm the observed mechanism dictating the settlements. Only during the first and second pulses of the last excitation (**Figure 3.41 (ii) (f_1)** and **(f_2)**) is there obvious upwards movement of the one edge of the footing. Note that this excitation ultimately leads the system to collapse.

Another significant characteristic observed repeatedly in the plotted results has to do with the fact that the developing moment of the skewed footing is in some cases lower than the value expected to develop, according to the experimental response. For a better understanding of this phenomenon, the reader is encouraged to refer to **Figure 3.42** which presents the undeformed mesh (**Figure 3.42(a)**) showing the trench, where the footing is embedded. The red frame highlights the initial dimensions of the trench. **Figures 3.42(b), (c), (d)** and **(e)** show the deformed mesh, focusing on the trench, during the Corralitos, El Centro, Pacoima Dam and Takatori (50%) seismic motions respectively. Again, the red frame highlights the dimensions of the undeformed trench, providing evidence in this way that during these motions a gap is created between the surrounding soil and the footing. As the footing rocks, as soon as it is forced to turn over to one side the developing moment of the system becomes bounded, since the soil surface to provide resistance to its motion is not in contact with it. It is important to understand that the strength of the system in reality has not changed. This means, ideally, that in the case that the motion stopped at the point when the footing rocks toward the soil, and the motion continued monotonically, ultimately the footing would come in contact with the embedding soil and the system's developing moment would ultimately increase, probably reaching the desired value. The only difference is that it would take longer, until this moment value is reached. In other words, these gaps introduce changing stiffness in the system. According to the sketch presented in **Figure 3.43** the modified response of the system in terms moment – rotation relation is characterized by a change in its stiffness, which is reduced. This happens only momentarily, as the footing cannot "find a surface" to provide resistance to its motion. Thus for the same rotational value, the developing moment in the skewed system is lower, than it would be according to its initial behavior. Of course, as the rotational values increase, ultimately the footing would touch the surrounding deformed soil and reach its capacity. This behavior in overall

approaches the one of a surface footing. This means that momentarily, the system behaves as if there was no embedment to provide further strength in its response. To corroborate this theory we calculate the moment capacity of the system, as it would be, without taking into account the contribution of embedment:

$$M_{c,foot} = \frac{Q * B}{2} * \left(1 - \frac{1}{FS_V}\right) \approx 170\ kNm$$

It is evident from the plots of the $M - \vartheta$ response of the skewed footing that this value is indeed within the range of exhibited moment values, during its response. Hence there is good chance that this interpretation is a valid one to shed light in the investigated problem.
By studying the $w - \vartheta$ as well as the rotational time histories of the skewed footing it is obvious that the developing rotations are also strikingly underestimated. This is attributed to a combination of the two aforementioned mechanisms:

- As the footing rotates, the minimized area in which the maximum vertical traction is distributed penetrates the soil causing plastic vertical deformation. The underlying soil surface becomes curved obstructing in this way to footing to develop equally large rotation in the other direction. The greatest amount of energy is expensed by the footing in an effort to push downwards the curved underlying soil in order to re-center. Thus we see only partially good fitting in the developing rotational values.
- The other possible explanation has to do with the system's changing characteristics. As reported in numerous publications (Tsatsis and Anastasopoulos, [2015], Gajan [2005]), as the soil surface underneath the footing becomes curved, due to deformations imposed by the rocking motion of the footing, the overall stiffness of the system decreases. Thus the developing value of acceleration and by extension the developing rotation are decreased. From the point of view of developing moments, this phenomenon has already been extensively discussed above.

Figure 3.44a and **b** presents the progression of settlements and rotations respectively, for the skewed footing, for all successive seismic motions, as they are measured by the FE analyses. The results are presented along with the corresponding outcome of the shake table tests, for the skewed specimen.

The symmetry in the testing response of the skewed footing, on which we commented repeatedly during the presentation and comparison of the results, does not lead us to any worthwhile conclusion. The difference in the response has only to do with the eccentricities developed in the system by preceding motions, which affect the behavior of the system for the excitations to come.

6. PSEUDO STATIC APPROACH

In these paragraphs is presented the pseudo static approach of the investigated problem, only to show the tremendous difference in design that this philosophy introduces.

For this reason utilizing the experimentally estimated and arithmetically verified natural period of the aligned and skewed system, we determine the spectral accelerations for each of the six investigated excitations developed at the deck mass. Based on these acceleration values, the maximum developing moment at the system is calculated according to the following expression:

$$M_{max} = a * g * M * h$$

where a is the developing acceleration at the deck mass, g is the gravitational field, M is the mass of the oscillator representing the deck and h is the total height of the structure (distance from the mass to the base of the footing).

In order for the foundation to be considered statically intact, the EC7 building code dictates that the loading eccentricity abide by the following limitation:

$e = M / N < B/3$, where N is the vertical load and is equal to $N = 250\ kN$.

Table 3.2 presents the six excitations, utilized in the investigation of the problem at hand. For each excitation the spectral acceleration corresponding to the natural frequency of each system is determined, from which is calculated the maximum developing moment, as well as the loading eccentricity. Apparently in all cases examined, the eccentricity is much larger than the upper limit of $\frac{B}{3}$. In fact, in order for this criterion to be met, the side of the rectangular footing should be multiple times larger than the prescribed value by the current design. The factor x in the last column of the table represents the *number of times* by which the current side length of the footing should be multiplied, in order for the eccentricity criterion to be satisfied. From these facts it is concluded that, based on this approach, in order for the system to survive each and every one of the excitations listed in Table 3.2, the current design needs to be changed.

As we already saw however, the system not only did not collapse during the experiments, but also the residual deformations were significant only after the deleterious sequence of six strong seismic motions. The analytical results may have shown a different outcome, but it has already been explained that there are weaknesses in the simulation and some existing mechanisms which ameliorate the accumulation of plastic deformations, cannot be considered in the FE model, thus the system fails in the case of the analyses. Regardless of that, in the unrealistic case of such a sequence, consisting of the first five instead of six seismic motions, the FE simulation would also provide quite encouraging results, as far as the advantageous behavior of the system is concerned.

In order to highlight even further the beneficial behavior of the rocking foundations we investigate the decoupling capability of the rocking system. After all the main scope of rocking isolation is the reduction of the inertia transmitted onto the superstructure. It is therefore critical to ensure that this effect is indeed present also in this problem. Following the pseudo static philosophy, we determine the critical acceleration, defined as the maximum acceleration developed under static conditions at the mass of the oscillator (representing the bridge deck), leading the system to its moment capacity. Considering that the moment capacity of both the aligned and the skewed structure is roughly the same, the value of the critical acceleration is calculated by the following expression:

$$a_c = M_{cap}/mgh$$

In our case, the $M_{cap} \approx 240\ kNm$ and $M = 25.5\ Mgr$.

Thus, $a_c \approx 0.32\ g$.

In **Figure 3.45** the acceleration A_{MAX} at the oscillator mass (representing the bridge deck), as it was recorded during testing and as it was measured in the FE analyses, is plotted as a function of the PGA of the seismic excitation, i. e the input motion for the case of the analyses or the base excitation recorded at the walls of the confining box, for the case of the tests. The results of both the shake table tests and the analyses are also compared with the previously discussed critical acceleration a_c, computed on the basis of the results of monotonic (static) pushover analyses. The two graphs in **Figure 3.43** refer to **(a)** the results of the aligned specimen and **(b)** the results of the skewed specimen.

As far as the decoupling capability of the system is concerned, we notice that in all cases examined, for both the aligned and the skewed specimen, in the experiments as well as in the analyses, the developing maximum acceleration is much lower than the imposed PGA. This leads us to conclude that the system successfully decouples the ground motion, bounding the inertia forces. Apart from that, it is evident in **Figure 3.45 (ii)** that the system exhibits also strikingly lower acceleration at the top of the oscillator than the corresponding spectral value, which would have been developed, in the case that the system were to behave elastically.

Moreover, as far as the analytical results are concerned, in all cases examined we notice that the developing maximum acceleration is lower than the calculated critical acceleration of the system. This comes as no surprise; in fact it is in alignment with the published literature (Drosos et al., [2012], Tsatsis and Anastasopoulos, [2015], according to which overstrength in terms of the developing acceleration is noticed in reduced values of FS_V. Only in the case of testing, there is an overrun of the critical acceleration for the Takatori motion (at 100%). Despite the developed acceleration being higher than the critical one, the specimen survives, an indication proving an existing overstrength probably attributed to the flowing of soil material underneath the footing.

FIGURES OF CHAPTER 3

$K_{R,elastic}$ (MNm / rad)	G_{max} (MPa)	ϑ_{el} (mrads)	ϑ_S (mrads)	$\vartheta_{el}/\vartheta_S$
420	190	0.06	0.20	0.3
320	140	0.09	0.20	0.45
310	140	0.04	0.20	0.2

Table 3.1 Elastic rotational stiffness and shear modulus estimated for the first three seismic motions.

ALIGNED T_{SSI} = 0.60 s	**SA (g)**	**M_{max} (kNm)**	**e = M/N (m)**	**e/B**	**B' = 3e (m)**	**B' = x*B**
Gilroy Array #1	0.58	439.6	1.76	1.16	5.28	3.47
Corralitos	1.09	826.2	3.30	2.17	9.91	6.52
El Centro	0.67	507.8	2.03	1.34	6.09	4.01
Pacoima Dam	0.57	432.0	1.73	1.14	5.18	3.41
Takatori (50%)	0.78	591.2	2.36	1.56	7.09	4.67
Takatori	1.56	1182.4	4.73	3.11	14.19	9.33

(a)

SKEWED T_{SSI} = 0.50 s	**SA (g)**	**M_{max} (kNm)**	**e = M/N (m)**	**e/B**	**B' = 3e (m)**	**B' = x*B**
Gilroy Array #1	1.21	917.1	3.67	2.41	11.01	7.24
Corralitos	1.45	1099.1	4.40	2.89	13.19	8.68
El Centro	0.53	401.7	1.61	1.06	4.82	3.17
Pacoima Dam	0.81	614.0	2.46	1.62	7.37	4.85
Takatori (50%)	0.87	659.4	2.64	1.74	7.91	5.21
Takatori	1.75	1326.4	5.31	3.49	15.92	10.47

(b)

Table 3.2 Pseudo static approach of the investigated problem: The maximum developing moment combined with the acting axial load leads to a much higher eccentricity than the allowable, hence leading to a rejection of the current design.**(a)** Refers to the aligned footing and **(b)** refers to the skewed footing. Factor x represents the *number of times* by which the current side length of the footing should be multiplied, in order for the eccentricity criterion to be satisfied.

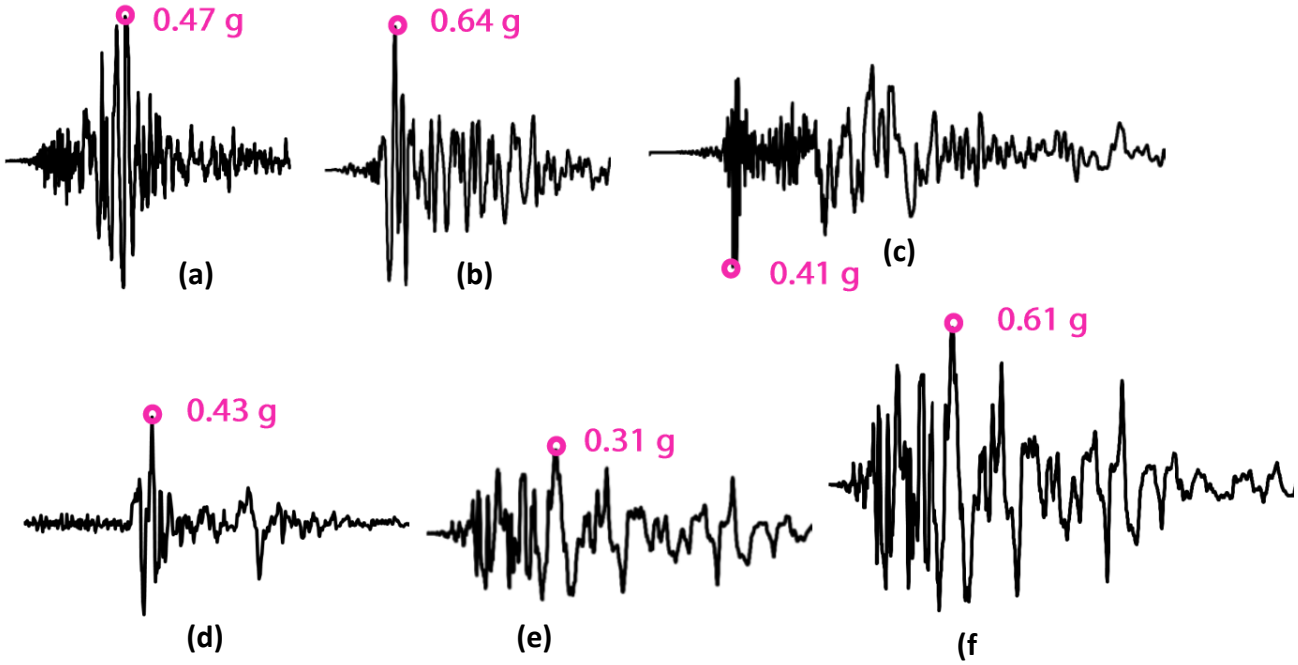

Figure 3.1 The original seismic excitations: **(a)** Gilroy Array, (Loma Prieta, 1989), **(b)** Corralitos, (Loma Prieta, 1989), **(c)** El Centro (Imperial Valley, 1979), **(d)** Pacoima Dam (Northridge, 1994), **(e)** Takatori de-amplified by 50% (Kobe, 1995), **(f)** Takatori, (Kobe, 1995)

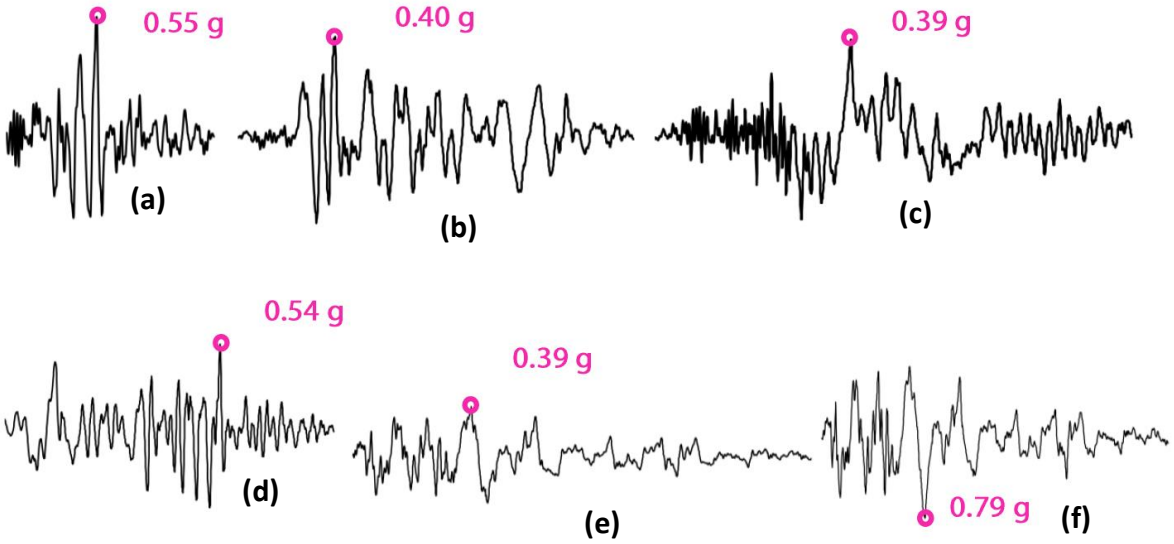

Figure 3.2 The recorded free field seismic excitations during the Test Day 1: **(a)** Gilroy Array, (Loma Prieta, 1989), **(b)** Corralitos, (Loma Prieta, 1989), **(c)** El Centro (Imperial Valley, 1979), **(d)** Pacoima Dam (Northridge, 1994), **(e)** Takatori de-amplified by 50% (Kobe, 1995), (f) Takatori, (Kobe, 1995)

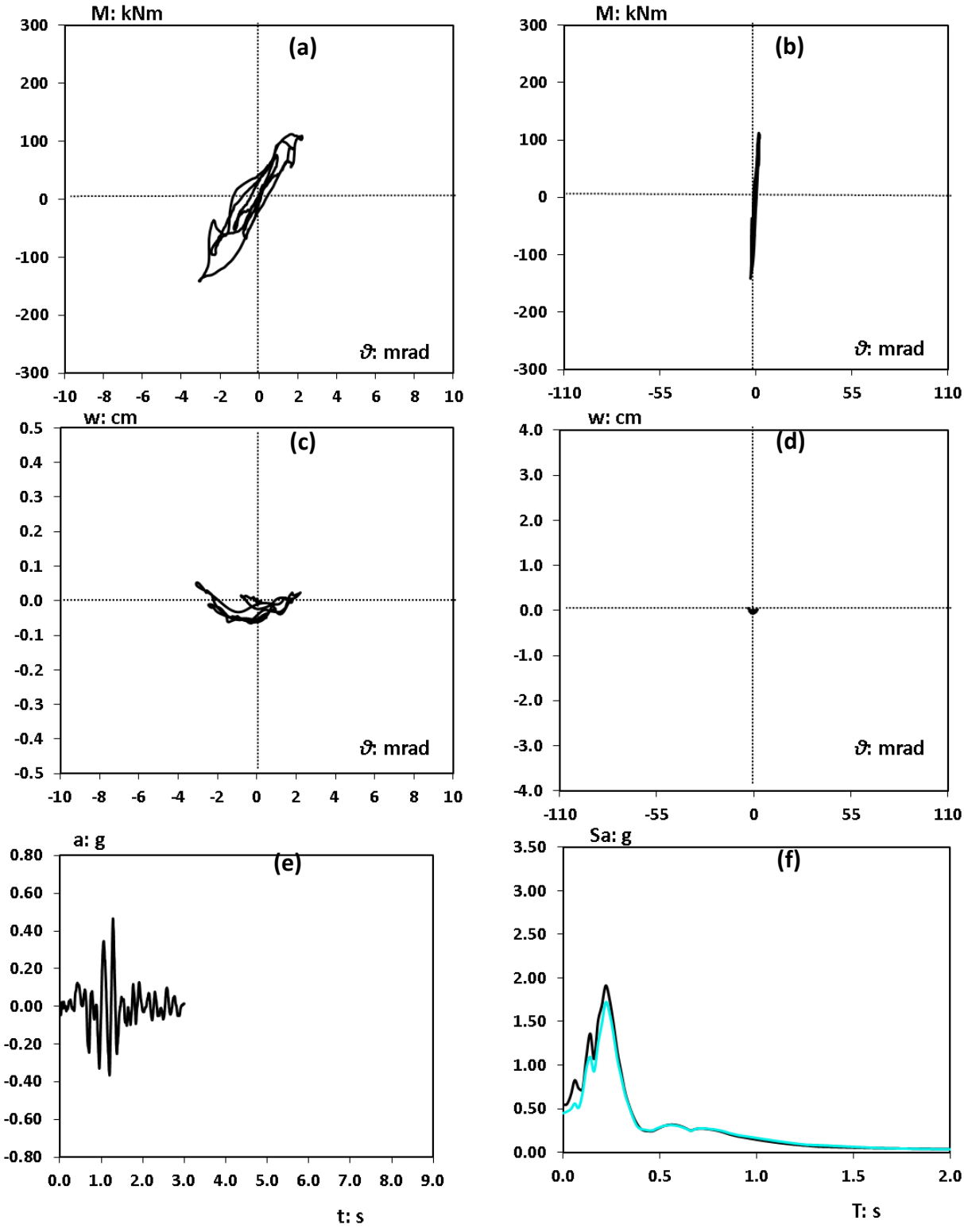

Figure 3.3 Results from the seismic excitation Gilroy Array #1 (Loma Prieta, 1989). **(a)** Cyclic $M-\vartheta$ curves; **(b)** cyclic $M-\vartheta$ curves in magnified scale. **(c)** Cyclic $w-\vartheta$ curves; **(d)** cyclic $w-\vartheta$ curves in magnified scale. **(e)** Acceleration time history recorded at the walls of the confining box, used as input motion for the FE analyses. **(f)** Comparison of spectral acceleration for the input motion (blue line) and the surface acceleration recorded at the elevation of the foundation, in the free field (middle of the box).

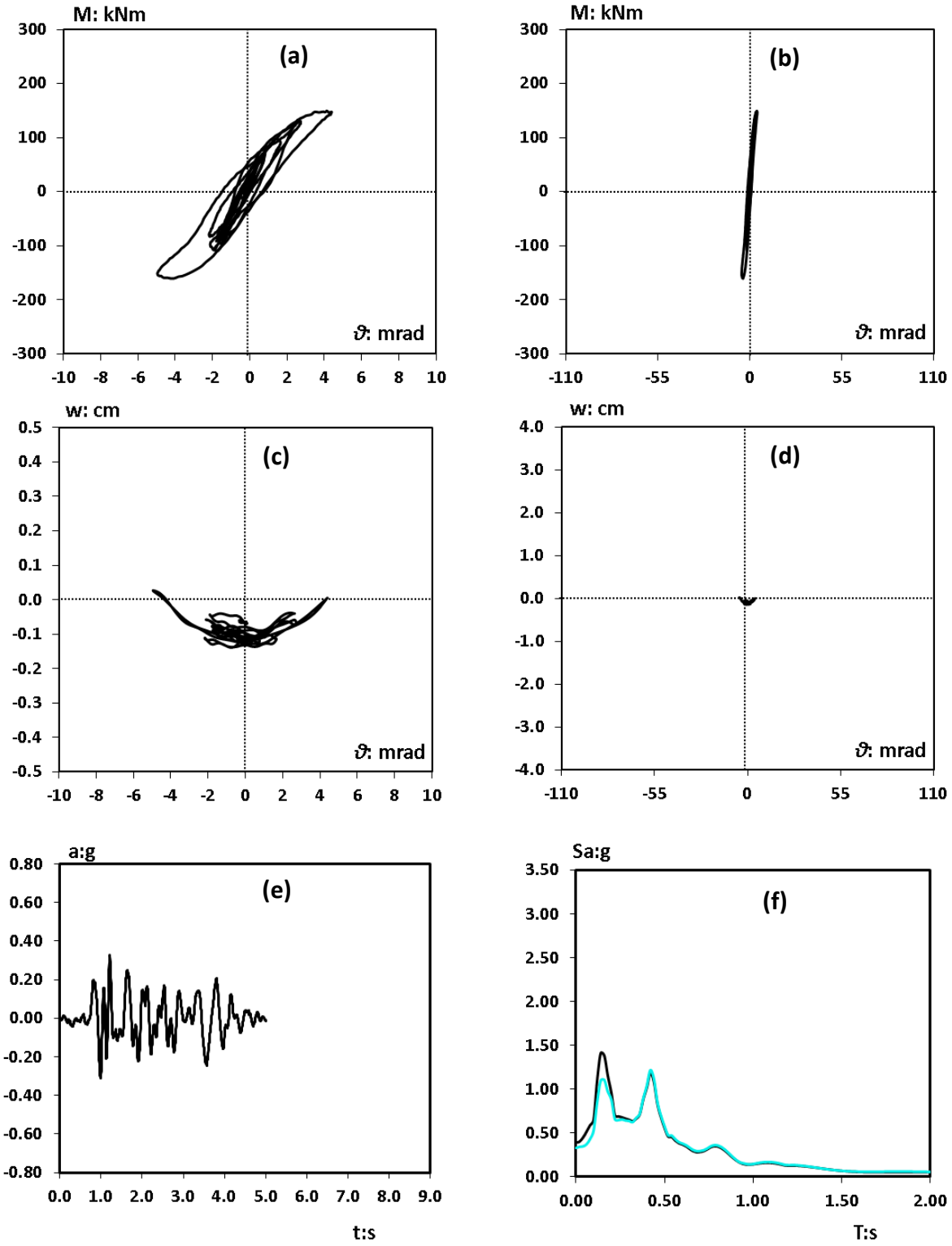

Figure 3.4 Results from the seismic excitation. **(a)** Cyclic $M-\vartheta$ curves; **(b)** cyclic $M-\vartheta$ curves in magnified scale. **(c)** Cyclic $w-\vartheta$ curves; **(d)** cyclic $w-\vartheta$ curves in magnified scale. **(e)** Acceleration time history recorded at the walls of the confining box, used as input motion for the FE analyses. **(f)** Comparison of spectral acceleration for the input motion (blue line) and the surface acceleration recorded at the elevation of the foundation, in the free field (middle of the box).

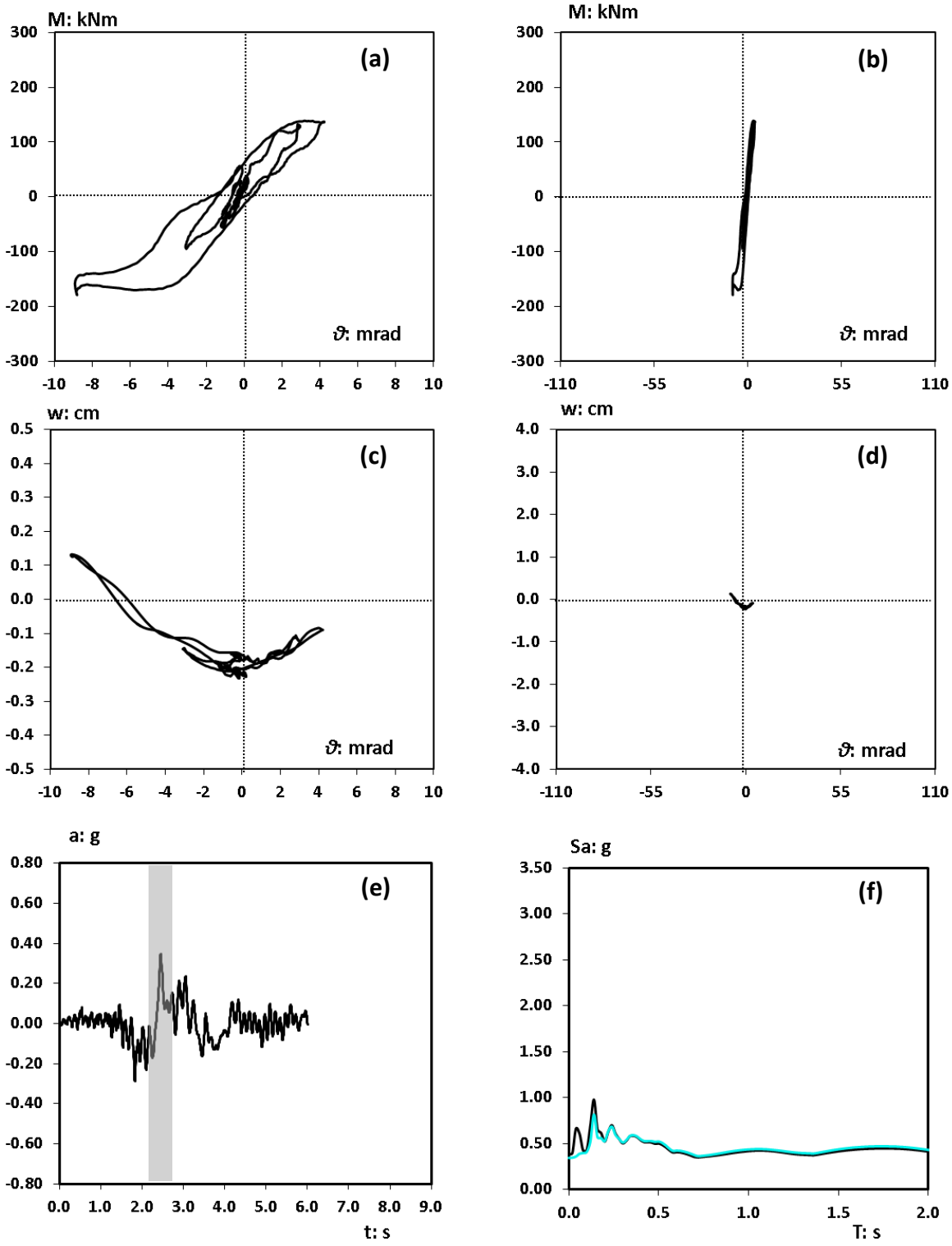

Figure 3.5 Results from the seismic excitation El Centro (Imperial Valley, 1979). **(a)** Cyclic $M-\vartheta$ curves in magnified scale; **(b)** cyclic $M-\vartheta$ curves. **(c)** Cyclic $w-\vartheta$ curves in magnified scale; **(d)** cyclic $w-\vartheta$ curves. **(e)** Acceleration time history recorded at the walls of the confining box, used as input motion for the FE analyses. **(f)** Comparison of spectral acceleration for the input motion (blue line) and the surface acceleration recorded at the elevation of the foundation, in the free field (middle of the box).

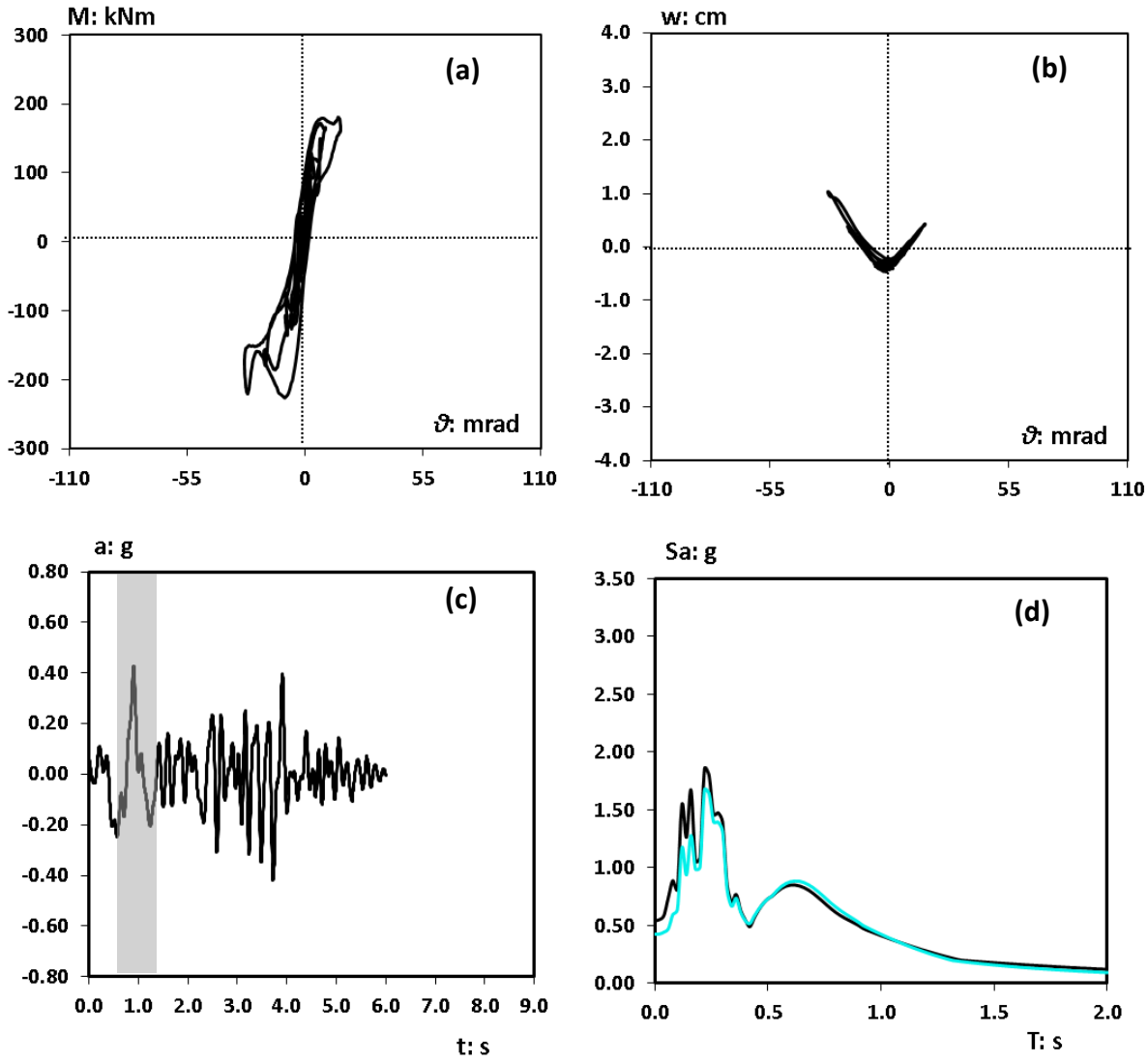

Figure 3.6 Results from the seismic excitation Pacoima Dam (Northridge, 1994). **(a)** Cyclic $M-\vartheta$ curves; **(b)** cyclic $w-\vartheta$ curves. **(c)** Acceleration time history recorded at the walls of the confining box, used as input motion for the FE analyses. **(d)** Comparison of spectral acceleration for the input motion (blue line) and the surface acceleration recorded at the elevation of the foundation, in the free field (middle of the box).

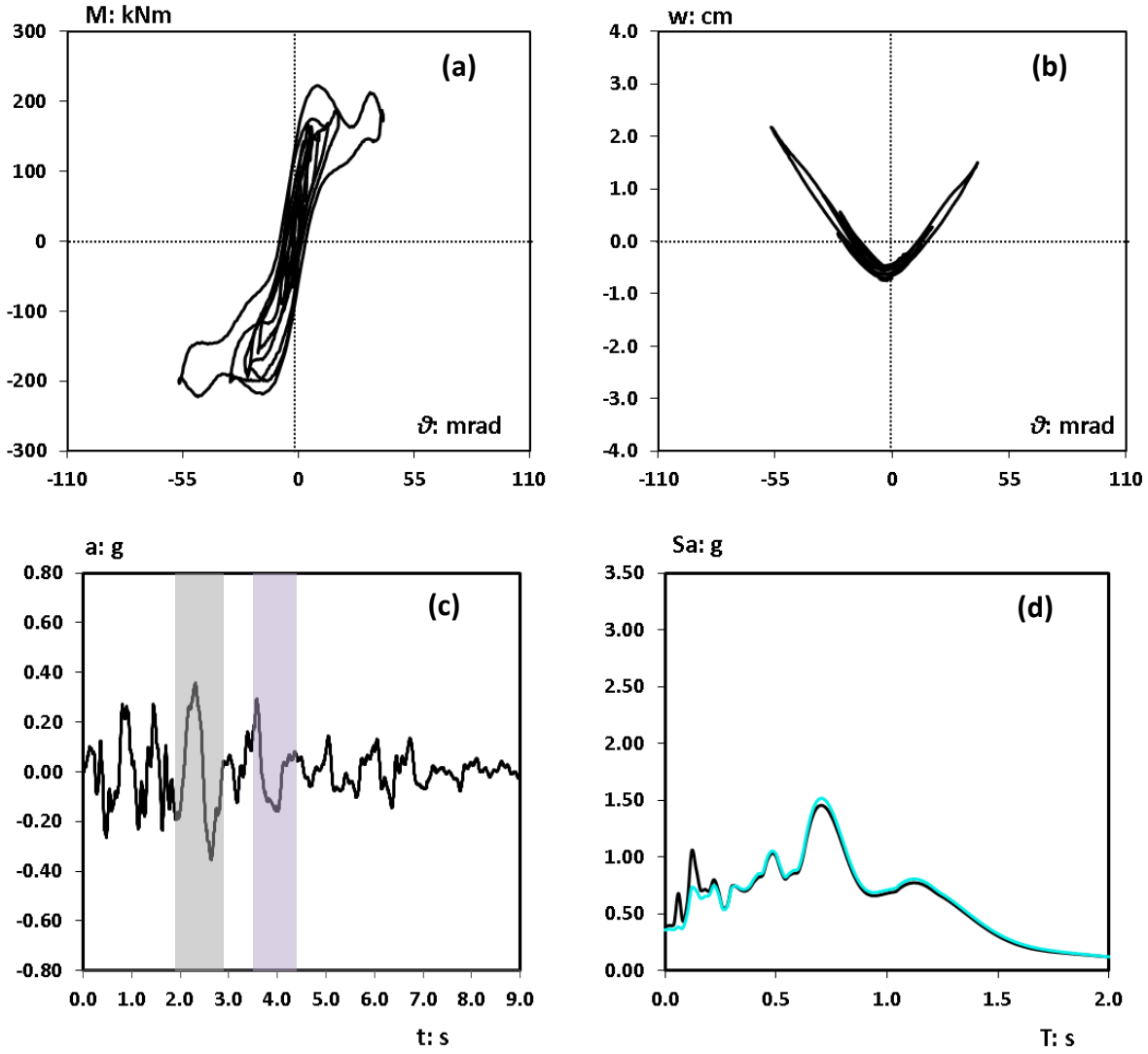

Figure 3.7 Results from the seismic excitation Takatori, scaled down by 50% (Kobe, 1995). **(a)** Cyclic $M-\vartheta$ curves; **(b)** cyclic $w-\vartheta$ curves. **(c)** Acceleration time history recorded at the walls of the confining box, used as input motion for the FE analyses. **(d)** Comparison of spectral acceleration for the input motion (blue line) and the surface acceleration recorded at the elevation of the foundation, in the free field (middle of the box).

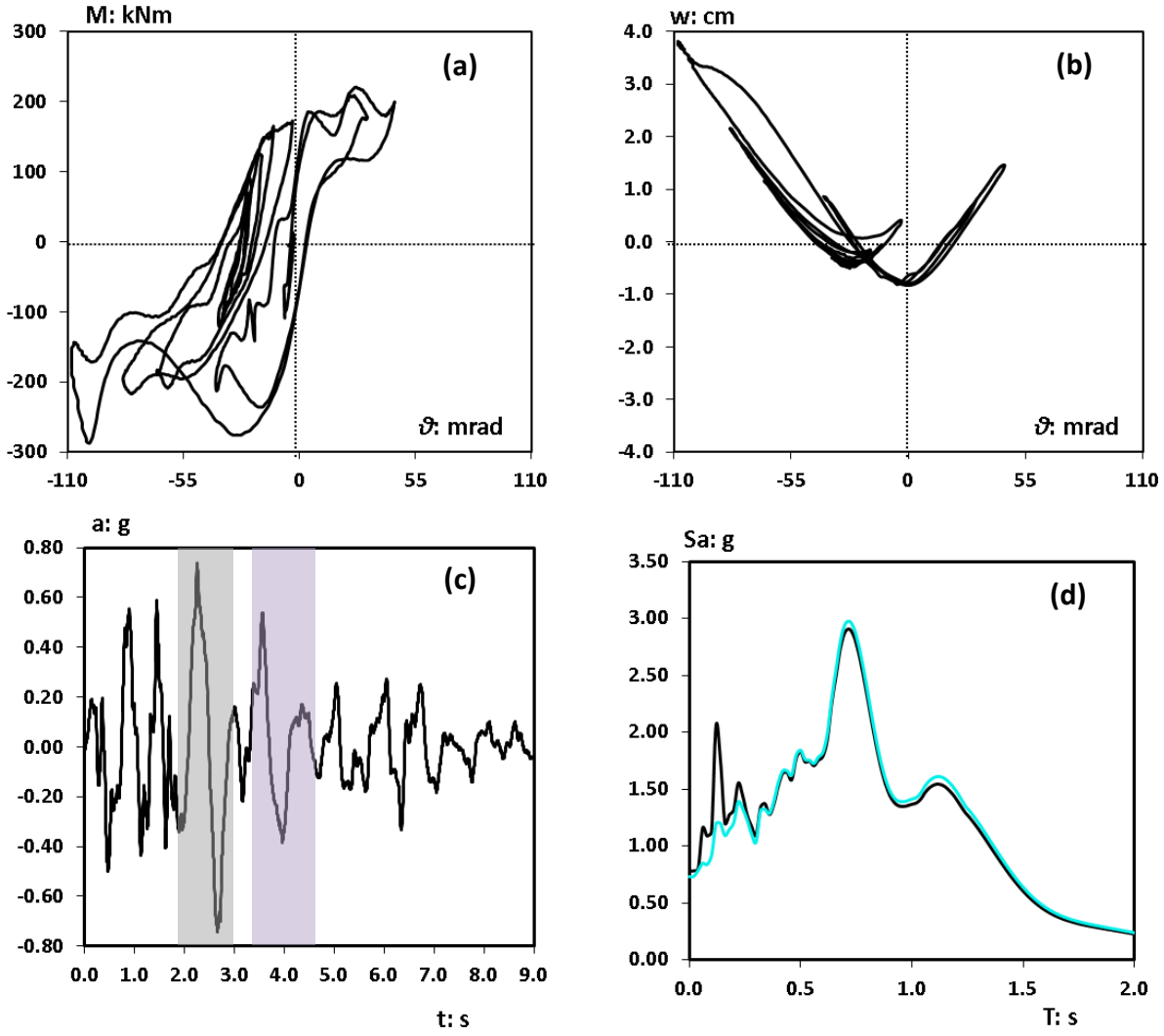

Figure 3.8 Results from the seismic excitation Takatori (Kobe, 1995). **(a)** Cyclic $M-\vartheta$ curves; **(b)** cyclic $w-\vartheta$ curves. **(c)** Acceleration time history recorded at the walls of the confining box, used as input motion for the FE analyses. **(d)** Comparison of spectral acceleration for the input motion (blue line) and the surface acceleration recorded at the elevation of the foundation, in the free field (middle of the box).

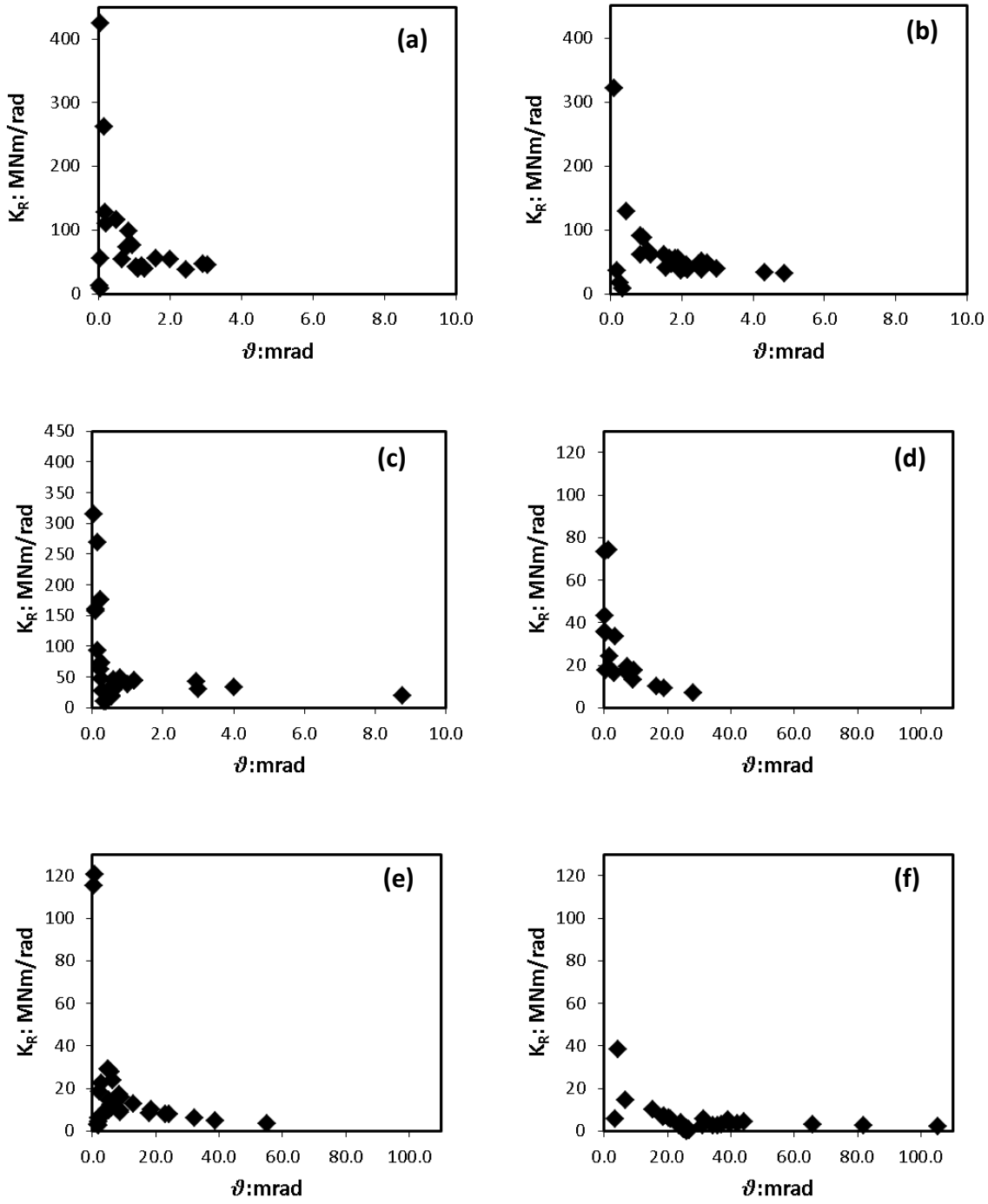

Figure 3.9 Decrease of rotational stiffness with increasing rotation during the **(a)** Gilroy Arrray #1 motion, **(b)** Corralitos motion, **(c)** El Centro motion, **(d)** Pacoima Dam motion, **(e)** Takatori scaled down by 50% motion and **(f)** Takatori motion.

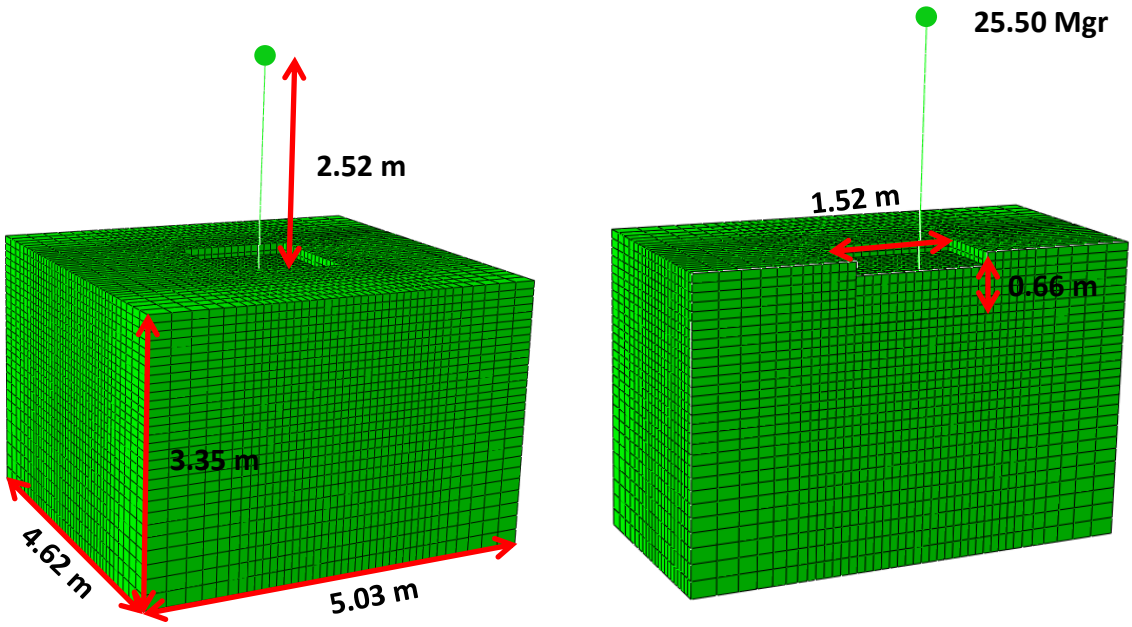

Figure 3.10 Numerical simulation in ABAQUS: presentation of geometry.

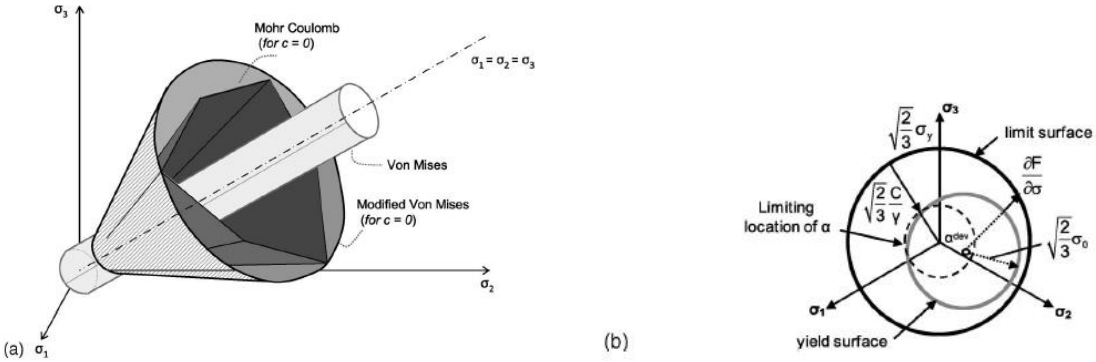

Figure 3.11 Simplified constitutive model: **(a)** representation of the extended pressure-dependent Von Mises failure criterion in the principal stress space (hashed shape) together with the Von-Mises (light grey shape) and the Mohr Coulomb failure criterion (dark grey shape); **(b)** projection of the failure surface at pressure $p = \frac{(\sigma_1+\sigma_2+\sigma_3)}{3}$ on the π-plane

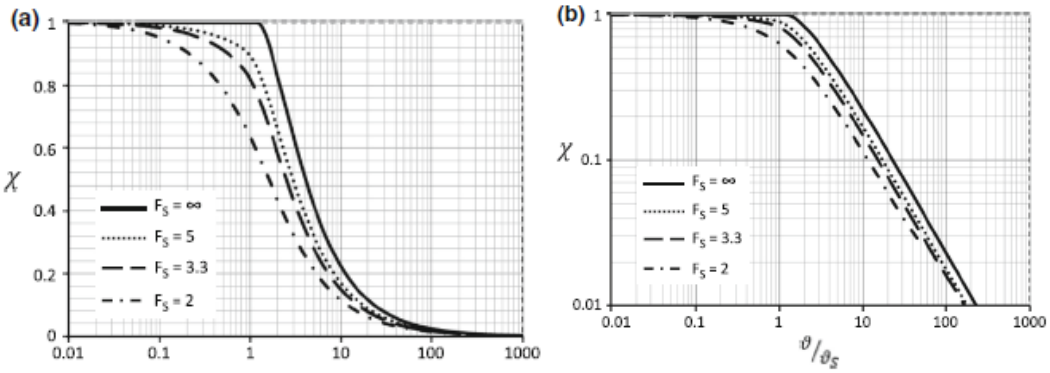

Figure 3.12 Plot of the function backslash χ versus $\vartheta/\vartheta_S$and four values of F_S : **(a)** logarithmic and **(b)** bi-logarithmic plots (allowing focus on small and large values of ϑ/ϑ_S, respectively). *(Adamidis et al., 2013)*

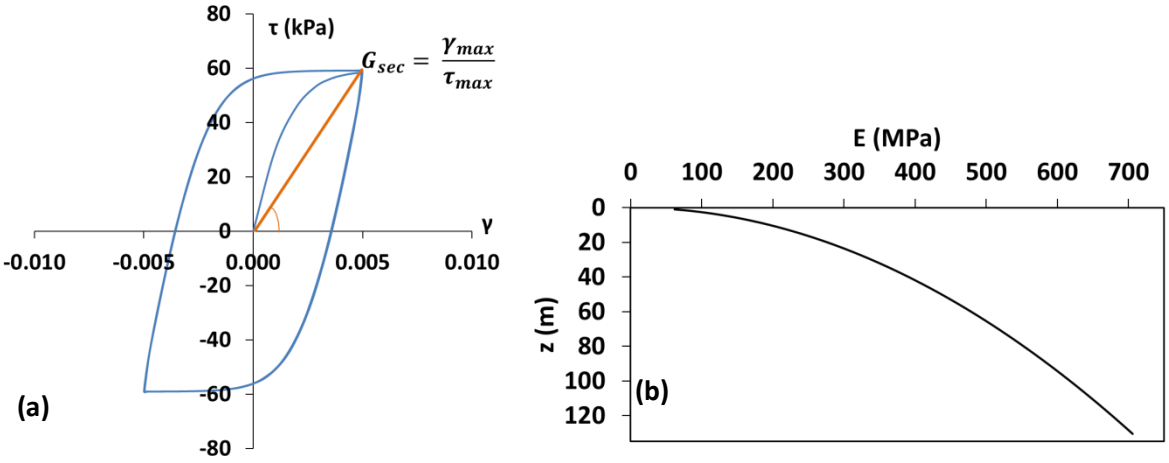

Figure 3.13 (a) Typical τ – γ loop calculated for the needs of calibrating the arithmetic model. **(b)** Parabolic distribution of elastic modulus with increasing depth.

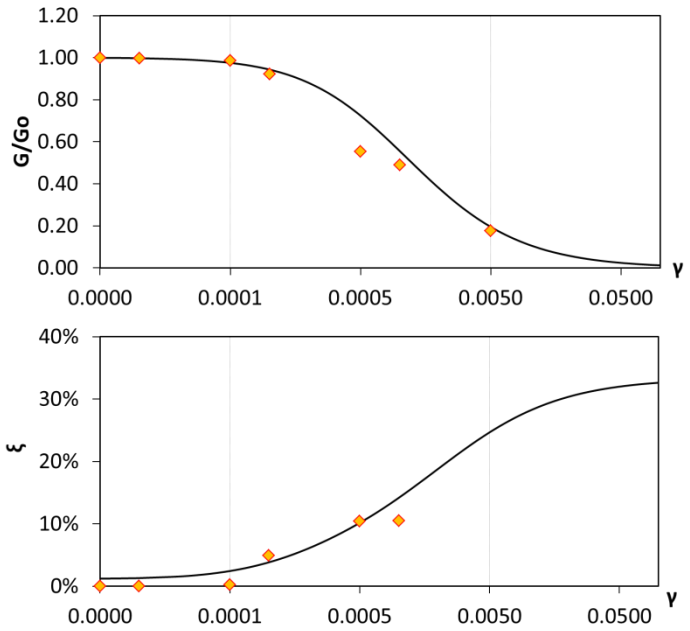

Figure 3.14 Fitting of the calibration results to the Ishibashi – Zhang, [1993], G – γ and ξ – γ curves.

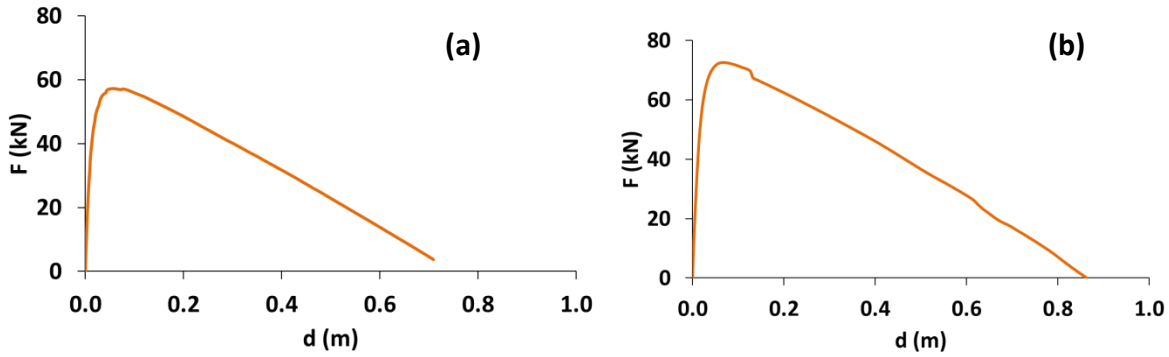

Figure 3.15 Results from nonlinear static pushover analyses on the aligned specimen considering SSI effects: **(a)** with the von Mises constitutive model and **(b)** with the Mohr – Coulomb model.

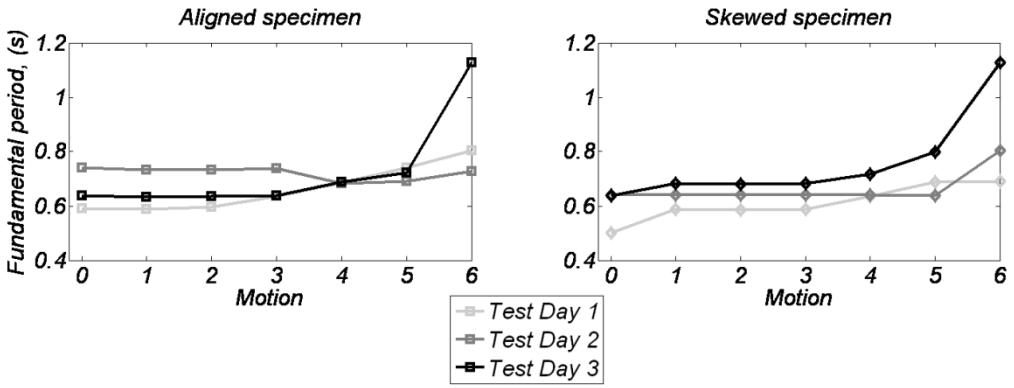

Figure 3.16 Fundamental period of specimens measured using white noise after each events (motion 0 refers to initial period). The initial period of the aligned system is estimated T ≈ 0.60 sec, whereas the initial period for the skewed is estimated T ≈ 0.50 sec *(Antonellis et al., [2015])*

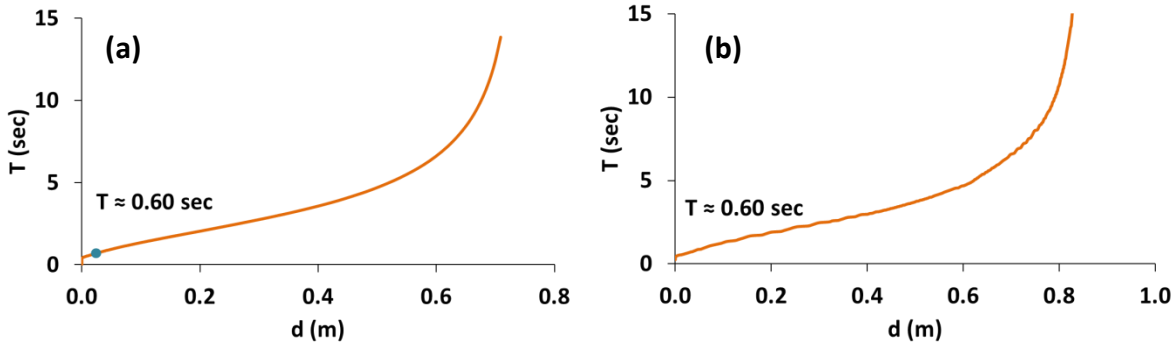

Figure 3.17 Natural period of the aligned system, considering SSI effects, as it progresses with increasing displacement. The denoted value corresponds to the elastic one, i. e for very small displacements. **(a)** Depicts the resulting value considering the von Mises constitutive model and **(b)** depicts the resulting value considering the Mohr – Coulomb failure criterion.

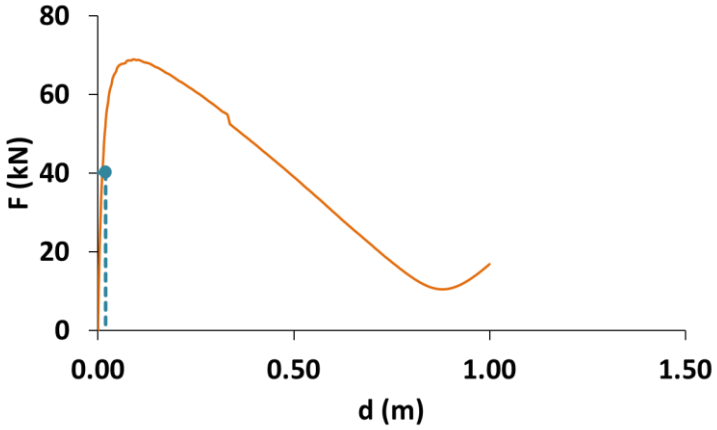

Figure 3.18 Results from nonlinear static pushover analyses on the skewed footing with the von Mises constitutive model.

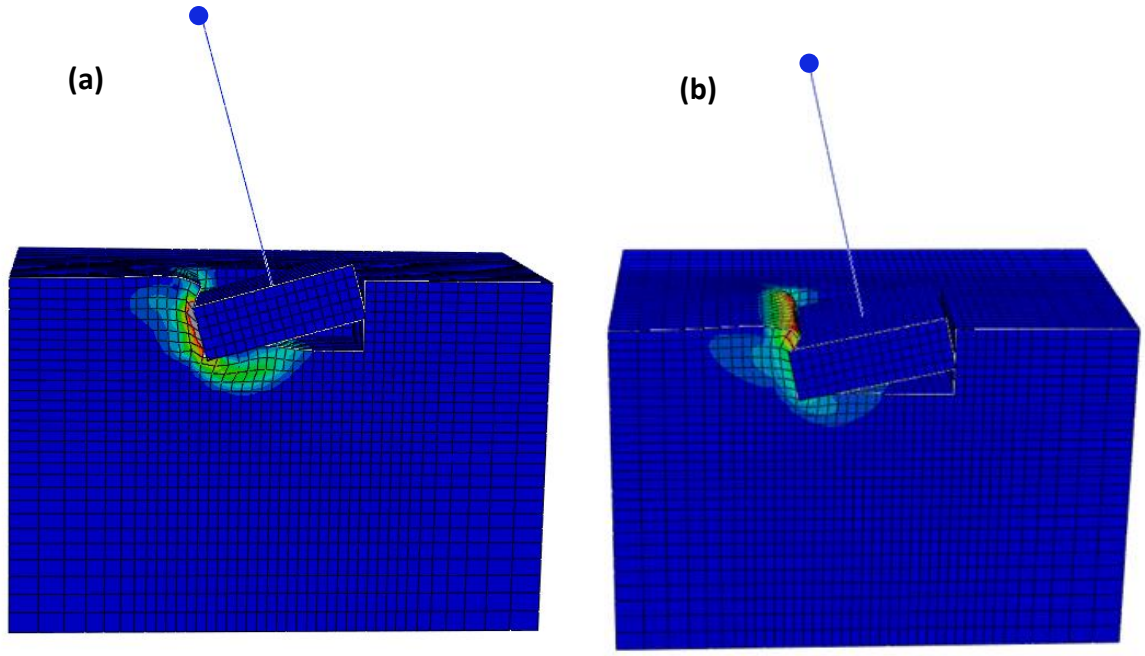

Figure 3.19 Snapshots at failure of static pushover nonlinear analysis for the aligned foundation, **(a)** considering the von Mises constitutive model and **(b)** considering the Mohr – Coulomb constitutive model.

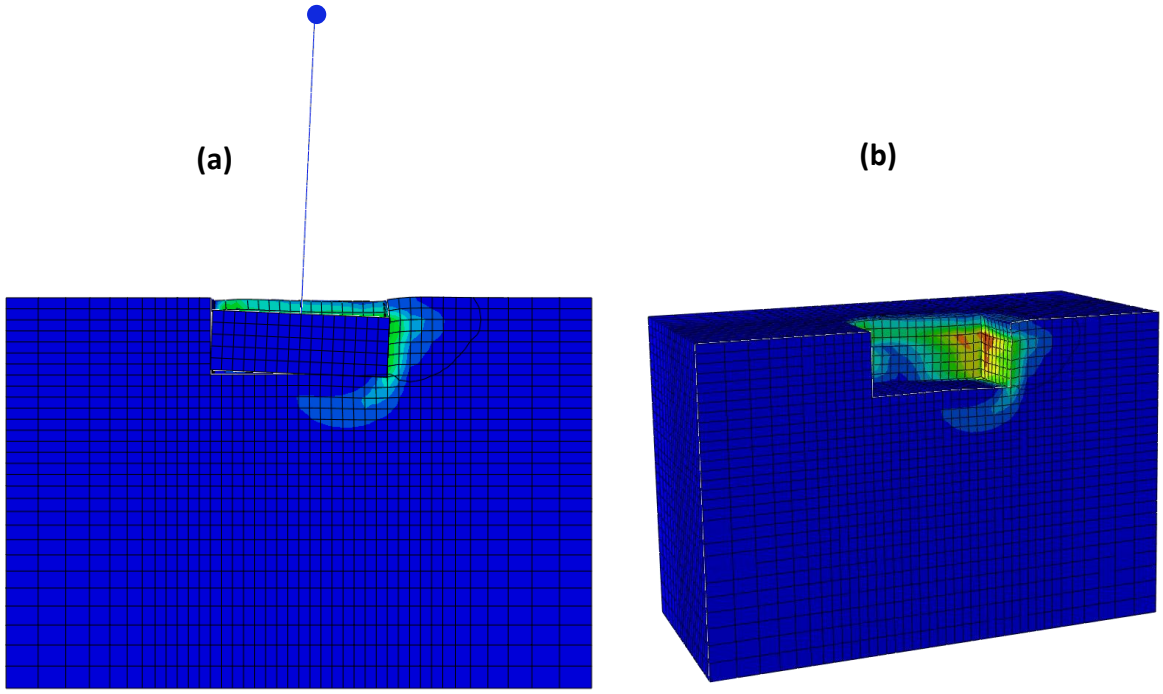

Figure 3.20 Snapshot of the plastic deformation contours at peak of static pushover response for the skewed foundation considering the von Mises constitutive model **(a)** showing the whole structure along with the deformed mesh, **(b)** showing the magnitude of plastifications.

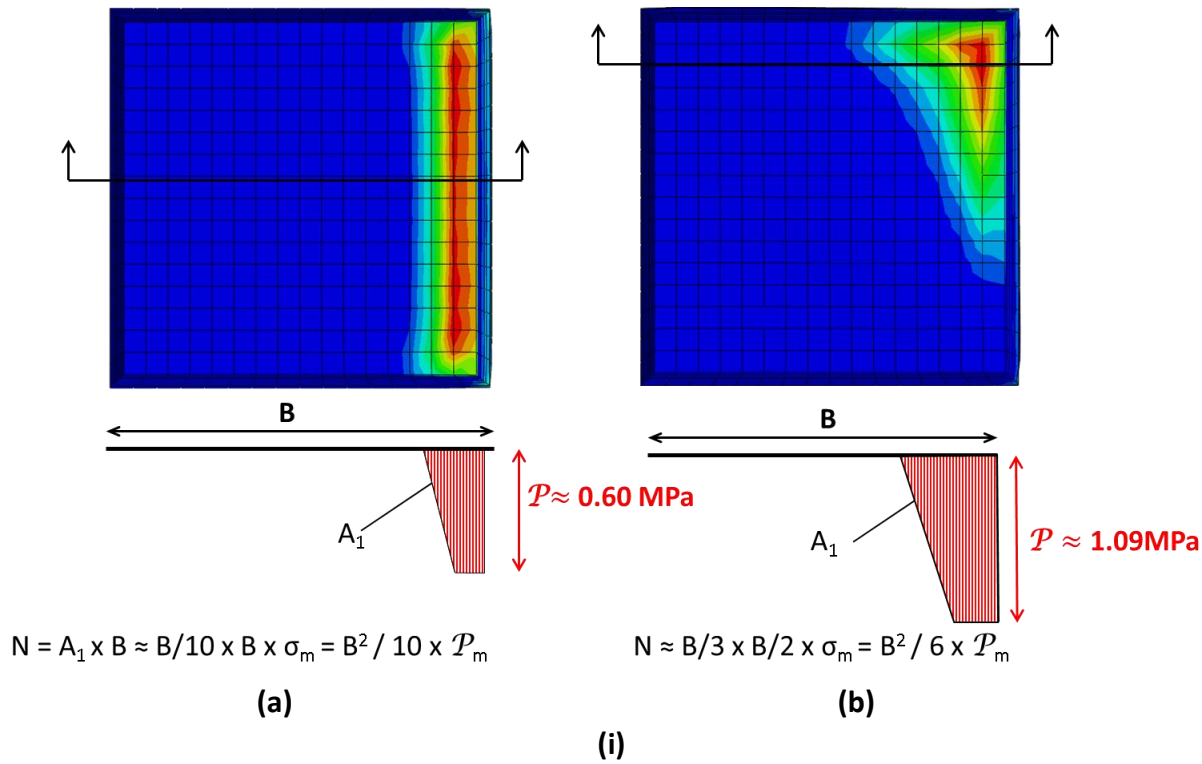

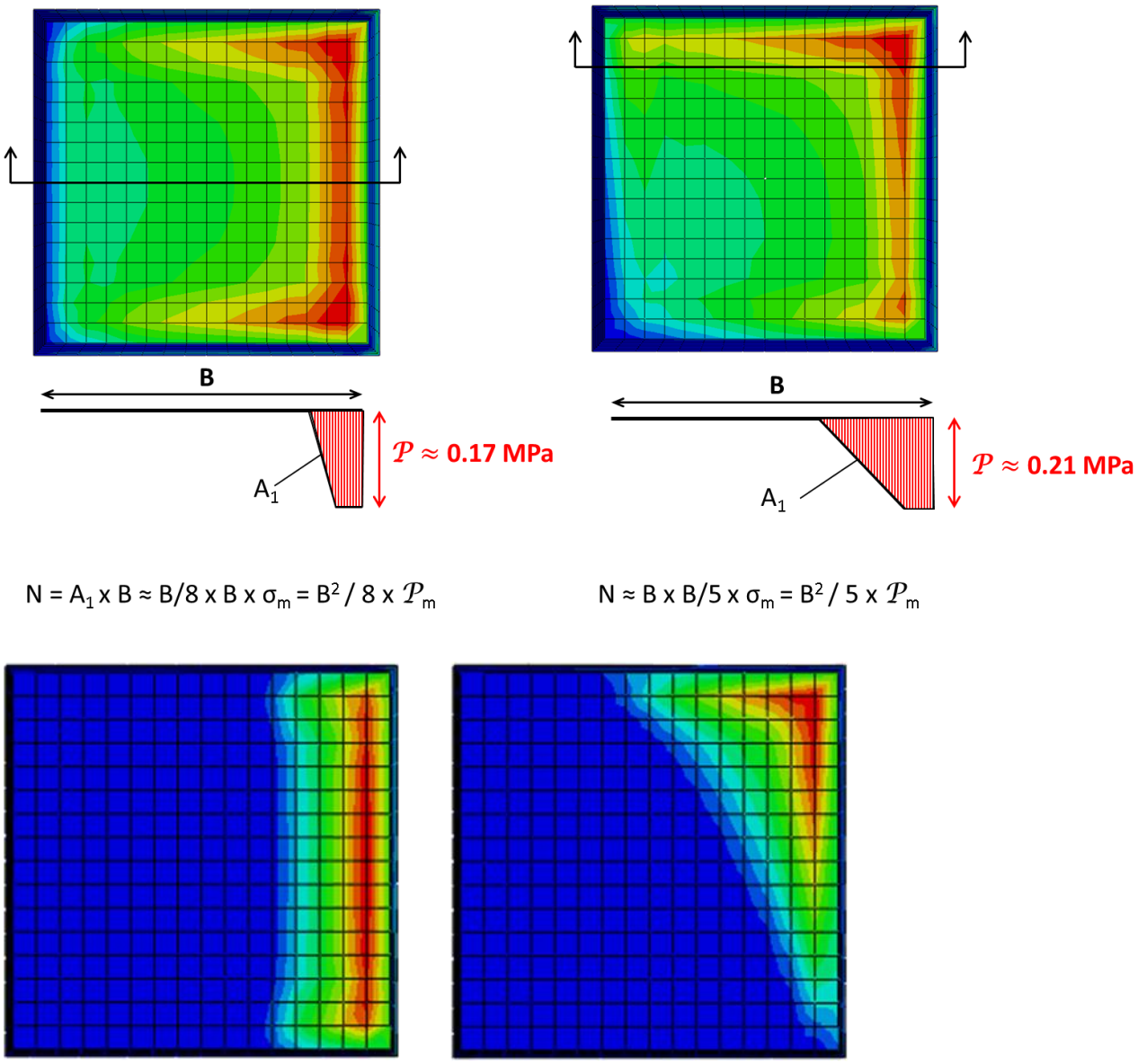

Figure 3.21 Snapshot from the nonlinear static pushover analysis with contours of maximum vertical traction P at the same applied displacement for the aligned footing (left) and the skewed footing (right). With $A1$ is denoted the effective area of the footing at each specific case, with the equivalent von Mises constitutive model **(i)** at the state when maximum vertical traction P are developed; **(ii)** at the initial state, for very small imposed displacement; **(iii)** at an intermediate state of approximate rotation $10\ mrads$.

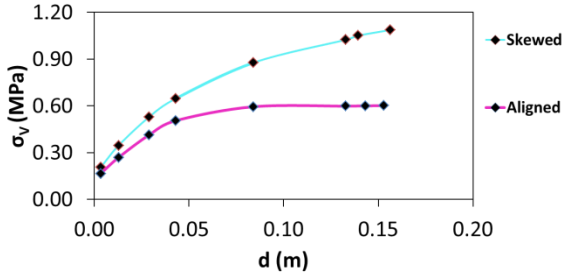

Figure 3.22 Comparison of the maximum developing vertical stress plotted against the imposed displacement on the aligned and the skewed footing.

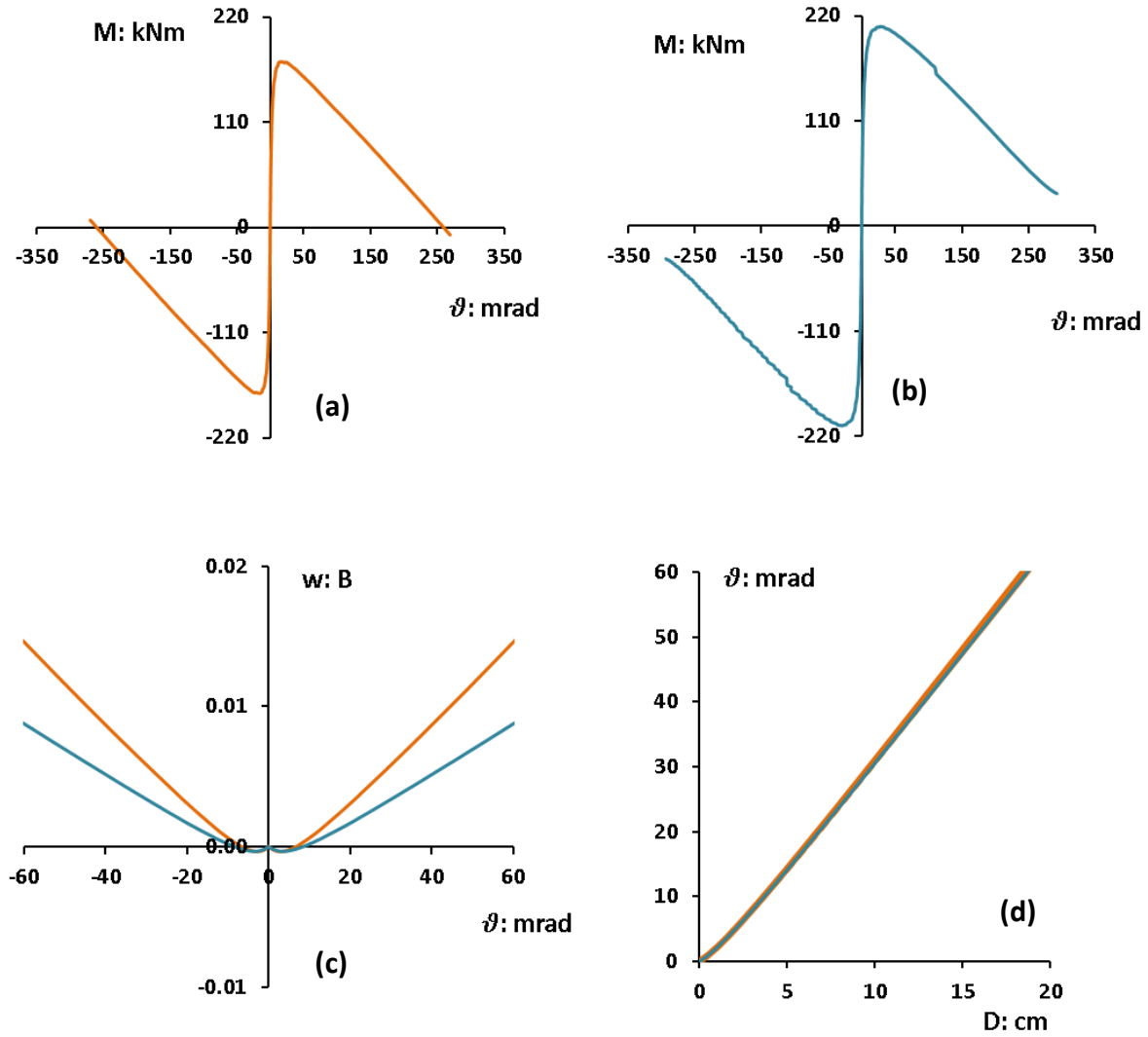

Figure 3.23 Presentation of **(a)** $M - \vartheta$ plots, **(b)** $w/B - \vartheta$ plots from the pushover analysis, with the equivalent von Mises constitutive model **(i)** for the aligned and **(ii)** for the skewed footing; **(c)** comparison of the vertical displacement measured at the rocking edges of **(i)** the aligned and **(ii)** the skewed footing as a function of system's rotation. **(d)** comparison of developing rotation with increasing total displacement between the aligned and skewed footing.

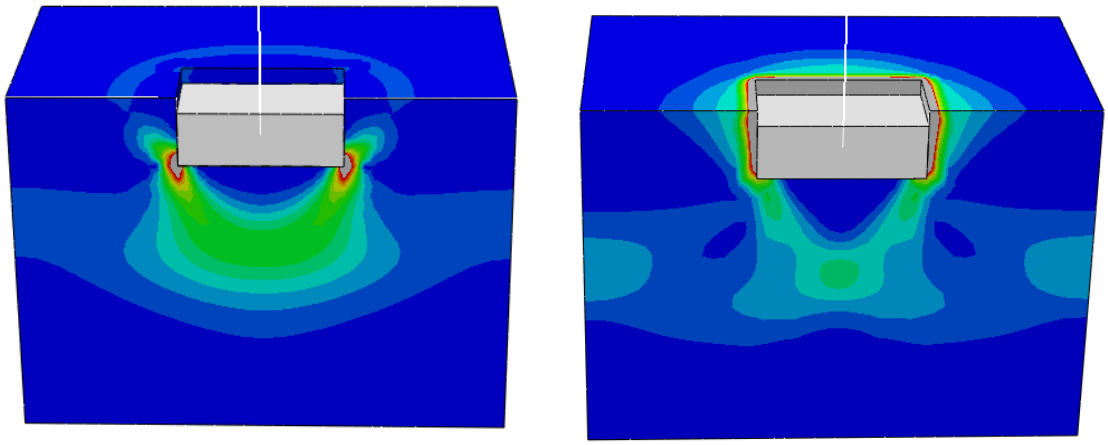

(a) **(b)**

Figure 3.24 Snapshots at failure of push–down nonlinear static analysis, **(a)** considering the von Mises constitutive model and **(b)** considering the Mohr–Coulomb model.

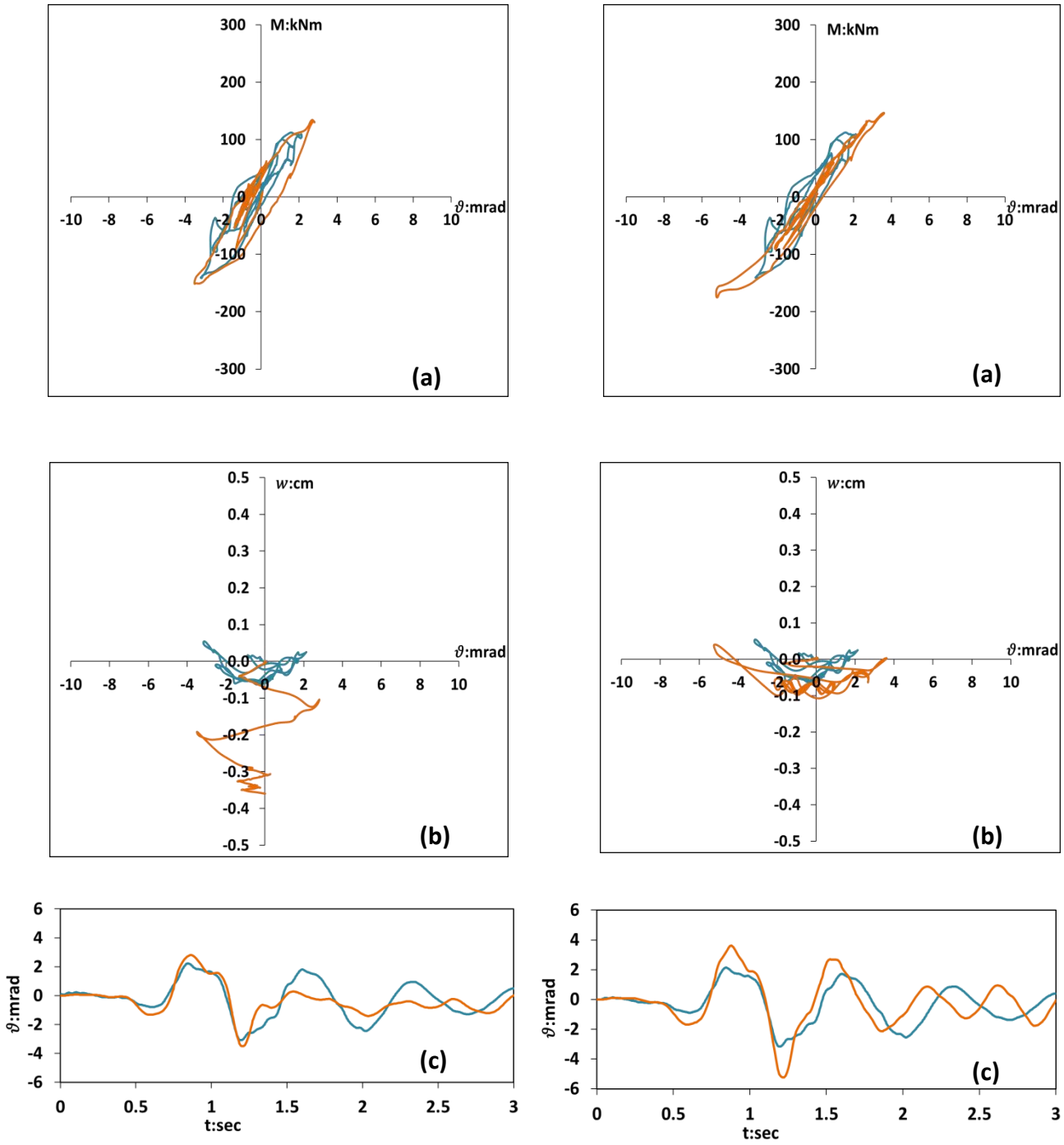

Figure 3.25 Comparison of the dynamic nonlinear FE analysis of the seismic motion **Gilroy Array #1** for the aligned footing between the equivalent **von Mises** constitutive model **(left)** and the **Mohr–Coulomb** failure criterion **(right)**. The blue lines denote the experimental results; the orange lines denote the analytical results.

(a) Overturning moment plotted against the footing rotation, **(b)** Settlement measured at the center of the foundation base plotted against the rotation and **(c)** Footing rotation time history

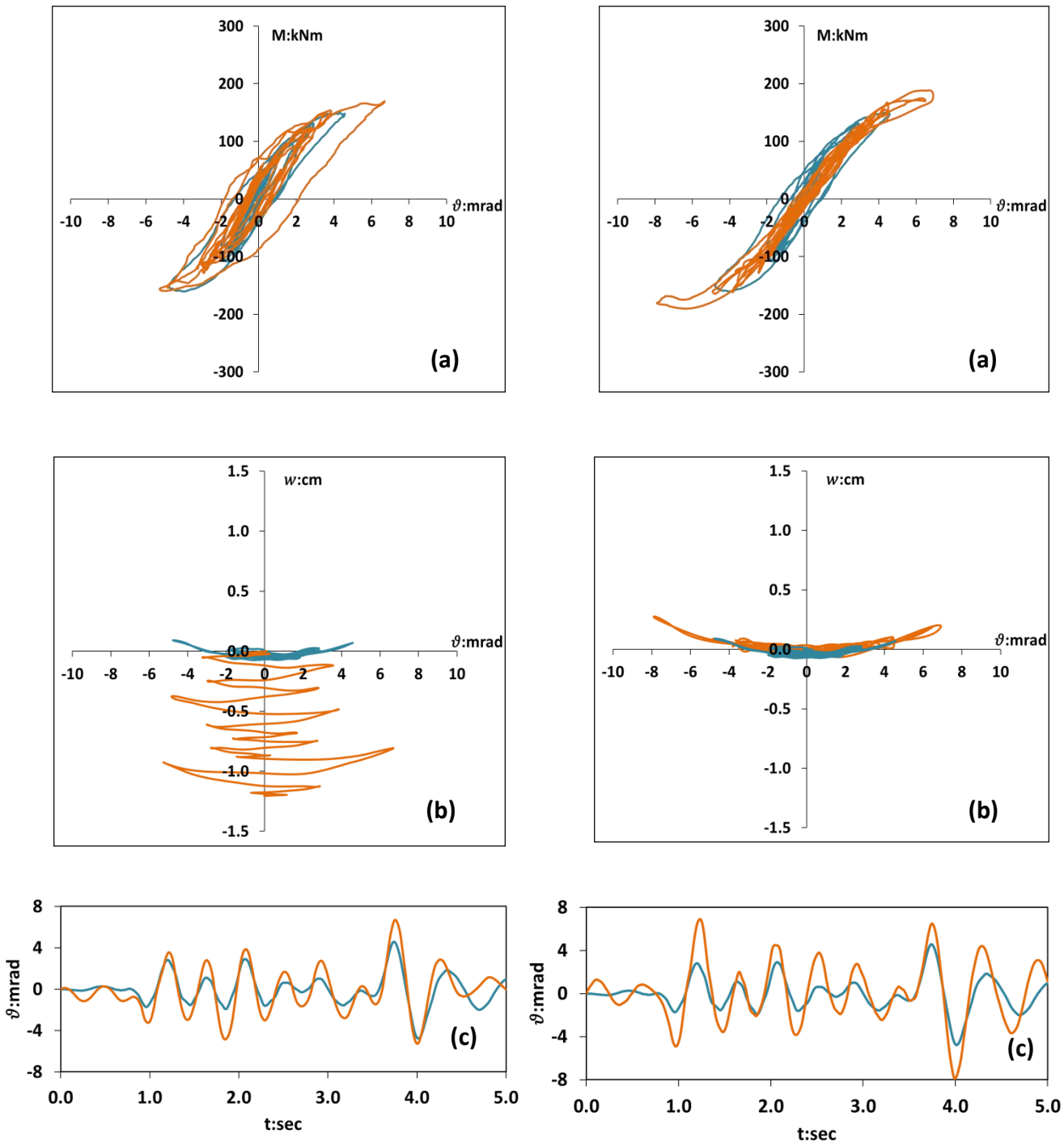

Figure 3.26 Comparison of the dynamic nonlinear FE analysis of the seismic motion **Corralitos** for the aligned footing between the equivalent **von Mises** constitutive model **(left)** and the **Mohr–Coulomb** failure criterion **(right)**. The blue lines denote the experimental results; the orange lines denote the analytical results.

(a) Overturning moment plotted against the footing rotation, **(b)** Settlement measured at the center of the foundation base plotted against the rotation and **(c)** Footing rotation time history

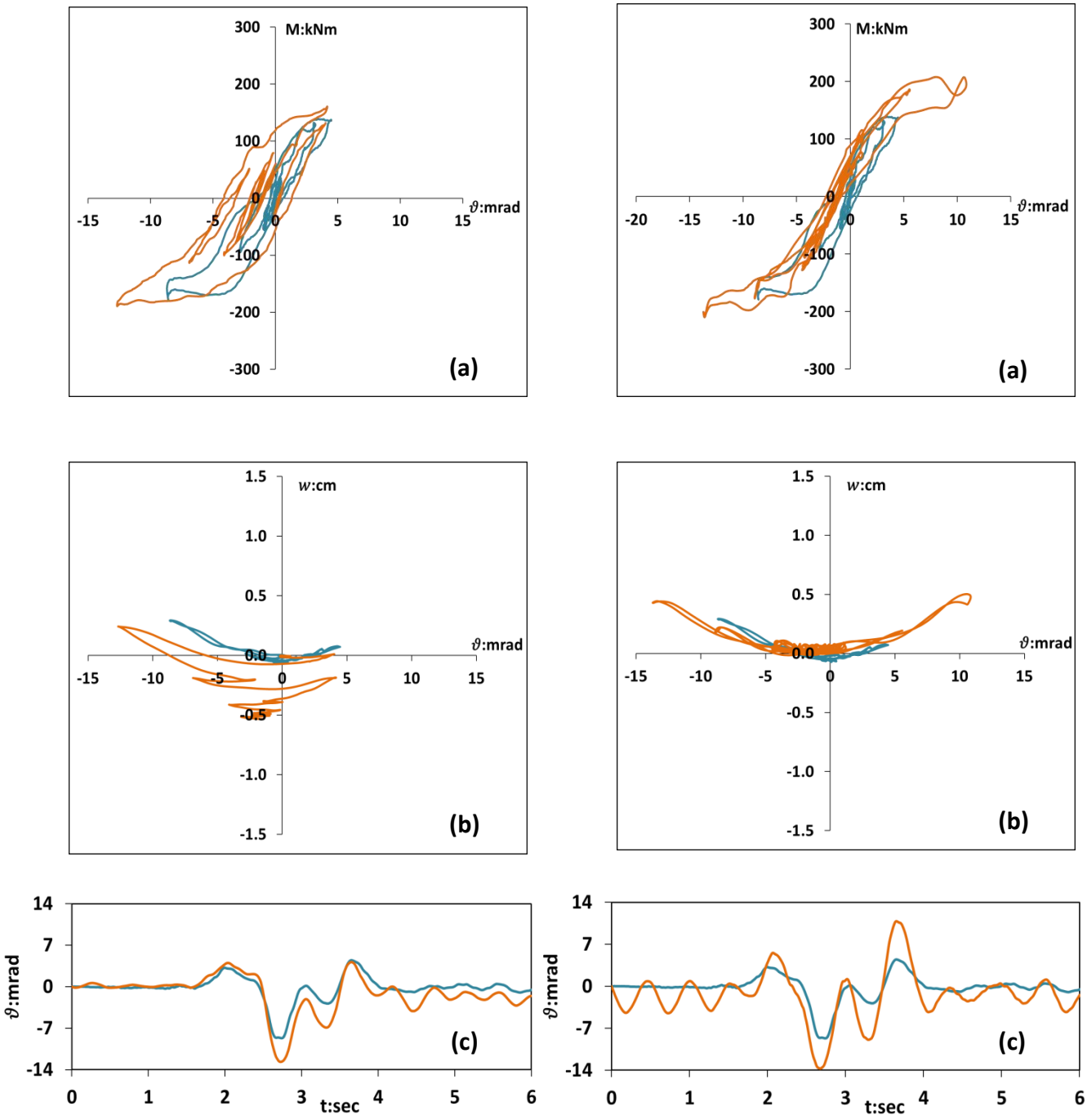

Figure 3.27 Comparison of the dynamic nonlinear FE analysis of the seismic motion **El Centro** for the aligned footing between the equivalent **von Mises** constitutive model **(left)** and the **Mohr–Coulomb** failure criterion **(right)**. The blue lines denote the experimental results; the orange lines denote the analytical results.

(a) Overturning moment plotted against the footing rotation, **(b)** Settlement measured at the center of the foundation base plotted against the rotation and **(c)** Footing rotation time history

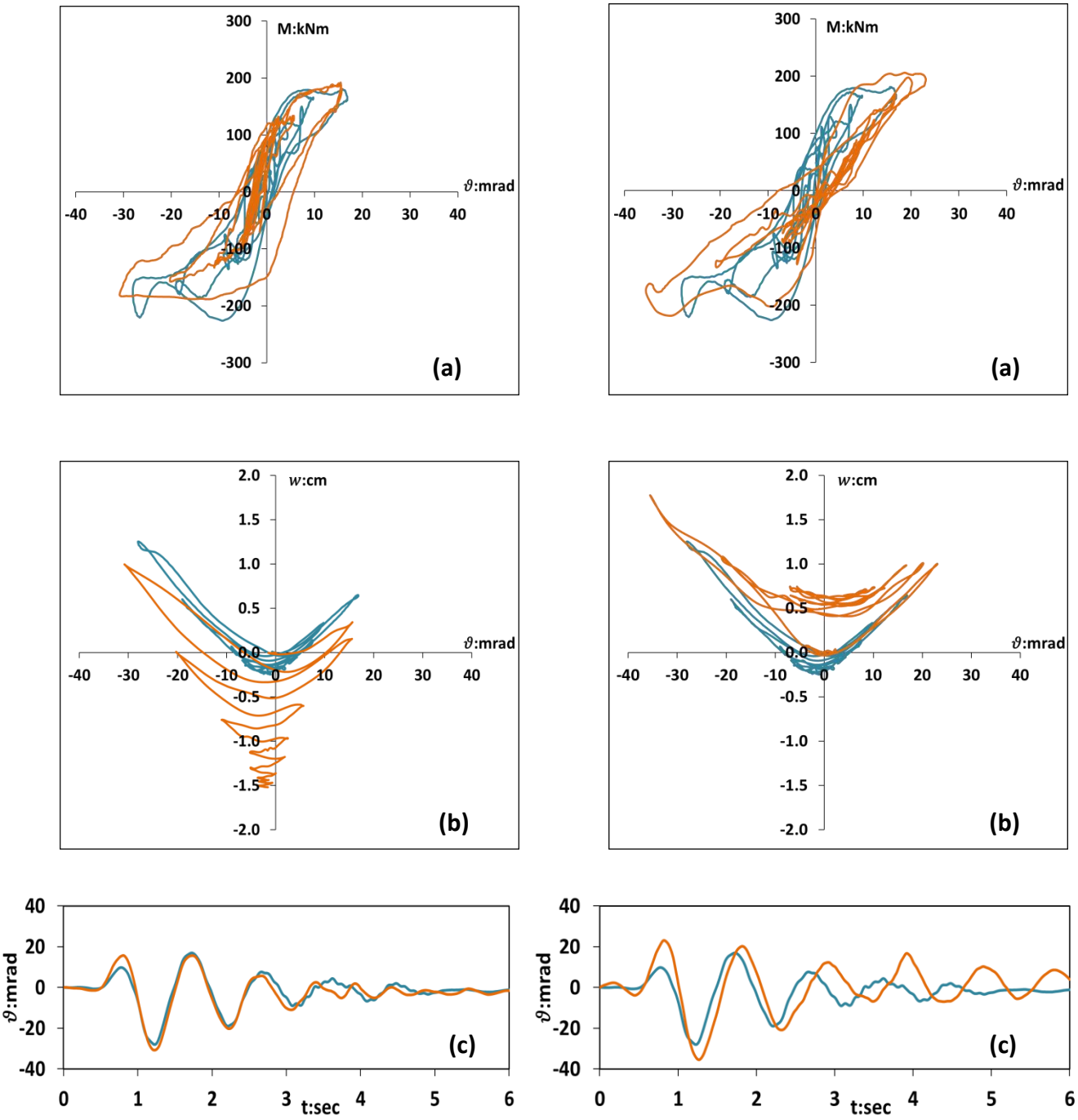

Figure 3.28 Comparison of the dynamic nonlinear FE analysis of the seismic motion **Pacoima Dam** for the aligned footing between the equivalent **von Mises** constitutive model **(left)** and the **Mohr–Coulomb** failure criterion **(right)**. The blue lines denote the experimental results; the orange lines denote the analytical results.
(a) Overturning moment plotted against the footing rotation, **(b)** Settlement measured at the center of the foundation base plotted against the rotation and **(c)** Footing rotation time history

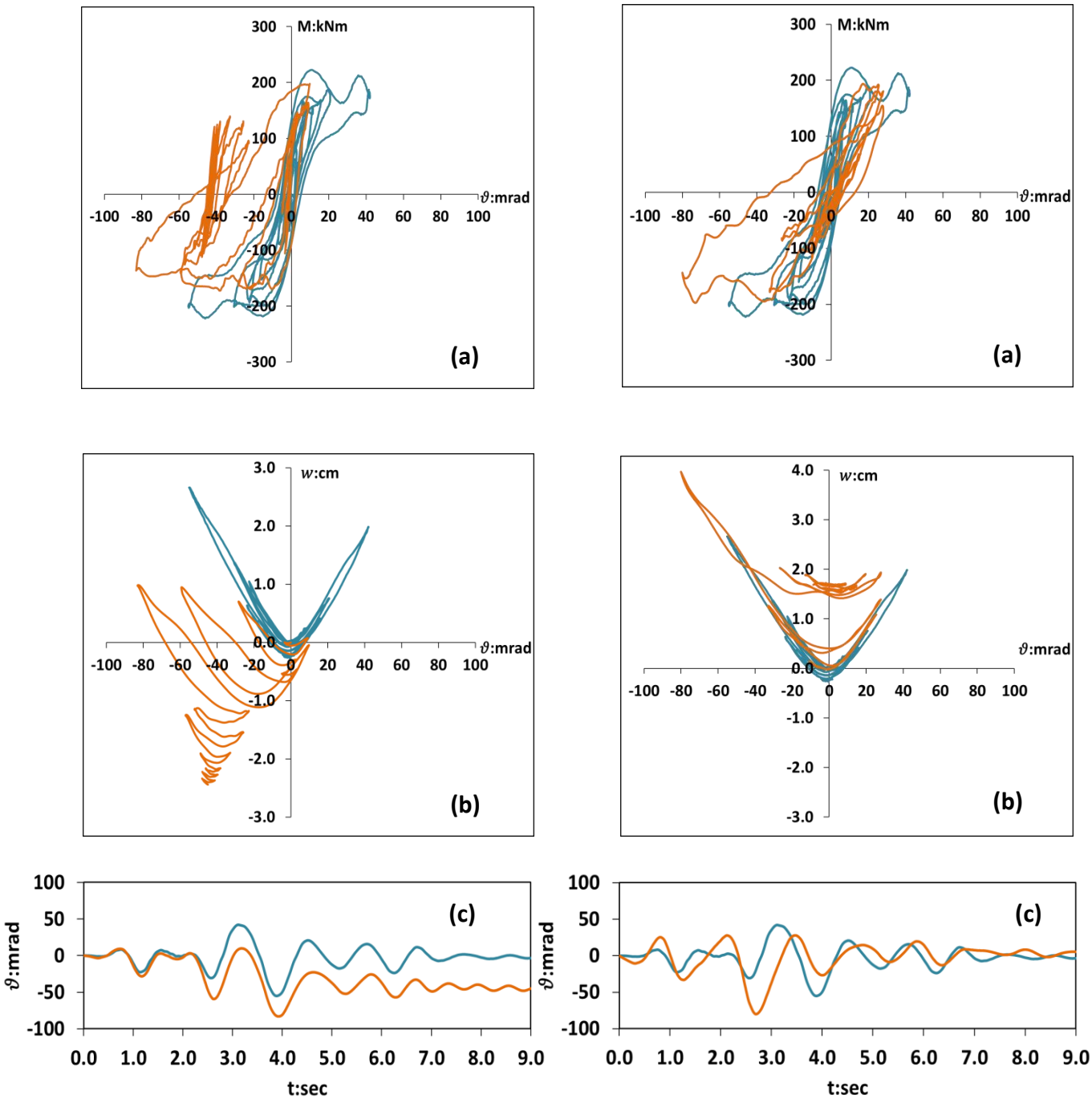

Figure 3.29 Comparison of the dynamic nonlinear FE analysis of the seismic motion **Takatori at 50%** for the aligned footing between the equivalent **von Mises** constitutive model **(left)** and the **Mohr–Coulomb** failure criterion **(right)**. The blue lines denote the experimental results; the orange lines denote the analytical results.

(a) Overturning moment plotted against the footing rotation, **(b)** Settlement measured at the center of the foundation base plotted against the rotation and **(c)** Footing rotation time history

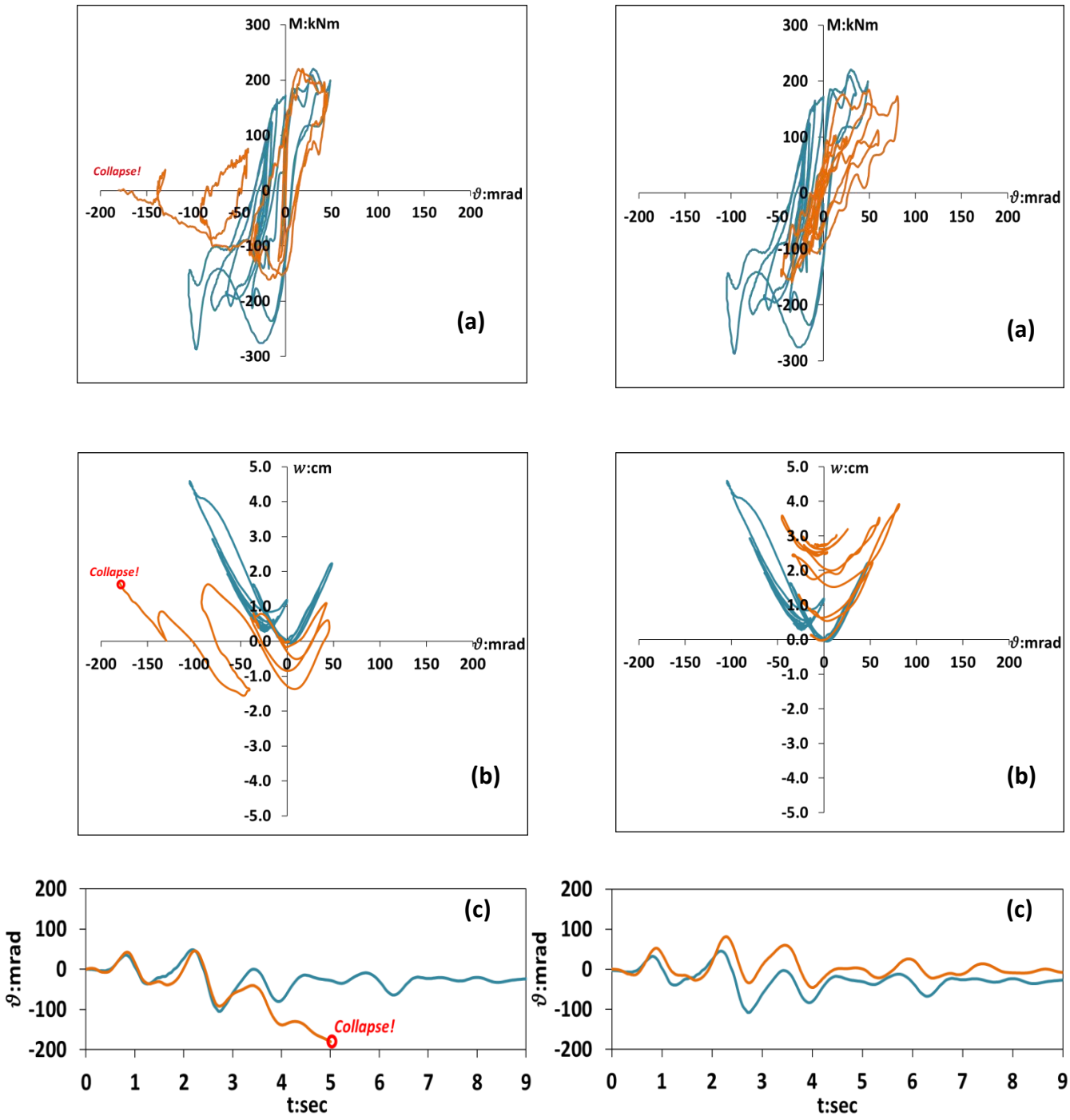

Figure 3.30 Comparison of the dynamic nonlinear FE analysis of the seismic motion **Takatori at 100%** for the aligned footing between the equivalent **von Mises** constitutive model **(left)** and the **Mohr–Coulomb** failure criterion **(right)**. The blue lines denote the experimental results; the orange lines denote the analytical results.

(a) Overturning moment plotted against the footing rotation, **(b)** Settlement measured at the center of the foundation base plotted against the rotation and **(c)** Footing rotation time history

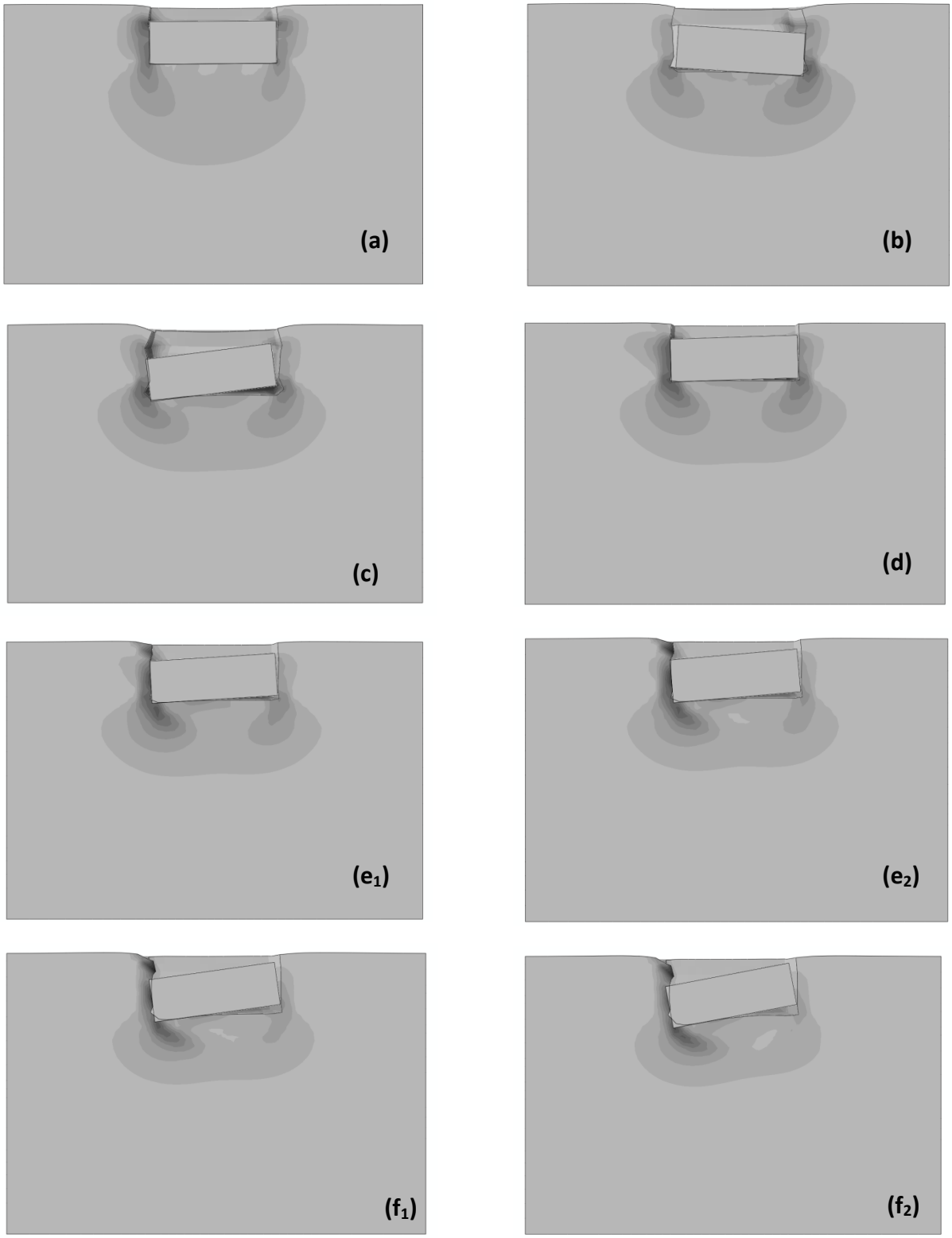

Figure 3.31 Plastification magnitude contours at the moment of the strong pulse of each seismic excitation based on the **von Mises** constitutive model. **(a)** Gilroy Array motion, scaled up by a factor of 10, **(b)** Corralitos motion, scaled up by a factor of 10, **(c)** El Centro motion, scaled up by a factor of 10, **(d)** Pacoima Dam motion, **(e_1)** first pulse of the Takatori (50%) motion, **(e_2)** second pulse of the Takatori (50%) motion, **(f_1)** first pulse of the Takatori (100%) motion, **(f_2)** second pulse of the Takatori (100%) motion.

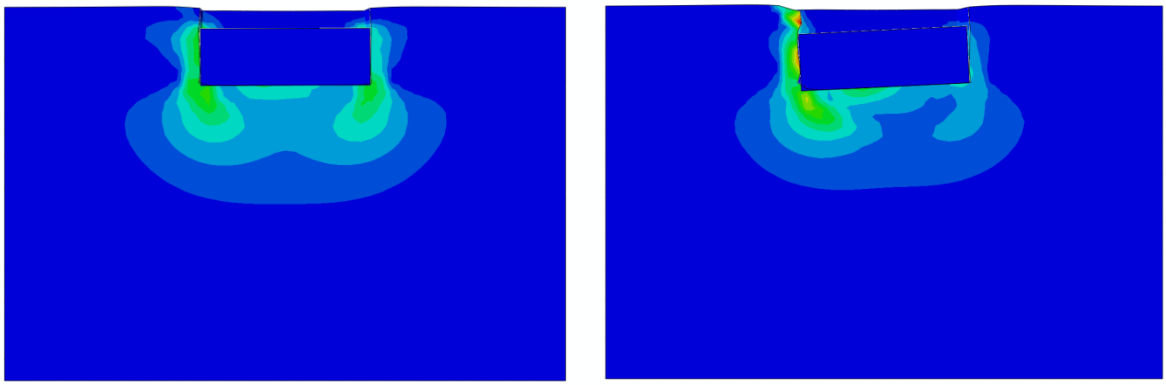

Figure 3.32 Snapshots of plastification magnitude **(a)** after the end of the fourth seismic excitation, Pacoima Dam and **(b)** after the end of the fifth seismic excitation, Takatori (50

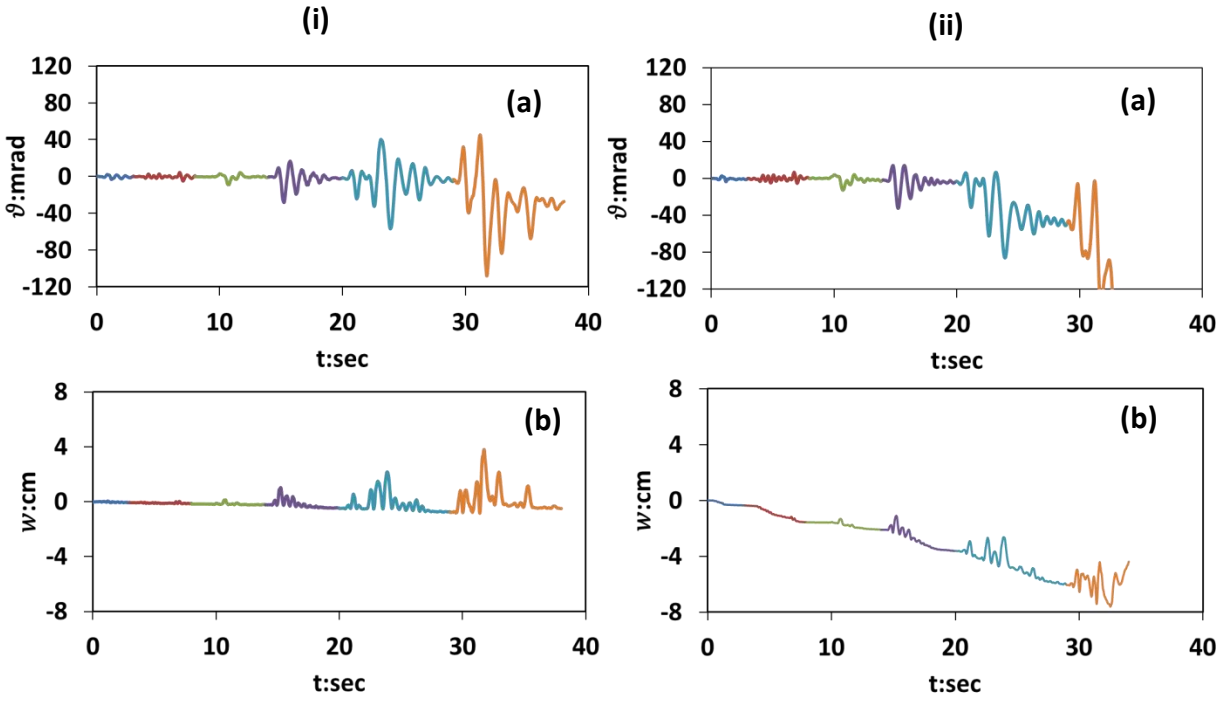

Figure 3.33 Comparison between the progression of **(a)** cumulative rotations and **(b)** cumulative settlements **(i)** as they were recorded during experiments and **(ii)** as they were measured during the FE analyses with the von Mises constitutive model for the aligned structure.

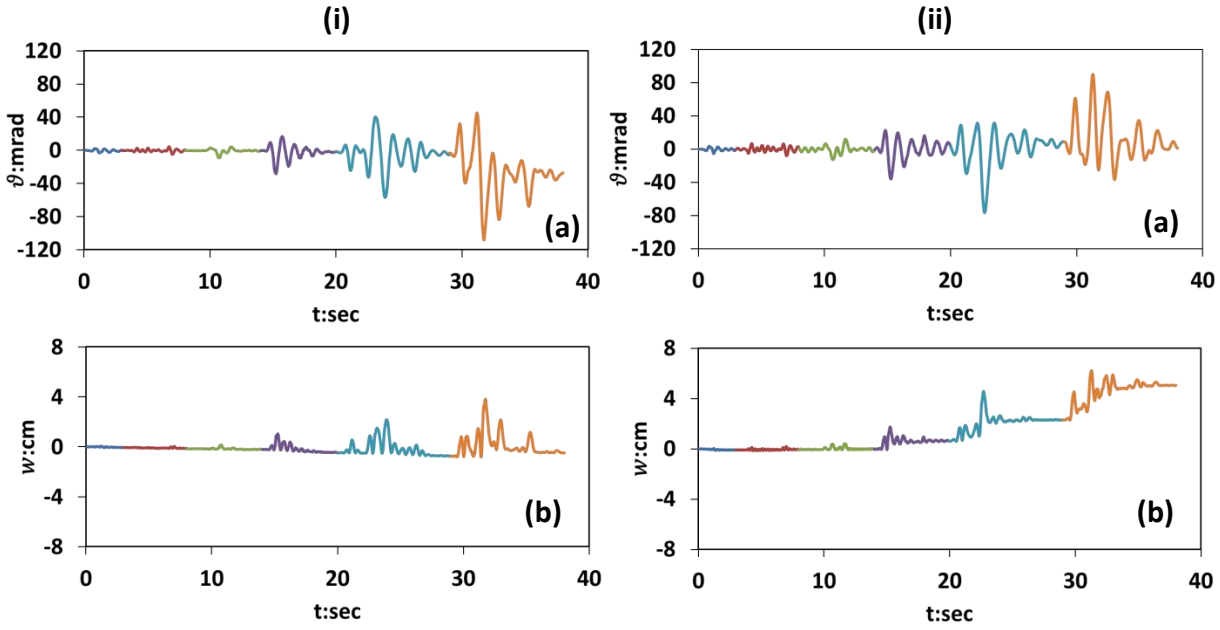

Figure 3.34 The six time histories of **(a)** rotation and **(b)** the settlement **(i)** as they were recorded during experiments and **(ii)** as they were computed during the FE analyses with the Mohr–Coulomb constitutive model.

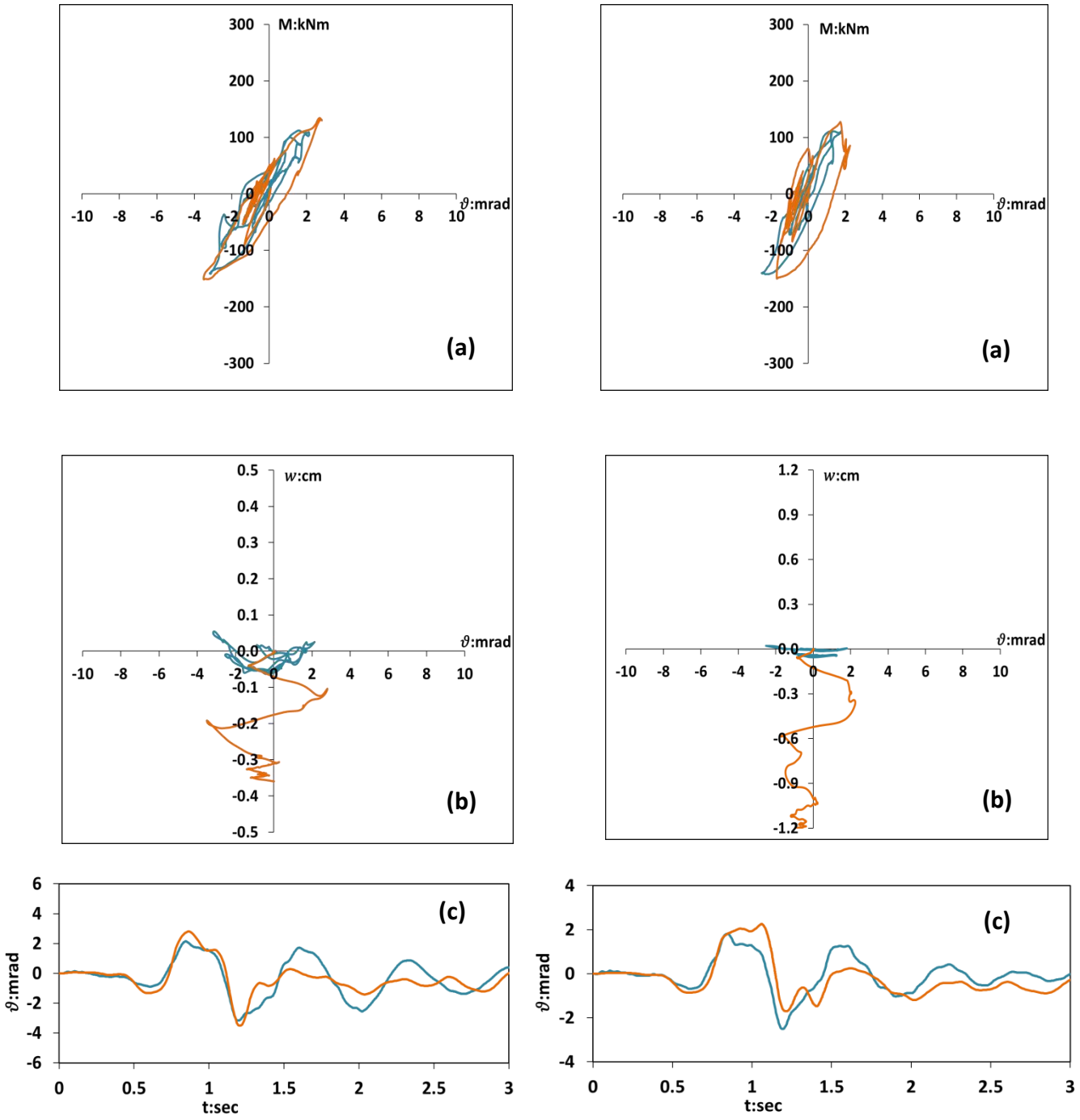

Figure 3.35 Comparison of the dynamic nonlinear FE analysis of the seismic motion **Gilroy Array #1** for the equivalent **von Mises** constitutive model between the **aligned footing (left)** and the **skewed footing (right).** The blue lines denote the experimental results; the orange lines denote the analytical results.

(a) Overturning moment plotted against the footing rotation, **(b)** Settlement measured at the center of the foundation base plotted against the rotation and **(c)** Footing rotation time history

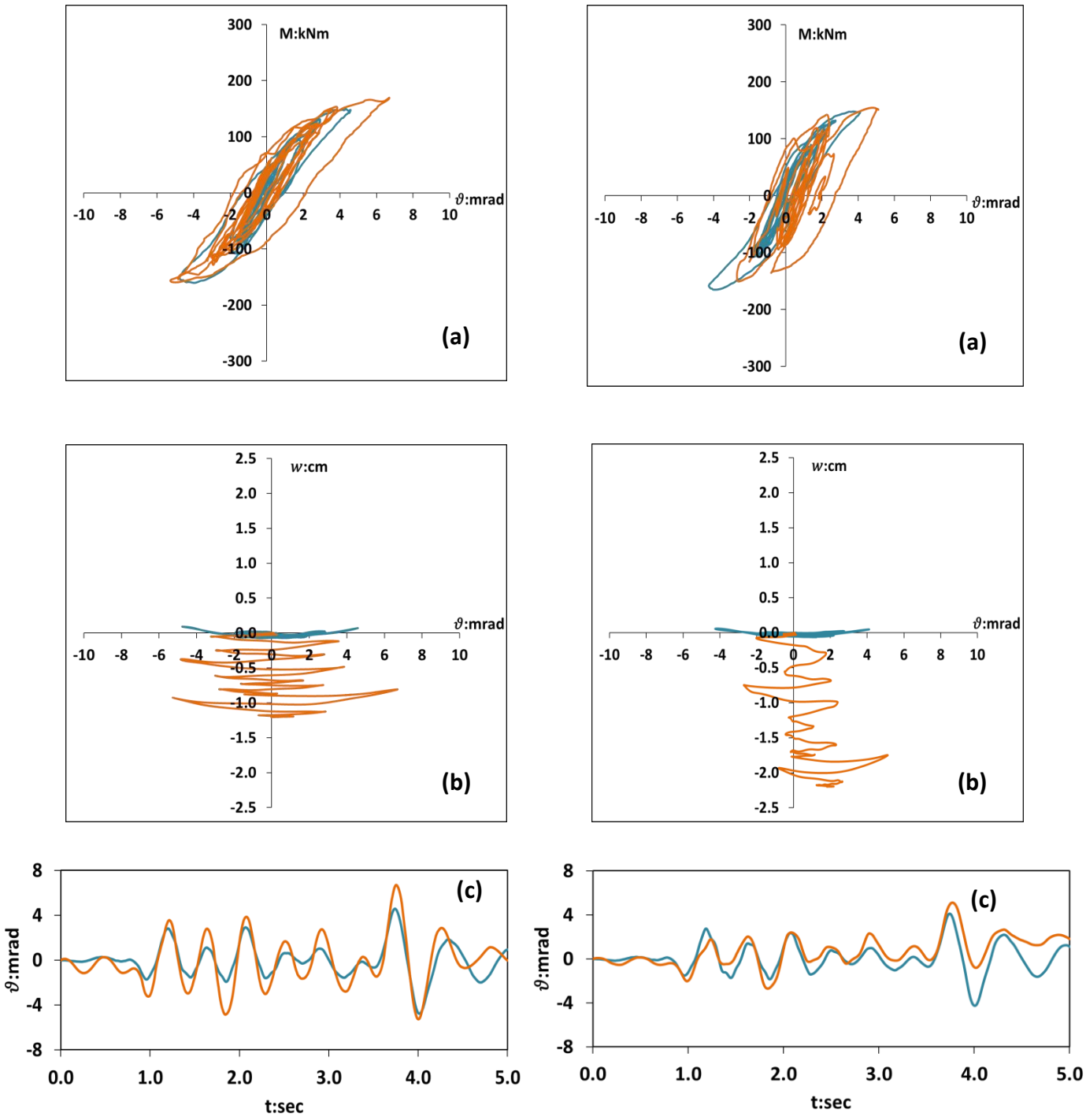

Figure 3.36 Comparison of the dynamic nonlinear FE analysis of the seismic motion **Corralitos** for the equivalent **von Mises** constitutive model between the **aligned footing (left)** and the **skewed footing (right).** The blue lines denote the experimental results; the orange lines denote the analytical results. **(a)** Overturning moment plotted against the footing rotation, **(b)** Settlement measured at the center of the foundation base plotted against the rotation and **(c)** Footing rotation time history

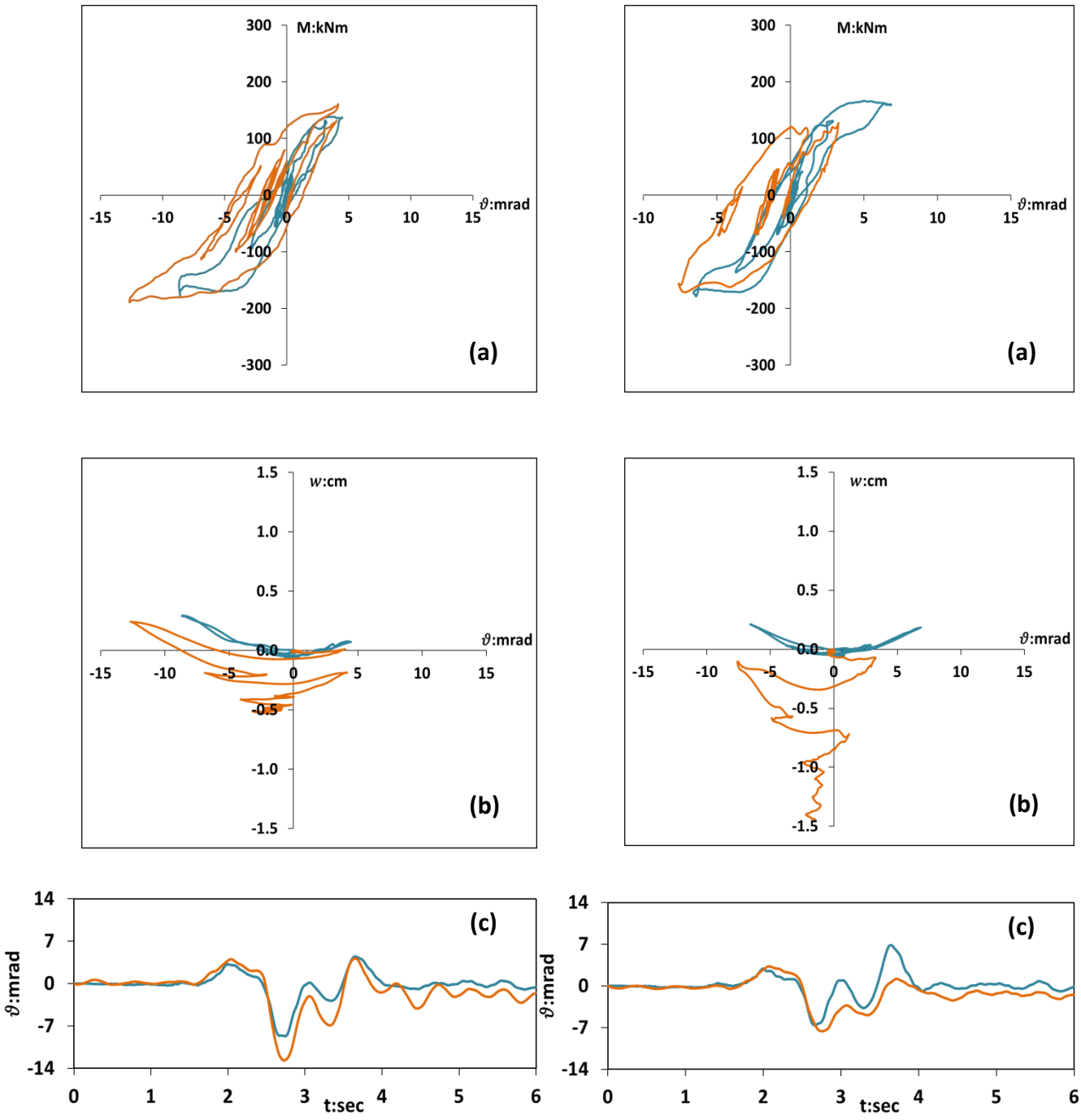

Figure 3.37 Comparison of the dynamic nonlinear FE analysis of the seismic motion **El Centro** for the equivalent **von Mises** constitutive model between the **aligned footing (left)** and the **skewed footing (right).** The blue lines denote the experimental results; the orange lines denote the analytical results. **(a)** Overturning moment plotted against the footing rotation, **(b)** Settlement measured at the center of the foundation base plotted against the rotation and **(c)** Footing rotation time history

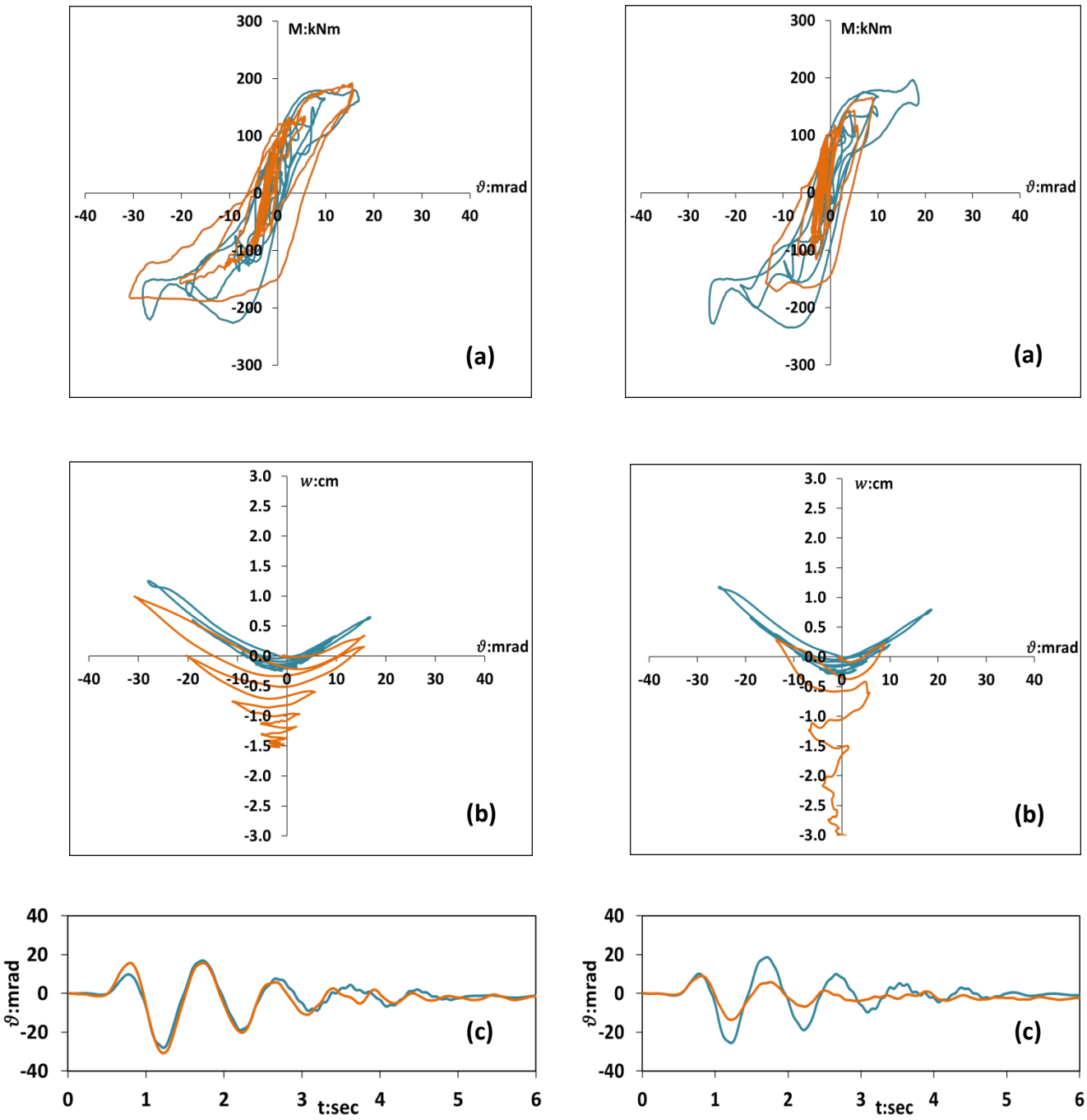

Figure 3.38 Comparison of the dynamic nonlinear FE analysis of the seismic motion **Pacoima Dam** for the equivalent **von Mises** constitutive model between the **aligned footing (left)** and the **skewed footing (right).** The blue lines denote the experimental results; the orange lines denote the analytical results.

(a) Overturning moment plotted against the footing rotation, **(b)** Settlement measured at the center of the foundation base plotted against the rotation and **(c)** Footing rotation time history

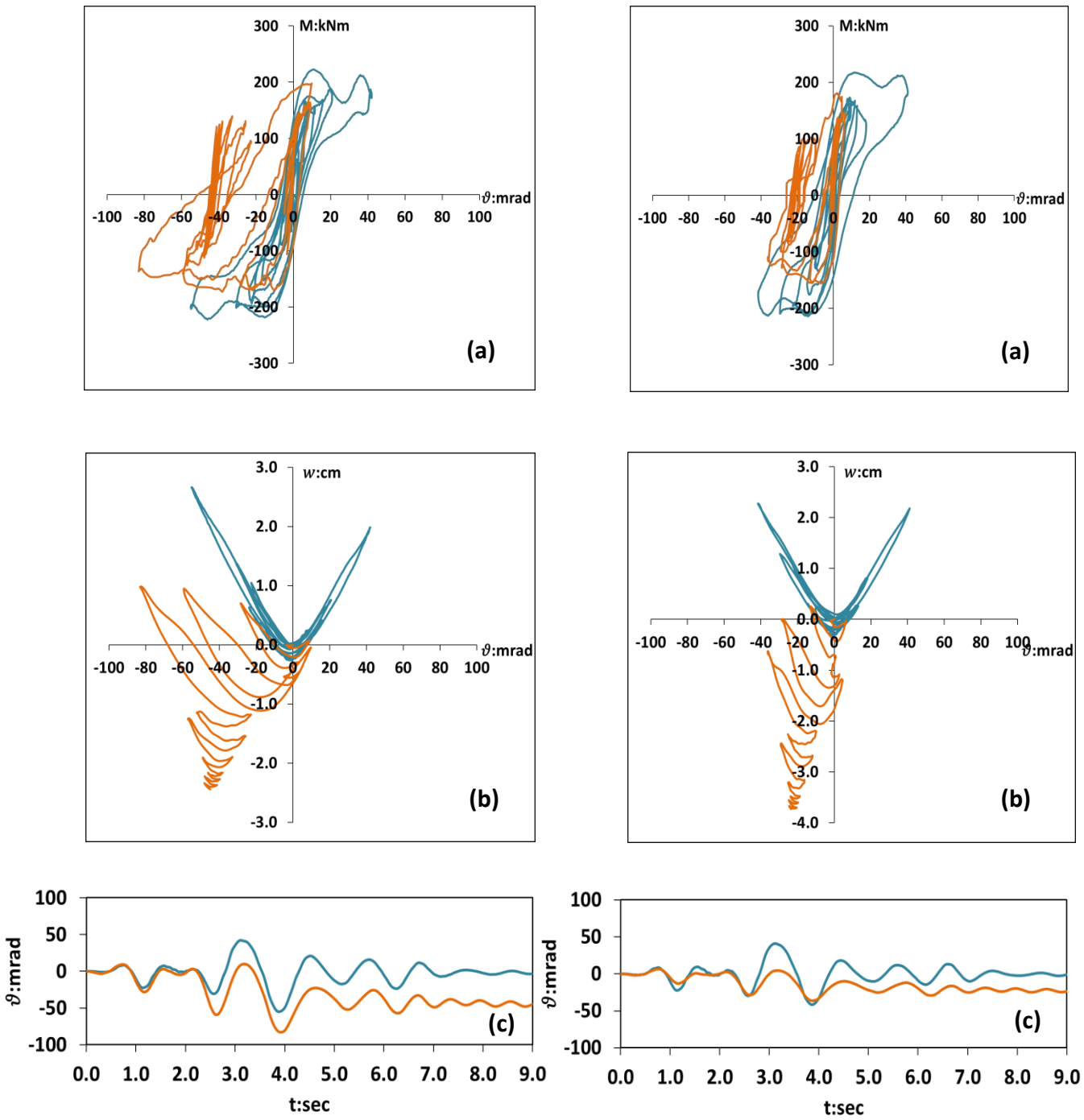

Figure 3.39 Comparison of the dynamic nonlinear FE analysis of the seismic motion **Takatori at 50%** for the equivalent **von Mises** constitutive model between the **aligned footing (left)** and the **skewed footing (right).** The blue lines denote the experimental results; the orange lines denote the analytical results.

(a) Overturning moment plotted against the footing rotation, **(b)** Settlement measured at the center of the foundation base plotted against the rotation and **(c)** Footing rotation time history

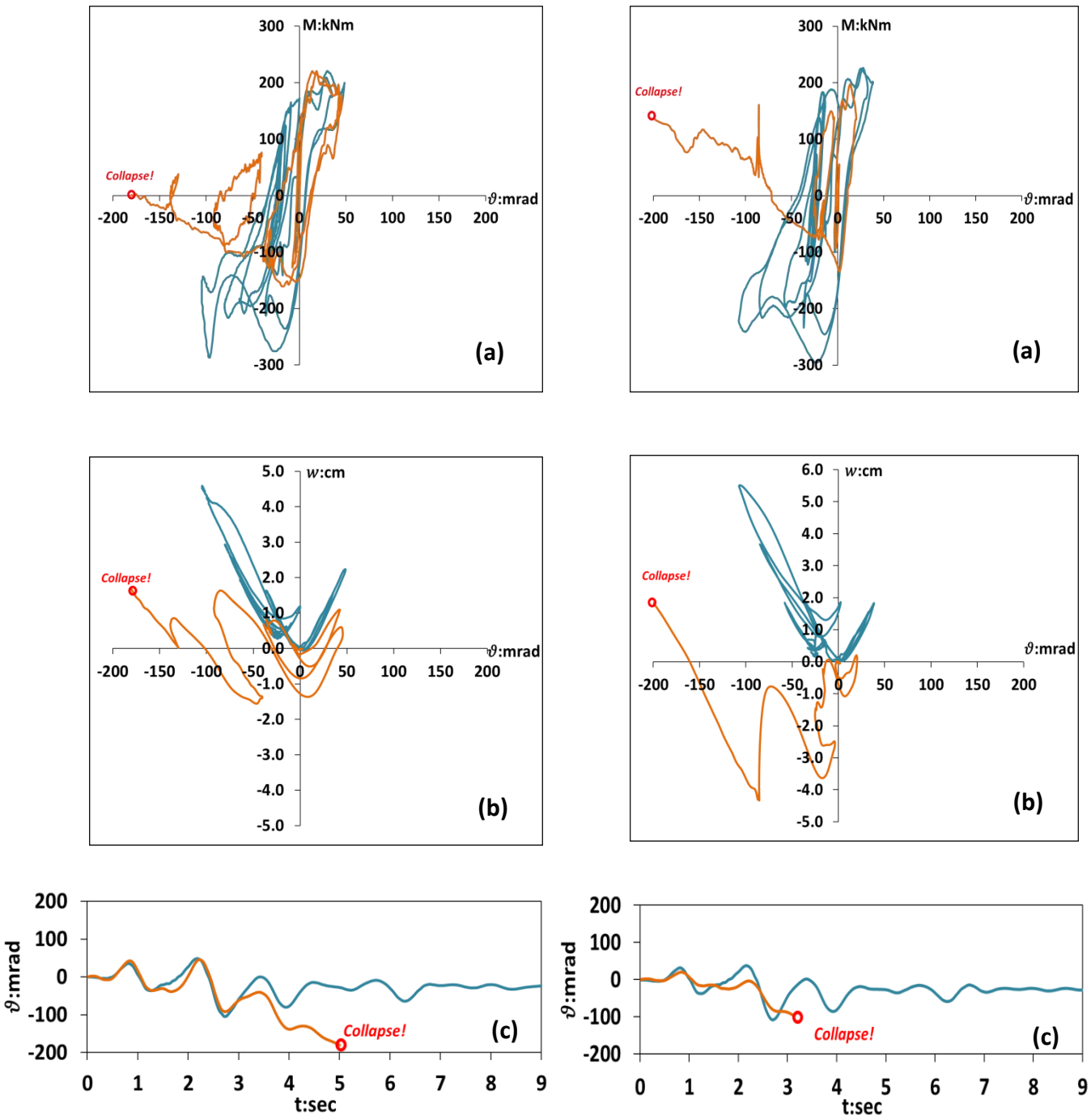

Figure 3.40 Comparison of the dynamic nonlinear FE analysis of the seismic motion **Takatori at 100%** for the equivalent **von Mises** constitutive model between the **aligned footing (left)** and the **skewed footing (right).** The blue lines denote the experimental results; the orange lines denote the analytical results.

(a) Overturning moment plotted against the footing rotation, **(b)** Settlement measured at the center of the foundation base plotted against the rotation and **(c)** Footing rotation time history

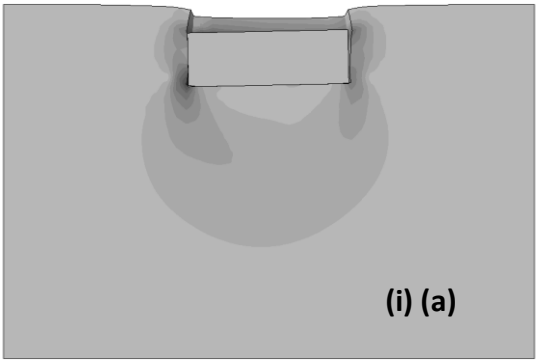

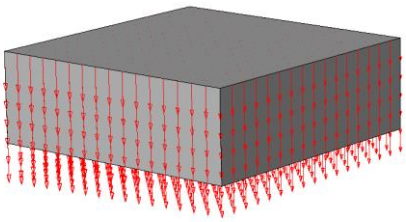

(ii) (a)

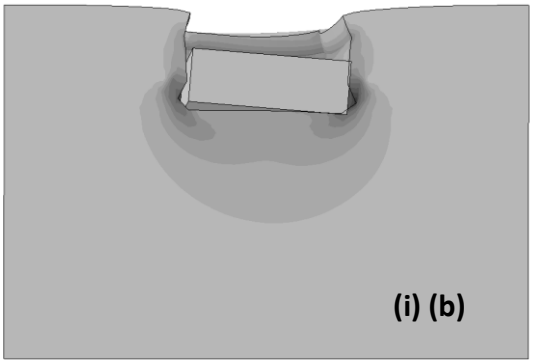

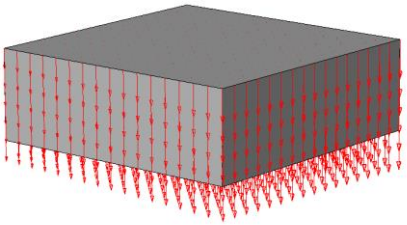

(ii) (b)

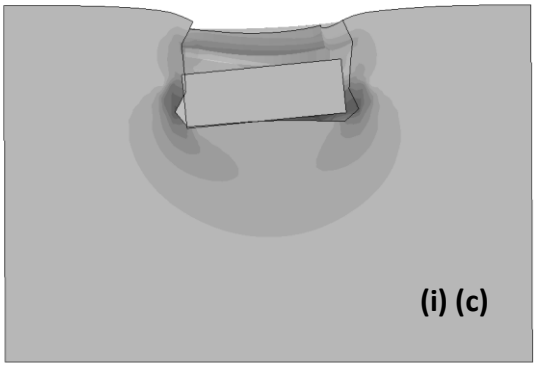

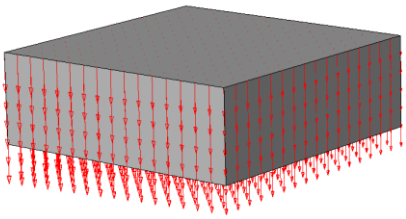

(ii) (c)

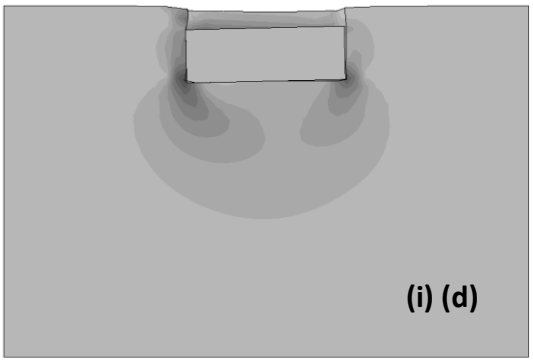

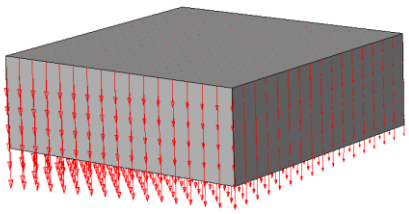

(ii) (d)

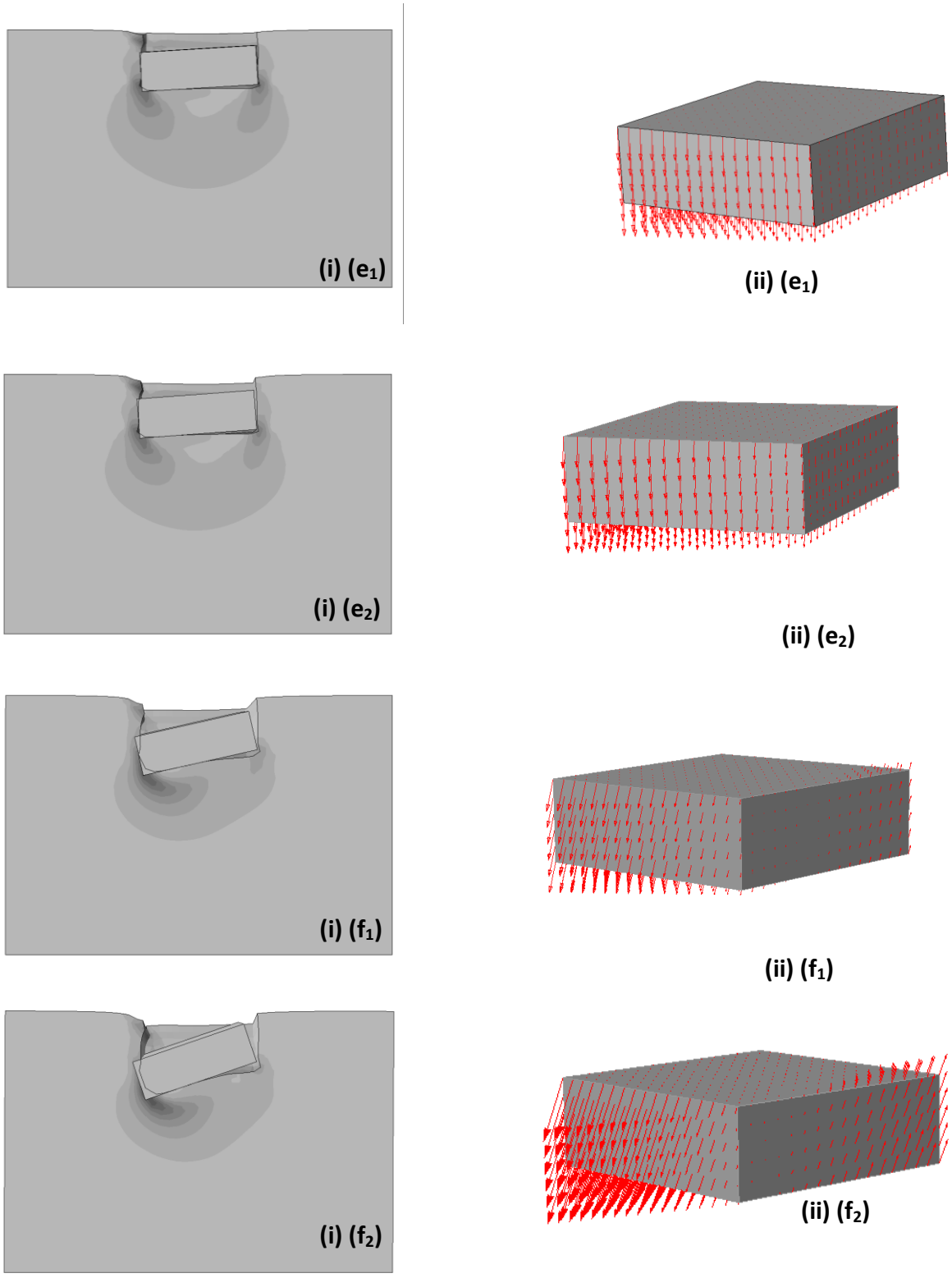

Figure 3.41 Snapshots of plastification magnitude and distribution of vertical displacements underneath the footing at the moment when the strong pulse of each seismic excitation acts. The results stem from the analysis with the **von Mises** constitutive model **(a)** snapshot at of the Gilroy Array motion, scaled up by a factor of 10, **(b)** snapshot of the Corralitos motion, scaled up by a factor of 10, **(c)** snapshot of the El Centro motion, scaled up by a factor of 10, **(d)** snapshot of the Pacoima Dam motion, **(e_1)** snapshot during the first pulse of the Takatori (50%) motion, **(e_2)** snapshot during the second pulse of the Takatori (50%) motion, **(f_1)** snapshot during the first pulse of the Takatori (100%) motion, **(f_2)** snapshot during the second pulse of the Takatori (100%) motion.

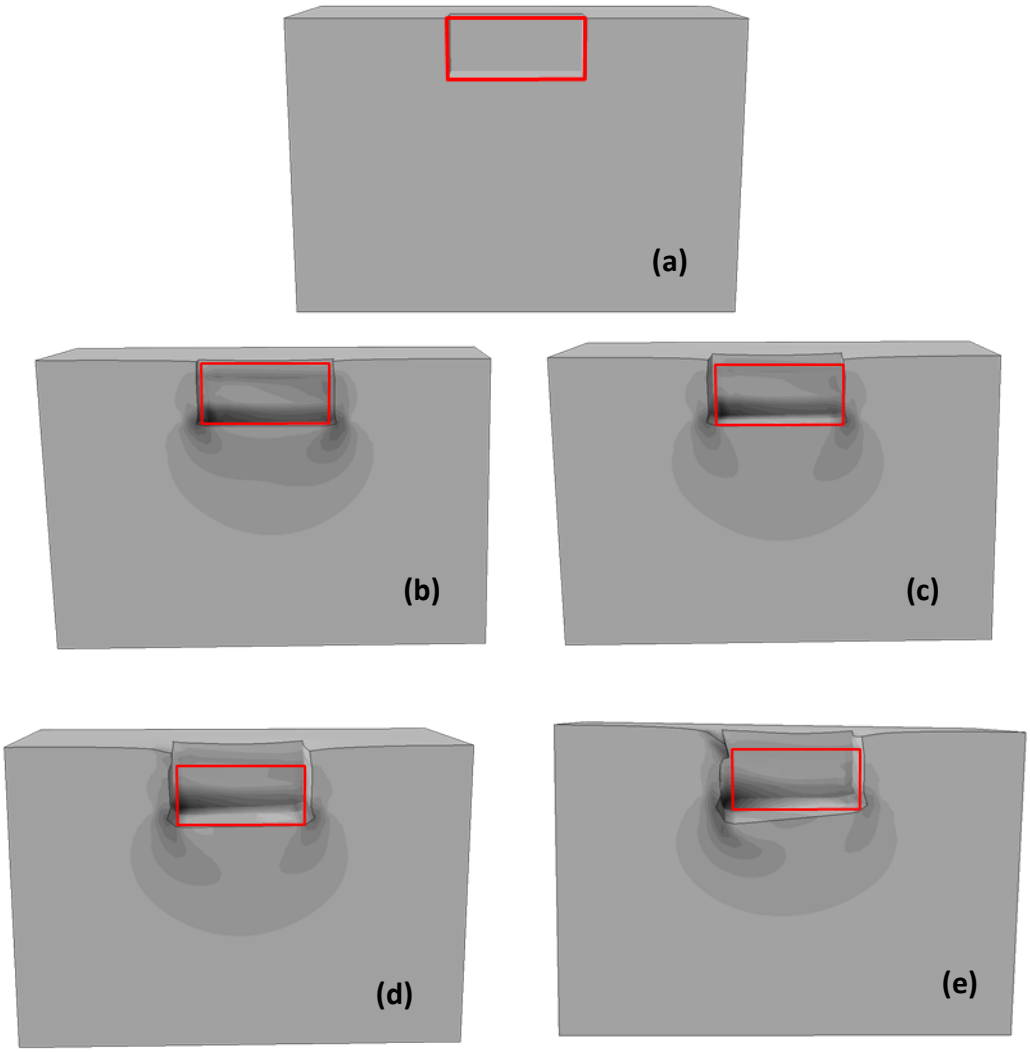

Figure 3.42 Snapshots of the deformed mesh showing with contous the distribution of the plastic deformation in and around the trench, where the footing is embedded. Red frame indicates the undeformed shape of the trench.

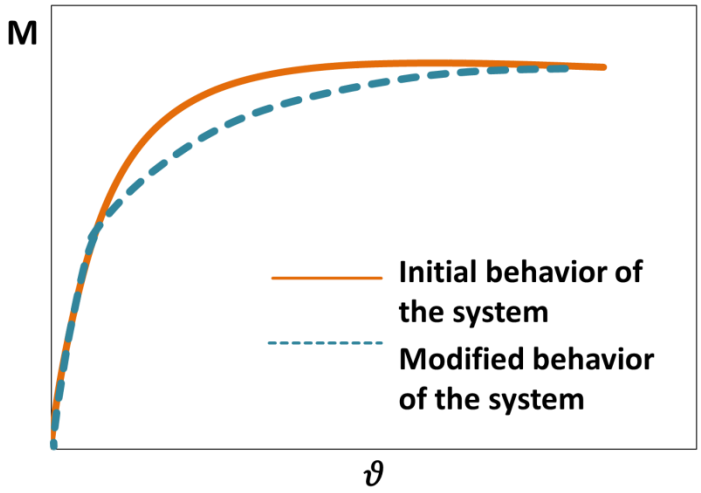

Figure 3.43 Sketch presenting the response in terms of M-ϑ. The orange line denotes the response in the undeformed trench, the blue line denotes the response in the permanently

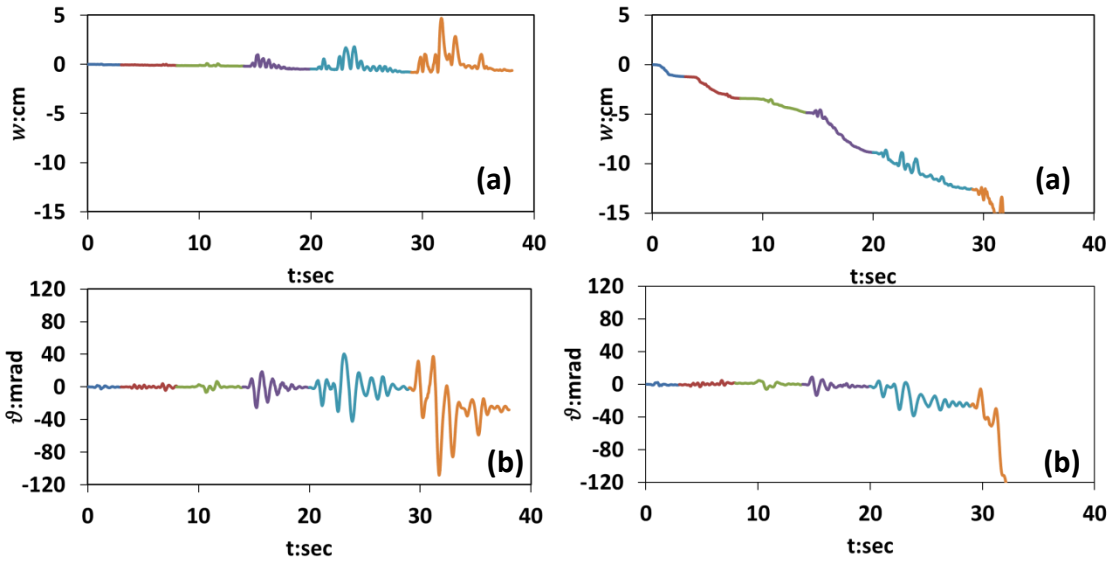

Figure 3.44 The six time histories of **(a)** rotation and **(b)** the settlement **(i)** as they were recorded during experiments and **(ii)** as they were computed during the FE analyses for the skewed footing with the **von-Mises** constitutive model.

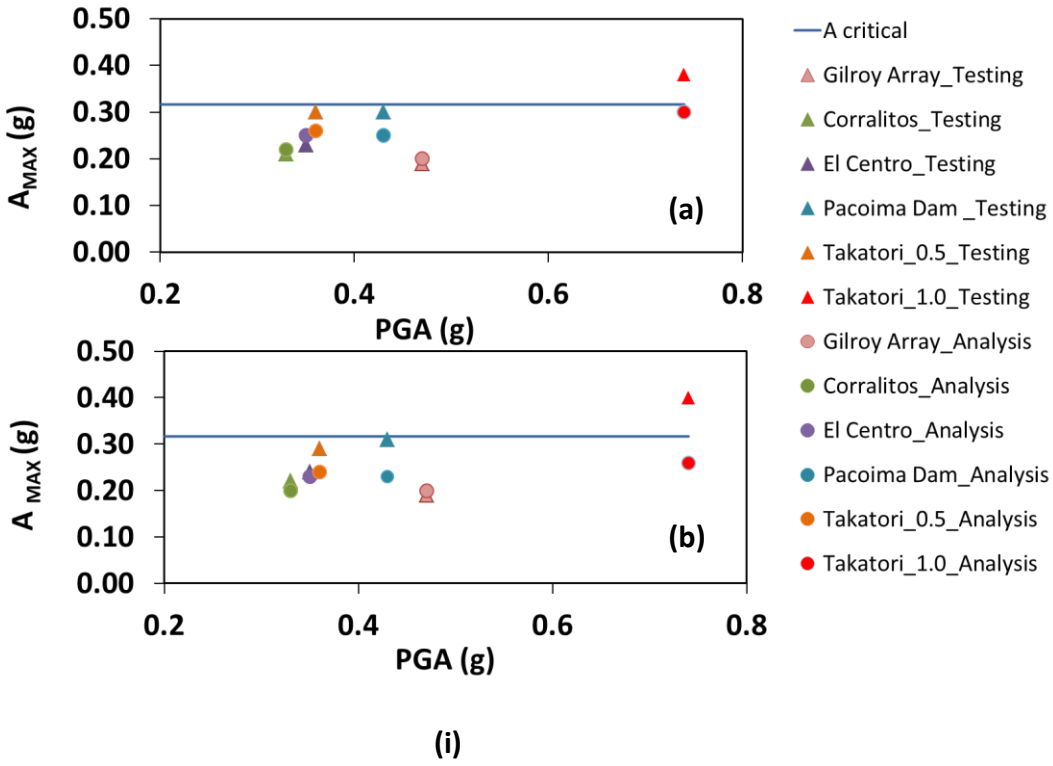

(i)

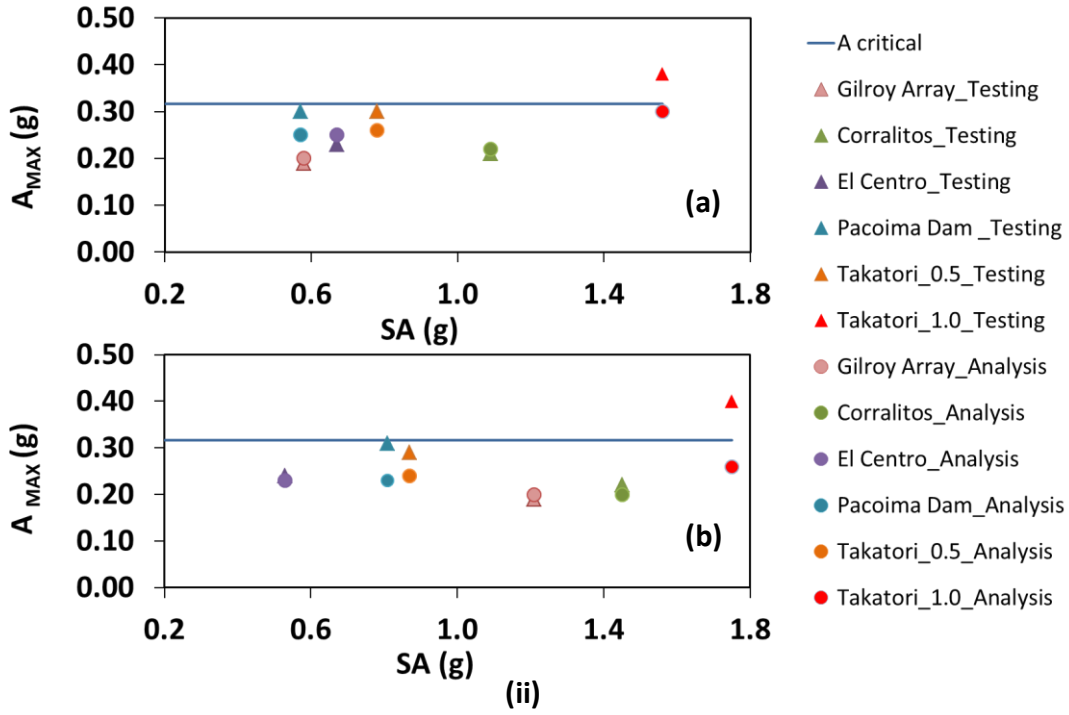

Figure 3.45 The maximum acceleration at the oscillator mass as it was recorded during testing and as it was computed with the FE analyses, is plotted as a function of the **(i)** PGA of each seismic excitation and **(ii)** Spectral Acceleration, which would have been developed in each case of the seismic excitations; **(a)** for the aligned footing and **(b)** for the skewed footing. The results of both the shake table tests and the analyses are also compared with the critical acceleration a_c, computed on the basis of the results of monotonic (static) pushover analyses.

Chapter 4

Chapter 4

Parametric Investigation of Dynamic Response in Biaxial Excitations

INTRODUCTION

As seen in the previous Chapter, when the loading is imposed in the two lateral directions, regardless of the nature of loading (static or dynamic), its behavior changes significantly, compared to the response in uniaxial loading. This difference in the response is attributed to the extremely localized concentration of normal traction on the soil-footing interface, forcing the rectangular footing to penetrate the underlying soil. Consequently, larger settlements occur, causing excessive plastifications on the soil surface. Especially when it comes to cyclic loading these plastic deformations curve the soil, thus obstructing the footing to re-center. In an effort to follow the cyclic motion, toward the opposite

direction, the footing pushes the curved soil downwards, leading to even greater settlements, without however being able to develop equally large rotation on the other side. This behavior results in the footing maintaining residual rotation, much earlier in the motion, compared to the aligned.

Since in reality the seismic motions do occur in two directions (three actually, but the vertical component is of negligible importance in such problems), in this chapter it is attempted to further investigate the rocking response under cyclic biaxial loading by parametrically varying the angle of the seismic motion. In this way useful conclusions are drawn, which shed light on the seismic response of a rectangular footing, when excited in two directions.

1. PARAMETRIC PUSHOVER ANALYSES

Three characteristic angles are investigated in the parametric study namely: 0˚, 15˚, 30˚ and 45˚. Obviously, due to the symmetrical shape of the footing, it would be needless to investigate angles outside the range of a quadrant. By varying the angle of the loading, practically we vary the relative intensity of the two components. In this way we change each time the width of the footing, i. e. the dimension parallel to the direction of loading and by extension we change the slenderness ratio, which as already mentioned, controls the uplifting response of the system. The alteration of the footing's effective width leads also to the fluctuation of the footing area, which remains in contact with the underlying soil, as the footing rocks. These geometrical characteristics influence significantly the response of the system, as presented below.

As a first step, monotonic static pushover analyses are performed, the results of which are plotted in **Figures 4.1, 4.2** and **4.3. Figure 4.1** demonstrates the results in terms of moment rotation for the four cases examined. Observe that in the case of the aligned footing (loading is imposed by 0˚) the system has an overall smaller moment capacity than any other case. This effect is much clearer in **Figure 4.3c**, where the results for all investigated angles are plotted in terms of M-ϑ. Another interesting fact is that the moment capacity is practically independent of the exact value of the angle, by which the loading is imposed. It is clear from **Figure 4.3** that, the $M_c \approx 170\ kNm$ for the aligned footing, whereas for all other cases $M_c \approx 210\ kNm$. This difference is attributed to the lateral confinement provided by the surrounding soil, since the footing is embedded. The contribution of embedment is much more efficient in the case of the biaxial loading, since in this way the soil offers resistance by means of passive pressures to the rotating footing in two directions instead of just one. In fact, as the angle grows the efficiency of the lateral soil confinement increases. This happens because, for larger angles, the load is distributed between the two sides of the footing in a more "uniform" way. For imposed loading rotated by 45˚ for instance, both sides are subjected to the same force: $F = P\frac{\sqrt{2}}{2}$. On the other

hand, for very small angles, e. g. 15˚, one of the two components is significantly larger than the other, hence leading to practically one side being loaded, since the other is subjected to a much smaller force. The evidence of this effect is presented in **Figure 4.4**, where the deformed mesh of the trench is presented for each of the pushover analyses performed, at the stage just before collapse. From the plastification magnitude presented with contours in this plot, it is evident that in the case of 45˚ (**Figure 4.4b)**, the soil is much more plasticized, in both sides, hence proving that both sides of the trench contribute significantly to offering resistance to the rotating structure. On the other hand, in **Figure 4.4a** exhibiting the deformed trench for the case of 15˚, it is obvious that the side subjected to the largest component is much more strained than the side perpendicular to that, subjected to the smallest component. Another characteristic which draws our attention is the created curvature on the walls of the trench, which is far more intense in the case of 45˚ than in the case of 15˚. This is explained, since in the former case both opposite edges of the rectangular footing are forced to uplift, hence pushing further the walls of the trench, as opposed to the 15˚ load, which forces the footing to uplift almost like the aligned footing, as seen on Chapter 3.

Moving on to interpreting the behavior of the system in settling (**Figure 4.2)**, we notice the awaited result of the aligned footing exhibiting a smaller critical rotational angle leading to its collapse. As mentioned in Chapter 1, this angle is defined for the rigid block as:

$$\vartheta_c \approx \frac{B}{h}$$

In other words, this index is directly related to the geometry of the system. It is straightforward to conclude that, the smaller the effective width of the footing, i. e the dimension of the footing parallel to the direction of loading, the smaller the critical angle of the system. Indeed, this theory is validated by the results presented in **Figure 4.2**, where the plots in terms of w-ϑ for all pushover analyses are presented. A better view of these results is exhibited in **Figure 4.3a**, where the monotonic w-ϑ curves from all analyses are plotted together. The same curves, presented in magnified scale (**Figure 4.3b)** provide evidence concerning the settling behavior of the system. Notice that the tendency of a skewed system to settle more quickly than the aligned, which has already been commented on in Chapter 3, here is validated. Interestingly however, we observe that regardless of the loading angle, the uplifting commences practically at the same rotational value. The only visible difference, which is however rather small, is presented between the aligned (0˚) footing and any other skewed one. At this point it has to be underlined, that a finer mesh locally underneath the footing and smaller increments in the loading of the system would contribute to us achieving better accuracy in the results, since these phenomena are extremely localized and even a sophisticated software like ABAQUS may fail to “depict” them precisely. Of course for the sake of saving computational cost and for the needs of the current thesis, it suffices to say that practically all systems seem to exhibit uplift approximately at the same rotational value, which also happens to be rather small.

Having underlined the fact that all systems are prone to uplift, we are led to the consequences of this response: **Figure 4.5** presents the contours of vertical traction distribution on the soil-footing interface for the case of 15˚ and 45˚ pushover analyses (**Figures 4.5a** and **b** respectively). The plots refer to the moment when the maximum traction on the soil-footing interface is developed. In **Figure 4.6** are presented at the moment of maximum developing normal traction the distribution of normal traction from all pushover analyses performed for 0˚, 15˚, 30˚ and 45˚. The red dashed line indicates the effective width of the footing, which is parallel to the direction of the imposed displacement. As we see, the larger the angle by which the loading is imposed, the larger the effective width of the footing, which controls as mentioned before the slenderness ratio and hence the rocking response of the system. This plot provides an overview of the effective width in each and every case of the four pushover analyses performed, indicated with red dashed line. Observe that as the angle increases, the normal traction become even more concentrated to a small area on the soil-footing interface, hence straining excessively the soil. **Figure 4.7** presents the progression of vertical traction on the soil-footing interface with increasing displacement. This graph verifies the aforementioned theory, that indeed by increasing the angle of loading, the imposed normal traction is significantly larger, hence causing more rapid plastification to the soil. However, it is worth underlining that the difference in the normal traction between 30˚ and 45˚ degrees is negligible. **Figure 4.8** presents the deformed mesh plotting the plastification magnitude contours of the system for 15˚ and 45˚ at the stage before collapse.

2. PARAMETRIC CYCLIC ANALYSES

Having approached the system's behavior in the static regime, as the loading angle varies; it is necessitated to investigate the response also under dynamic cyclic loading. For this reason the system is subjected to two artificial sinus motions aiming at exciting the structure in a way to develop smaller rotational angles and thus accumulate settlements and in a way to develop large rotational angles, thus exhibiting significant uplift. Bearing in mind the dynamic characteristics of the system and using as guide for the selection of the motions the exhibited response during the seismic motions, the following motions are utilized:

1. Sinus motion with T=0.35 s and A=0.15g, 10 cycles in total (**Figure 4.9a**)
2. Sinus motion with T=0.70 s and A=0.30g, 10 cycles in total (**Figure 4.9b**)

Both motions are imposed on the system, by 0˚, 15˚, 30˚ and 45˚. The results are as follows:

Figure 4.10 a and **b** present the M-ϑ loops for the aligned and the 15˚ system. **Figure 4.11 a** and **b** present the M-ϑ loops for the 30˚ and 45˚ system. Observe that in neither case does the system reach its capacity, regardless of the evident nonlinearity in its response. From **Figure 4.10 c** and **d** it is evident that both systems behave practically in the same way

as far as the settlements are concerned. An essentially similar view is presented in **Figure 4.11 c** and **d** showing the w-ϑ curves for 30˚ and 45˚. As awaited, the response in all cases is sinking dominated, with evidently larger rate of settlement accumulation during the first cycle of the motion.

Focusing on this area of the graph, it is clear that as the angle of the imposing load increases the developing settlement decreases. In the same notion, the residual settlement calculated for the 45˚ is somewhat smaller than the 30˚ and rather smaller than 15˚ and 0˚. Although the difference in the residual settlement is not exaggerated, the different trend observed during these analyses has to be commented on, so that the mechanism describing the response of the system be explained. Interestingly this behavior is opposed to the exhibited settling behavior during the seismic motions. In that case, the skewed system was forced to settle multiple times more than the aligned one. However, this difference in the case of the weak sinus motion comes as no surprise.

Bearing in mind that the motion is rather weak in amplitude and its predominant frequency little excites the nonlinear system, sinking response is expected. Consequently, small rotational values are developed and the effect of the localized high normal traction is not present in this case. **Figures 4.10 e** and **f** and **Figure 4.11 e** and **f** present the rotational time history of the system for 0˚, 15˚, 30˚ and 45˚ respectively, verifying that the rotational values in all cases are practically the same and remain rather low. This ensures us, that indeed the soil does not sustain any extreme values of normal traction imposed by the edge of the footing.

In an effort to shed light on the exhibited settling response, we present the view of the normal traction during the first pulse in **Figure 4.12**. Observe that already from the first cycle, where the maximum rotational response is developed, the normal traction is indeed the highest for 45 degrees than for any other case, but in absolute terms, the soil does not sustain significant stresses (**Figure 4.7**). Moreover, from **Figure 4.12** it is evident that the effective width (denoted also as B_{eff}) of the footing decreases as the angle rises. This is explained by the fact that, a higher normal traction imposed on the soil, leads to larger deformation and thus to more intense curvature of the soil-footing interface. As a result, the more curved the soil surface, the smaller the area of the footing being in touch with it, for the same rotation. Bearing in mind that the settlement is directly dependent on the effective width of the footing, it is justified why in 45˚ the developed settlement during the first cycle is lower than in any other case.

Observing the settling response macroscopically and based on the same way of thinking, we plot the contours (**Figure 4.13**) showing the distribution of the normal traction developed on the soil-footing interface at an intermediate stage of the motion, after the majority of the cycles have passed (approximately 2.89 sec). From this view we conclude the following:

1. The values of the developing normal traction are lower than the ones during the first cycle, although the maximum and minimum values are still developed for 45˚ and 0˚ respectively.

2. B_{eff} has significantly increased for all cases, although the maximum and minimum values are still developed for 0˚ and 45˚ respectively.

The aforementioned points combined with the information provided by the contours lead us to assume that the increased surface of the footing, which is in touch with the underlying soil, imposes lower normal tractions, compared to the ones during the first cycle. The only logical explanation justifying this effect is that the underlying soil is much more curved in the case of 45˚ than in any other case. Evidently, **Figure 4.14a**, presents the settlements of the soil at the edge of the footing and the settlements of the soil at the center of the footing for all investigated cases. The settlement values are normalized with the value of the soil settlement underneath the center of the footing. The largest difference in the vertical displacement between the center and the edge is indeed developed for the 45˚ system, whereas 30˚, 15˚ and 0˚ follow. Observe that for the cases of 15˚ and 0˚ the system behaves practically in the same way. This proves that the soil-footing interface is indeed more curved for the 45˚ than any other case. Consequently, the footing not only rocks in all cases mainly on its surface rather than between its edges, but the width being in touch with the soil is significantly lower, as the curvature of the soil becomes more and more intense.

Having showed that the effective width of the footing is the smallest for 45˚ and the largest for 0˚, it comes as natural conclusion that the stress bulb in the former case is much shallower than in the latter. Hence, it is logical that the accumulated settlements in the case of the 45˚ footing shall be lower than those in 30˚, 15˚ and 0˚.

The results of the analyses with the strong, low-frequency sinus confirm the mechanisms described above. In the case of the strong sinus motion we expect higher rotational values and greater soil plastifications, since the system is much more vulnerable in long period excitations.

As shown in **Figures 4.15** and **1.16**, again the system responds with the first cycle being significantly stronger than the others. This pulse is not a realistic part of the response, since it has merely to do with the fact that the sinus as a motion commences with a velocity pulse, i. e. the initial velocity of the system is not zero. This creates a numerical issue in the code, hence leading to this difference in the response. It is evident from **Figures 4.15a, b** and **4.16 a, b,** which present the M-ϑ loops for 0, 15, 30 and 45 degrees respectively, that the system responds within its moment capacity, at least for the majority of the cycles, which constitute the main part of the motion. Observe that although in the case of the aligned model the system reaches its capacity, in all other cases the maximum developing moment is smaller. As discussed also in Chapter 3 this is attributed to the trench of the footing being significantly deformed in the latter cases, compared to the aligned footing, hence changing the stiffness of the system. For the same imposed acceleration and by

extension for the same developing rotation, in the cases of 15, 30 and 45 degrees the footing does not reach the wall of the surrounding soil, thus not being able to exhibit greater moment values. Snapshots of the deformed trench, indicating the contours of the plastifications magnitude are presented in **Figure 4.17**. Observe that for the case of the aligned footing (**Figure 4.17b)** the trench has maintained practically its undeformed shape, hence contributing to the system exhibiting the awaited moment capacity.

Another significant difference stemming from these graphs has to do with the hysteretic damping being offered by the system. It is remarkable that the hysteresis loop seems to be largest in the case of 15˚, whereas in shrinks a little in the case of 30˚. Both cases have a common characteristic, which probably accounts for this significant difference: The footing exhibits a combined motion in its response: Rocking and spinning along its circumference. This means that apart from its edges also its sides participate in the rocking motion. This leads to slightly larger rotational values, as shown also in **Figures 4.15 e,f** and **4.16 e, f** and hence to slightly broader hysteretic loops. On the other hand, for the cases of 0˚ and 45˚, where the footing rocks along a specified dimension, the hysteretic damping seems to be lower.

Moving on to the settlements mechanism, it is evident again in **Figures 4.15 c, d** and **4.16 c, d** that as the angle of the imposed motion increases, the settlements tend to accumulate at a slower pace. The explanation is the same as described in the case of the weak sinus:

As soon as the first pulse acts, a maximum rotation of about $40\ mrads$ is developed. This leads to the underlying soil being significantly strained. Observe in **Figure 4.18** that the imposed normal traction on the soil-footing interface increases as the angle of the motion becomes larger, whereas the total area, where the maximum normal traction is distributed decreases significantly. This creates the “penetration” effect, described also in Chapter 3. However, in this case, thanks to the purely symmetrical nature of the motion, the system does not acquire permanent rotation, but rather manages to exhibit practically equal rotation to the opposite direction as well. The price to pay from this cyclic, symmetrical motion is the excessive curvature of the underlying soil. Notice in **Figure 4.14 b**, that the normalized relative settlement of the soil underneath the center and the edge of the footing, is strikingly larger in the case of the strong sinus, compared to the weak (**Figure 4.14a).** This deformation has dual effect:

1. The footing rocks mainly on its surface, rather than between its edges, hence reducing the imposed traction on the underlying soil, as indicated in **Figure 4.19**, where the contours showing the distribution of normal traction on the soil-footing interface at the moment of maximum developing rotation are presented. Observe that the spinning motion of the footing in the case of 15˚ and 30˚ leads to more intense concentration of traction in the underlying soil, which is very close in value with the developing traction in the case of 45˚.

2. The curvature on the underlying soil interface leads also to a significantly reduced part of the footing width to be in touch with the soil, as the footing rocks. Indeed,

the larger the angle of the imposed motion, the narrower the strip of the footing being in touch with the soil. This leads to shallower stress bulb during the motion and hence accounts for the reduced settlements in the case of 45˚ compared to all other angles.

Figure 4.20 shows the contours of the imposed normal traction on the soil-footing interface, during at the moment of zero rotation. It is verified from these plots, that the soil surface is indeed curved, since the edges of the footing are not in contact with it. Apart from that, notice the red dashed line, which indicates approximately the effective width of the footing being in touch with the soil. It is evident that the cases 0˚ and 15˚ as well as 30˚ and 45˚ have exhibit similar values of B_{eff}. As mentioned before, for the case of the weak sinus, the effective width is larger for the smaller angles, however, the discrepancy of the B_{eff} values is not large enough to account alone for the difference in the settlements. In the same plot are indicated the values of the maximum imposed normal traction on the soil surface. There is a striking difference not so much in the values but the area where they are being distributed. It is evident that in the case of the aligned footing, the area of maximum normal traction is multiple times larger than the one in 15˚, 30˚ and 45˚ degrees. This explains why the stress bulb is quite shallower in all other cases, as the angle of the motion increases. This is also demonstrated in **Figure 4.21** which plots the stress bulbs at the same moment presented also in **Figure 4.20**, when the rotation is zero, after more than half of the motion has passed. This plot provides evidence supporting our theory, since it shows that the bulbs affect even thinner layer of the soil formation as the angle of the motion increases, and thus lead to smaller settlements.

FIGURES OF CHAPTER 4

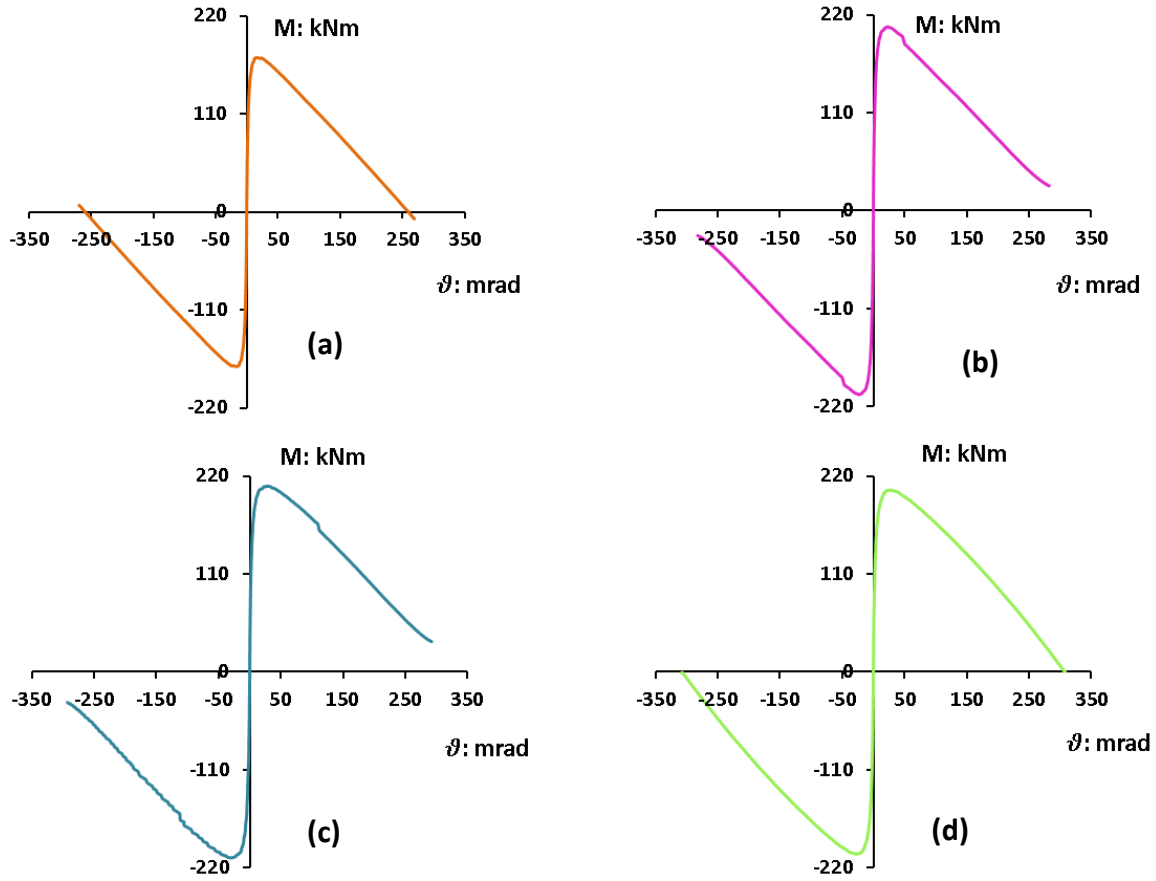

Figure 4.1 Monotonic pushover results in terms of M-ϑ when the loading is imposed by **(a)** 0˚, i. e aligned footing with the loading, **(b)** 15˚, **(c)** 30˚ and **(d)** 45˚

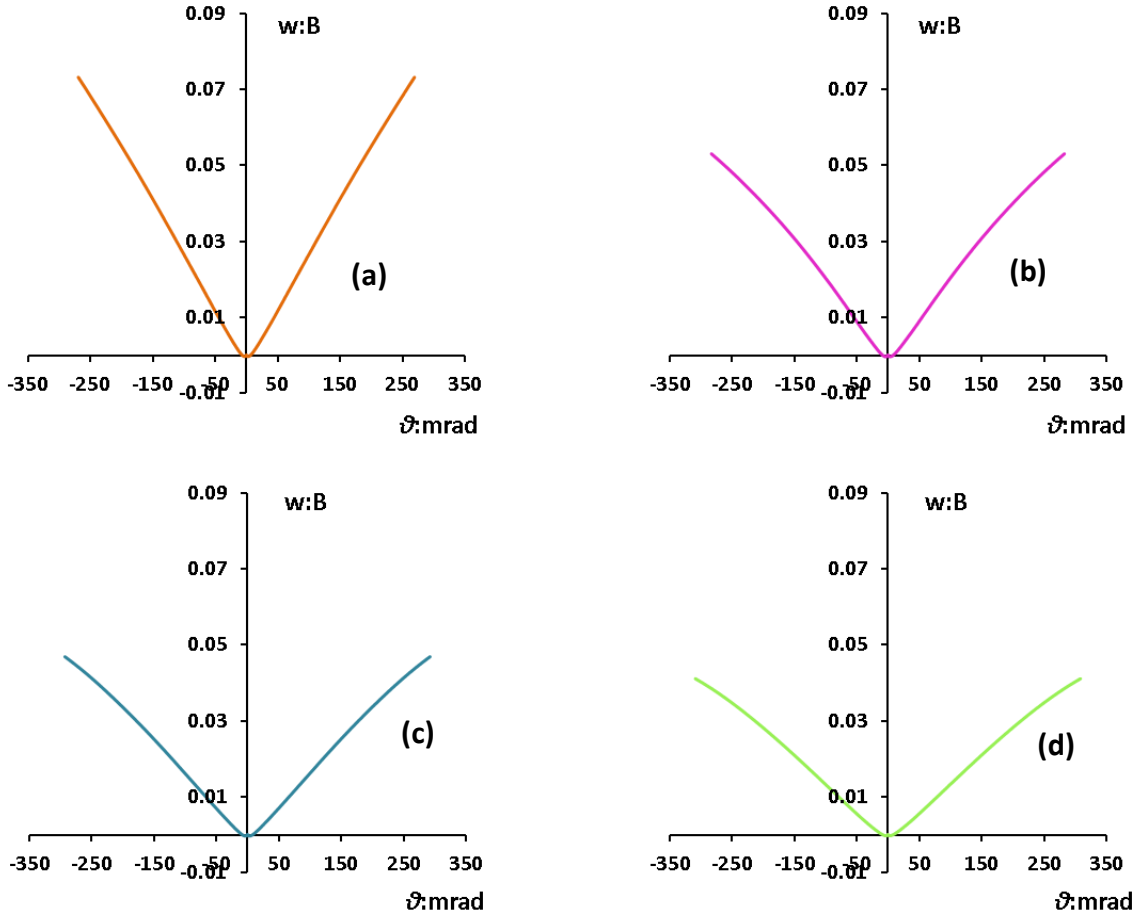

Figure 4.2 Monotonic pushover results in terms of w-ϑ when the loading is imposed by **(a)** 0˚, i. e aligned footing with the loading, by **(b)** 15˚, **(c)** 30˚ and **(d)** 45˚

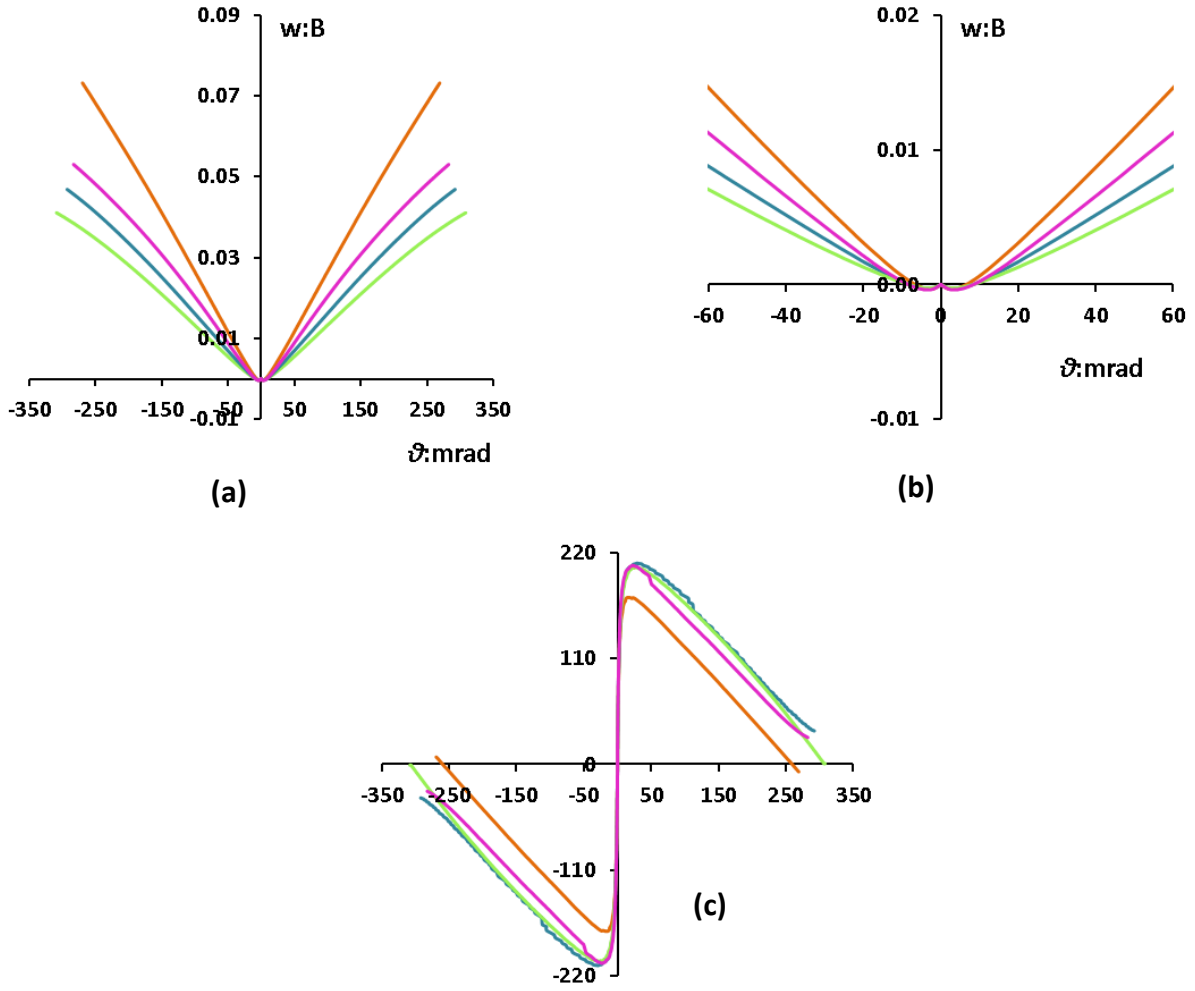

Figure 4.3 Overview of the pushover results in terms of **(a)** M-ϑ, **(b)** w-ϑ and **(c)** w-ϑ in magnified scale. The colors represent the various investigated angles, as they are presented in **Figures 4.1** and **4.2**.

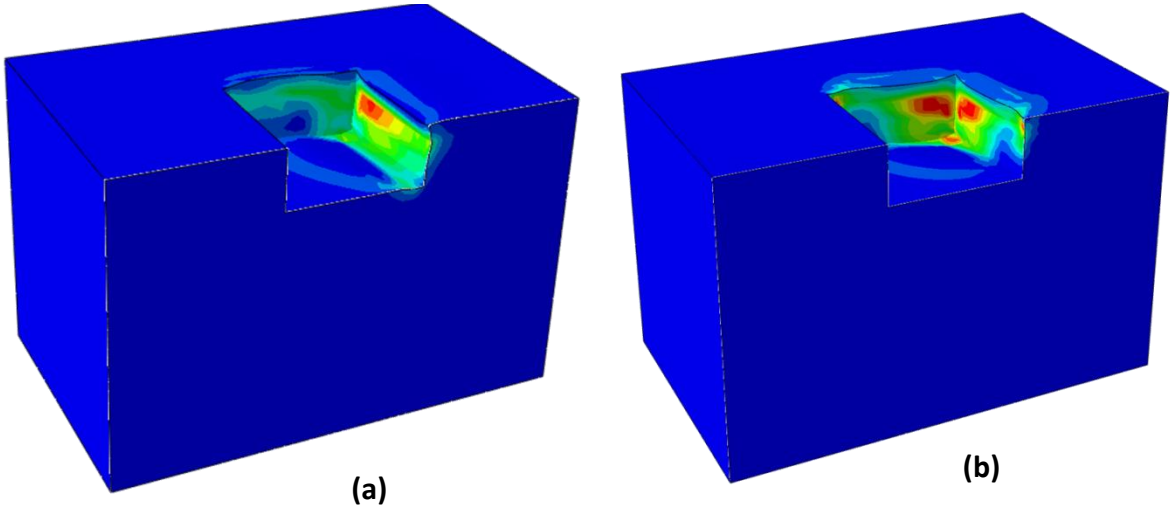

Figure 4.4 Contours showing the magnitude of plastifications inside and around the trench, where the footing is embedded. **(a)** Refers to the pushover analysis with the displacement being imposed by 15˚ and **(b)** refers to the pushover analysis with the displacement being imposed by 45˚.

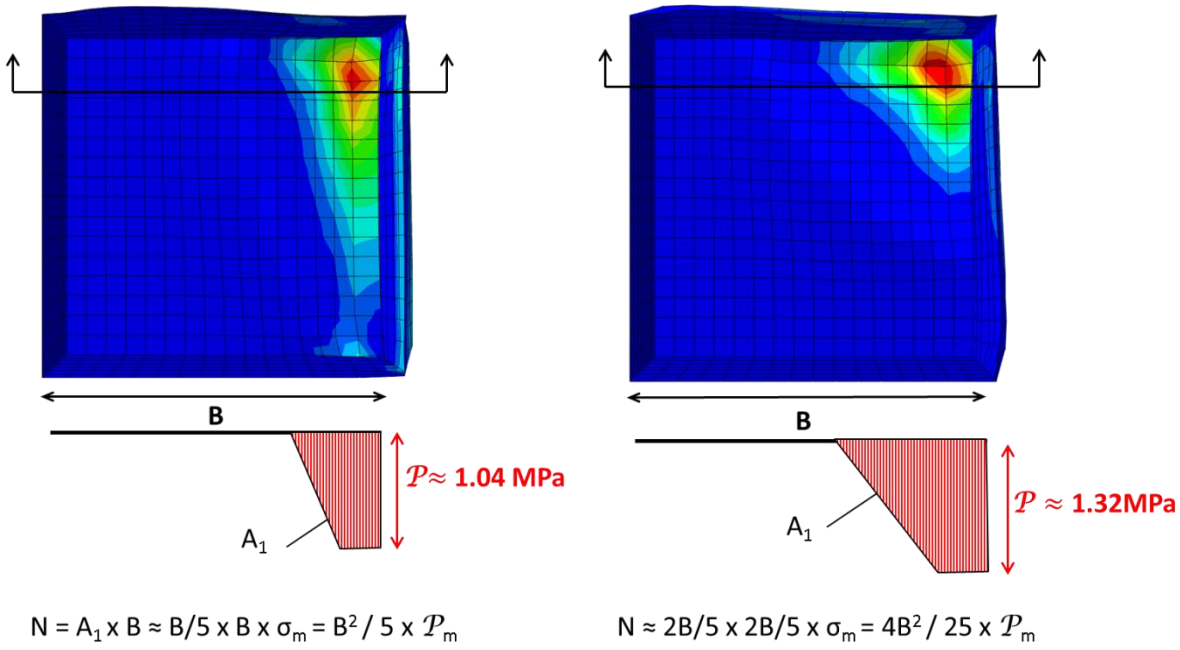

Figure 4.5 Contours showing the distribution of the maximum vertical traction on the soil-footing interface. **(a)** Refers to the pushover analysis with the displacement being imposed by 15˚ and **(b)** Refers to the pushover analysis with the displacement being imposed by 45˚. The red dashed line indicates the effective width of the footing.

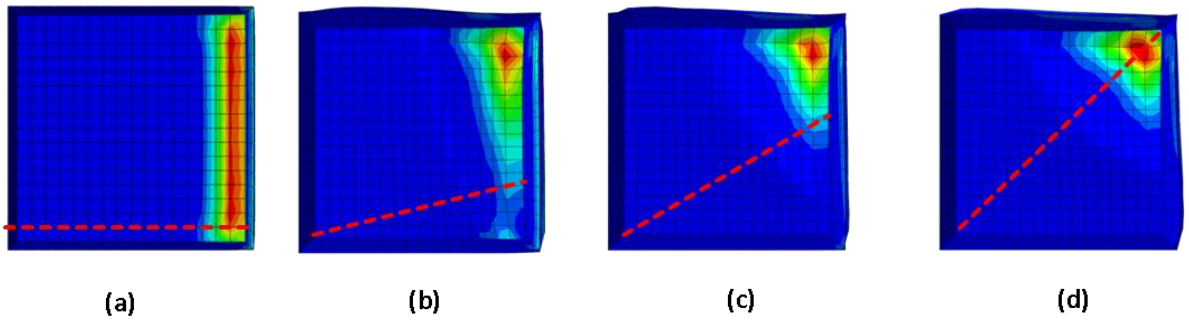

Figure 4.6 Presentation of the maximum normal traction distribution on the soil-footing interface for **(a)** 0˚, **(b)** 15˚, **(c)** 30˚ and **(d)** 45˚ respectively. The red dashed line indicates the effective width of the footing, parallel to the direction of loading.

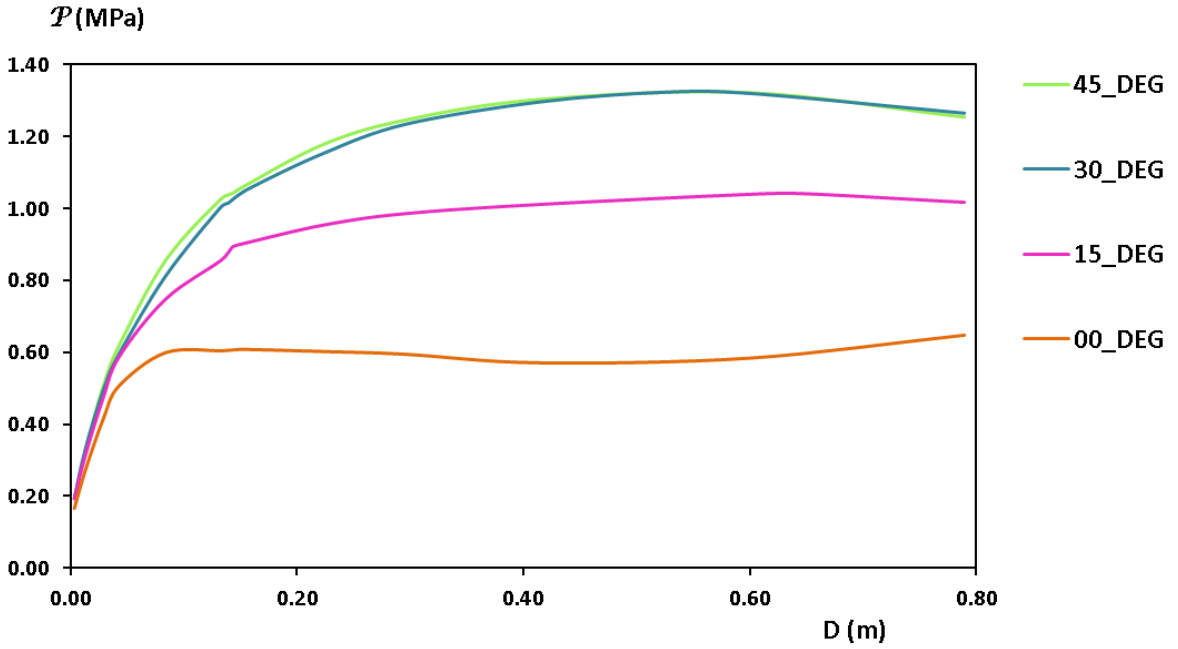

Figure 4.7 Comparison of the maximum developing vertical traction $\mathcal{P}$ plotted against the displacement, when imposed by **(a)** 0˚, **(b)** 15˚, **(c)** 30˚ and **(d)** 45˚ respectively.

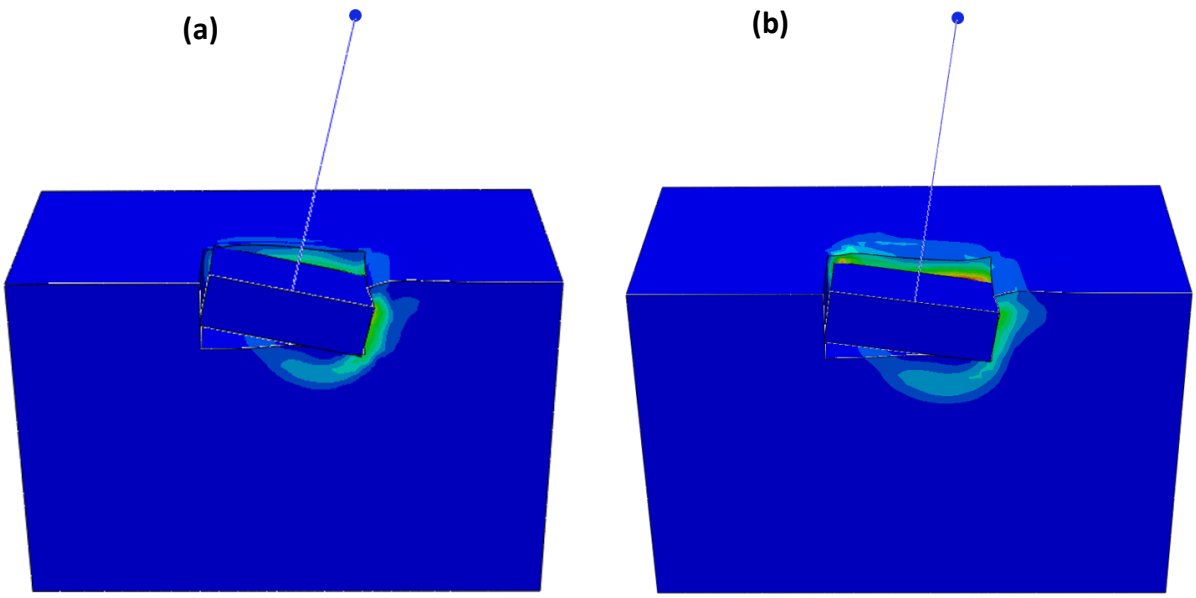

Figure 4.8 Contours showing the magnitude of plastifications at the stage before collapse for the pushover analyses with **(a)** 15˚ and **(b)** 45˚ rotation of the imposed displacement.

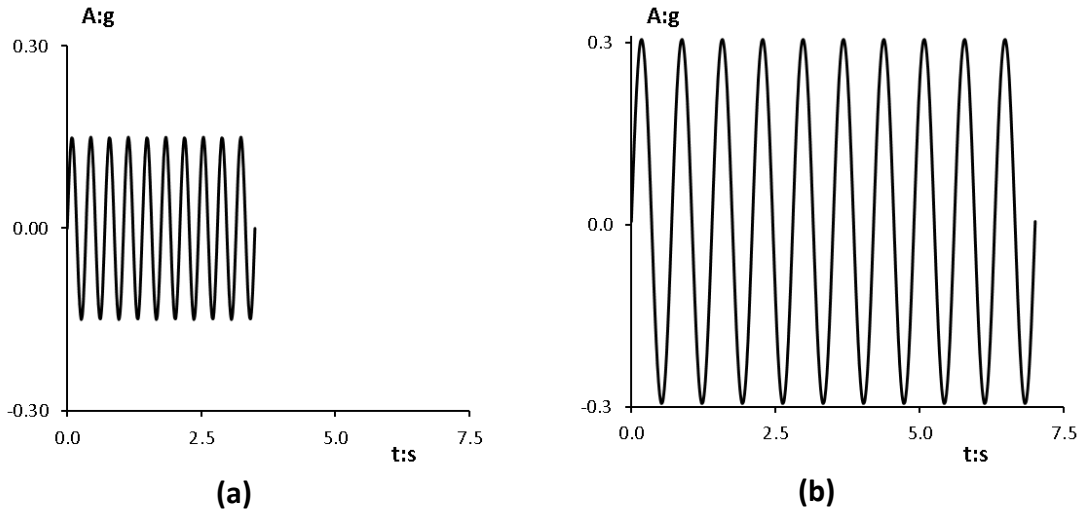

Figure 4.9 Sinus motions utilized at the parametric analyses. **(a)** Is the weak motion forcing the system to exhibit sinking response and **(b)** is the strong motion, forcing the system to respond mainly with uplift.

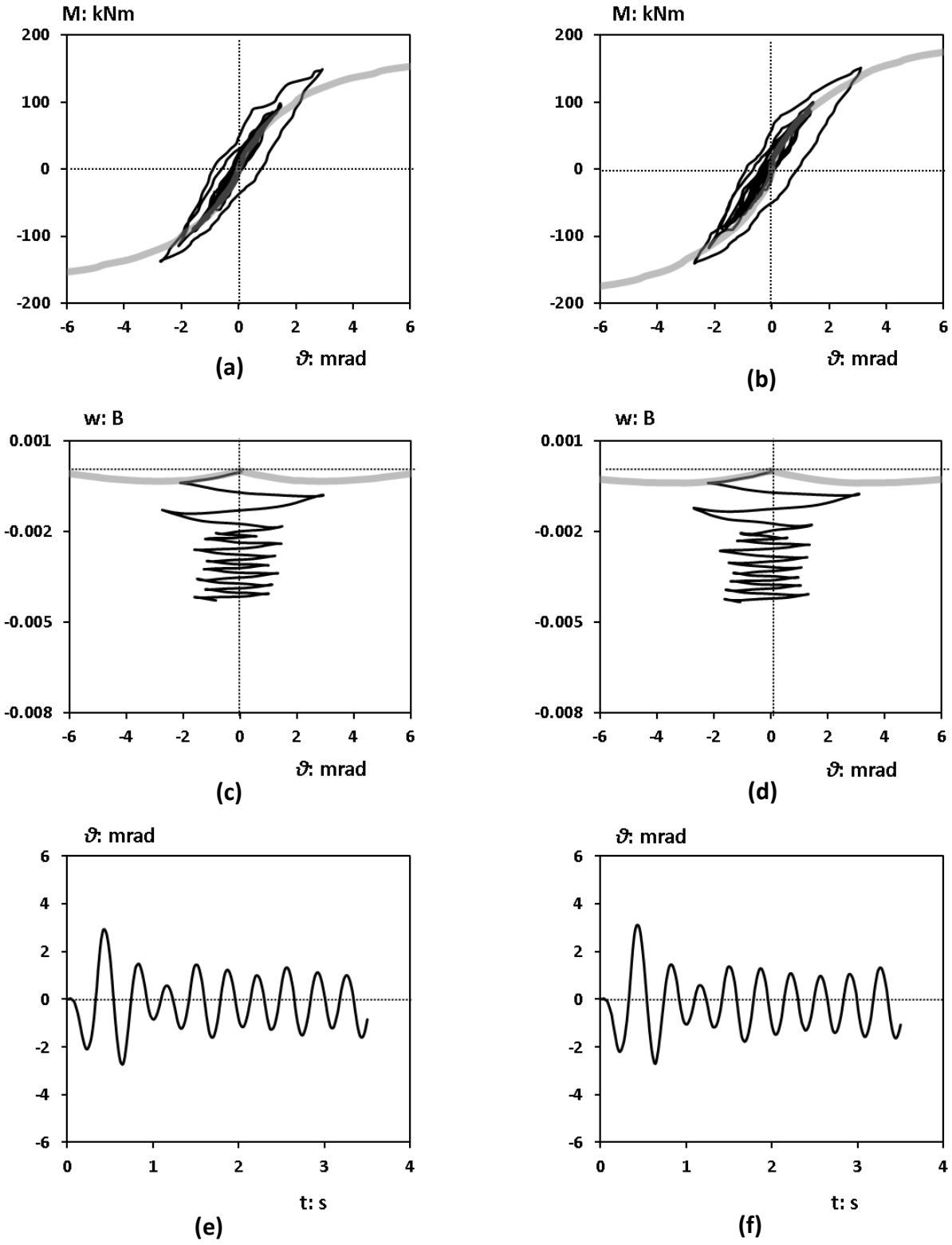

Figure 4.10 Results from the dynamic analyses utilizing the weak sinus motion. Moment-rotation loops for the weak sinus acting in **(a) 0˚** and **(b)** 15˚; Settlement normalized to the effective width of the footing for the weak sinus acting in **(c)** 0˚ and **(d)** 15˚ and rotational time history of the system for the weak sinus acting in **(e)** 0˚ and **(f)** 15˚.

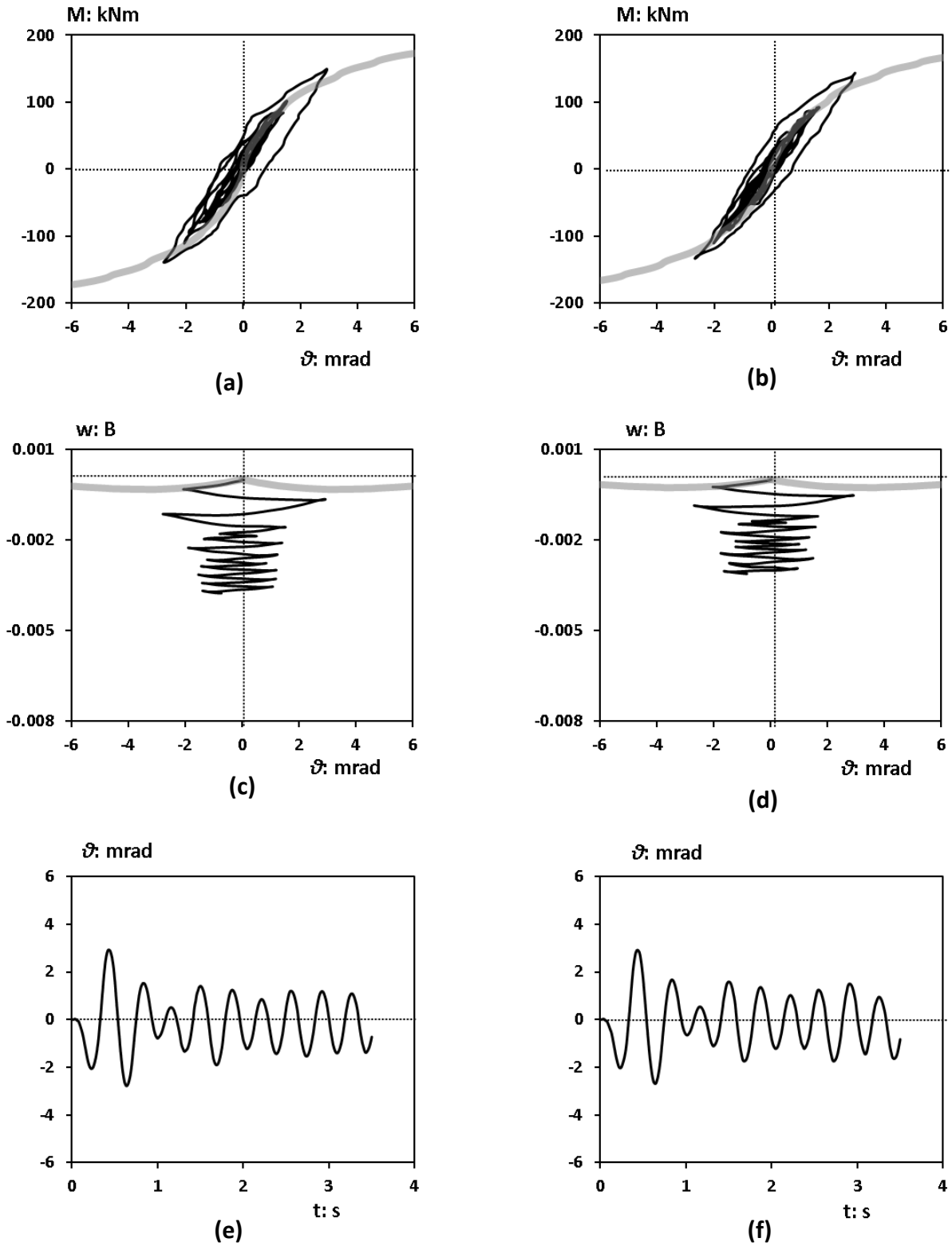

Figure 4.11 Results from the dynamic analyses utilizing the weak sinus motion. Moment-rotation loops for the weak sinus acting in **(a)** 30˚ and **(b)** 45˚; Settlement normalized to the effective width of the footing for the weak sinus acting in **(c)** 30˚ and **(d)** 45˚ and rotational time history of the system for the weak sinus acting in **(e)** 30˚ and **(f)** 45˚.

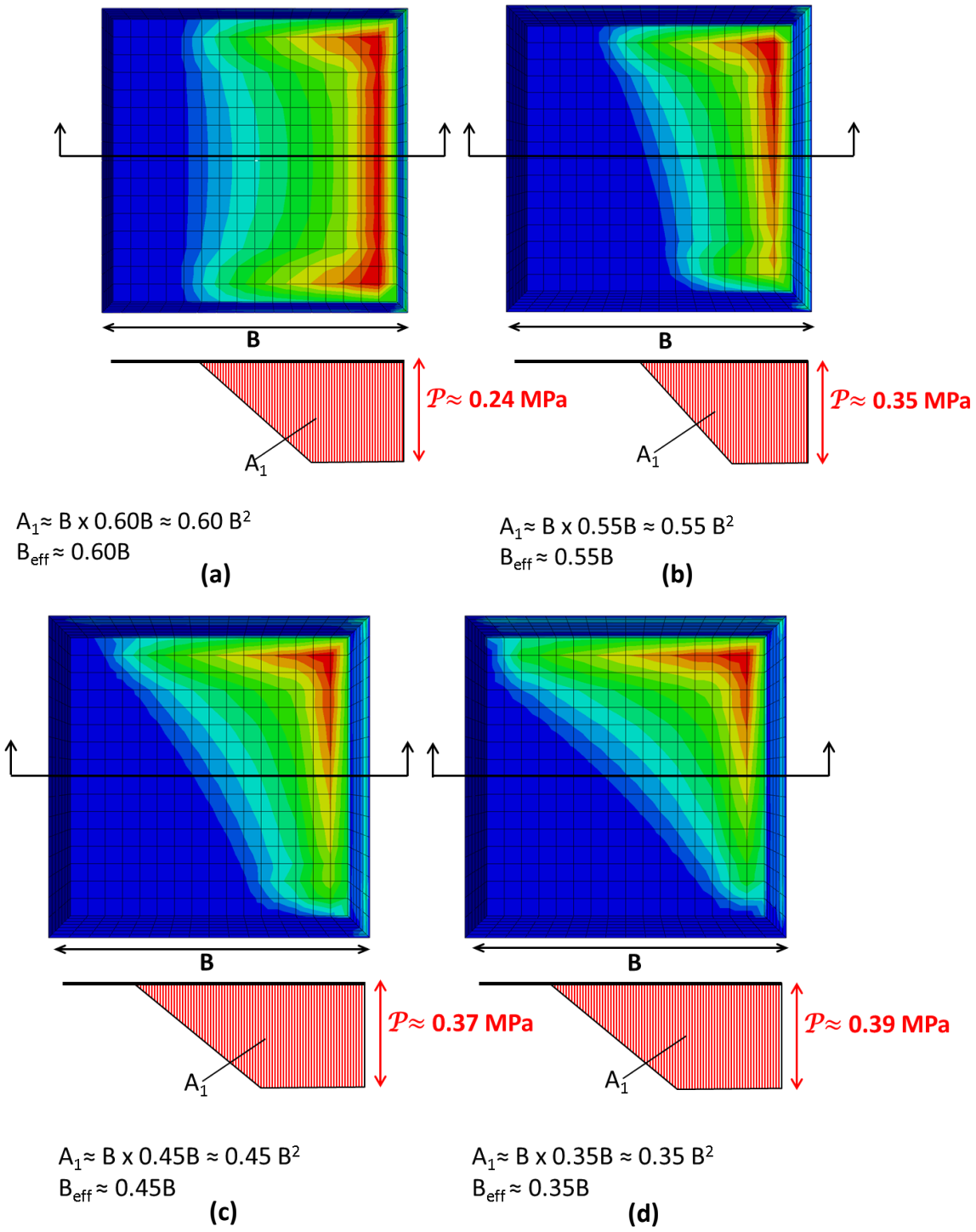

Figure 4.12 Contours showing the distribution of normal traction on the soil-footing interface during the first cycle of the weak sinus motion. The estimated B_{eff} is approximately the width of the footing, which is in touch with the underlying soil, at this moment. **(a)** Refers to 0˚, **(b)** refers to 15˚, **(c)** refers to 30˚ and **(d)** refers to 45˚.

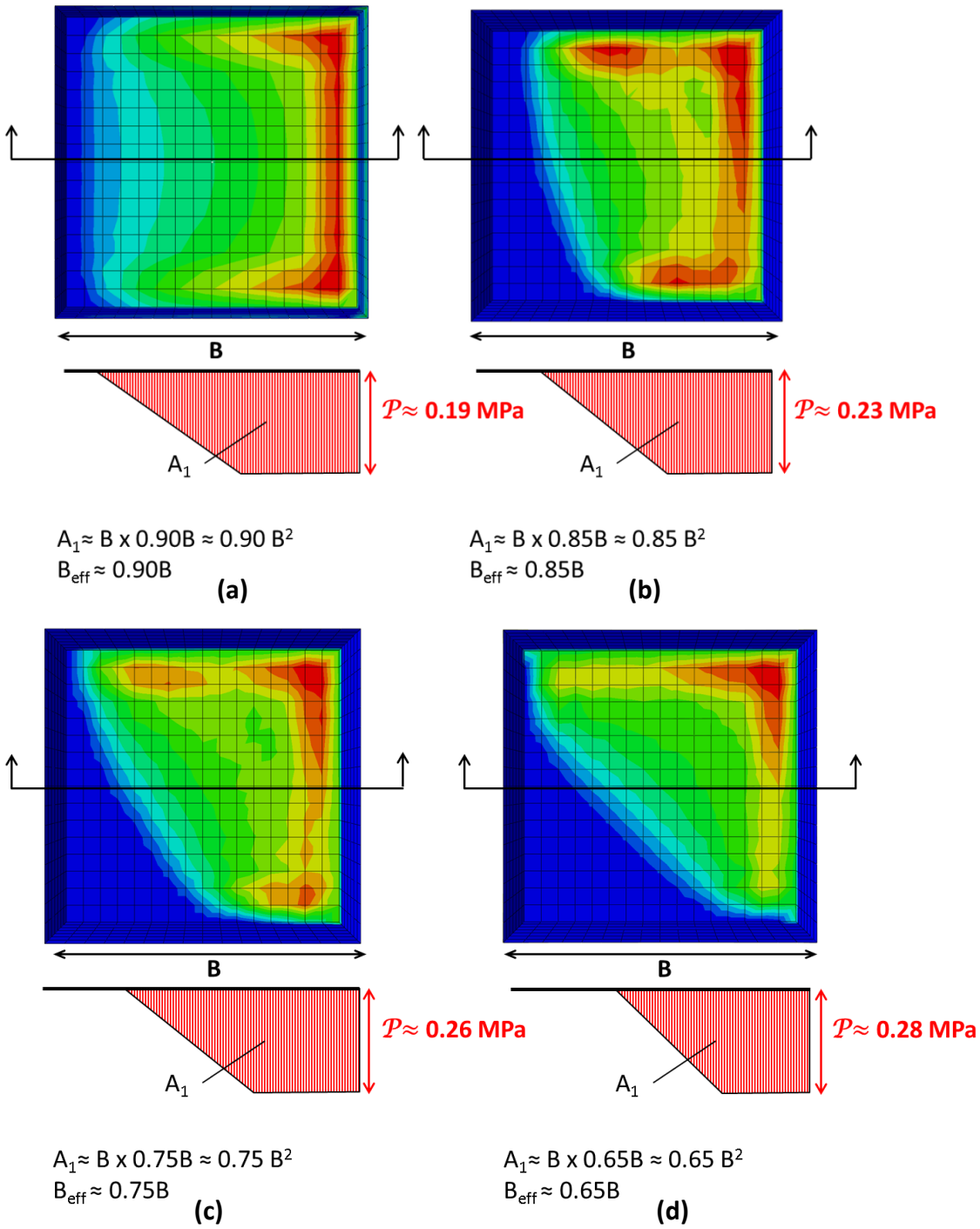

Figure 4.13 Contours showing the distribution of normal traction on the soil-footing interface at an intermediate stage toward the end of the weak sinus motion. The estimated B_{eff} is approximately the width of the footing, which is in touch with the underlying soil, at this moment. **(a)** Refers to 0˚, **(b)** refers to 15˚, **(c)** refers to 30˚ and **(d)** refers to 45˚.

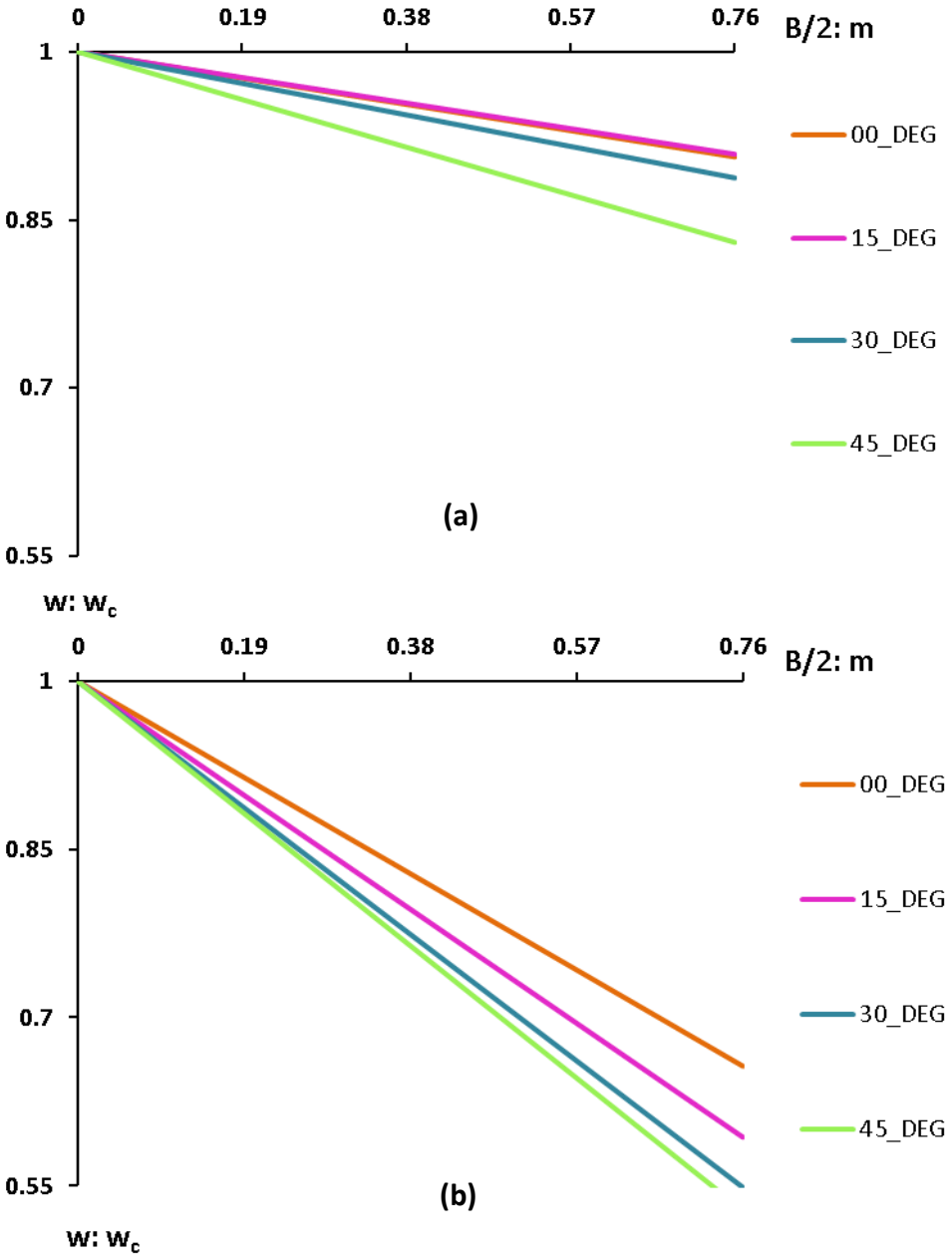

Figure 4.14 Graph showing the settlement of the soil underneath the center and the edge of the footing, normalized with the settlement of the soil underneath the center of the footing, at an intermediate stage toward the end of **(a)** the weak and **(b)** the strong sinus motion.

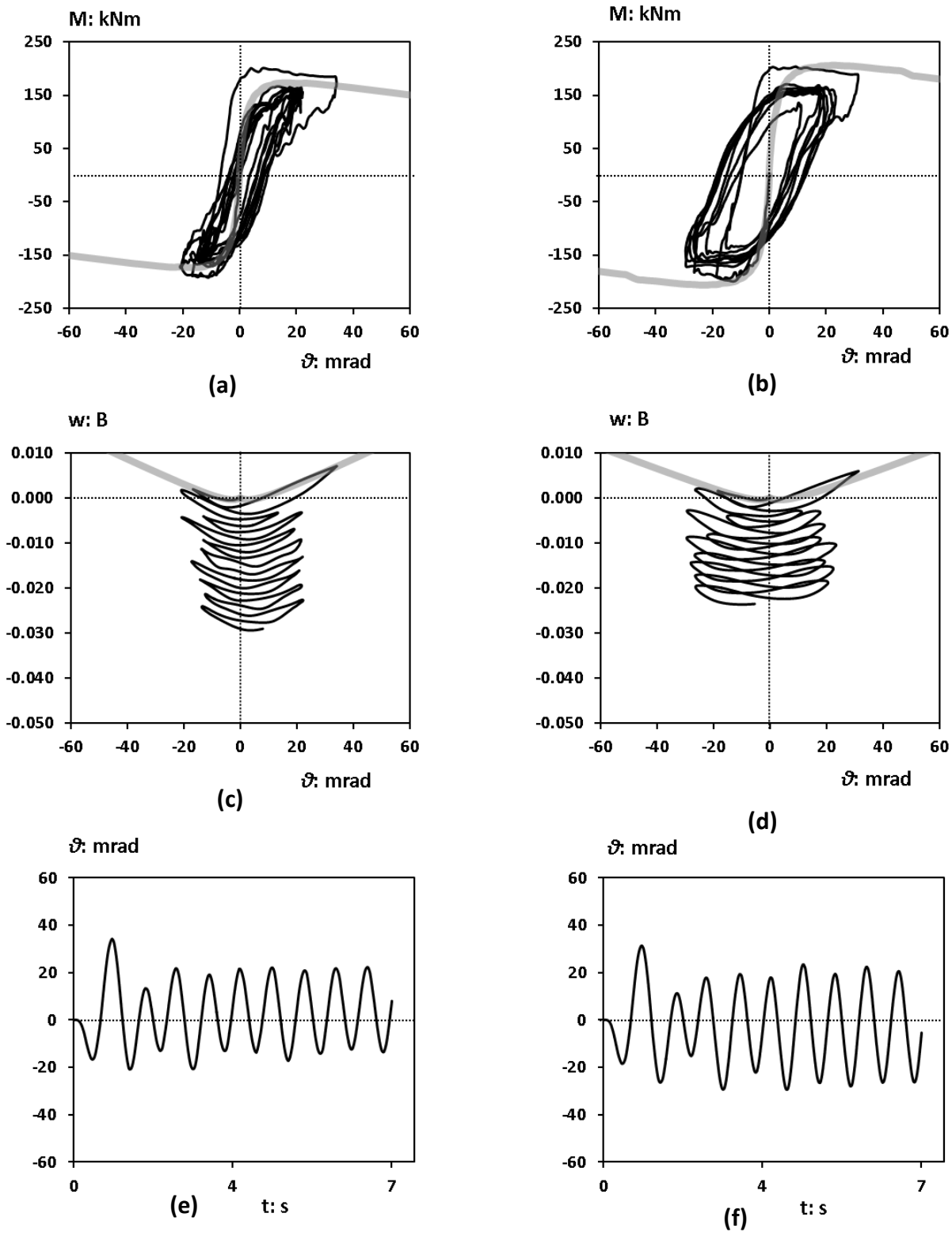

Figure 4.15 Results from the dynamic analyses utilizing the strong sinus motion. Moment-rotation loops for the weak sinus acting in **(a) 0˚** and **(b)** 15˚; Settlement normalized to the effective width of the footing for the weak sinus acting in **(c)** 0˚ and **(d)** 15˚ and rotational time history of the system for the weak sinus acting in **(e)** 0˚ and **(f)** 15˚.

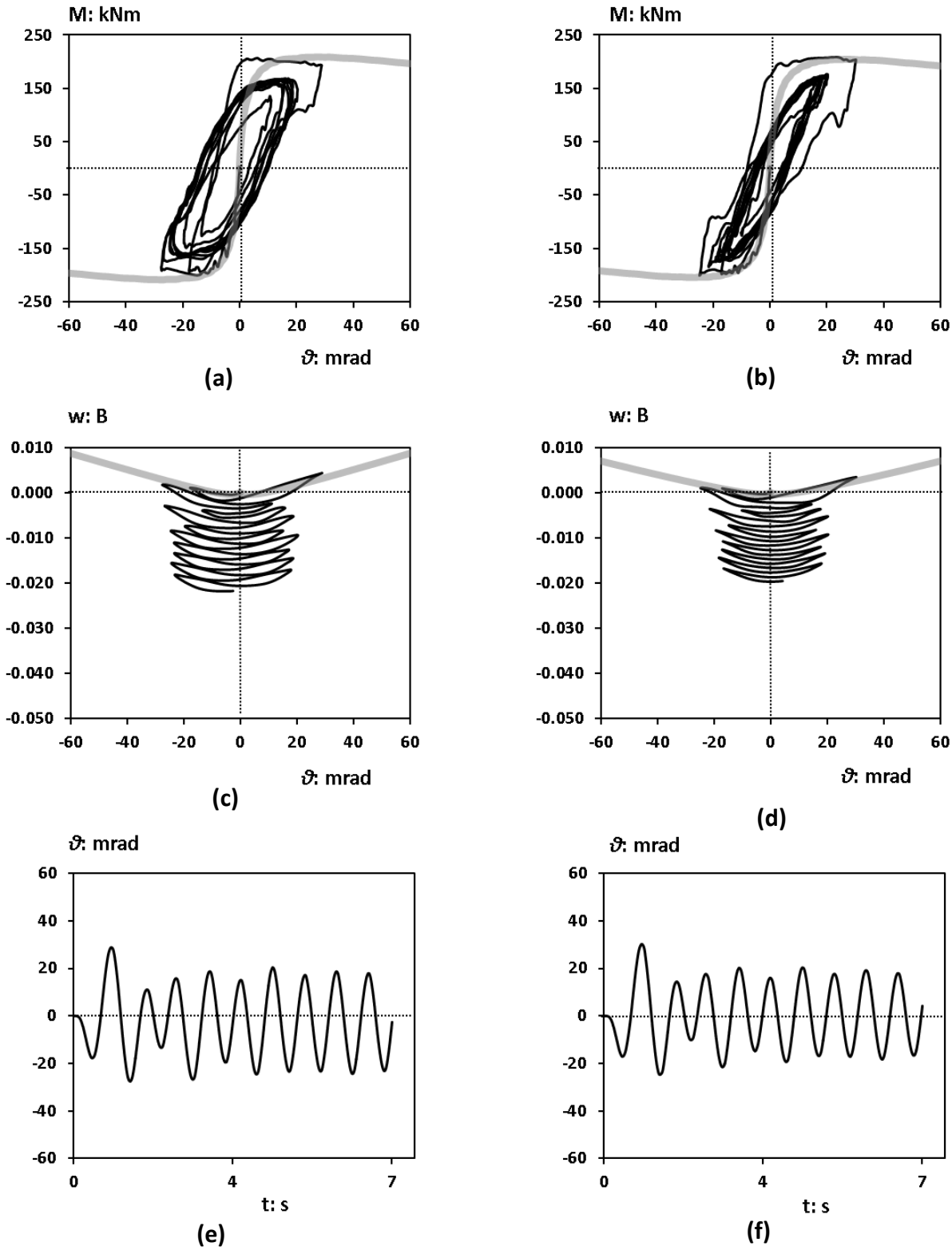

Figure 4.16 Results from the dynamic analyses utilizing the strong sinus motion. Moment-rotation loops for the weak sinus acting in **(a)** 30˚ and **(b)** 45˚; Settlement normalized to the effective width of the footing for the weak sinus acting in **(c)** 30˚ and **(d)** 45˚ and rotational time history of the system for the weak sinus acting in **(e)** 30˚ and **(f)** 45˚.

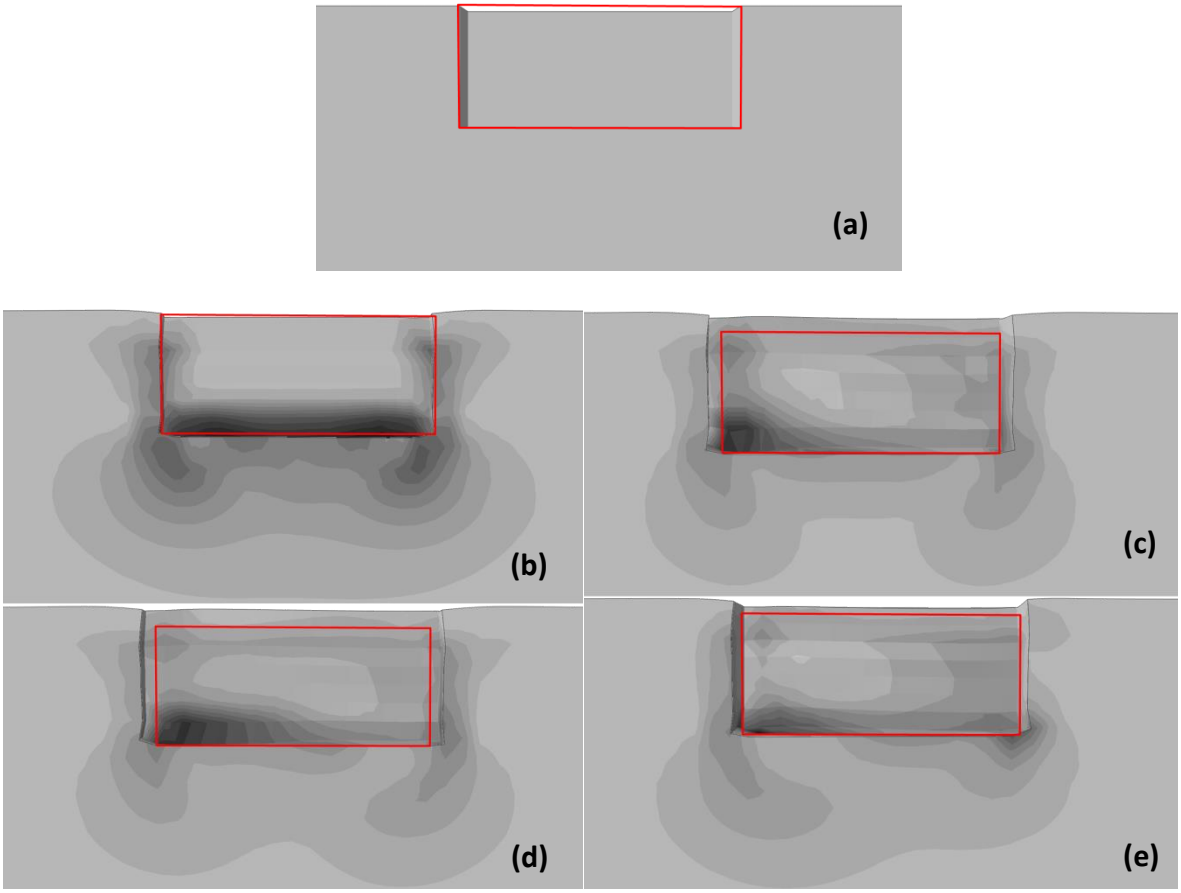

Figure 4.17 Distribution of the plastification magnitude focusing on the deformed trench at the end of the motion for **(a)** 0˚, **(b)** 15˚, **(c)** 30˚ and **(d)** 45˚. The red rectangular indicates the shape of the undeformed trench.

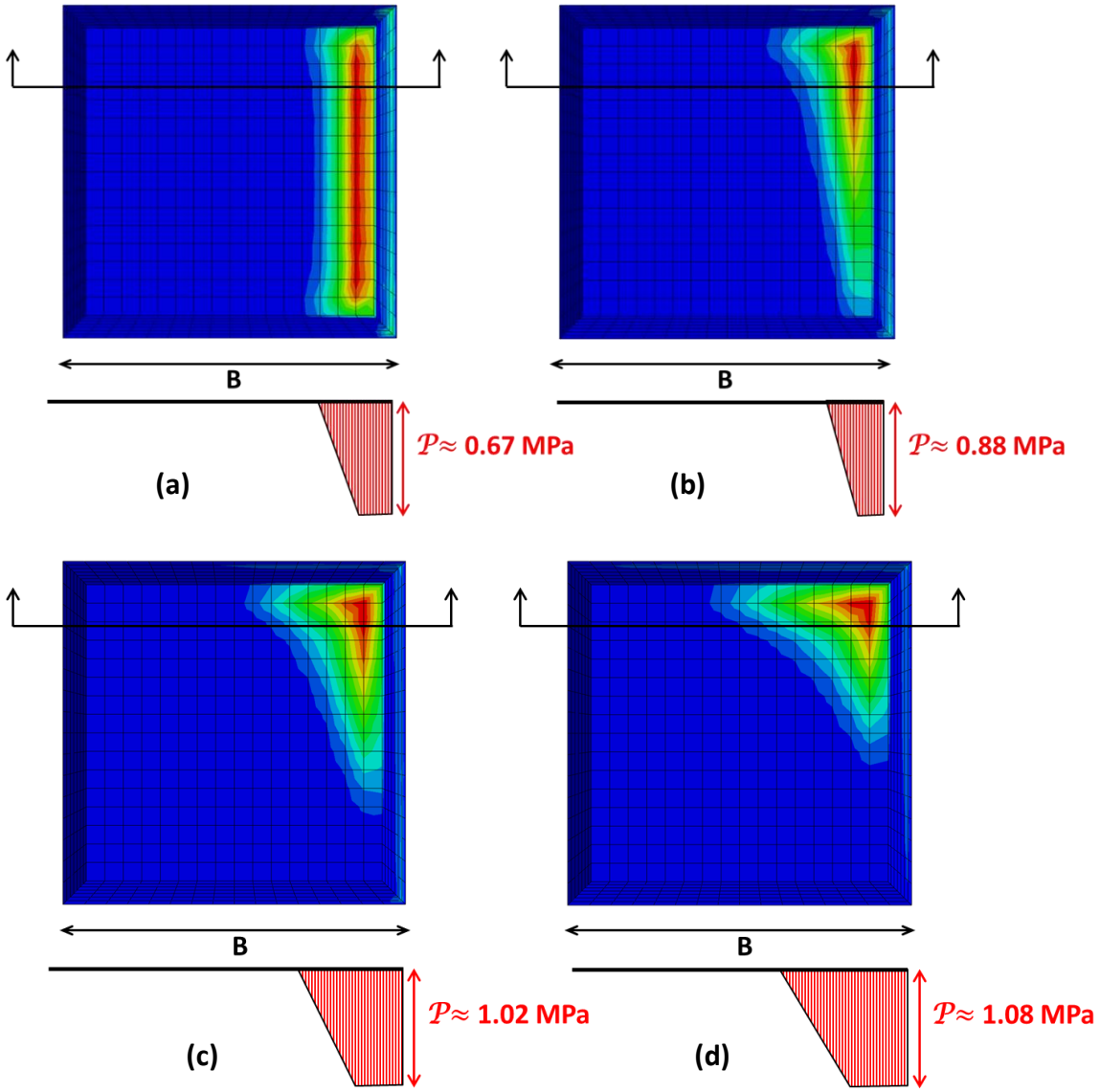

Figure 4.18 Contours showing the distribution of normal traction on the soil-footing interface during the first cycle of the strong sinus motion. **(a)** Refers to 0˚, **(b)** refers to 15˚, **(c)** refers to 30˚ and **(d)** refers to 45˚.

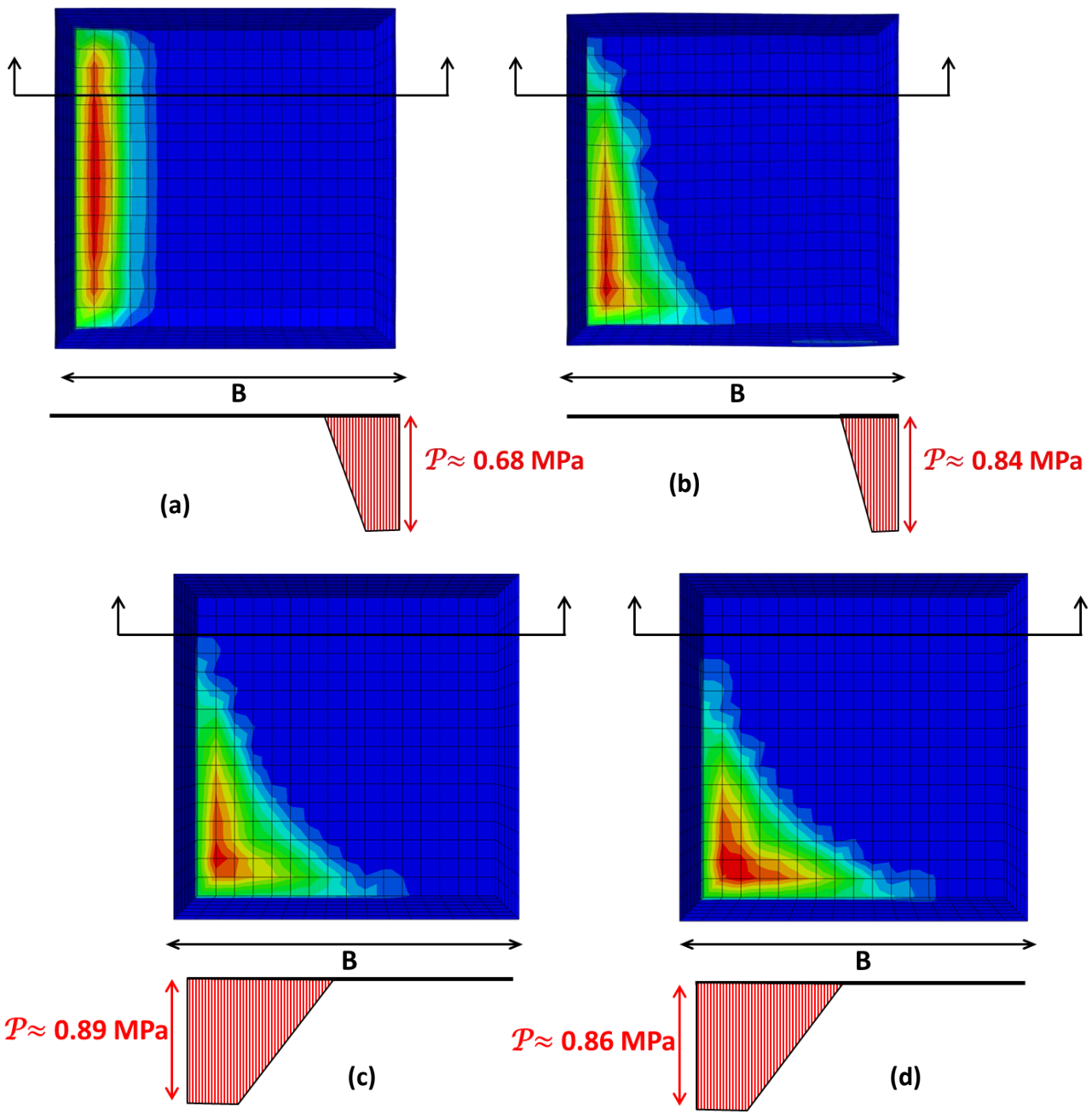

Figure 4.19 Contours showing the distribution of normal traction on the soil-footing interface at the moment of maximum developing rotation, during the strong sinus motion. **(a)** Refers to 0˚, **(b)** refers to 15˚, **(c)** refers to 30˚ and **(d)** refers to 45˚.

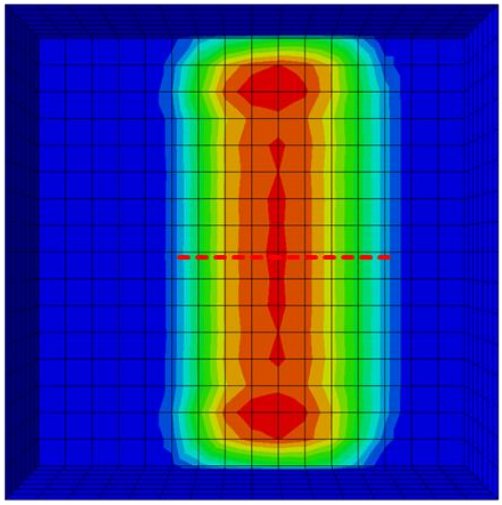

$\mathcal{P}$=0.33 Mpa
B_{eff}=0.50B
(a)

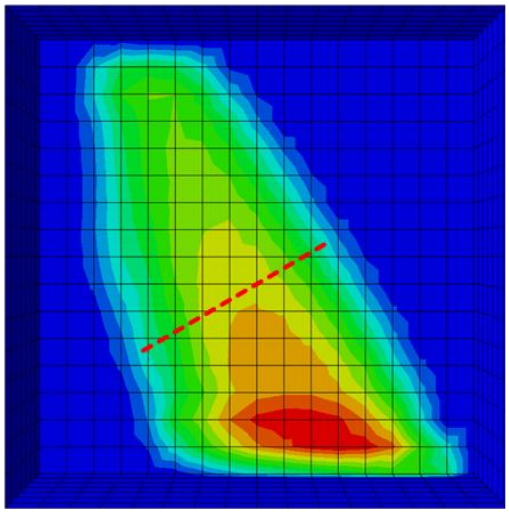

$\mathcal{P}$=0.30 Mpa
B_{eff}=0.50B
(b)

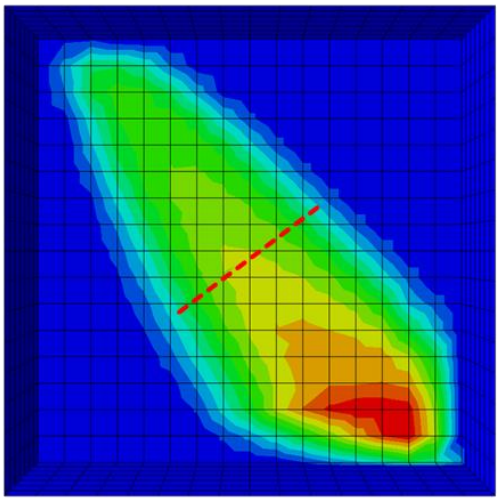

$\mathcal{P}$=0.28 Mpa
B_{eff}=0.375B
(c)

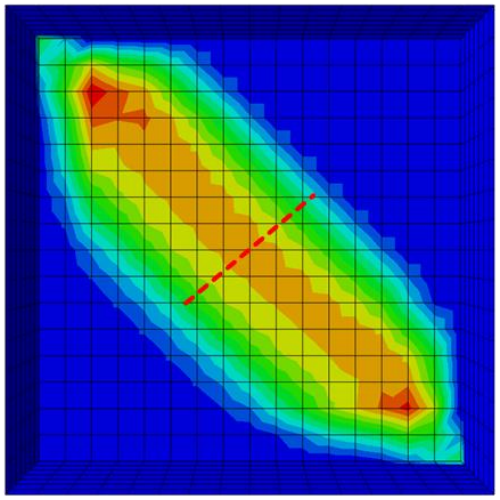

$\mathcal{P}$=0.25 Mpa
B_{eff}=0.30B
(d)

Figure 4.20 Contours showing the distribution of normal traction on the soil-footing interface at the moment of zero rotation, when already more than half of the cycles have passed. **(a)** Refers to 0˚, **(b)** refers to 15˚, **(c)** refers to 30˚ and **(d)** refers to 45˚.

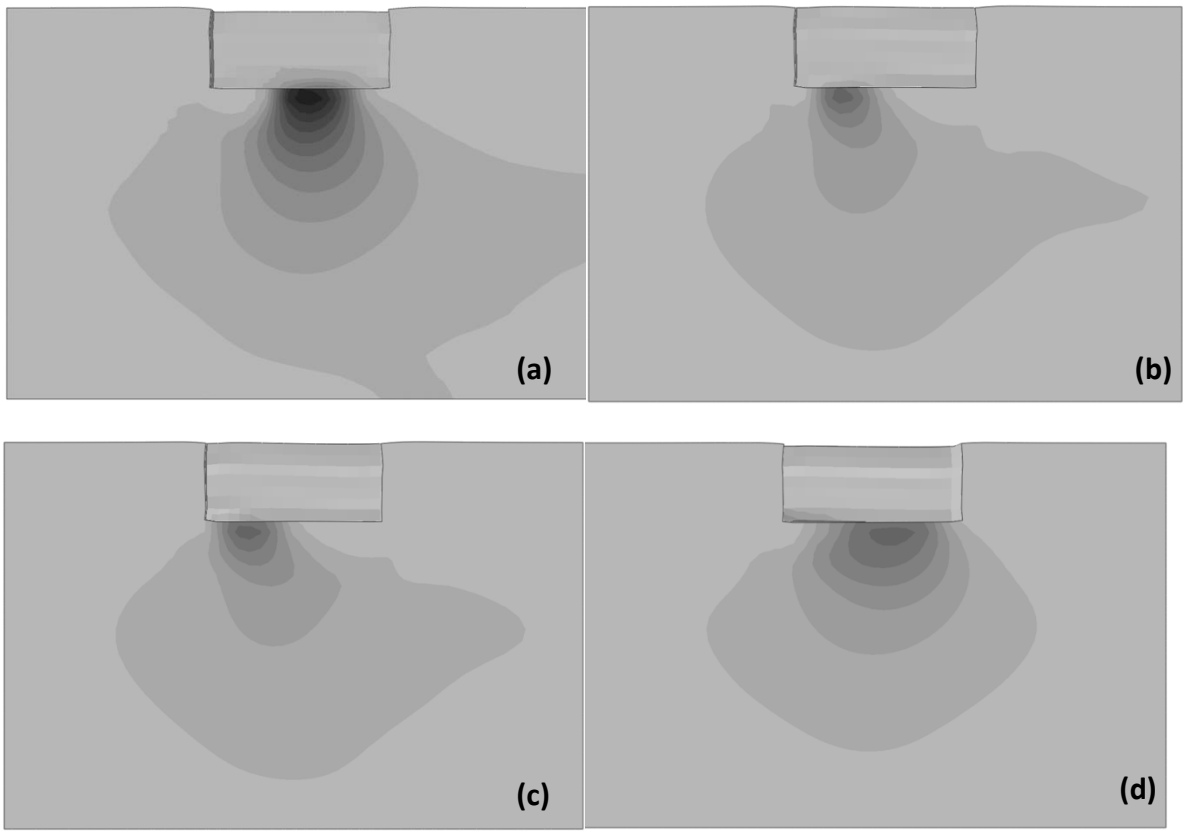

Figure 4.21 Contours showing the stress bulbs underneath the footing at the moment of zero rotation, when already more than half of the cycles have passed. (a) Refers to 0˚, (b) refers to 15˚, (c) refers to 30˚ and (d) refers to 45˚.

Chapter 5

Chapter 5

Comparative Evaluation of Experimental Results & Conclusions

INTRODUCTION

After a thorough study of the most recent experimental research work, the fundamental principles which dictate the response of a rocking system have been established. Based on this overview, this thesis' objective was to simulate the latest large shake table tests performed at the University of California, San Diego. After validating the numerical simulation against the experimental response and motivated by the complex behavior of the rectangular foundation when subjected to dynamic loading, a parametric study was performed varying the angle of loading, either static or dynamic. In this Chapter are presented the conclusions drawn from this MSc thesis. The conclusions are presented in

three sections. The first one compares in a collective way the concluding remarks drawn from literature. A comparative evaluation is performed, approaching the extracted assumptions from a number of aspects concerning the response. In the sequel follow the conclusions drawn from the validation of the numerical FE simulation and the assumptions stemming from the parametric study. Last but not least are proposed topics which would be crucial for further investigation.

1. COMPARATIVE EVALUATION OF LITERATURE CONCLUSIONS

A general conclusion drawn from the literature is that rocking isolation design consistently exhibits superior performance compared with conventional capacity design, regardless of the tested shaking scenario. Nonlinear response of the soil footing interface essentially acts as an effective and resilient energy dissipation 'fuse' showing substantially increased ductility capacity and resistance against cumulative damage despite the successive and intense seismic shaking it has sustained, as mentioned in the various reports. A rocking-isolated pier survives the excessive demands imposed by particularly strong shaking sequences, which may cause catastrophic structural failure of a conventionally designed pier (Loli et al., 2014). Shallow foundations are common components that, if allowed to rock, have the potential to economically introduce energy dissipation and re-centering tendencies into soil-foundation-structure systems. They should be considered as a viable alternative to relatively complicated structural energy dissipation and base-isolation devices.

One of the main characteristics of the rocking response exhibited by a SDOF structure is the fact that vertical displacement and rotation are coupled and the residual displacement depends on the number of cycles during an excitation as well as on the intensity of the excitation. The uplift significantly affects the foundation behavior such as the shape of hysteresis loop, the degradation in the rotational stiffness and the elongation of the system's natural period (Shirato et al., 2008).

1.1. M-ϑ Response

Gajan et al., [2005] suggested that the moment–rotation behavior during slow cyclic and dynamic tests agree very well and that slow cyclic tests may be appropriate for simulating moment–rotation behavior in dynamic events. In other words the backbone curves of load-displacement loops can be modeled based on the load-displacement curves for monotonic loading, as claimed by Shirato et al., [2008]. Deng and Kutter, [2012] extracted results, which were in agreement with the so far published claiming that rocking foundation has a robust and non-degrading rocking moment capacity, as shown from rocking moment versus rotation curves. This behavior is advantageous over a concrete column, which typically exhibits degrading flexural moment capacity.

As far as the interaction between the safety factor against vertical load and the M-ϑ response is concerned, Anastasopoulos et al., [2012] indicated that the shape of the M-ϑ loops is an acute "S", for high FS_V values and oval for low FS_V. This remark had already been highlighted by Shirato et al.,[2007] and others.

Another significant factor, needed to be taken into account is the influence of the P-Δ effects in the moment-rotation response of a rocking system. Even in the case of different FS_V values, the moment loading changes very little and consequently permits similar levels of inertial loading to be transmitted onto the superstructure. This similarity in the capacity can be attributed to two observations:

1. The lateral load capacity being principally controlled by the slenderness ratio, h/L, and thus being insensitive to changes in the foundation out-of-plane dimension; and
2. during cyclic loading, an overstrength mechanism has been observed to take place and affect mainly the capacity of small foundations. This overstrength may be attributed on one hand to the footing becoming gradually embedded as the motion progresses. In this way the system displays additional resistance form the soil through passive pressures. On the other hand, P-Δ effects seem to have a reverse role in rocking systems, since when the rotation changes sign, due to P-Δ effects the system can sustain further rotation, hence exhibiting higher moment resistance.(Drosos et al., 2012)

Of course, in case the lateral displacement of the rocking-isolated system is excessive, the P–Δ effects are mainly the cause of the observed strength degradation. Nonetheless, for the case of a conventionally designed footing, the degradation of strength is mainly the outcome of damage accumulation in the "plastic hinge". This remark is mentioned also in Deng et al., [2012], who underline that for a hinging column, the P-Δ moment is always destabilizing. Cumulative column yielding results in large permanent deformation, whereas for a rocking system, the P-Δ moment provides a restoring mechanism. For this reason Anastasopoulos et al., [2013] argue that the lateral capacity of the rocking isolated system will keep degrading at the same rate with increasing imposed displacement, without exhibiting any rapid strength degradation. Overturning collapse finally takes place at much larger displacement.

1.2w-ϑ Response

A comment made practically in all experimental studies presented herein, especially for the cases of medium sand, is that the increase of permanent settlement seems to be the only substantial drawback of rocking-isolation (Drosos et al., 2012, Anastasopoulos et al., 2013). Of course this phenomenon has mainly to do with the relative density of the sand as backfill soil. This assumption is supported also by Loli et al., [2014], who claimed that the rocking foundation was found to accumulate significant settlement exhibiting what is known as a 'sinking response', this being identified as the only drawback of the rocking isolation

design. Naturally, owing to its significantly lower FS_V, the rocking foundation is prone to suffering increased settlements in comparison with the overdesigned foundations involved in conventional capacity design.

At this point it has to be underlined, that the effect of such settlements on the performance of the bridge have not been measured in any of the presented tests, where the continuity of the deck and the interaction between consecutive piers have not been taken into account. This omission from the specimen's design creates an obstacle, in our drawing a safe conclusion concerning the impact of the residual settlements on the functionality and the design of the bridge. However, as other researchers have pointed out (Antonellis et al., 2015) settlements are expected to be significantly limited should the pier be founded on a denser soil stratum ($Dr > 60\%$), dense enough to actually support the option of a shallow foundation or be subjected to a less deleterious shaking. Moreover, this drawback may be remediated through soil improvement measures, as shown by Anastasopoulos et al., [2012].

Another remark, which needs to be mentioned, is that for small rotational values, settlements prevail. This has been highlighted by Anastasopoulos et al., [2012] and has also been underlined in this thesis as well.

Another significant factor for a rocking foundation is the critical contact length, L_c, which has been introduced by Gajan et al., [2005]. Considering the results reported by Deng and Kutter [2012] as well as the results reported by Gajan and Kutter [2008], settlement occurs during seismic loading when $\frac{L_f}{L_c} \leq 15$, whereas uplift occurred $\frac{L_f}{L_c} > 15$. The critical $\frac{L_f}{L_c}$ that separates cases of residual settlement and uplift probably depends on other factors such as embedment depth and soil backfill type. The mechanisms of the uplift include: (i) the sand falling into the gaps; and (ii) the dilatancy of the soil beneath the footing. The mechanisms of the settlement are: (i) the compaction of soil beneath the footing; and (ii) the bearing failure along the loaded contact interface pushing soil out from under the footing.

1.3Impact Of FS_V

The FS_V affects the development and accumulation of permanent displacements, since as shown by Drosos et al., 2012 the decrease in FS_V leads to increased settlement. An important observation made on systems with intermediate values of FS_V is the soil densification, which takes place during the excitation. This phenomenon is also known as dynamic densification of sand and constitutes an additional cause of settling. Thanks to this effect the soil gradually improves, at a cost however of higher residual vertical displacements.

According to Anastasopoulos et al., [2012], when the factor of safety against vertical loads is relatively large ($FS_V > 10$ for sand) the rocking response of the foundation is mainly uplifting-dominated, not accumulating substantial settlement during sequential cycles of loading. For lower FS_V values (even of the order of 5 for sand) soil yielding takes place underneath the foundation and its response becomes sinking-dominated, leading to

substantial accumulation of settlement. Moreover, in accordance to the point made in the previous paragraph concerning w-ϑ response, that for small rotational values settlements prevail, it is concluded that the higher the FS_V, the smaller the angle leading to uplift (Anastasopoulos et al., [2012]).

One of the most important conclusions drawn by Tsatsis and Anastasopoulos, [2015] is that however similar the behavior of two different systems with the same FS_V may seem (Anastasopoulos et al.,2012), in reality no such connection based solely on the similarity of the factor of safety against vertical load can be made.

By comparing the behavior of two systems with the same FS_V: a lightly loaded system lying on loose sand and a heavily loaded system lying on dense sand, it was found that the two systems exhibit remarkably different behavior: not only does the heavily loaded system accumulate less settlement but also the rotation amplitude of its oscillation is notably smaller as well. This proves that the FS_V alone cannot describe the dynamic response of two systems subjected to the same excitation. As shown in other studies (Kourkoulis et al.,2012), the response of two rocking systems of the same FS_V and aspect ratio h/B subjected to the same excitation can be similar provided that there is the appropriate analogy in the stiffness of the foundation soil. In this case, the loose sand deposit proves to be relatively less stiff leading thus to increased rotation and settlement accumulation for the lightly loaded system.

1.4Impact of Number Of Cycles

As claimed by Anastasopoulos et al., [2012], the rate of settlement decreases with the increase of loading cycles. This decrease is even more pronounced in loose sand, which tends to densify with repeated cycles of loading.

1.5Symmetry And Asymmetry Of Motion

As Drosos et al., [2012] point out, in cases of sinusoidal motions, owing to the inherent symmetry of the excitations, the rocking foundations do not suffer considerable permanent rotation. However, real earthquake excitations include sometimes deleterious asymmetric pulses, which may cause significant permanent foundation rotation. This notion is supported also by Anastasopoulos et al., [2013] claiming that, with respect to rotation, the performance is more sensitive to the "details" of the shaking history. When the preceding seismic events are symmetric, the rotational response is practically insensitive to the shaking history. In stark contrast, when the preceding seismic events are nonsymmetrical (such as directivity affected records), the system accumulates settlement *and* rotation. Consequently, when the already tilted system is subjected to the next seismic event, it is prone to increased accumulation of rotation.

1.6De - Coupling Capability

A significant outcome is the experimental verification—proof of concept—of the potential effectiveness of rocking isolation as a means of seismic protection of a bridge pier. Encouraging evidence has been provided by Drosos et al., [2012] in favor of the idea of changing the philosophy of foundation design toward a less conservative, even unconventional, treatment. Acting as a safety fuse, full mobilization of foundation capacity (in the form of uplifting and soil yielding) constrains the acceleration transmitted onto the superstructure to a value below the critical acceleration, a_c, which is directly associated with foundation capacity, M_{ult}, and, hence, decreases with reducing foundation size. Evidently, under designed foundations drastically reduce the maximum acceleration, a_{max}, transmitted to the deck. For low values of FS_V the dynamic amplification is weaker, in other words the achieved de-coupling is more effective, since the natural period of the system has elongated.

Of course it has to be mentioned at this point, that this significantly advantageous behavior of rocking foundations refers mainly to excitations of high intensity. Seismic events of moderate intensity do net seem to lead to significant structural damage for a conventional system and their response compared to the rocking isolated system does not differ much (Anastasopoulos et al., [2013]).

1.7Frequency Effect

The fundamental frequency of the motion has proven to influence significantly the response of a SFS system: For low period motions the degradation of stiffness is much more intense since the exhibited rotations are multiple times higher. Moreover, the fundamental frequency of the motion overshadows the influence of FS_V (even systems with the minimum FS_V exhibit sizeable uplift). The latter is probably attributed to dynamic densification of the underlying sand. A long-period motion forces the structure to develop large rotational values, thus leading to impact between the footing and the supporting soil. In this way, as the footing performs the first 1-2 cycles of the motion, already leads to rapid densification of the soil (Drosos et al., 2012).

This effect has been highlighted also by Tsatsis and Anastasopoulos, [2015], for the case of having crust of ‘healthy soil” on top of the stratum. The efficiency of shallow soil improvement is also dependent on the fundamental frequency of the motion. While for smaller rotation the foundation is in full contact with the supporting soil, generating a deeper stress bulb, and hence, being affected by the underlying loose sand layer, when uplifting is initiated the effective foundation width is drastically decreased, reducing the depth of the generated stress bulb. Hence, a larger portion of the rocking-induced stresses are obtained by the “healthy” soil material of the crust, improving the performance of the system. Quite interestingly, the decrease of settlement accumulation is much more intense

when the frequency of excitation is lower. In this case, the first two or three cycles are enough to cause substantial dynamic compaction of the soil, and as a result, the remaining strong motion cycles are not leading to any substantial additional settlement.

1.8Preceding Motions

Drosos et al., [2012] and Anastasopoulos et al., [2013] both comment on the plausible effect of preceding motions enhancing the behavior of the system, leading to exhibited overstrength. This effect is probably due to acquired settlement (embedment) from previous excitations. When the rocking-isolated system has sustained a number of shaking events (symmetric or not), it tends to accumulate substantially reduced settlement. Such performance amelioration is presumably due to soil densification taking place during the preceding shaking events.

1.9Shallow Soil Improvement

Anastasopoulos et al., [2012] presented an extensive work on the shallow soil improvement in the context of rocking isolation. Foundation rocking maybe desirable to limit the inertia forces acting on the superstructure but incorporates the peril of unacceptable settlements in case of low FS_V. Hence, in order to ensure that rocking is materialized through uplifting rather than sinking, an adequately large FS_V is required. Although this is feasible in theory, soil properties are not always well-known in reality, tending to limit the applicability of the whole concept of rocking isolation. However, since rocking-induced soil yielding is only mobilized within a shallow layer underneath the footing, ‘‘shallow soil improvement’’ is considered as an alternative approach to release the design from the jeopardy of an unforeseen inadequate FS_V (due to overestimation of soil properties).

The concept of shallow soil improvement is proven to be quite effective. In the case of a lightly-loaded system (having $FS_V > 10$ in ideal soil conditions), a z/B=1 dense sand crust is enough to achieve practically the same performance with the ideal case of dense sand. A shallower z/B=0.5 soil improvement may also be considered effective, depending on design requirements. Although results are highly dependent on inherent nonlinearities in the formation of the stress bulb, it may be conservatively concluded that an improvement layer of depth equal to the foundation width offers a safe solution for practical applications.

The effectiveness of shallow soil improvement is ameliorated with the increase of the cyclic rotation amplitude, since with the increase of soil improvement depth z/B, uplifting is promoted for a wider rotation range.

While for small rotations the foundation is in full contact with the supporting soil, generating a deeper stress bulb and hence being affected by the underlying loose sand layer, when uplifting is initiated the effective foundation width is drastically decreased, reducing

the depth of the generated stress bulb. The same conclusion is practically drawn for a heavily-loaded structure.

Another idea, coming from Deng and Kutter, [2012] of soil improvement includes the introduction of concrete pads in the design of a rocking isolation system. Slow cyclic loading and seismic shaking tests showed that the settlement was reduced to some varying extent by concrete pads near the edges of the footing. The rocking moment capacity of footings with concrete pads was observed to be larger than that of footings without pads. The use of pads or some other form of ground improvement would enable a controllable mechanism for reducing rocking-induced settlements while taking advantage of rocking.

1.10 Correlation of Static And Dynamic Loading Results

As mentioned before, the moment–rotation behavior during slow cyclic and dynamic tests agree very well and slow cyclic tests may be appropriate for simulating moment–rotation behavior in dynamic events. This notion is supported by both Gajan et al., [2005] and Shirato et al., [2007].

However, the situation is strikingly different when it comes to settlements, as highlighted by Tsatsis and Anastasopoulos [2015]. The tests presented therein confirm the key conclusions of the static experiments but they also reveal substantial differences, which are attributed to kinematic soil response and dynamic compaction–mechanisms that cannot possibly be simulated through static pushover testing. Although qualitatively the shake table tests confirm the findings of the slow-cyclic pushover tests, from a quantitative point of view, there are very substantial differences. These differences can only be attributed to the dynamic response of the soil, which cannot possibly be captured through slow cyclic loading. Under dynamic loading, the deformation of the soil underneath the footing is not only due to the stresses imposed by the rocking foundation (inertia loading) but is also affected by the shear stresses that develop within the soil due to the seismic shaking itself (kinematic loading). Even in the absence of a rocking foundation, due to the developing shear stresses within the soil (kinematic loading), the sand would settle: dynamic compaction. However, compared to the free field where the soil is compacted under zero normal stress at the surface, the soil underneath the footing is compacted under the weight of the footing, leading thus to increased settlements.

1.11 Re-centering And Energy Dissipation

Ideal structural systems should have both the ability to dissipate large quantities of energy and the ability to re-center after dynamic loading; however, these two abilities tend to oppose each other, in other words, there is a tradeoff between the energy dissipation and re-centering ability. For example an elastic column with perfect re-centering ability has no energy dissipation, whereas an elastic perfectly plastic column is a very good energy

dissipater but it will end up with a large residual displacement if subjected to a unidirectional load pulse.

A rocking footing on a rigid ground re-centers itself but is not able to absorb energy when the zero hysteretic and radiation damping is assumed during rocking. Rocking foundations on competent but not rigid soil also provide a good mix of beneficial effects of re-centering and energy dissipation. In fact, Deng and Kutter, [2012], proposed that rocking foundations with $\frac{L_f}{L_c} = 10 \div 30$ may provide optimal good tradeoff. If the ground is too soft, the re-centering is lost; if the ground is too rigid, then the energy dissipation is lost. For poor soil conditions, ground improvement can be used to produce a superior combination of energy dissipation and re-centering for rocking foundations.

However, in the application of concrete pads, utilized by Deng and Kutter, [2012] a slimmer rocking moment versus rotation hysteresis and better re-centering was observed in the dynamic shaking tests, proving exactly the previously described trade-off effect. The rocking foundation has an advantage of being simpler and more economical, but we do not yet have procedures for precise control over the balance between energy dissipation and re-centering.

A rocking footing with large $\frac{L_f}{L_c}$ has a good mix of energy dissipation and re-centering ability that will produce good seismic performance for soil-foundation-bridge systems. The dissipated energy increases as $\frac{L_f}{L_c}$decreases and as the amplitude of footing rotation increases. The performance of the rocking isolated system as energy dissipater may also be increased and re-centering hindered by sand falling into the gap beneath an uplifting footing.

1.12 Foundation Shape

Hakhamaneshi and Kutter, [2015] conclude that for rectangular footings the effect of the shape is characterized by the ratio b/L_c, where b is the width of the footing; whereas for H-shaped footings the shape is characterized by both the missing area ratio MAR and b/L_c. The researchers found that under the same critical contact ratio, wider rectangular rocking footings, i. e. footings with higher b/L_cratio, settle less than narrow rocking footings. For a rectangular footing with large b/L_c, the soil deformations associated with the localized bearing failure would be expected to be primarily in the plane of rotation.

Due to less lateral confinement around the rocking edge and the 3D nature of failure mechanism for narrow footings, a larger fraction of soil displaced by bearing failure at the loaded edges is pushed out from underneath the footing; hence larger settlements are expected for narrow footings. In the case of wide rectangular footings, lateral confinement reduces out-of-plane soil displacements and settlements. For an H-shaped footing, it is observed that footings with larger MAR suffer larger settlements, which can be attributed to the smaller lateral confinement around the rocking edge (flange).

The general notion is that factors hindering the re-centering of the rocking footing, lead to an increase in the damping ratio and an increase in the amplitude of residual settlement or uplift. For surface and embedded footings, the widest rectangular footing had the greatest re-centering behavior, the smallest damping ratio and the lowest potential for residual uplift or settlement. The H-shaped footings with large MAR, have the poorest re-centering behavior, the largest damping ratios and the greatest potential for residual settlement or uplift.

1.13 Embedment Effect

The aforementioned researchers drew significant assumptions concerning the effect of embedment as well. They introduce the concept of a *critical embedment*. According to their results, a foundation-superstructure system may reach a single value of ultimate embedment, regardless of its initial embedment. At critical embedment, the uplift due to soil falling under the footing balances the settlements due to local bearing failure and hence this might be useful design embedment target. However difficult the accurate prediction of the critical embedment depth may be, still as a concept it is considered useful for understanding the mechanisms of residual settlement and uplift.

For footings embedded in sand with a small ρ_{ac}, rocking results in residual uplift. This outcome could be attributed to the sand falling into the gap, which cyclically opens and closes as the footing rocks. The magnitude of normalized residual uplift is greater for footings with small b/L_c, especially at large amplitudes or rotation. The test results of the embedded H-shaped footings showed that as the MAR increases, the residual uplift increases accordingly.

The researchers point out that it is not possible to correlate settlement uniquely to the ρ_{ac} or the footing shape because the tendency for settlement also depends on other factors such as embedment, and possibly on the amplitude of sliding compared to the amplitude of rotation. As depth increases, the uplift mechanisms (dilation and soil raveling, sliding or being scraped into the gap under the footing) become more important and the settlement mechanisms (bearing failure and densification) become less significant. The researchers are led to a hypothesis that there is some value of critical embedment at which the settlement mechanisms balance the uplift mechanisms. Despite of this concept being useful, they conclude that the critical depth of embedment cannot be predicted, due to a variety of factors (soil type and moisture conditions) involved.

2. CONCLUSIONS FROM THE VALIDATION OF THE NUMERICAL MODEL

In this paragraph are presented the conclusions drawn from the effort to validate the numerical simulation against the latest large shake table tests performed at the University of California, San Diego.
The validation of the numerical model was performed in both static and dynamic terms. For academic reasons, two constitutive models are utilized: the equivalent von Mises and the Mohr Coulomb.

2.1 Static Results

- The computed moment capacity by means of FE analyses for the aligned footing is in rather good agreement with the calculated value of Antonellis et al., [2015]. Both constitutive models lead to an ultimate lateral load of the system strikingly close to the target value. The same conclusion is valid also for the skewed footing, which has been checked only with the equivalent von Mises constitutive model.
- Unanimity between the computed and the experimental results is reached also for the natural period of the system, for both cases: the aligned and the skewed footing.
- In terms of the achieved safety factor against vertical load, the equivalent von Mises constitutive model led to underestimated value of strength. The “omission” of the dilatancy from this failure criterion, as a key parameter controlling the soil behavior, influents significantly the results in the push down tests. The obstructed tendency of the soil to swell due to external loading provides strength to the soil skeleton. Hence it is logical for the case of the equivalent von Mises constitutive model to underestimate the bearing capacity of the soil formation, since the sand dilation is not accounted for.
- In terms of the achieved safety factor against vertical load, the Mohr-Coulomb constitutive model led to overestimated strength. Due to the proximity and the nature of the boundaries the mechanism has not developed fully and thus a plasmatic overstrength is exhibited in the analysis.

2.2 Dynamic Results

- For the aligned footing and the equivalent von Mises constitutive model it is evident that the numerical simulation provides results, which are in strikingly good agreement with the experimental outcome, in terms of the developed moments and rotations. The rotational stiffness of the system as shown in the M-ϑ loops, as well as the frequency content of the rotational time history confirm that the simulation represents satisfactorily the tested setup.

- For the aligned footing and the equivalent von Mises constitutive model it is evident that there is inherent weakness in the numerical simulation to reach the values of settlement exhibited during the experiments. The omission of dilatancy combined with the fact that the simulated soil formation is already more compliant than it "should" led to settlements which are larger than the ones presented in the experimental report.
- The same results, i. e moment-rotation, and settlement-rotation computed with the Mohr-Coulomb constitutive model present a different view. The system seems to behave in a much more elastic way, displaying much slimmer M-ϑ loops. This indicates that the hysteretic damping in this case is largely underestimated, an indication of which, is also the quite larger rotational values demonstrated in the system's response. Apart from that, although the settlements seem to be negligible, hence achieving the "uplifting-dominated" response exhibited during the experiments, the effect of dilatancy distorts the results. Its inevitably high value (since the friction angle is so high) leads to permanent uplift of the system, which by no means reflects the reality.
- Concerning the skewed footing computed based on the von Mises constitutive model, the settlements seem to be overestimated even more, compared to the analytical results for the aligned model. This is attributed to the complex response of a skewed footing, as it demonstrates high rotations, hence imposing extremely localized high normal traction. This leads to penetration of the underlying soil, creating locally plastic deformations. As the footing tends to rotate toward the opposite direction, its residual rotation hinders its tendency, thus forcing it to push the curved soil downwards. Therefore, the exhibited response is "sinking" dominated. After all, as underlined before, the simulated backfill soil is compliant enough to encourage such response.
- Another implication in the response of the skewed footing has to do with the fact that after the first strong motions pass, it fails to reach the expected moment and rotational values. The former is attributed to the permanent deformation of the trench, leading to degradation in the system's overall stiffness. The deformation of the trench leads also to the maximum exhibited moment approaching practically the moment capacity of surface foundation. The reduced rotational values are attributed on one hand to the fact that the natural period of the system has been elongated, thus leading to lower developing accelerations and thus lower rotational values. On the other hand it has to do with the intense curvature of the soil-foundation interface, obstructing in this way the footing to exhibit equally large rotational values in both directions.
- Based on the two last points, it comes as preliminary conclusion that the rectangular shape for a footing seems to introduce significant issues to its response, having mainly to do with the geometric nonlinearities involved. Were the footing of circular shaped, such effects of extremely localized vertical tractions, would have been

avoided. Further investigation concerning the effect of biaxial dynamic motion on the response of the footing, is presented in the conclusions of the parametric analyses.

3. General Assumptions

The effort to validate the numerical model led to interesting assumptions which are discussed below:

- As shown from the inherent weaknesses to approach the performed tests, it is arisen as compelling need that static pushover and pushdown tests be performed, before the system is checked dynamically. However widely accepted and acknowledged may be the efficacy of certain formulas, in reality and especially in large scale experiments, the uncertainties involved dictate that the experimental method verifies the analytical.
- The experimental results of both the aligned and the skewed footing in the experiments show that the concept of rocking isolation is rather persuasive of its efficacy, especially when utilized in combination with backfill soil of high D_r.
- In both cases the response is uplifting dominated ending up to a total settlement of $1cm$ for both the aligned and the skewed footing.
- In terms of moment capacity, the system behaves within its bending strength, showing momentarily slightly larger values of moment (overstrength) due to the soil falling underneath the footing.
- The raveling of the soil underneath the footing is evident, as shown by the videos during the tests and as highlighted also by Antonellis et al., [2015]. Moreover, this effect has been widely discussed also by Hakhamaneshi and Kutter, [2015], being held responsible for the limited settlements exhibited during the rocking response of the footings.
- Of course, such behavior cannot be possible captured by a Finite Element software, but rather it would require sophisticated coding, accounting for large deformations. Even in this case though, it has to highlight that such an effect is highly random and thus is difficult to be simulated in the frame of formulas describing its exact mechanism.
- It is confirmed by both the static and dynamic analytical results, that the Mohr-Coulomb constitutive model is inappropriate for simulating dynamic cyclic problems, because of its bilinear nature. Its use entails an underestimation of the hysteretic damping, provided by the cyclic soil behavior, in a significant range of deformations; the soil behaves as an elastic material. There is no foresight in this model for the gradual degradation of the initial shear modulus and the increase of damping ratio as the shear deformations increase, which is also an erroneous approach of the dynamic soil response.
- As shown by the results from the computations with the equivalent von Mises constitutive model, although in terms of strength, the simulation *is* accurate

compared with the described soil conditions in the confining box, in terms of deformation, there are *inherent* weaknesses in the constitutive law.

- From the aforementioned, the necessity for a more sophisticated constitutive model is underlined, so that the behavior of cohesionless soils be more accurately approached, without omitting crucial parameters affecting the soil's behavior.

4. CONCLUSIONS FROM THE PARAMETRIC STUDY

The results of the parametric study using two symmetrical (sinusoidal) motions, one of high frequency and low amplitude and one of low frequency and high amplitude led to interesting findings concerning the rocking response of a square footing. The two motions were applied in 0, 15, 30 and 45 degrees and the concluding remarks concerning the exhibited response are as follows:

- The sinusoidal motion introduces a numerical inaccuracy in the FE model, since it bears an inherent fault of commencing with a velocity pulse. In other words, the initial velocity not being zero modifies the exhibiting response by forcing the system to exhibit an initial larger pulse, compared to the following ones.
- A motion of high frequency and low amplitude, will force the system to respond well within its bending strength, developing small rotational values and exhibiting predominantly sinking settling mechanism. This behavior is the same regardless of the angle by which the motion is imposed on the system.
- A motion of low frequency and high amplitude, will force the system to respond differently, depending on the angle of imposed motion: an aligned footing, shall reach its moment capacity, whereas all skewed ones, due to the higher deformation of the trench they cause through their response, will respond exhibiting lower moment values than the system's capacity. In fact, they practically behave like surface foundations, since the lateral confinement of the soil seems to be less effective, when the trench has suffered significant plastic deformations. This behavior has been underlined also in the case of seismic motions.
- As long as the footing rocks on a clearly defined dimension (side or diagonal), the hysteretic damping of the system seems to be less compared to cases where the footing exhibits a combined response of rocking and spinning along its circumference. In the latter case, applicable for 15˚ and 30˚ the M-ϑ loops are slightly broader. Such an effect is visible only in cases, where the system is excited immensely, by a strong long-period motion.
- A motion of low frequency and high amplitude, will force the system to develop small rotational values and exhibit uplift. Of course settlements are still accumulating, leading to higher residual settling values, compared to the ones exhibited in the case of the weak sinus.

- In both motions the same trend appears, which contradicts the exhibited behavior during seismic motions: In the case of symmetrical motions, the larger the angle of the imposed motion, the smaller the value of residual settlements.
- The soil becomes intensely curved, due to the cyclic symmetrical rocking response of the footing. In fact the curvature is much more intense for the case of the strong sinus, than for the weak one. This leads to the footing rocking only on a small part of its width, which decreases as the angle of imposing motion increases. For this reason large motion angles lead to shallower stress bulbs, and hence to smaller settlements.
- The difference between a symmetrical motion and a seismic excitation including strong unsymmetrical pulses is clearly mirrored in the settling response of the system. The footing penetrates the soil, when it is subjected to a strong long-period pulse. In case the pulse is unsymmetrical, the footing cannot fully re-center and exhibit equally large rotation toward the opposite direction, hence maintain residual rotation. However, thanks to the purely symmetrical nature of the sinus motions, the system does not acquire permanent rotation, but rather manages to exhibit practically equal rotation to the opposite direction as well. The price to pay from this cyclic, symmetrical motion is the excessive curvature of the underlying soil.
- It is confirmed by the aforementioned results that a different footing shape, circular perhaps to avoid the edges, or maybe a rectangular but not a square, may be more beneficial in the system's response under biaxial dynamic loading.

5. SUGGESTIONS FOR FURTHER INVESTIGATION

The scope of this MSc thesis was to further investigate the rocking response of socking shallow footings, by means of combining analysis and real-scale testing. The limited framework of this research work led to conclusions, which shed light on the dynamic response of square shallow footings, when subjected to dynamic cyclic loading, uniaxially and biaxially.

However, there are still crucial issues to be investigated, in order for a better view of the problem to be acquired and safer, more generalized conclusions to be drawn.

To begin with, it is necessitated that more sophisticated constitutive models be developed and tested on such problems concerning soil backfill, in order to achieve better accuracy concerning the dynamic soil response also in terms of deformations.

A variety of motions, symmetrical and nonsymmetrical, stemming both from real earthquake records as well as artificial should be utilized on such systems, in order for a better view of the response to be acquired. These motions should be applied in a variety of angles to the system.

Moreover, it is of major importance that the footing shape is investigated as a varying parameter, so that the extent and the way the shape of the footing affecting the response of the system is determined.

At the moment there is an inherent weakness to simulate physically a whole structure, e. g. a bridge, on rocking foundations and test it. However, FE analyses overcome this obstacle; hence it is important that such research be headed toward the implementation of the whole structure in the model, so as to be certain whether the developing deformations affect the structure's continuity and by extension its design and functionality.

APPENDIX A

Who	When	Type	Loading	Testing Method	Slenderness Ratio	Soil Type	FSv	Dr	Intensity	Maximum Footing Rotation (mrad)	Residual Footing Rotation (mrad)	Residual Settlement (mm)
Paolucci et al. Shirato et al.	2007	ST	slow cyclic and dynamic (seismic)	Large Scale	1.5	Dry Sand	29.0	80%	NA	40	161*	17.6* (3.52%)
Drosos et al.	2012	ST	static, slow cyclic and dynamic (sinusoidal)	Reduced Scale	`	Dry Sand	7.5	85%	moderate severe severe¥	1.3 4 18	0.4 1 3	20 (1.20%) 34 (2%) 75 (4%)
					1.9		3.4		moderate severe severe¥	1 4.5 18	0.3 1.3 1	25 (1.8%) 60 (4.3%) 100 (7.14%)
					1.9		2.3		moderate severe severe¥	1.1 5 17	0.5 2 1	27 (2.4%) 70 (6.14%) 130 (11.4%)
Anastasopoulos et al.	2012	ST	static, slow cyclic	Reduced Scale	3	Dense Sand	14 (A) 5 (B)	93% 93%	NA	100 92	8.4 8.4	7.5 (5%) 18.75 (12.5%)
						Loose Sand	5 (A) 2.6 (B)	45% 65%	NA	120 92	33 8.4	22.5 (15%) 36 (24%)
						z/B = 0.5 z/B = 1.0	7.1 (A) 9.9 (A)	NA	NA	92 92	0 0	7.5 (5%) 10.5 (7%)
						z/B = 0.5 z/B = 1.0	4.1 (B) 3.7 (B)	NA	NA	92 92	8.4 8.4	27 (18%) 18.75 (12.5%)

Who	When	Type	Loading	Testing Method	Slenderness Ratio	Soil Type	FSv	Dr	Intensity	Maximum Footing Rotation (mrad)	Residual Footing Rotation (mrad)	ResidualSettlement (mm)
Tsatsis & Anastasopoulos	2015	ST	dynamic (seismic)	Reduced Scale	3	Dense Sand z/B = 1.0 z/B = 0.5 Loose Sand	14 (A) 7.1 (A) 9.9 (A) 5 (A)	NA	MODERATE (Aegion, 1995)	10	0.3 2 2.5 10	20 (13%) 54 (36%) 80 (53%) 120 (80%)
									SEVERE (Pacoima Dam, 1971)	40 40 Collapse Collapse	12 45 - -	75 (50%) 125 (83%) - -
									SINUS (2Hz)	5 5 7 -	0 0 4.5 -	25 (16.7%) 58 (38.7%) 84 (56%)
									SINUS (1Hz)	10 10 20 -	7 7 15 -	20 (13%) 27 (18%) 33 (22% -
						Dense Sand z/B = 1.0 z/B = 0.5 Loose Sand	5 (B) 4.1 (B) 3.7 (B) 2.6 (B)		SINUS (2Hz)	6 6 6 20	2 2 4 20	32 (21.3%) 43 (28.7%) 56 (37.3%) 79 (52.7%)

Who	When	Type	Loading	Testing Method	Slenderness Ratio	Soil Type	FSv	Dr	Intensity	Maximum Footing Rotation (mrad)	Residual Footing Rotation (mrad)	Residual Settlement (mm)
Anastasopoulos et al.	2013	ST	dynamic (seismic)	Reduced Scale	1.2 1.9	Dense Sand	6.9 3.3	0.85	MODERATE (Aegion, 1995)	4 5	0 1	27 (2.5%) 29 (4.1%)
									STRONG (Gilroy, 1989)	3.4 7.2	1 1.8	11 (1.0%) 32 (4.6%)
									EXTREME (Rinaldi, 1994)	26 25	7 14	58 (5.3%) 103 (14.7%)
									"Virgin State"¤	24	20	280 (40%)
									"After multiple non-sym."¤	49	50	120 (17.1%)
									"After multiple sym."¤	23	25	70 (10%)
Antonellis et al.	2015	ST	dynamic (seismic)	Large Scale	2 1.72	Dense Sand	24	0.9	Gilroy Array	3 2.5	0.36 2.4	0.6 (0.04%) 0.5 (0.04%)
									Corralitos	5 4.3	0.05 4.3	1 (0.07%) 0.7 (0.05%)
									El Centro	9 6.8	0.11 6.6	0.7 (0.05%) 1.3 (0.04 %)
									Pacoima Dam	28 25.4	1.54 25.4	2.4 (0.16%) 5 (0.33%)
									Takatori (50%)	55 42.2	1.67 41.6	2.8 (0.19%) 3.5 (0.23%)
									Takatori (100%)	103 105.8	22 26	0.5 (0.04%) 0.2 (0.01%)

Who	When	Type	Loading	Testing Method	Slenderness Ratio	Soil Type	FSv	Dr	Intensity	Maximum Footing Rotation (mrad)	Residual Footing Rotation (mrad)	Residual Settlement (mm)
Deng and Kutter	2012	C	static, slow cyclic dynamic (seismic)	1:49	≈2	MediumSand	>30 NA 9 - 10	73% 73% 44%	slow cyclic	50 30[#] 50	0 8[#] 10	0 (0%) 50 (0.75%)[#] 100 (2.10 %)
							11 NA	38% 38%	dynamic (seismic)	10 14[#]	0 0	12.9 (0.18%) 10.5 (0.14%)
Loli et al.	2014	C	dynamic (seismic)	1:50	1.43 2.7	Medium Density Sand	18 3.5	0.6	Increasing (Sc. A)	23 4	17 4	150 (2%) 60 (1.5%)
									Decreasing (Sc. B)	35 5	26 4	125 (1.67%) 90 (2.25%)

* After the Case S1 - 4

¥ for severe shaking with F_E = 1 Hz.

¤ only for the FSv = 3.3

\# with concrete pads

REFERENCES

[1]. M. Apostolou, G. Gazetas, E. Garini, *"Seismic response of slender rigid structures with foundation uplifting"* ELSEVIER Soil Dynamics and Earthquake Engineering 27 (2007) 642–654

[2]. Ntritsos Nikolaos Diploma Thesis: "Inelastic Response of Embedded Foundations", March 2012

[3]. Gavras Andreas - Gerasimos Diploma Thesis: "*Metaplastic Analysis Of Rocking 1 – Dof Systems On Two Layered Soil*", November 2010

[4]. Kokkali Panagiota Diploma Thesis: "*Metaplastic Rocking Response Of 1 – Dof Systems: Dimensional Analysis*", October 2010

[5]. George Gazetas n, Ioannis Anastasopoulos, Evangelia Garini "*Geotechnical design with apparent seismic safety factors well-below 1*" ELSEVIER Soil Dynamics and Earthquake Engineering 57 (2014) 37 – 45

[6]. Grigorios Antonellis; Andreas G. Gavras; Marios Panagiotou, Bruce L. Kutter, Gabriele Guerrini, Andrew C. Sander, Patrick J. Fox, "Shake Table Test of Large-Scale Bridge Columns Supported on Rocking Shallow Foundations", ASCE Journal of Geotechnical and Geoenvironmental Engineering , May 2015, Vol. 141, No. 5

[7]. New Zealand bridge-manual-3rd-edition-section-5 "Earthquake Resistant Design of structure", The NZ Transport Agency's *Bridge manual* SP/M/022 Third edition, Effective from May 2013

[8]. P. Adebar, R. DeVall, P. Bazargani, and D.L. Anderson "Seismic Design Of Foundations: The 2015 Canadian Building Code", Tenth U.S. National Conference on Earthquake Engineering, Anchorage, Alaska

[9]. Hsiao-Hui Hung, Kuang-Yen Liu, Tzu-Hui Ho and Kuo-Chun Chang "An experimental study on the rocking response of bridge piers with spread footing foundations", Earthquake Engng Struct. Dyn. 2011; 40:749–769

[10]. Lijun Deng; Bruce L. Kutter; and Sashi K. Kunnath "Centrifuge Modeling of Bridge Systems Designed for Rocking Foundations", 2012 American Society of Civil Engineers.

[11]. Bruce L. Kutter, Tara C. Hutchinson, Mark A. Moore, Sashi Kunnath, Lijun Deng, "Influence of Physical Modeling on Adoption of Rocking Foundations in Practice" 2012 American Society of Civil Engineers

[12]. I. Anastasopoulos, G. Gazetas, M. Loli, M. Apostolou, N. Gerolymos "Soil failure can be used for seismic protection of structures", Bull Earthquake Eng (2010) 8:309–326

[13]. Sivapalan Gajan, Bruce L. Kutter, , Justin D. Phalen, Tara C. Hutchinson, Geoff R. Martin, "Centrifuge modeling of load-deformation behavior of rocking shallow foundations", Soil Dynamics and Earthquake Engineering 25 (2005) 773–783

[14]. I. Anastasopoulos, M. Loli, T. Georgarakos, V. Drosos," Shaking Table Testing of Rocking—Isolated Bridge Pier on Sand", (2013): Shaking Table Testing of Rocking—Isolated Bridge Pier on Sand, Journal of Earthquake Engineering, 17:1, 1-32

[15]. I. Anastasopoulos, Th.Kontoroupi "Simplified approximate method for analysis of rocking systems accounting for soil inelasticity and foundation uplifting", Soil DynamicsandEarthquakeEngineering56(2014)28–43

[16]. O. Adamidis, G. Gazetas, I. Anastasopoulos, Ch. Argyrou, "Equivalent-linear stiffness and damping in rocking of circular and strip foundations", Bull Earthquake Eng (2014) 12:1177–1200

[17]. Roberto Paolucci, Masahiro Shirato and M. Tolga Yilmaz, "Seismic behaviour of shallow foundations: Shaking table experiments vs numerical modeling", Earthquake Engng Struct. Dyn. 2008; 37:577–595

[18]. Ioannis Anastasopoulos, Rallis Kourkoulis, Fani Gelagoti, Efthymios Papadopoulos, "Rocking response of SDOF systems on shallow improved sand: An experimental study", Soil DynamicsandEarthquakeEngineering40(2012)15–33

[19]. Tsatsis A. and Anastasopoulos I. (2015) "Performance of rocking systems on shallow improved sand: shaking table testing. Front. Built Environ. 1:9. doi: 10.3389/fbuil.2015.00009

[20]. I. Anastasopoulos; F. Gelagoti; R. Kourkoulis; and G. Gazetas, "Simplified Constitutive Model for Simulation of Cyclic Response of Shallow Foundations: Validation against Laboratory Tests, (2011) American Society of Civil Engineers.

[21]. T. B. Algie, L. Deng, E. Erduran, B. L. Kutter and S. Kunnath, " Centrifuge Modeling Of Innovative Foundation Systems To Optimize Seismic Behavior Of Bridge Structures", 14th World Conference on Earthquake Engineering October 12-17, 2008, Beijing, China

[22]. Gajan S., Kutter B. L. "Capacity, settlement, and energy dissipation of shallow footings subjected to rocking."Journal of Geotechnical and Geoenvironmental Engineering, ASCE2008;134(8):1129–41.

[23]. Panagiotidou AI., Gazetas G.,Gerolymos N. "Pushover and seismic response of foundations on stiff clay: analysis with P-D effects", Earthquake Spectra, 2012

[24]. Morris DV. Dynamic soil–structure interaction modeled experimentally on a geotechnical centrifuge. Canadian Geotechnical Journal 1981; 18(1):40–51.

[25]. Gajan S, Kutter BL. Effects of moment-to-shear ratio on combined cyclic load–displacement behavior of shallow foundations from centrifuge experiments. ASCE Journal of Geotechnical and Geoenvironmental Engineering 2009; 135(8):1044–1055. DOI: 10.1061/(ASCE)GT.1943-5606.0000034.

[26]. Deng L, Kutter BL, Kunnath SK. Centrifuge modeling of bridge systems designed for rocking foundations. ASCE Journal of Geotechnical and Geoenvironmental Engineering 2012 (in press). DOI: 10.1061/(ASCE) GT.1943-5606.0000605

[27]. Trombetta NW, Mason HB, Chen Z, Hutchinson TC, Bray JD, Kutter BL. "Nonlinear dynamic foundation and frame structure response observed in geotechnical centrifuge experiments". Soil Dynamics and Earthquake Engineering 2013; 50:117–133.

[28]. Hakhamaneshi M., Kutter B. L., "Effect of footing shape and embedment on the settlement, re-centering and energy dissipation of shallow footings subjected to rocking". (in print)

[29]. Ugalde JA, Kutter BL, Jeremic B. "Rocking response of bridges on shallow foundations", Pacific Earthquake Engineering Research Center Report 2010/101, University of California, Berkeley, California, 2010.

[30]. Gajan S, Kutter BL. "Capacity, settlement, and energy dissipation of shallow foundations subjected to rocking". ASCE Journal of Geotechnical and Geoenvironmental Engineering 2008; 134(8):1129–1141. DOI: 10.1061/(ASCE)1090-0241(2008)134:8(1129).

[31]. Kourkoulis, R., Anastasopoulos, I., Gelagoti, F., and Kokkali, P.(2012). "Dimensional analysis of SDOF systems rocking on inelastic soil." J. Earthquake Eng. 16, 995–1022. doi:10.1080/13632469.2012.691615

[32]. Pecker A. [1998] " Capacity design principles for shallow foundations in seismic areas. " In : Proc. 11th European conference on earthquake engineering, A.A. Balkema Publishing

[33]. Perry J. [1881] " Note on the rocking of a column. " Trans. Seismol. Soc. Jpn 1881(3), 103-106

[34]. Poulos H.G., Carter J.P., Small J.C. *2002+ "Foundations and retaining structures – research and practice" Proc. 15th International Conference on Soil Mechanics, Instanbul, 4: 2527-2606

[35]. Priestley M.J.N., Seible F., Calvi G.M.[1996] " Seismic design and retrofit of bridges. " John Wiley and sons, New York.

[36]. Psycharis I., Jennings P. [1983] " Rocking of slender rigid bodies allowed to uplift. " Earthquake Eng. Struct. Dyn. 11, 57-76

[37]. Psycharis I. [1991] " Effect of base uplift on Dynamic Response of SDOF structures. " Journal of Structural Engineering, ASCE 117, 733-754

[38]. Raychowdhury P., Hutchinson T.C. [2009] " Performance evaluation of a nonlinear Winkler – based shallow foundation model using centrifuge test results. " Earthquake Engng Struct. Dyn. 38, 679– 698

[39]. Raychowdhury P., Hutchinson T.C. [2010] " Performance of seismically loaded shearwalls on nonlinear shallow foundations. " Int. J. Numer. Anal. Meth. Geomech., published online.

[40]. Taiebat H., Carter J.P. [2003] " Contact between soil and circular foundations under eccentric loading. " Proc. 2nd MIT Conf. Computational Fluid and Soil Mechanics, Mass., 674-677

[41]. Terzaghi K. [1943] " Theoretical soil mechanics. " Wiley, New York.

[42]. Ukritchon B., Whittle A.J., Sloan S.W.,[1998] " Undrained limit analysis for combined loading of strip footings on clay. " J. Geotech. Geoenvon. Eng. ASCE 124(3), 265-276

[43]. Wang C.X. *2000+ "Large deformation analysis of strip footings on layered purely cohesive soils" Proc. 4th Australia - New Zealand Young Geotechnical Professionals Conf., Australian Geomechanics Society, 229-234

[44]. Wang C.X., Carter J.P. *2000+ "Penetration of strip and circular footings into layered clays. Advances in Theoretical Geomechanics" Proc. of the John Booker Memorial Symposium, Sydney, 193-210

[45]. Zhang J., Makris N., [2001] " Rocking Response of Free - Standing Blocks under cycloidal Pulses. " Journal of Engineering Mechanics ASCE 127(5), 473-483

[46]. Gourvenec, S. [2007] "Shape effects on the capacity of rectangular footings under general loading," Géotechnique 57(8), 637–646.

[47]. Houlsby, G. T., Amorosi, A., and Rojas, E. [2005] "Elastic moduli of soils dependent on pressure: a hyperelastic formulation," Géotechnique 55(5), 383–392.

[48]. Housner, G. W. [1963] "The behavior of inverted pendulum structures during earthquakes," Bulletin of the Seismological Society of America 53(2), 404–417.

[49]. Huckelbridge, A. A. and Ferencz, R. M. [1981] "Overturning effects on stiffened building frames," Earthquake Engineering & Structural Dynamics 9(1), 69–83.

[50]. Kourkoulis, R., Gelagoti, F., Anastasopoulos, I. [2012] "Rocking isolation of frames on isolated footings: design insights and limitations," Journal of Earthquake Engineering 16(3), 374–400.

[51]. Kutter, B. L., Martin, G., Hutchinson, T. C., Harden, C., Gajan, S., and Phalen, J. D. [2003] "Status report on study of modeling of nonlinear cyclic load–deformation behavior of shallow foundations," PEER Workshop, University of California, Davis, California.

[52]. Mergos, P. E. and Kawashima, K. [2005] "Rocking isolation of a typical bridge pier on spread foundation," Journal of Earthquake Engineering 9(2), 395–414.

[53]. Meyerhof, G. G. [1951] "The ultimate bearing capacity of foundations," Géotechnique 2(4), 301–332.

[54]. Muir Wood, D. [2004] Geotechnical Modelling, Spon Press, London

[55]. Negro, P., Paolucci, R., Pedretti, S., and Faccioli, E. [2000] "Large-scale soil–structure interaction experiments on sand under cyclic loading," Proc. of the 12th World Conference on Earthquake Engineering, Auckland, New Zealand, Paper 1191

INTERNET REFERENCES

[1] http://nees.ucsd.edu/facilities/

[2] http://nees.ucsd.edu/facilities/shake-table.shtml

[3] https://www.youtube.com/watch?v=LO9ffdJ258A